University of Strathclyde Engineering

AN INVESTIGATION INTO THE DYNAMICS OF GRAVITATIONAL AND SURFACE-TENSION DRIVEN FLOWS IN DISCRETELY HEATED SYSTEMS

BY

WASIM WARIS

A DISSERTATION

Submitted to the Department of Mechanical and Aerospace Engineering

University of Strathclyde

For the degree of

Doctor of Philosophy

April 2023

Supervised by

MARCELLO LAPPA

Abstract:

Periodically distributed wall-mounted hot blocks located at the bottom of a layer of liquid with a free top interface are representative of a variety of technological applications in several fields (including, but not limited, to mechanical engineering, materials science, and the energy sector; related examples being power plants, solar energy collectors, nuclear reactors, energy storage systems and furnaces or crucibles). All these systems tend to create patterns in their surrounding fluid that are reminiscent of the classical modes of Rayleigh–Bénard or Marangoni–Bénard convection. In the present thesis, these subjects are investigated giving much emphasis to understanding how ensemble properties arise from the interplay of localized effects, i.e., different sources of heat. In particular, the problem is addressed from both numerical and experimental points of view. First numerical simulations are used to get relevant information about the dynamics of discretely heated systems for the case of opaque fluids (liquid metals) for which experiments are not possible, then the case of a transparent oil is considered. Through the used numerical framework, the emerging planforms are identified, and the statistics of the associated heat transport mechanisms are put in relation with the spatially averaged behavior of the underlying thermal currents. It is shown that in some cases, all these features can be directly mapped into the topography at the bottom of the layer. In other circumstances, these systems contain their own capacity for transformation, i.e., intrinsic evolutionary mechanisms are enabled, by which complex steady or unsteady patterns are produced. It is shown that self-organization driven by purely surface-tension or mixed buoyancy–Marangoni effects can result in 'quantized states', i.e., aesthetically appealing solutions that do not depend on the multiplicity of wall-mounted elements. The problem is also investigated experimentally considering an oil with temperature-dependent properties. By means of a concerted approach based on the application of a thermographic visualization technique, multiple temperature measurements at different points and a posteriori computer-based reconstruction of the spatial distribution of wavelength, it is shown that tuning of the physical topography at the bottom and the difference of temperature between the liquid and the external (gaseous) environment can still be used to enable internal feedback control over the spontaneous flow behavior. For a fixed geometry and temperature difference, variations in the emerging pattern can also be produced by changing the thickness of the liquid layer, which indirectly provides evidence for the additional degree of freedom represented by the relative importance of buoyancy and Marangoni effects. As a final variant, the case where the fluid container is inclined to the horizontal direction is also considered and it is shown that this fluid-dynamic system is prone to develop a rich set of patterns, which include spatially localized (compact) cells, longitudinal wavy rolls, various defects produced by other instabilities and finger-like structures resulting from an interesting roll pinching mechanism.

Acknowledgement:

First and foremost, I would like to thank my esteemed supervisor **Marcello Lappa** for his invaluable supervision and support during the course of my PhD degree. His exceptional knowledge and experience have encouraged me in all the time of my academic research. I would like to thank my friends, lab mates, colleagues and research team for a cherished time spent together in the lab, and in social settings. Finally, I would like to express my gratitude to my parents and siblings. Without their exceptional support and encouragement in the past few years, it would be impossible for me to complete my study.

List Of Publications:

The following papers were published/submitted during the completion of my PhD.

1. M. Lappa, A. Sayar and W. Waris, (2021), Topographically Controlled Marangoni-Rayleigh-Bénard Convection in Liquid metals, FLUIDS (ISSN: 2311-5521), 6(12), 447 (23 pages).DOI: 10.3390/fluids6120447.

2. M. Lappa and W. Waris, (2022), On the role of heat source location and multiplicity in topographically controlled Marangoni-Rayleigh-Bénard convection, Journal of Fluid Mechanics (ISSN: 0022-1120), 939, A20 (39 pages). DOI: 10.1017/jfm.2022.175.

3. Waris, Wasim and Lappa, Marcello (2023) Patterning behaviour of hybrid buoyancy-Marangoni Convection in inclined layers heated from below. Fluids, 8 (1). 12. ISSN 2311-5521 (https://doi.org/10.3390/fluids8010012)

4. W. Waris and M. Lappa, (2023), Thermographic Analysis of Topographically Controlled Thermal Convection in a Fluid with Temperature-dependent Properties, Ready for submission.

Table of Contents:

Contents:

List of Figures:

List of Tables:

List of Abbreviations:

Abbreviation	Meaning
AR	Aspect Ratio
Ca	Capillary Number
CPPE	Consistent Pressure Poisson Equation approach
Ga	Galileo Number
LSA	Linear Stability Analyses
LR	Longitudinal Rolls
Ma	Marangoni Number
MB	Marangoni-Bénard
RB	Rayleigh-Bénard
Nu	Nusselt Number
PBC	Periodic Boundary Conditions
Pr	Prandtl Number
Q	Wave Number
Ra	Rayleigh Number
RBC	Rayleigh-Bénard Convection
SV	Skewed Varicose
TR	Transverse Rolls
Bi	Biot number

List of Symbols:

Symbol	Meaning
A_x	Aspect Ratio of Fluid Domain
A_{xbar}	Aspect Ratio of Block
Bo_{dyn}	Dynamic Bond number
β_T	Thermal Expansion Coefficient
d	Characteristic Depth of the Fluid Layer
g	Gravitational Acceleration
k	Thermal Conductivity
l_{horiz}	Horizontal Length of Block
l_{vert}	Thickness of Block
L_x	Horizontal Extensions of Fluid
L_z	Horizontal Extensions of Fluid
Nu	Nusselt Number
T_{ref}	Ambient Temperature
ν	Fluid Kinematic Viscosity
V_r	Characteristic Flow Velocity
q	Wavenumber
Ω	Effective Volume
σ	Surface Tension
ρ	Density of the liquid
ΔT	Characteristic Temperature Difference
α	Thermal Diffusivity
Δt	Time Integration Step
ω	Angular Frequency
ξ_x	Distance Between Blocks

Chapter 1:Introduction:

In many different types of thermal convection, the nature of the force driving fluid motion and the direction of the prevailing temperature gradient can have a paramount importance in determining the properties of the flow. As an example, the different outcome in terms of convective structures and related hierarchy of bifurcations when the cases of temperature difference parallel or perpendicular to gravity are examined is one of the main reasons for the existence of a fundamental dichotomy in the literature, i.e. the distinction between Rayleigh-Bénard (RB) convection (Busse, 1994) and the equivalent buoyancy flow in laterally heated systems (the so-called Hadley problem) (Gelfgat, 2020; Melnikov and Shevtsova, 2005; Kaddeche, Henry, and Benhadid, 2003). A similar concept holds if variations of density are replaced with gradients of surface-tension: the different orientation of the imposed temperature difference with respect to the free interface (temperature gradient perpendicular or parallel to it) gives rise to two different variants of surface-tension driven convection, generally known as Marangoni-Bénard (MB) (Kawamura, Ueno, and Kurosawa, 2002) and thermocapillary (or simply Marangoni) flow (Shevtsova, Nepomnyashchy and Legros, 2003; Lappa, 2007; Lappa and Ferialdi, 2017; Nadjib, Adel, Djamel and Abderrahmane, 2018).

These well-established paradigms have instigated much research leading to a significant amount of knowledge. Most of this success has come from the remarkable simplicity of the related kinematic and thermal boundary conditions (smooth surfaces and uniform temperature distributions) and the associated possibility to conduct experiments in well-controlled conditions. At the moment, the results are spread in myriad papers and those who wish to get in touch with the field may consider some relevant books where such knowledge has been collected in a structured way (Koschmieder 1993; Getling 1998; Colinet, Legros & Velarde 2001; Lappa 2009, 2012). It should be remarked, however, that although studies on these fundamental modes of convection and the related hierarchy of bifurcations are not showing any obvious sign of reaching a limit yet (relevant investigations being still produced at a constant rate), the need to place part of these efforts in a more practical context has stimulated the development of ‘alternate’ lines of inquiry.

This endeavor, which has not yet been fully explored, has been produced essentially by the ambition (and/or concrete need) to increase the translational applicability of this type of research to technological problems where fluid motion can be brought about by many mechanisms working ‘in parallel’ (i.e., coexisting). This typically happens in circumstances where the thermal boundary conditions are not uniform, the solid boundaries delimiting the fluid are not flat and point-like, spot-like or finite-size (extended in the three-dimensional space) sources of energy are present, which result in a complex distribution of differently oriented gradients of temperature.

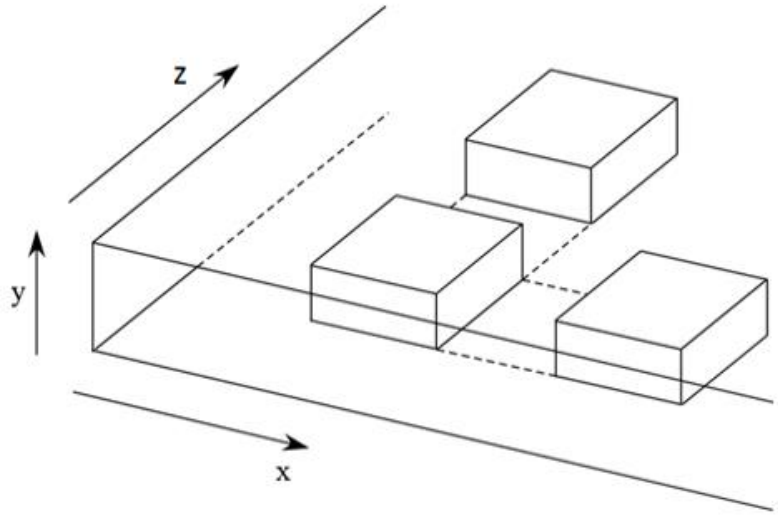

Figure 1: Three-dimensional view of the fluid layer hosting an array of square bars resting on the bottom wall (hot blocks), uniformly spaced along the x and z (horizontal) directions (spacing, width and height can be systematically varied).

Along these lines, fluid systems with a discrete distribution of heat sources have received appreciable attention in recent years by virtue of their omnipresence in engineering. Relevant examples at a relatively small scale are represented by the electronic boards of computers and other electronic devices. These systems typically consist of memories and CPUs able to generate heat, which can be regarded as independent finite-size sources of thermal energy. In these cases, natural convection is generally regarded as cheap and convenient cooling strategy because it does not require auxiliary electromechanical equipment. Although, the fluid in contact with such hot elements is typically air, cases exists where these components and other electronics are submerged in thermally conductive dielectric liquids as in this way the cooling efficiency can be increased. Liquids are also used as electrical insulators in high voltage applications where they prevent rapidly extinguish electric discharges. Other relevant examples of systems with localized sources of heat include power plants, solar energy collectors, nuclear reactors, energy storage systems and furnaces or crucibles (Widawski, Rawiso and François, 1994; S. Khan, 2017; Ismagilov, Rosmarin, Gracias, Stroock, and Whitesides, 2001). Some relevant examples are shown in Figures 2-5.

Figure 2: Battery-based energy storage systems (APR Energy, 2018).

Figure 3: Fossil fuel-based power generators (APR Energy, 2018).

In the majority of cases, buoyancy convection is the dominant mechanism of natural convection. As explained before, however, for cooling purposes liquids can also be used. Often these exhibit a free surface. i.e., an interface where they are in contact with a gas. In these situations, surface-tension driven (thermocapillary, i.e., Marangoni) convection is also produced. Given its relevance to several technological applications (see again Figures 2-5), the overarching aim of the present thesis is to explore the dynamics of thermal convection in systems with localized sources of heat. To do so a 'general' model is considered (see Figure 1), which consists of a layer of liquid with a free interface at the top and a set of three-dimensional blocks (rods) of square cross-section (parallelepipedal shapes) regularly arranged at its bottom along two perpendicular horizontal directions (thereby resembling the squares of a checkerboard or the elements of a structured grid).

As explained before, this simple problem is representative of, or it is intended to model a variety of technological systems at different scales (electronic boards, energy storage systems, power plants, nuclear reactors, etc.). The problem is addressed here by means of numerical simulations and experiments. With regard to the numerical simulations, both cases with buoyancy convection and mixed (hybrid) buoyancy-Marangoni convection are considered. For the latter case, no results exist in the literature (as illustrated in chapter 2, most of the existing results for fluid systems with discrete sources of heat are for buoyancy convection only).

Obviously, in addition to the purely theoretical implications represented by the inclusion of a new driving force (surface tension effects) in this specific line of research, the present thesis also aims to build new information potentially supporting the introduction of new technologies in other fields with respect to those highlighted in the preceding text. Indeed, micro-patterned surfaces delimiting a liquid in contact with an external gas are critical to the development of moulds or scaffolding for forming ordered microstructures. They can be used as model substrates for a variety of applications in surface science and are at the root of several lab-on-chip devices. A relevant example is represented by the preparation of porous polymer membranes for innovative processes where the biggest challenge is represented by the need to control both the size distribution and the relative positions of the pores (Ismagilov, Rosmarin, Gracias, Stroock and Whitesides, 2001). They also find application in controlled release of drugs or other bioactive species (Zhao et al., 2001) and enhanced cell culturing (Wang, Yu, Mei and Xue, 2017). Last but not least, engineered surfaces with topographies that scale favorably at small length scales can be used for the production of nanocrystals or to assemble microscopic particles into regular lattices; in these applications, the ability to control the fluid-dynamic conditions is the key to obtain desired deposition conditions or to generate lattices with well-defined properties.

Figure 4: Electronic board with related CPUs and memories (Parm, 2009).

Figure 5: Bars or nuclear fuel in nuclear reactor (water being used as cooling fluid) (ANS Nuclear Cafe, 2014).

The present thesis is structures as follows: In Chapter 2 after a brief survey of the existing literature for the classical modes of convection represented by Rayleigh-Bénard (RB) and Marangoni-Bénard (MB) convection in layers uniformly heated from below, an exhaustive review is elaborated for thermal convection in systems with localized sources of heat (discretely heated systems). Chapter 3 is dedicated to a presentation of the equations governing the behavior and evolution of these types of convection, together with the related boundary conditions. The related numerical method is discussed in Chapter 4, together with a validation study and a mesh refinement analysis. Chapter 5 includes a description of the experimental facilities and tools used to conduct the experiments performed with water, oil and other transparent liquids considered in this thesis.

Chapter 5 is concerned with numerical results obtained for the cases of liquid metals. These liquids are opaque and therefore, numerical simulation is the only way to study the properties of convection generated by localized sources of heat. In Chapter 6, the numerical treatment is extended to the case of oil, for which the dynamics become much more complex. In Chapter 8 and 9, the main outcomes of the experiments conducted using the methods described in Chapter 7 are analyzed.

Chapter 2: Literature Review

As already outlined in Chapter 1, thermal Convection is a type of heat transfer mechanism in which heat is transferred from one place to another due to movement of the fluid induced by "natural" forces. In the presence of gravity, a fluid expands when heated and becomes less dense due to which it starts to rise upward. In the presence of a free surface, fluid moves along the interface from the hot side to the cold side as, in general, surface tension is a decreasing function of temperature. Fluid flow properties are determined by various parameters, but the two most important factors are the nature of force which drives fluid motion and the direction of the temperature gradient. Different convective structures emerge depending on whether the temperature gradient is parallel or perpendicular to the gravity. Additional details are briefly reported in the following two sections for the cases where convection is induced by gravity and surface tension, respectively (Sects. 2.1 and 2.2). Thereafter, the existing literature for discretely heated systems or systems with a topography (the main subjects considered in the present thesis) is also reviewed (Sects. 2.3 and 2.4).

2.1 Rayleigh-Benard Convection:

2.1.1 Primary mode of convection:

Rayleigh Benard Convection (RBC) is a type of natural convection occurring in a plane horizontal layer of fluid heated from below. The simplest pattern which can occur in RBC consists of straight and parallel rolls. Most of studies have also discussed the stability of the quiescent state of nonconfined fluid layer when heated from below. In that case, a fluid layer with a horizontal extent that is large as compared to vertical depth has been typically considered. The temperature on the bottom surface of the fluid layer is increased and accordingly its density decreases. Fluid over hot fluid has high density due to which it starts to break down and an overturning process is enabled. Driving forces and dissipation of energy are the main factors behind the emerging flow structures which are known as dissipative structures.

When fluid is heated from below then buoyancy forces of the hot fluid side cause instability which is then counteracted by viscous forces and thermal diffusion of the fluid. In theoretical investigation of that configuration three different possible boundary conditions were considered which are (a) stress-free isothermal horizontal boundaries, (b) no-slip isothermal horizontal boundaries and (c) stress-free thermally insulated upper and no-slip isothermal lower boundary. Actually, Ra depends on the height of the fluid layer and in all these three conditions it was 657, 1707 and 669, respectively. In these cases, instability was driven by two dimensional perturbations of diffusive state and fluid motion produced a regular and organized set of parallel rolls which were aligned along an arbitrary direction.

Jeffreys (1926) was the first person who conducted a stability analysis for a fluid layer which was confined between two well-conducting parallel plates. He obtained $Ra_{cr}=1707$ where Ra_{cr} is the critical Rayleigh number (see Sect. 3.2 for the definition of Ra) i.e., the minimum value of the characteristic parameter needed to obtain convection. In 1958 Malkus and Veronis used nonlinear equations describing the fields of motion and temperature for stress-free condition and concluded that there are infinite number of steady-state finite amplitude solutions which satisfy these equations (Malkus and Veronis, 1958).

They also explained the relation between Prandtl number and the amplitude of the convection. They said for large Prandtl numbers the amplitude of the convection can be determined by distortion of the distribution of temperature and by the self-distortion of disturbances. But when Pr number becomes less than unity then self-distortion factor plays dominant role in determination of the amplitude. According to these studies expected nondimensional diameter of the emerging convective cells is the half of critical wavelength which depends on the horizontal wavenumber at the onset. Horizontal size of these cells in no-slip conditions was found very close to the height of the fluid layer but larger in diameter in case of stress-free conditions. Marginal stability curve for Rayleigh-Benard convection is shown in Fig 6, where regions are defined on the basis of wavenumber (q) and marginal Rayleigh number. Fig 7 is showing the shadowgraph image of two-dimensional convection for Pr=1, where Rayleigh number is twice of critical Rayleigh number. This figure actually shows the implementation of theoretical findings by Malkus and Veronis in real experimentation, where it can be seen that apart from the irregularities in fluid motion and defects in convective pattern, the velocity field of roll convection appears nearly two-dimensional.

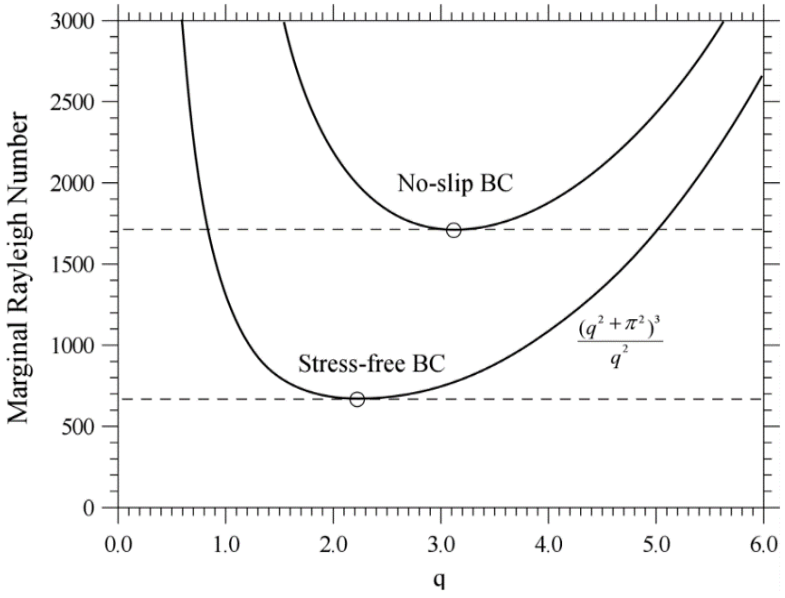

Figure 6: Marginal stability curves for Rayleigh-Benard Convection in an infinite layer. (Pellew and Southwell, 1940)

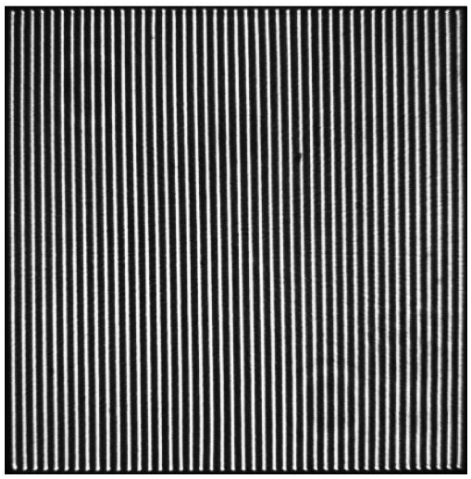

Figure 7: Shadowgraph image of two-dimensional convection (Pr=1 and Ra=2Ra_{cr}). (Plapp and Bodenschatz, 1996).

2.1.2 Secondary Convective Modes:

The simplest convective pattern which can occur in RBC is the straight and parallel rolls for dimensional whose horizontal length is twice of the depth of the fluid layer. But this convective pattern becomes more complicated when Ra starts to increase. For every Ra which is higher than Ra_{cr}, there is a range of the wavenumbers for which the convective rolls can exist. In Fig 8, schematic diagram of rolls in RBC is shown where it can be seen that for a laterally unlimited domain, the fluid motion is regular and organized as a set of horizontal parallel rolls. But not all of these rolls exist in stable state because there is a set of secondary instabilities which restrict the domain for which stable convection exists. Busse and co-workers described all these possible secondary instabilities which can occur in RBC when infinite layers are bounded from below and above by isothermal solid walls. They analysed stability of two-dimensional rolls with respect to three dimensional disturbances. Convective rolls were found unstable for Pr number less than 5 with respect to an oscillatory instability which was investigated in the case of free boundaries. They presented an expression which can be used to predict ideal straight rolls in a convection process (Clever and Busse, 1974). They predicted different modes of secondary instabilities which are Eckhaus, cross-roll, knot, zigzag and others.

$$\sum_{m,n} a_{m,n}^{(i)} \exp\,(imqx) G_n^{(i)}(y)$$

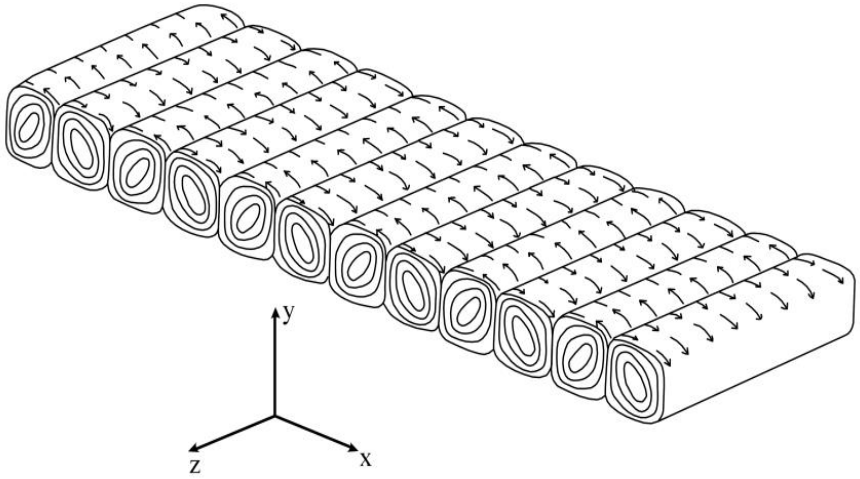

Figure 8: Schematic diagram of rolls in RBC: for a laterally unlimited domain, the fluid motion is regular and organized as a set of horizontal parallel rolls. (Clever and Busse, 1974).

Busse balloon is the region defined by wavenumber and other control parameters where convective rolls are found stable and its form depends on the Prandtl number. In primary mode, primary onset of convection remains same while secondary instabilities take different shapes according to different Prandtl numbers. Inside this balloon periodic structure of the rolls is stable but becomes destabilized by secondary instabilities on crossing the defined boundaries.

According to three-dimensional sketch of Busse balloon shown in Fig 9, possible instabilities are identified on the basis of wavenumber, Prandtl number and the ratio of Rayleigh to Critical Rayleigh number.

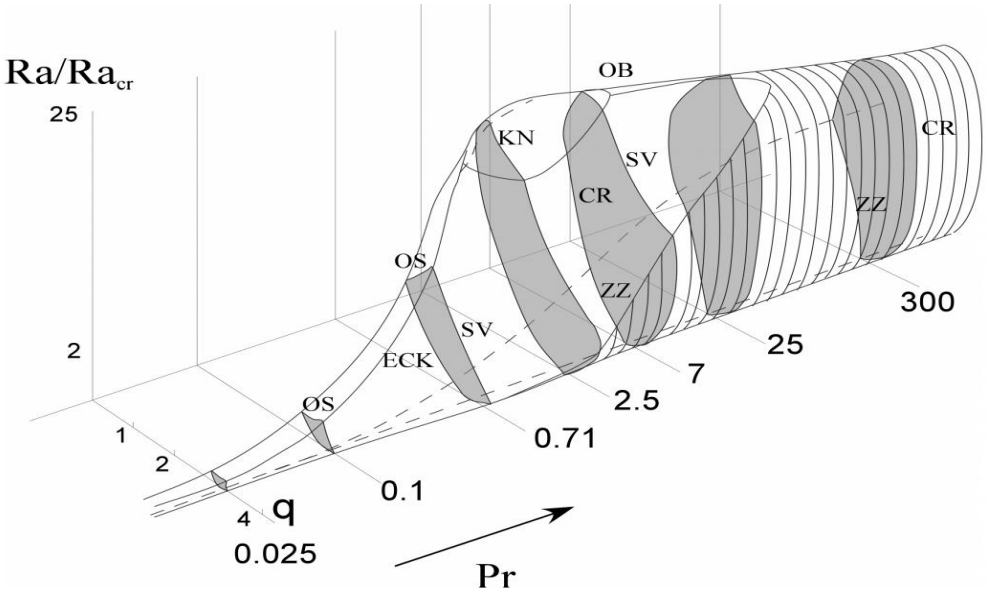

Figure 9: Sketch of Busse balloon in three dimensions: Ra, Prandtl number and wavenumber. The various solid curves mark boundaries outside of which two-dimensional convecting rolls of wavenumber q are stable. (Clever and Busse, 1974).

Eckhaus instability with a long wavelength modulation of the form $e^{iqx}.e^{iS_x x}$ is known as the simplest instability of secondary instabilities. In this expression, q is the wavenumber of the pattern while S_x is the floquet wavenumber along the axis of the rolls. i is an imaginary unit number whose value is $\sqrt{-1}$. Presence of iota in exponential function indicates that waves or patterns could be analysed from both real and imaginary axes. On the other hand, x represents the direction of the plane in which the roll pattern exists and to be analysed. If a roll pattern is near Eckhaus boundary at some Ra and q, then due to decrement in Ra evolution of this instability produces another roll pair with increment in wavenumber. This instability is a slow growing instability due to which in some cases cross-roll instability will occur before it due its short wavelength and fast-growing ability. Fig 10 is showing the snapshot of a totem structure where cross-roll instability was found for Pr=1 and ratio of Rayleigh to critical Rayleigh number was 1.7.

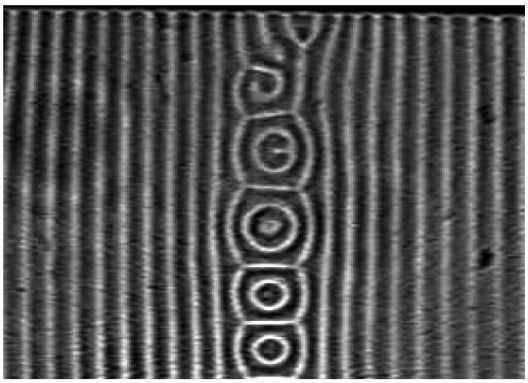

Figure 10: Snapshot of a totem structure (cross-roll instability, Pr=1.09, Ra/Ra_{cr}=1.7). (Plapp and Bodenschatz, 1996).

Busse and Whitehead (1971) performed an experiment on the stability of convection rolls in a high Prandtl number fluids. They concluded that in cross-roll instability rolls emerge at right angles to the original pattern of rolls. They also concluded that when Ra becomes higher than 23000 then convective rolls become unstable for all wavenumbers and replaced by three-dimensional stationary convection which named as bimodal convection.

When Ra increases then wavenumber in cross-roll instability becomes higher than critical wavenumber due to which a steady boundary layer type structure appears, and its evolution produce a new form of convection which is known as **bimodal Convection**. Sketch of Bimodal convection is shown in Fig 11. Bimodal convection was found more efficient in term of heat transportation than two dimensional rolls due to its small wavelength factor.

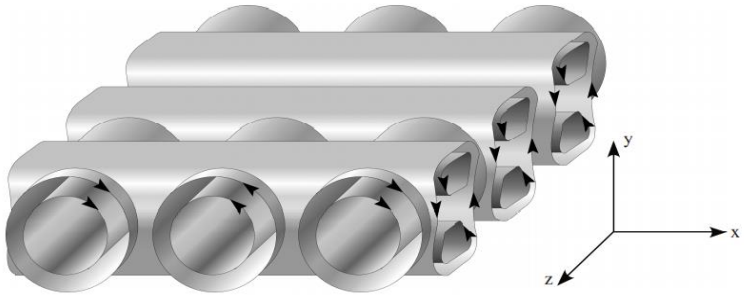

Figure 11*:* Sketch of Bimodal Convection. (Busse and Whitehead, 1971).

Busse continued his investigations on instabilities of convection rolls for different Prandtl numbers.Busse and Clever (1979) considered moderate Prandlt number in their investigations on instabilties of convective rolls and presented knot instability which were found a more efficient convective heat transport. Knot instabaility acts same like cross-roll instability but has smaller wavenumber along axis of the rolls. When Ra becomes higher than 30000 then plumes evolve along currents of rising and descending liquids and streamers feed these plumes by evolving in the thermal boundary layers. In shadowgraph of this convection process these features were found like knots due to which this instability were named as **knot instability**. It disappers where Prandlt number in fluids becomes small or large.

Skewed Varicose instability is modulated by following expression $e^{iqx}.e^{iS_x x+iS_z z}$ where S_x, and S_z were found less than wavenumber. Fig 12 is showing the snapshot of skewed varicose instability which was found by Plapp and Bodenschatz for Pr=1.07, Ra=3.26Ra_{cr}. According to Clever and Busse investigations this instability produces a shearing effect across the rolls due to which roll pair splits in two parts by creating two different defects in the roll pattern. Then these defects remove a roll pair from its original pattern and decrease the wavenumber. Angle of SV instability relative to original roll pattern was found close to 45^o. SV instability disappears in the limit of high and small Prandtl numbers.

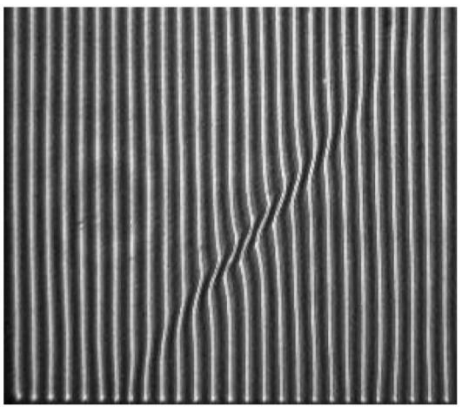

Figure 12: Snapshot of Skewed Varicose instability (Pr=1.07, Ra=3.26Ra_{cr}). (Plapp and Bodenschatz, 1996).

Busse and Clever (1987) performed numerical analysis and showed that Oscillatory instability appears as a short wavelength propagating along the rolls which is described by following expression $e^{iS_z z}.e^{i\omega t}$ where ω is the angular frequency of the wave. They performed numerical analysis on three-dimensional time dependent solutions which bifurcate from two-dimensional convection rolls at the onset of the oscillatory instability. When Ra increases then this bifurcation factor causes forward and backward periodic shifting and deformation of the convection rolls. This instability does not destroy the convection roll structure but simply adds a wave which propagates along the rolls.

Clever and Busse (1991) calculated oscillatory instabilities of long ,straight and parallel rolls and found them in the form of travelling waves (See Fig.13, where Snapshot of travelling wave related to OS instability is shown which was produced by Plapp and Bodenschatz). They also concluded that with no-slip boundary conditions in the limit of low Pr number when Ra becomes 1854 then thermal convection of the rolls in fluid layer which is heated from below starts to convert into travelling waves. For Pr<0.02 they found travelling wave convection in stationary state with respect to a moving frame of reference.

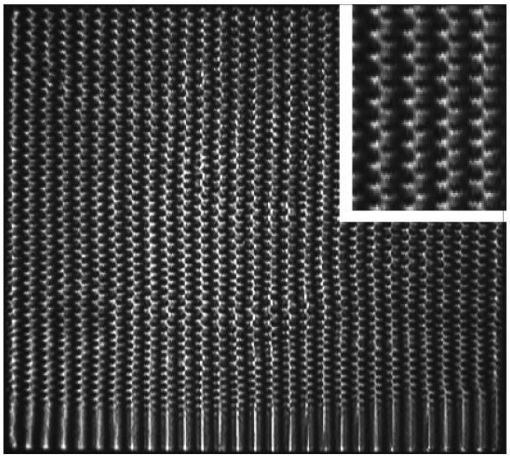

Figure 13*:* Snapshot of travelling wave related to OS instability (Pr≅1 and $Ra/Ra_{cr} \cong 6$). (Plapp and Bodenschatz, 1996).

2.1.3 Spoke pattern convection:

According to the discussion in previous section, different possible secondary instabilities which can exist become more complex when the Rayleigh number becomes higher. These instabilities occur in different modes at different Pr numbers. In primary mode two-dimensional but time-dependent rolls were found but according to Busse balloon, time dependence factor exists at low Pr and Ra then due to secondary instabilities rolls at high Pr and Ra were found in three-dimensional time-dependent states. In 1970 Ruby Krishnamurti performed an experiment on the transition to turbulent convection. In that experiment he used different fluids with different Pr numbers from 1 to 10000. The main objective was to analyze the Rayleigh number at which steady convective flow changes to time-dependent flow. In final results he found a systematic increase in related critical Ra when Pr number becomes higher (Krishnamurti, 1970).

Busse and Whitehead (1974) performed experimental study on transition from steady bimodal convection to time-dependent convection. They found that oscillatory instability of bimodal

cells introduces standing waves which are similar to those which occurred in low Pr number convection (Busse and Whitehead, 1974). In their experimental results it was observed that oscillations occur in the form of standing waves on the boundary of short-wavelength components of bimodal convection but disappear on long-wavelength components.

Busse and Clever (1989) studied three-dimensional convection flows which were induced by knot instability of two-dimensional convection rolls and their final solution showed knot-like structure superimposed on the basic convection rolls (Busse and Clever, 1989). After both studies a notable similarity was found in oscillatory form of knot and bimodal convection. In both convections mechanism of transition from steady to time-dependent state was due to emergence of hot and cold blobs from hot and cold boundary layers.

Busse and Whitehead (1974) discussed oscillatory instability of bimodal convection but also found another instability which was Collective Instability. Collective instability introduced spoke-pattern convection which was characteristic for turbulent large Prandtl number convection. Spoke pattern convection was observed when a fluid layer was heated from below and Ra became higher than 30000 (See Fig. 14). In that case Pr number was greater than 10. Upper and lower boundaries of the fluid layer were unstable which caused eruption of hot and cold fluid sheets which moved radially inwards towards central plumes.

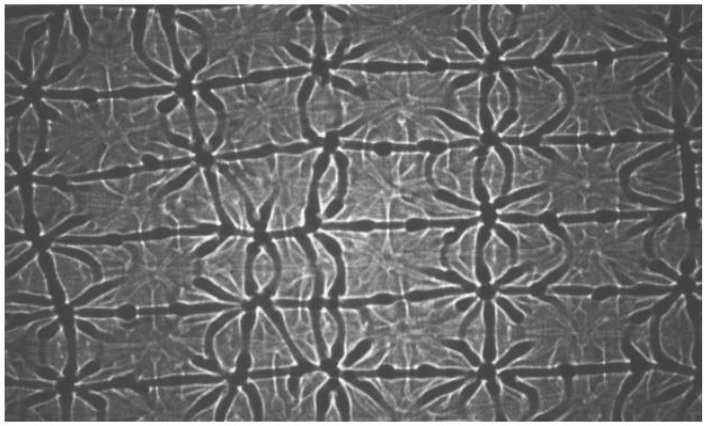

Figure 14: Shadowgraph image of spoke pattern convection in a layer of silicon oil for Pr=63. (Busse and Whitehead, 1974).

When amplitude of oscillation of a cell on basic roll becomes large then it starts to combine with neighbouring cell on the same roll. Knots structure present at the intersection of bimodal cells with basic rolls gravitates towards a common centre of the basic rolls and produce spoke structure. Boundaries with short wavelength produce spoke pattern but continue to oscillate at roughly the same frequency. Spoke pattern convection exists at Ra>30000 but starts to fluctuate when Ra becomes higher than 10^6. Wavelength in spoke pattern convection is a distance between centres of two spokes with same sign. Wavelength has inverse relation with Pr number of the fluid. M. Lappa performed numerical simulation in which Ra was set to 50000 and Pr was changed from 7 to 15.

In spoke pattern convection process of eruption of thermal blobs from the boundary layer and their transport in the form of plumes was already seen in knot convection which existed due to instability of two-dimensional convection rolls. It means that oscillatory knot convection can be considered as initial stage of spoke pattern convection at moderate Pr number.

2.2 Marangoni-Benard Convection:

In Rayleigh-Benard convection section, it already has been discussed that in buoyancy-driven convection flows patter formation process is driven by a vertical temperature gradient. This section explains another significant class of patterns in which convective phenomenon originates from another kind of driving force which arises as consequence of the dependence of surface tension on temperature. When temperature gradient is applied perpendicular to the free surface of the fluid layer then this type of convection is known as Marangoni-Benard Convection. Benard first time observed the hexagonal pattern resembling the architecture created by bees for their honeycomb (Benard, 1900).

Block (1956) provided experimental demonstration on the role of surface tension in formation of these planforms. He observed convective cells at $Ra<Ra_{cr}$ when thermogravitational mechanism was not active. Pearson did theoretical investigations on the linear stability analysis of flows in which he used same mathematical framework which was already employed in RBC. Fig 15 is showing Marginal stability curve for pure Marangoni-Benard Convection in infinite layers. He neglected gravitational term in momentum equation and replaced upper boundary conditions for velocity and temperature with those modelling a Marangoni stress and heat exchange with ambient (Pearson, 1958).

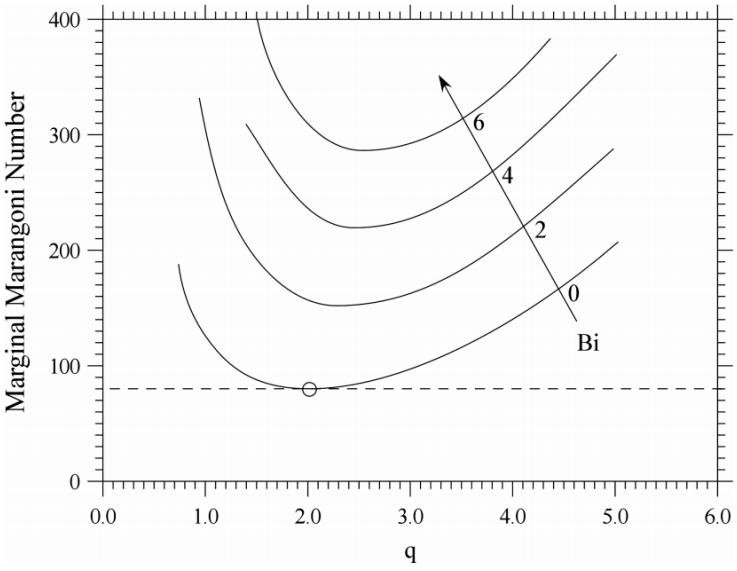

Figure 15: Marginal stability curve for pure Marangoni-Benard Convection in infinite layers.

Nield (1964) provided important evidence of the fact that surface tension forces are main drivers of Marangoni instability in layers with depth of millimetres. Ma number scales linearly with the depth of the fluid layer but Ra shows cubic dependence on the depth. Pearson's linear stability analysis showed that system becomes unstable above Ma=79.607, where Ma is the so-called Marangoni number (see Sect. 3.2 for its definition), but Davis proved that system is

unconditionally stable below Ma=56.77 (Davis, 1968). Presence of convective cells induced by this type of flow on the free surface of the liquid layer can be detected by different experimental techniques. Experimental results of surface tension driven convection are more-sparse as compared to Rayleigh Benard Convection. In Fig 16, shadowgraph and schlieren images produced through optical visualization method are showing photographs of final results of surface cells observed over free surface of silicon oil.

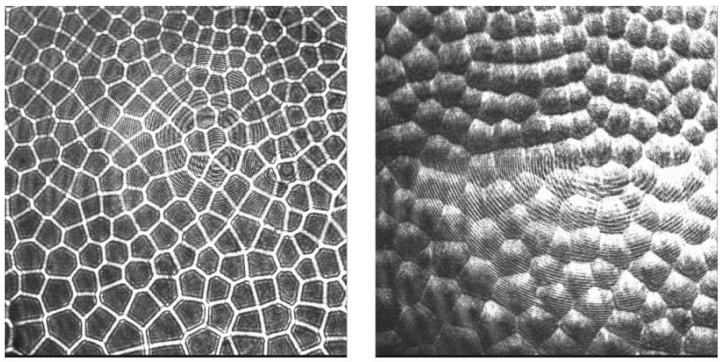

Figure 16:. Photographs of surface cells in silicon oils over free surface provided by different optical visualization methods: (a) Shadowgraph image (b) Schlieren image (Lappa, 2009).

High Pr number fluids were used in experiments when the disturbances were responsible for the onset of convection saturates their amplitude then pattern was characterised by hexagonal cells. Fig 17 is showing the thermographic image of the fluid layer with free surface. Comparison between velocity and temperature fields related to this pattern is shown in fig 18 which were obtained through computer simulations. This structure is known as typical feature of Marangoni Benard Convection which can also be observed in RBC at specific conditions.

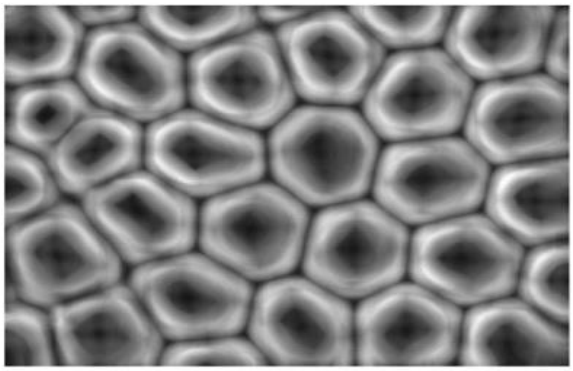

Figure 17: Thermographic image of surface cells in silicon oils over free surface (digitally enhanced) (Lappa, 2009).

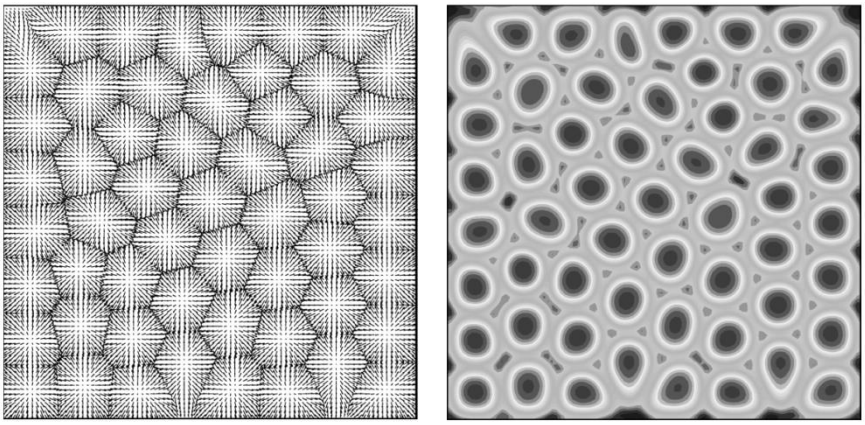

Figure 18: Hexagonal cells due to Marangoni-Benard convection, observable on free surface of silicon oil of 1 cSt covered by layer of air, having depth of 1mm and horizontal extension $L_x=L_z=2$cm with Ma=200: (a)velocity field (b) temperature distribution (numerical simulation, Lappa, 2009).

Convective cells over free surface become more stable with increment in Marangoni number (Echebarria and Pérez-García, 2001). For moderate supercriticalities $\frac{Ma-Ma_{cr}}{Ma_{cr}} \cong 1$, size of hexagon cells decreases with Ma. At certain Ma number a new secondary pattern emerges in which hexagonal cells are replaced by square convective cells which become new persistent dominant feature of the flow. Transition from hexagon to square cells arises due to local change in topology in which vertices of initial hexagon cells become fourfold (Bestehorn, 1996). During transition, an edge which separates two vortices shrinks to zero length and two vortices coalesce to form intersection of four edges. As the vertices coalesce the angle between adjacent edges changes from 120 to 90. Initially this process produces pentagon cells which then convert into square cells. This means transition from hexagon to square cells is mediated by occurrence of pentagonal cells. Fig 19 is showing an example of convective pattern in the form of square cells (due to Marangoni-Benard convection) observed on the free surface of silicon oil which was covered by layer of air.

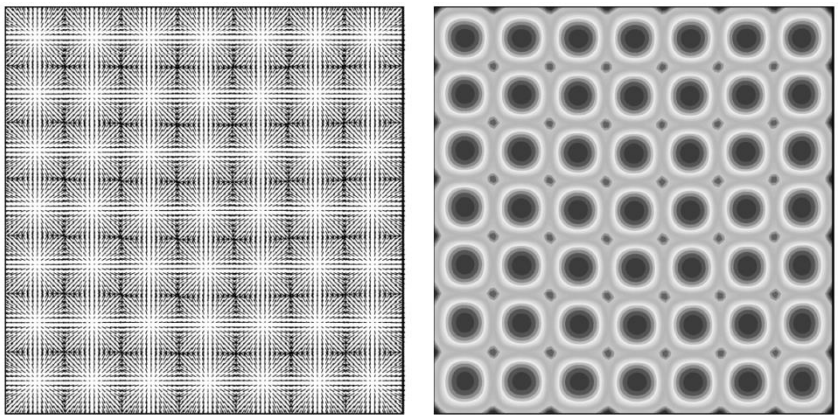

Figure 19: Square cells due to Marangoni-Benard convection, observable on free surface of silicon oil of 1 cSt covered by layer of air, having depth of 1mm and horizontal extension $L_x=L_z$ =2cm with Ma=400: (a)velocity field (b) temperature distribution (numerical simulation, Lappa, 2009).

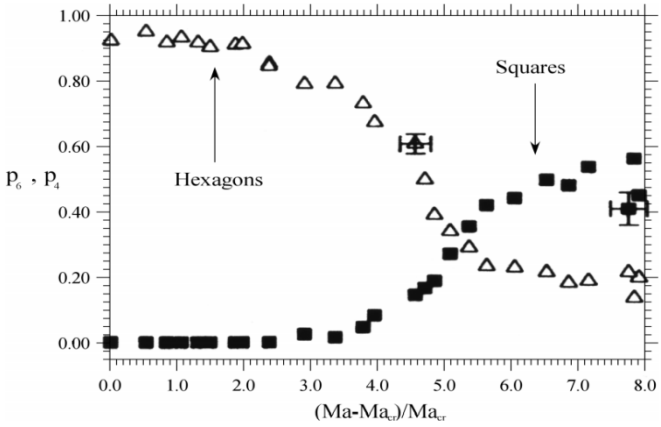

Figure 20: Fraction of cell class P_i as a function of $(Ma-Ma_{cr})/Ma_{cr}$. P_i is defined as the ratio between number of cells of a given planform and number of complete cells. After experiments of (Eckert,1998) for $Pr=10^2$.

2.3 Buoyancy flow in discretely heated systems:

Incropera (1988) studied convection and heat transfer in electronic equipment cooling and suggested that engineers should determine an efficient method for heat transfer from electronic devices, to maintain the thermal environment in electronic components. He also explained that this problem involves two types of components which are internal and external components. In these components heat transfer occurs by conduction through different materials and interfaces which separates devices from package surfaces and convection mechanism exists from surface to coolant.

For design analysis of these components and assessment of thermal performances, a model with horizontal flow over wall mounted cubes was developed in which these cubes act as heat-producing sources. Many researchers have tried to evaluate the related heat transfer coefficients, which are important for durability and reliability of microprocessors and memories. In electronic components, heat transfer coefficients depend on various geometrical

factors which are size of the chip, its position with respect to other electronic components and the channel height.

Conjugate heat transfer process involves temperature variations within solids and fluids due to thermal interaction between solid and fluid. Heating or cooling process of a solid object by the flow of air indicates conjugate heat transfer process. This process actually involves coupling of conduction in solid objects and convection in fluids and provide heat transfer path from heat source to the fluid. In most of studies of natural convection heat transfer from discrete heat sources this phenomenon was ignored, and idealised thermal conditions were applied at the interface of solid and fluid.

Heindel, Ramadhyani and Incropera (1995) developed two-dimensional (2-D) and three-dimensional (3D) conjugate models to predict flow and heat transfer within a discretely heated cavity. They also performed experimental measurements in which they used small heat sources and obtained flow visualization which were compared with numerical predictions (Heindel, Ramadhyani and Incropera, 1995). In this study they focused on investigations of coupled conduction and natural convection transport from an array of discrete and isoflux heat sources which were placed to one vertical wall of a cavity. Isothermal and adiabatic conditions were applied on opposite vertical wall and horizontal walls, respectively. Two different fluids water (Pr=5) and fluorocarbon (Pr=25) were simulated in calculations. The main objective of this study was to explain the nature and extent of 3-D effects on both flow and heat transfer. Fig 21 is showing schematic of the geometry which was modelled in 3-D numerical predictions. On vertical wall 3×3 array of discrete sources was mounted on a substrate of different thermal conductivity. An isoflux condition was imposed at the back of each heat sources.

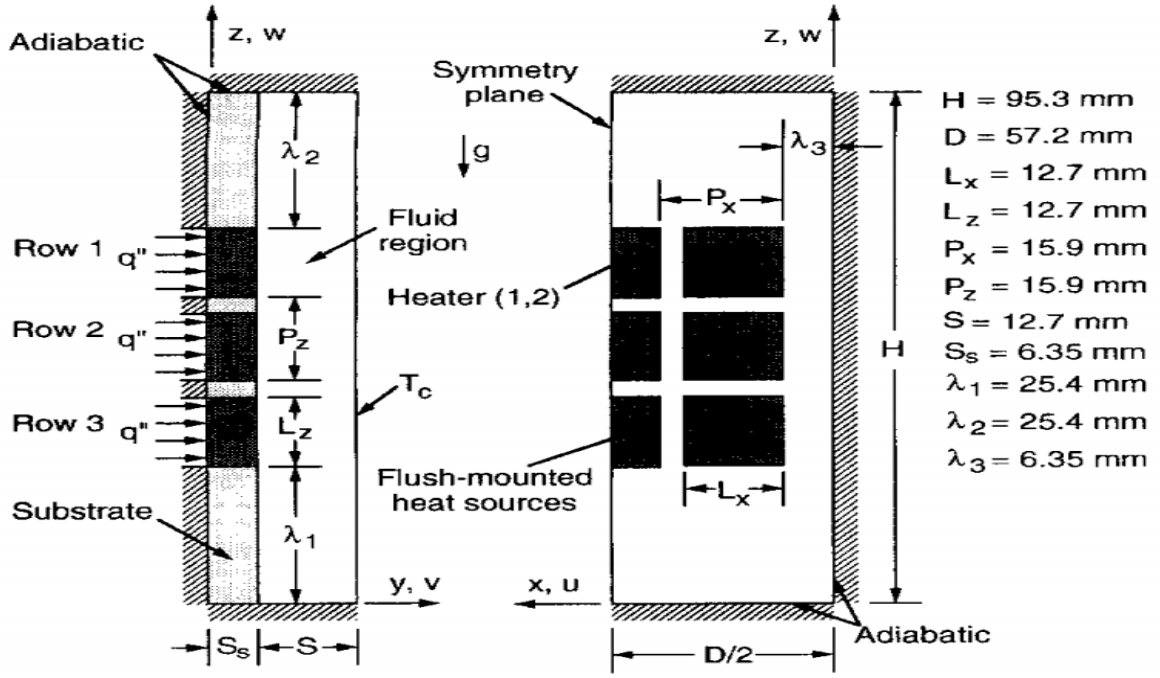

Figure 21: Numerical and Experimental geometry and nomenclature (Heindel, Ramadhyani and Incropera, 1995).

In governing equations for fluid and solid regions, the steady-state heat transfer was considered with constant thermal physical properties. Resistance between substrate and heater was negligible while Boussinesq approximation was considered in this case. Initial grid studies were performed in fluid region before conjugate calculations process, to ensure the boundary layers were satisfactorily resolved. Grid size was changed from 30×68 to 40×96 and average heat transfer rate on each heated surface was changed by 2%. But 30×68 grid size provided a good compromise between computational effort and accuracy in fluid region. But for conjugate calculations grid size in fluid region was changed to 29×80.

In experimental setup, test cell was consisted of 3×3 array of copper elements flush mounted in fiberglass substrate. Opposite cold plate and Lexan spacer plate were compressed between two aluminium clamping plates. Dimensions of each heater was 12.7mm× $12.7mm$ ×9.5mm. Cold copper plate was actually used for data collection and flow visualisation and due to large thermal conductivity, it was almost isothermal and maintained at 15℃. For flow visualisation, pliolite particles with small diameters were used in deionised water and it was assumed that these particles closely follow the fluid motion.

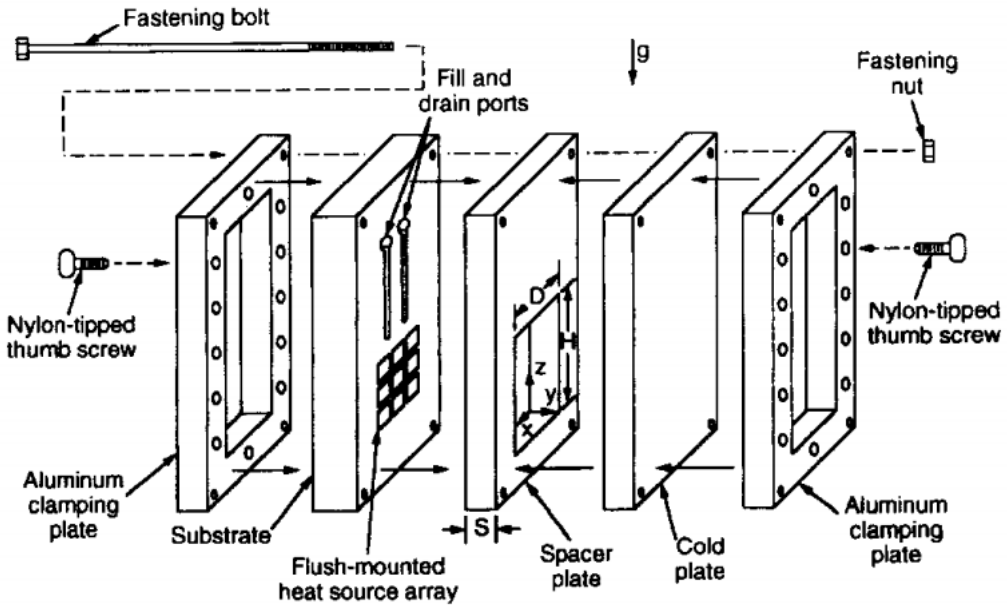

Figure 22: Schematic of the experimental test cell assembly nomenclature (Heindel, Ramadhyani and Incropera, 1995).

Range of modified Ra for water and fluorocarbon was $10^5 \leq Ra \leq 10^8$ and $10^5 \leq Ra \leq 10^9$, respectively. In numerical predictions, they found that thermal conductivity ratio of substrate/fluid has a significant effect on the shape of the vertical velocity profile in a discretely heated cavity. When substrate/thermal fluid conductivity ratio was 4.7 then thermal spreading process occurred through substrate and energy entered the fluid through substrate/fluid interface below the heater array. Fluid motion starts when this transport causes buoyancy forces below the heater. When fluid reaches near third row then buoyancy forces adjacent to heat source increase fluid momentum due to which velocities exceed the value predicted by nonconjugate model. When substrate/fluid thermal conductivity ratio increases then fluid flow

becomes more two dimensional while heat transfer remains uninfluenced by 3-D edge effects and thermal spreading in x-direction.

At low values of Rs (which is substrate/fluid thermal conductivity ratio measured by solid thermal conductivity/ fluid thermal conductivity), large spikes were found in heat flux near the edges of each heater. When Rs value becomes higher, then these spikes are smoothed out by substrate conduction which leads to lower heater temperature than predicted by 2-D model. As Rs value increases then variations in local heat flux and temperature along solid/fluid interface start to decrease. Flow visualisation confirmed the flow patterns predicted by conjugate models and values of average surface temperatures were in excellent agreement with experimental data.

In second part of this study, numerical investigations were performed on coupled conduction and natural convection transport from an array of discrete sources which was placed to one vertical wall of the cavity. Opposite vertical wall and horizontal walls were assumed to be isothermal and adiabatic, while Pr number and heater/fluid thermal conductivity were set to 25 and 2350, respectively (Heindel, Ramadhyani and Incropera, 1995).

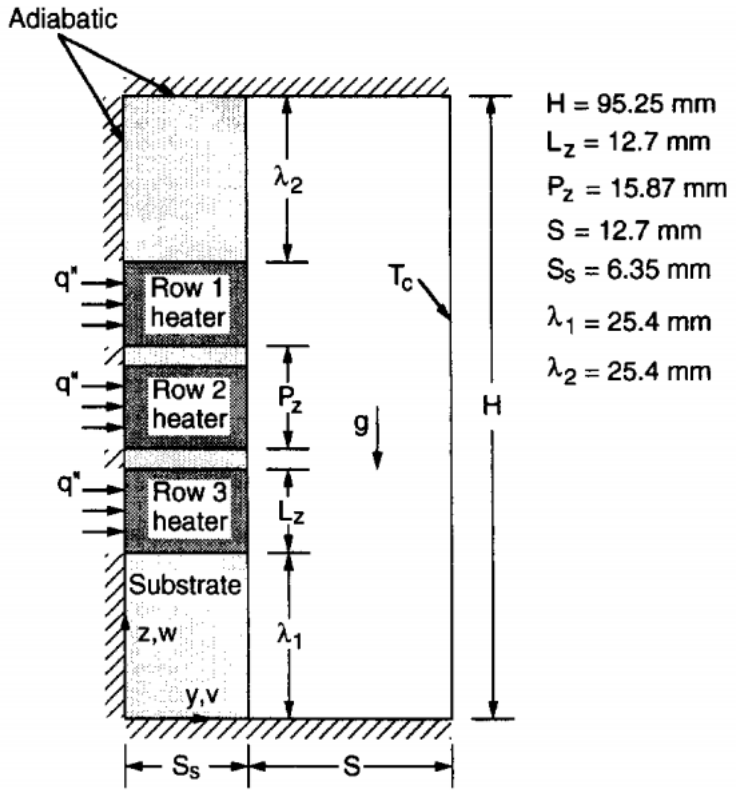

Figure 23: Schematic of discretely heated cavity nomenclature (Heindel, Ramadhyani and Incropera, 1995).

Main objective of this study was to analyze the effect of modified Rayleigh number and substrate/fluid thermal conductivity ratio Rs. Prandtl number was fixed at 25, while Aspect ratio of the cavity geometry was set to 7.5(AR=Cavity height/Width of cavity fluid region). Thermal conductivity of heater and heater/fluid region were 148W/ mK and 2350, respectively.

In Calculations, range of modified Rayleigh number was set to $10^4 \leq Ra_{Lz} \leq 10^9$ and substrate/fluid thermal conductivity was used between 0.1 to1000. Ra_{Lz} is the modified Rayleigh number which was calculated by following expression $Ra_{Lz} = g\beta q {L_z}^4 / k_f \alpha_f v$ where q is the local heat flux applied to the heater, L_z represents vertical heater length and k_f is thermal conductivity of the fluid.

Modified Rayleigh number was changed by altering the power supply to each heat source and its effect on fluid flow were shown in the form of streamlines. At modified Rayleigh number=10000, flow was found unicellular and weak with 8.2 dimensionless streamlines factor. In this case fluid flow produced a thick boundary layer which covered a small core of nearly stagnant flow above the center of the enclosure. In Fig 24(b), you can see that when modified Rayleigh number was increased to 10^9 then boundary layers became thin and core region started to increase in size. Flow became more complex due to additional recirculation zones and multiple cells in the central region of the cavity. At modified Rayleigh number=10000, fluid and solid regions showed vertical isotherms and heat transfer in fluid region was dominated by conduction When modified Rayleigh number was increased to 10^9 then central region of the fluid was found stratified with thin hot and cold boundary layers. Each heater face appears isothermal due to their higher thermal conductivity, but their temperature varies from heater to heater.

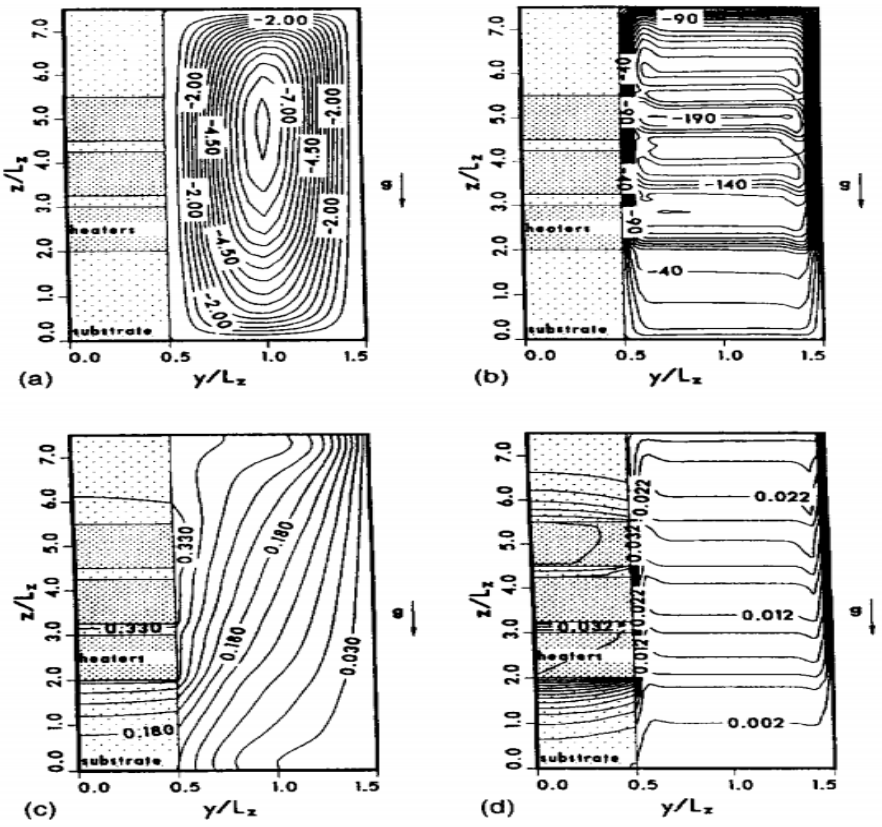

Figure 24: Dimensionless streamlines at (a)$Ra_{Lz} = 10^4$; (b) $Ra_{Lz} = 10^9$ and isotherms at (c)$Ra_{Lz} = 10^4$; (d)$Ra_{Lz} = 10^9$ for Pr=25, R_h=2350 and Rs=10 nomenclature (Heindel, Ramadhyani and Incropera, 1995).

Next step was to analyse the effect of substrate/fluid thermal conductivity ratio on fluid flow, for that modified Rayleigh number was fixed to 10^6. At R_s=0.1, flow below third row was found non-existent with stagnant core region near top of the cavity.

At this stage dimensionless streamline factor was 47. In fig 25(b), you will see that when substrate/fluid thermal conductivity ratio was increased to 1000 then fluid flow was also observed below third row with core descending toward the center of the cavity. Isothermal hot and cold walls were found in the cavity with stagnant core in the center of the fluid region. At lower substrate/fluid thermal conductivity ratio, lower region of the cavity was found isothermal. Each heater face was isothermal due to high thermal conductivity. But lower fluid region was no longer isothermal when R_s ratio was increased to 1000. When substrate/fluid thermal conductivity ratio increases then maximum dimensionless temperature starts to decrease because more thermal spreading occurs throughout the substrate before energy is transferred to the fluid. At R_s=1000, fluid isotherms were found almost diagonally symmetric.

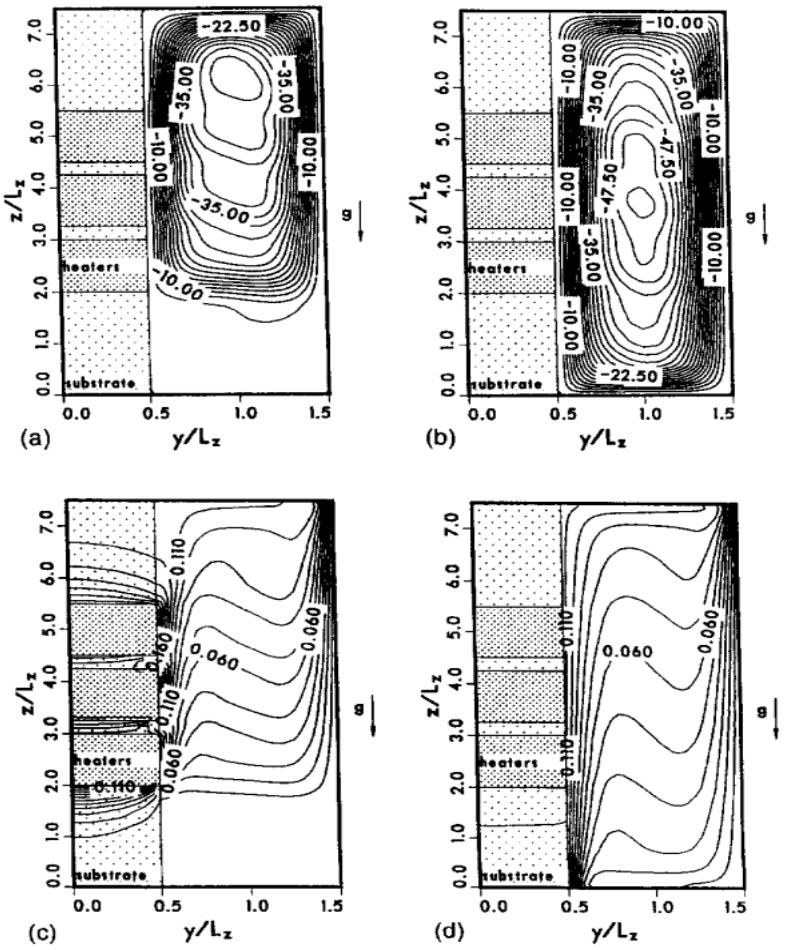

Figure 25*:* Dimensionless streamlines at (a)$R_s = 10^{-1}$; (b) $R_s = 10^3$ and isotherms at (c)$R_s = 10^{-1}$; (d)$R_s = 10^3$ for Pr=25, R_h=2350 and $Ra_{Lz} = 10^6$ nomenclature (Heindel, Ramadhyani and Incropera, 1995).

In Convection cooling process heat is transferred from the hot object by the flow of the surrounding fluid. Surrounding fluid can either be air or any suitable liquid. During cooling process heat causes expansion of the fluid and makes it less dense. Then due to density differences fluid starts to flow and heat is transferred into the surrounding fluid in the form of thermal energy. Effectiveness of cooling process depends on various factors which are temperature difference between the hot object and surrounding fluid, viscosity of the fluid, shape, and size of the hot object. In Natural convective cooling process heat is transferred from the hot object by surrounding air without any use of fan or blower.

Meinders, Van Deer Meer and Hanjalic (1997) performed experimental investigation in which they measured local heat fluxes and heat transfer coefficients of packed array of wall mounted cubical protrusions in vertical channel flow. They analysed temperature distribution of the surface which was heated internally through various heated elements and calculated local heat convective fluxes. In their investigation they considered a rectangular channel of width 50mm and height 500mm. Nine cubical protrusions of size 15 were placed on vertical wall at half of the channel hight. Space between these cubes was 15mm. Measurements were performed at different Reynolds numbers, 795, 2086, 3278 and 5066 which was set according to bulk velocity and cube height. First 6 cubes were packed in an array and used to calculate local heat transfer coefficients. Remaining cubic protrusions were used to identify the location of the obstacles and to provide an appropriate environment for in situ calibration. These cubes were made of internal copper cubical core of size 12.5mm with an epoxy mantle of 1.5mm.

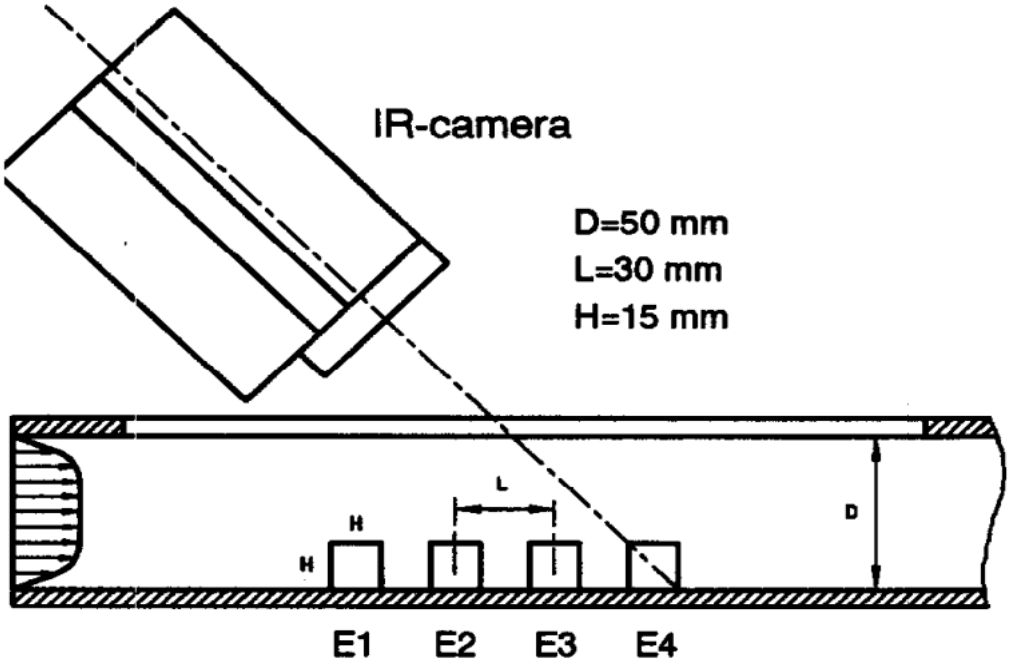

Figure 26: Schematic diagram of test configuration and composed temperature measurement (Meinders, Van Deer Meer and Hanjalic, 1997).

Cubical protrusions were placed on the bottom surface of the channel and its other five faces were exposed to air. So infrared imaging system was used to analyse temperature distribution on these five faces. For high thermal radiations, surface of the cube was coated with a paint whose emissivity was 0.95. For better infrared temperature measurements Liquid crystal method was used as a second technique in this experiment. Five different liquid crystals were mixed which provided five different temperature events.

Two different calibration methods were used to obtain correct temperature measurement at the very sharp colour changes from green to red. In first method heated surface was brushed with mixture of same liquid crystal. In second method copper element was used and fixed at constant temperature with tolerance of 0.05℃.

At large Reynolds number flow recirculation is a common process due to which in this experiment local heat transfer phenomenon were found dominating at lateral and top faces of the leading element. At side faces vortex tube separation minimized convective heat transfer. In this experiment they found non-uniformity in local heat transfer coefficients due to vortex structure of flow-fields around the elements. Flow separates and reattaches at the top and side faces which produces arch-shaped vortices and gives rise to significant difference in heat transfer coefficients. Buoyancy effect also played an important role and showed significant effect on heat transfer coefficients for lowest Reynolds numbers. Asymmetric heat transfer distribution was found between the space of these elements which was due to vertical fluid motion.

In immersion cooling technique, IT components and other electronics are submerged in thermally conductive dielectric liquids and heat is transferred from the system by circulating liquid into direct contacts with the hot components. Dielectric liquids are also used as electrical insulators in high voltage applications where they prevent rapidly extinguish electric discharges. But researchers found that indirect liquid cooling has failed to meet harsh thermal requirements due to poor thermal conductance at solid-solid interface. In late 90's direct cooling with inert dielectric liquids was suggested as the solution for computers. But this idea couldn't gain much importance due to lack of the understanding of transport phenomenon.

Zhang, Tso and Tou (1999) performed three-dimensional numerical analysis of natural convection cooling on 3×3 array of discrete heat sources which were placed on one vertical wall of a rectangular enclosure which was filled with various liquids and cooled by opposite wall (Zhang, Tso and Tou, 1999). Main objective of this study was to cover a wider range of Rayleigh (Ra=$10^4$to 10^8) and Prandtl (Pr=5 to 130) numbers and to analyse the effect of the enclosure aspect ratio (AR=1 to 20).

Fig 27 is showing the schematic sketch of considered rectangular enclosure in which 3×3 array of discrete and iso-flux heat sources was installed on one of the vertical walls and its opposite wall was considered isothermal at low temperature. All other walls were considered adiabatic. Simulations were performed by considering water, FC-72, FC-77, and ethylene glycol with Pr=5, 9, 23 and 130, respectively. Modified Rayleigh number was varied from $10^4$to 10^8.

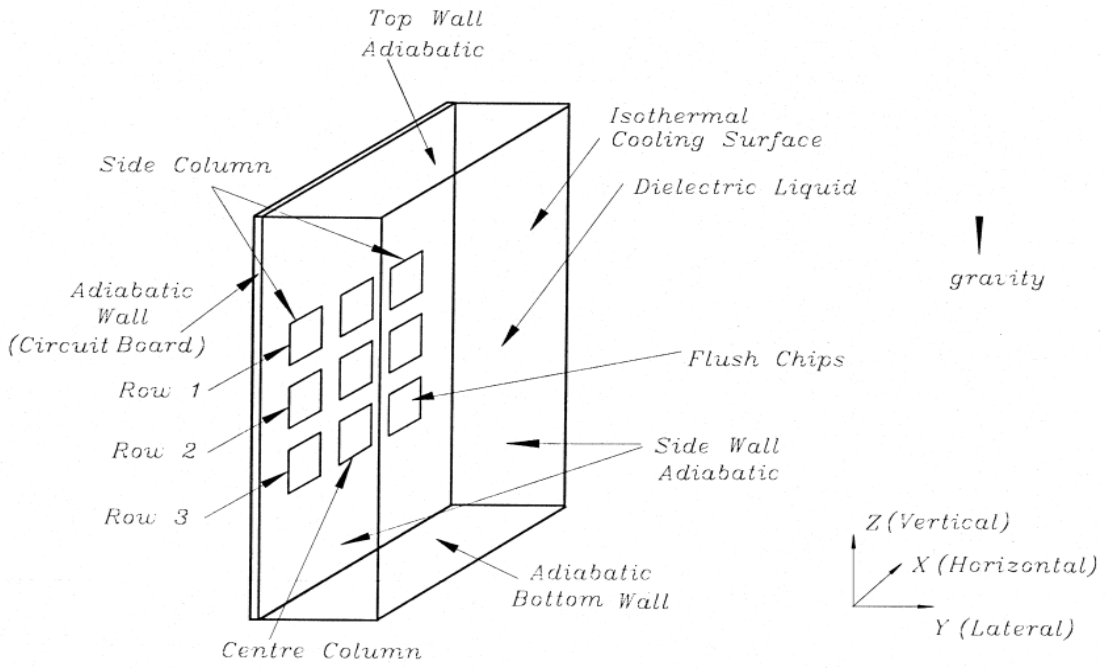

Figure 27: Enclosure Geometry (Zhang, Tso and Tou, 1999).

In result section, they considered various parameters and explained the 3-D nature of the fluid flow with temperature fields and explained the effects of modified Rayleigh number and enclosure aspect ratio on fluid flow. Enclosure aspect ratio was measured by ratio of height of enclosure along z-axis/ depth of enclosure along y-axis. At Ra=10^7, Pr=9 and AR=7.5, w-component in velocity profile was found higher than other two components and represented the primary fluid motion in enclosure. But the strength of this higher velocity component was weak at the bottom of the region which proved that fluid is practically stagnant. Near and adjacent to heated wall, buoyancy forces cause fluid flow and then fluid accelerates from bottom and produces primary flow in vertical direction. Maximum velocities were found across heater array at the mid-section of all three columns where Z (dimensionless coordinate in z-direction) was 3. Near ceiling zone (Z=6.5) two main opposite streams were found in enclosure because near ceiling, rising plume started to decelerate and fluid diverged towards both sides ceiling and cold wall.

Maximum Surface temperature on heater, is one of the most important parameters in electronics cooling applications which could be found at the top row of these simulations where fluid motion is weak but bulk fluid temperature is high near ceiling. But at the bottom row scenario was totally opposite with low bulk fluid temperature. For Ra $<10^5$, W-velocity component showed direct relation with the modified Rayleigh number. When modified Rayleigh number increases then w-velocity component becomes more stronger because buoyancy forces start to dominate the fluid motion and convective heat transfer becomes more effective. When modified Rayleigh number becomes higher than 10^7 then this velocity component starts to diverge in enclosure central region and takes a shape of paired rotating cells whose strength were found less than main helical cells.

Simulations were also performed with different enclosure aspect ratio, A=1, 1.5, 2, 5, 7.5 and 20. Numerical results were obtained to find the effect of enclosure aspect ratio on fluid flow in which range of modified Rayleigh number was set 10^5 to 10^7. In numerical results, it was found that row-averaged Nusselt number is maximum when aspect ratio is increased from 3 to 20 but Nusselt number starts to decrease when aspect ratio becomes less than 3. It was also observed that averaged Nusselt number is lower at the top row and higher at the bottom row. This factor showed that regardless of lowest averaged Nusselt number at the top row, highest heater surface temperature occurs at the top row. Prandtl number showed negligible effect on fluid flow and heat transfer. It means water would also be applicable to dielectric liquids.

In previous studies, most of the researchers studied natural convection cooling by assuming an array of discrete heat sources in vertical enclosure. Main challenge of numerical simulations with inclined or horizontal surface of discrete heat sources was that around horizontal orientation field is essentially of Rayleigh-Benard type. Then in 1993, Mukutmoni and Yang reported evolution of Rayleigh-Benard convection from stable bimodal convection to unstable convection and motivated other researchers to study interactions of thermal and internal fluid flow fields in which discrete heat sources were assumed in an inclined rectangular cavity (Mukutmoni and Yang, 1993). In 2004 Tso, Jin, Tou and Zhang presented experimental data which then used for numerical simulations. Main objective of their studies was to analyze flow patterns and temperature contours at different inclination angles. They also discussed the role of Prandtl number in inclined orientations (Tso, Jin, Tou and Zhang, 2004).

In this study they considered a rectangular cavity which was filled with liquid and can be rotated about x-axis for different inclination angles. An array of 3×3 discrete heat sources was placed on one of its sidewalls while its opposite wall was assumed to be uniform cold surface. All other sides were insulated from the surrounding. Fig 28 is showing the geometrical and physical model which was considered in this study.

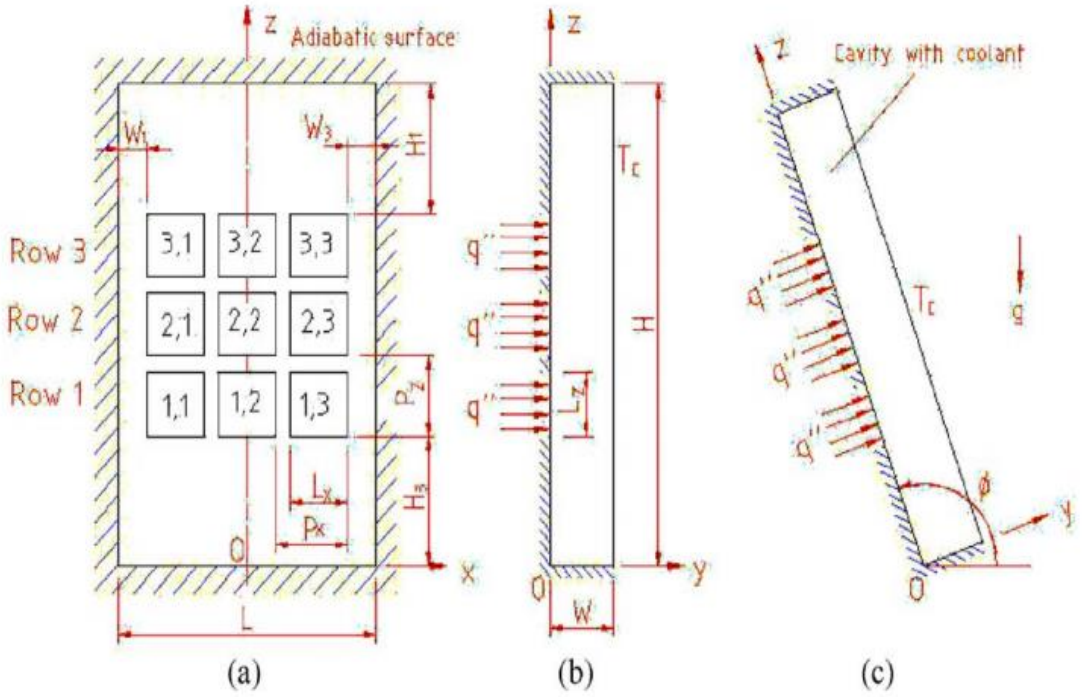

Figure 28: Physical configuration: (a) heaters position; (b) side view; (c) inclined position (Tso, Jin, Tou and Zhang, 2004).

In this study, Range of Rayleigh number was extended to as low as 100. Different and better mesh sizes were used due to complex flow fields for different inclined angles. From 0° to 135° inclined angles, grid size was $40 \times 20 \times 80$ which was increased to $60 \times 30 \times 120$ when inclined angle became greater than 135°.

Fig 29 is showing the arrangement of thermocouples in supposed experimental setup for this study in which you can see that a substrate plate was used to provide a support for holding 3×3 array of discrete heat sources with free copper blocks which were placed at 3.2mm apart. Thin square plate resistive heaters were used to provide heating to each block. Heater walls and other side walls were bonded with sponge to reduce heat loss whose thermal conductivity was 0.038 Wm/k. Degassed and Deionized water was used in these experiments. Equal power was supplied to all heaters and power inputs were recorded by HP data acquisitions system interfaced to a PC. Universal protractor and balance were used to put the cavity at any required angle.

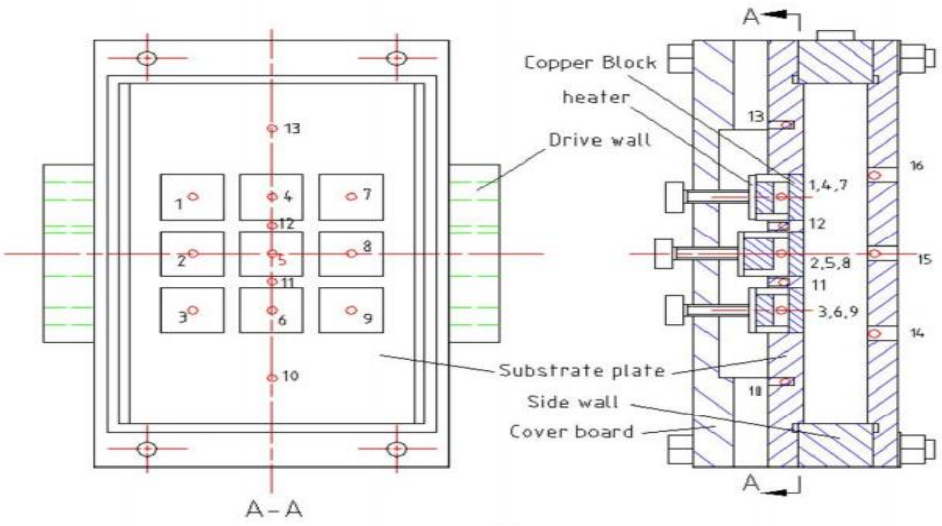

Figure 29: Arrangement of the thermocouples in Experimental Setup (Tso, Jin, Tou and Zhang, 2004).

In result section, they explained the effect of inclination to flow pattern evolution, to distortion of temperature field and to local heat transfer rate. When angle of inclination was zero ($\emptyset = 0^{\circ}$) then the flow field looked very complex in multicellular form. Even in this case velocity magnitude was very small due to which it did not affect the temperature field. At vertical orientation ($\emptyset = 90^{\circ}$) two dimensional but unicellular flow structure was observed which then converted into three-dimensional multicellular flow pattern when angle of inclination was further increased to ($\emptyset = 180^{\circ}$)at horizontal direction. Toroidal convection occurred at low Ra because hot fluid rises in central region due to buoyancy forces and then turns outward, towards cold walls where it is cooled and turns downward. On the bottom wall, imposed restrictions force the fluid to turn radially inward where it receives heat when passes above the heat sources. When Ra increased then bimodal convection occurred in which flow pattern was consisted of two rolls rotating clockwise at the short side of the enclosure. R-B convection occurred at very high Ra in which the convection pattern took the form of four-roll pattern.

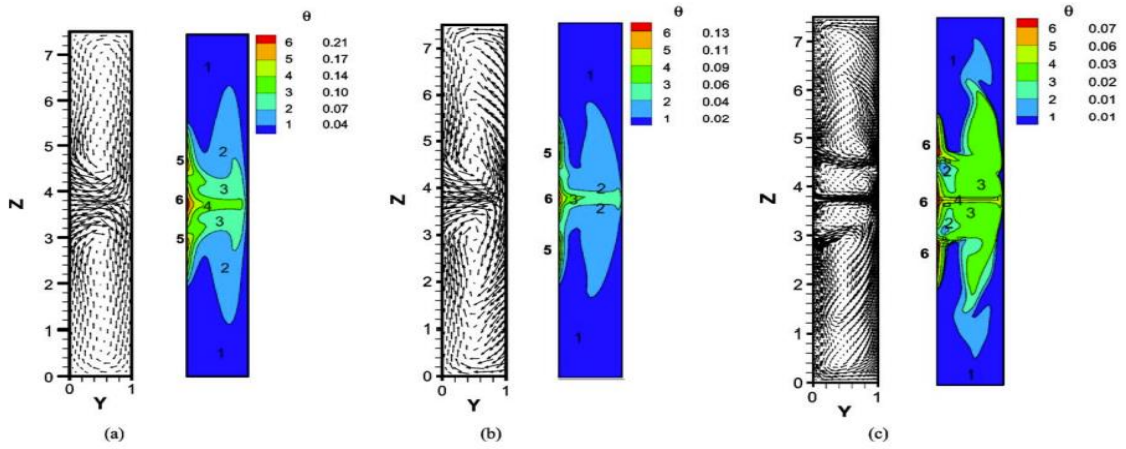

Figure 30*:* Flow and temperature field for Y-Z plane at X=0 for water in horizontal orientation: (a)toroidal convection $Ra \approx 4.6 \times 10^5$; (b)bimodal convection$Ra \approx 4.6 \times 10^6$; (c)R-B convection$Ra \approx 2.5 \times 10^7$ (Tso, Jin, Tou and Zhang, 2004).

Distortion in temperature field occurred when angle of inclination approached horizontal orientation ($\emptyset = 180^{\circ}$) and increased at the top rows of heaters. From vector plots, it was observed that there is a sharp velocity increase from fringe to the heater but at the heater velocity magnitude was constant. Some fluid was pushed from fringe to heater which produced span-wise motion which was weak but found negligible at the heater. Velocity profile showed two peaks at the heaters which corresponded to the two local high temperature regions and proved the distortion in temperature field. Regarding heat transfer rate, it is obvious that horizontal orientation is best for heat transfer because in horizontal orientation lowest Nu number among the three rows was higher than other orientations. They also concluded that the liquids whose Pr is higher than , the effects of Pr are negligible.

In previous studies, most of the researchers considered cases, in which they used a set of heated elements on horizontal adiabatic wall which was interacting with air or other fluids. These cases can be performed in different conditions for example different cavity aspect ratios, variable horizontal or vertical size of elements or different boundary conditions can be used for top and bottom walls. Bazylak and Djilani performed computational analysis of heat transfer in which an array of distributed heat sources was placed on bottom wall of a horizontal enclosure (Bazylak, Sinton and Djilani, 2006). Main purpose of their study was to analyse the effect of an infinite array of distributed heat sources in a horizontal air-filled plenum for which Rayleigh number was used between 0.1 to 10,000 with dry air temperature difference from 10℃ to 160℃.

Periodic boundary conditions were applied on side walls. Top wall was set at constant temperature while bottom wall was considered with zero heat flux boundary condition. They found that heat transfer rate increases as the spacing length between the sources increases. They also noticed transition from conduction-dominated regime to convection-dominated regime when source length was used from 0.1H (H is the height of plenum) to 1.8H and Rayleigh number was between 500 to 2000. At this transition region, Rayleigh-Benard cell structure starts to change when source size is decreased.

In conduction-dominated regime weak and more cells were found which then replaced by stronger cell pairs in convection-dominated regime. When Ra was increased from 5800 to 8100 then Rayleigh-Benard cell developing structure changed from cell pairs over heat sources to cell pairs over each individual heat source and this factor showed sudden reduction in heat transfer.

In recent years, it has been seen that most of the people are moving towards urban areas due to recent developments in technology and a lot of other facilities which are rare in rural life. This factor increased the release of hazardous material in urban areas. Due to which understanding of the wind flow and dispersion of hazardous material into the environment is becoming an important topic day by day. In 2021, Basheer A. Khan and Arun K. Saha performed direct numerical simulation on turbulent flow and heat transfer over a heated cube which was placed in a matrix of unheated cubes (Khan and Saha, 2021).

This type of flow was actually modelled to study heat transfer and flow characteristics in the design of printed circuit board. Main objective of this research was to investigate instantaneous,

and time average flow characteristics and heat transfer phenomenon associated with the cube at different blockage ratios. In their numerical simulations the size of the computational domain was 4H × 4H ×h. H was the size of the cube and h was representing height of the channel. Three different blockage ratios were considered by varying channel height and wall-normal height.

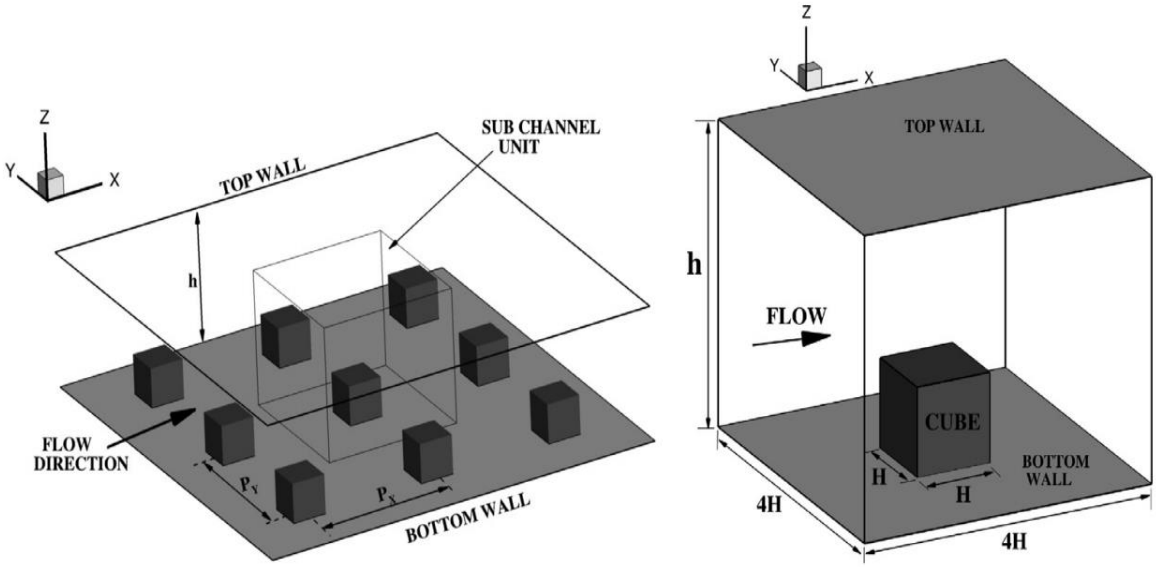

(a) (b)

Figure 31: (a) Schematic diagram of the matrix of wall mounted cubes (b) Computational domain over which simulation is performed (Khan and Saha, 2021).

Air is used as a working fluid in cooling process of electronic components that's why the Prandtl number in these simulations was set to 0.712. No-slip boundary conditions were applied at all walls while for pressure, zero normal derivative of pressure was applied at each wall.

For temperature, periodic boundary condition was applied only in transverse direction. In result section, they explained the effect of Blockage ratio on temperature filed and heat transfer. They concluded that when blockage ratio increases then higher fluctuating field in the form of finer vertical structures leads to higher momentum and heat transport. Lowest heat transfer was observed on the rear surface of the cube which starts to increase with increment in blockage ratio. Heat transfer on the top surface was found to be almost unaffected while side surfaces of the cube showed higher heat transfer with increment in blockage ratio. They found a strong relation between Nu number, wall shear stress and friction factor with blockage ratio. All these factors showed direct relation with the increment in blockage ratio. On other hand relative increase in overall heat transfer was found maximum (24.3%) between lower blockage ratios (0.0735 and 0.125). Main factors behind heat transfer improvement with increase in blockage ratio were increased Reynolds shear stresses and turbulent heat fluxes.

2.4 Marangoni flow in layers with a Topography:

Most of existing studies for Marangoni-Benard convection have considered flat boundaries with a uniform temperature. In 2001 Ismagilov et al. performed some experiments, in which first time he used periodically patterned plates on bottom wall and used infrared imaging technology to observe the emerging pattern form different surface structures of imposed topography. Actually, the main objective of this study was to analyse the competition of intrinsic and topographically imposed patterns in Marangoni-Benard Convection (Ismagilov, 2001). In Marangoni-Benard Convection systems, convection starts when critical value of Marangoni number is exceeded. But in this study the depth of fluid layer was not uniform that's why convection was supposed to be exist for all non-zero values of Marangoni number. When dimensions of intrinsic convection cells were changed to below the period of lattice of posts, the structure of the convective cells changed from triangles to hexagons, but area of these cells was smaller than original triangles. When same dimensions were changed close to lattice spacing then square lattice of posts was observed.

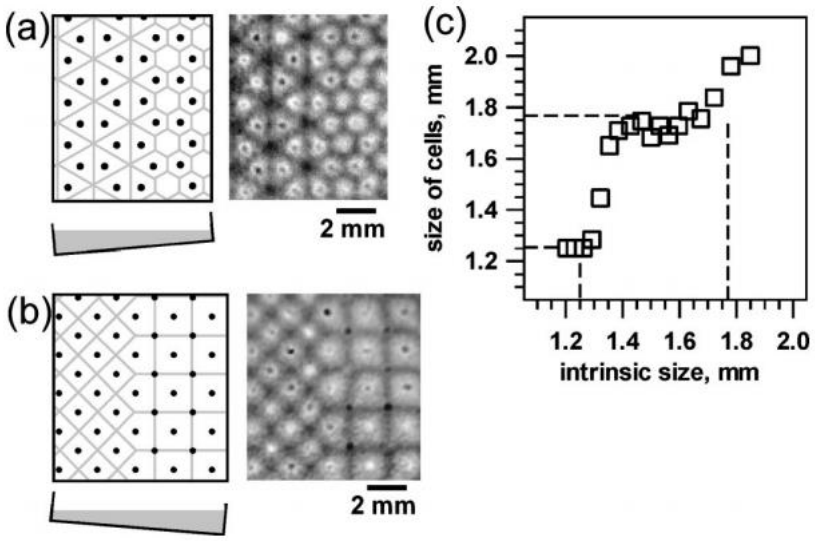

Figure 32: (a) and (b) IR images of convection cells over patterned surfaces undergoing transition in size to (a) smaller length scale (b) larger length scale than scale of imposed system. (c) Dependence of square cells on intrinsic size of cells (Ismagilov, 2001).

Chapter 3: Mathematical Model and Numerical Method:

3.1 The geometry:

As anticipated in the first chapter, the hallmark of the present study is the consideration of a 'patterned' surface delimiting the considered liquid from below, where the attribute 'patterned' is used to describe both the physical morphology of the boundary and its thermal features. Put simply, this fixed imposed topography consists of wall-mounted hot rods with square cross-section (having side length ℓ_{horiz}) and thickness ℓ_{vert}. Successions of such box-shaped blocks, evenly distributed in space, are implemented along both the x and z (horizontal) directions. As shown in Fig. 33, this results in a horizontal wall displaying a regular distribution of NxM elements protruding vertically (along the y axis) into the liquid. Depending on the specific perspective taken by the observer, this distribution might also be seen as a set of staggered solids, arranged in N distinct 'rows' or M 'columns', respectively (a kind of wall 'roughness' with well-defined geometrical properties).

For the sake of completeness, two disjoint situations are considered in which the floor (the portions of flat bottom boundary between adjoining elements) are either adiabatic or set at the same temperature T_{hot} of the blocks (hot floor case). This actually enriches the problem with an additional degree of freedom (with respect to those enabled by the possibility to change the spacing among the rods, their number and size).

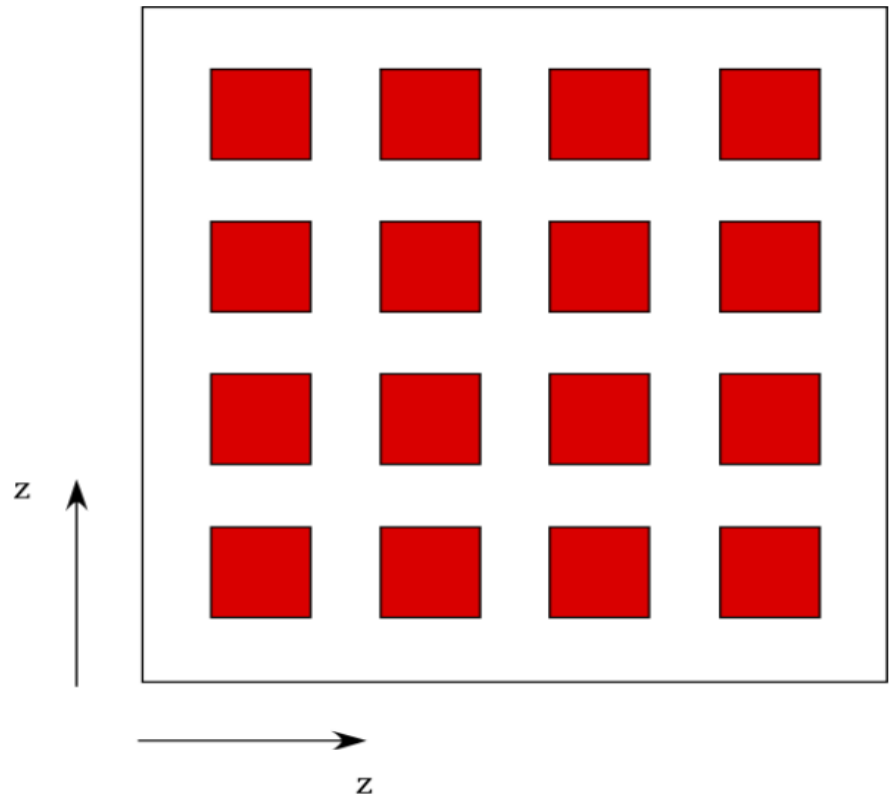

Figure 33: Sketch of the fluid layer with series of square bars evenly arranged on the bottom wall along two perpendicular directions.

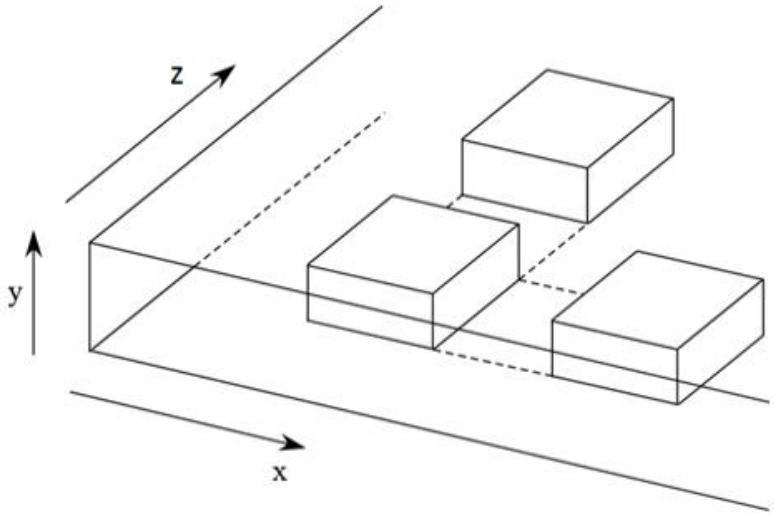

Figure 34: Three-dimensional view of the fluid layer hosting an array of square bars resting on the bottom wall (hot blocks), uniformly spaced along the x and z (horizontal) directions (spacing, width and height can be systematically varied).

Not to increase excessively the overall problem complexity, however, the free interface separating the liquid from the overlying gas is assumed to be flat and undeformable. This simplification holds under the assumption that the Galileo and Capillary numbers take relatively small values (the related rationale can be found, e.g., in Lappa, 2019bc and references therein). These can be defined as $Ga_c=\mu V_r/\Delta\rho g d^2$ and $Ca=\mu V_r/\sigma$, respectively, where μ is the liquid dynamic viscosity, g is the gravity acceleration, d is the characteristic depth of the fluid layer, $\Delta\rho\cong\rho$ is the difference between the density of the liquid ρ and that of the overlying gas, σ is the surface tension and V_r is a characteristic flow velocity, which can be expressed as $V_g=\rho g\beta_T\Delta T d^2/\mu$ or $V_{Ma}=\sigma_T\Delta T/\mu$ depending on whether buoyancy or Marangoni effects are dominant (β_T and σ_T being the thermal expansion coefficient and the surface tension derivative with respect to temperature, respectively; ΔT being a characteristic temperature difference). For $Ga_c<1$ or $Ca<1$, the non-dimensional deformation δ experienced by a free surface under the action of viscous forces can be estimated in terms of order of magnitude as $\delta=O(Ga_c)$ or $\delta=O(Ca)$, respectively. Following a common practice in the literature, δ can therefore be neglected provided $Ga_c<<1$ and/or $Ca<<1$ (see again Lappa, 2019bc and references therein).

3.2 The governing equations:

In line with earlier studies on the classical MB and RB systems, the thesis relies on the self-consistent framework of continuum mechanics where, vital information on thermal convection in liquids (and the related hierarchy of instabilities) is obtained through solution of the balance equations for mass, momentum and energy properly constrained by the assumption of incompressible flow and the related Boussinesq approximation. The Boussinesq approximation is used to solve non-isothermal flows, such as natural convection problems, without having to solve for the full compressible formulation of the Navier-Stokes equations. This approximation is considered valid when density variations are small as this factor reduces the nonlinearity of the problem. It assumes that variations in density are very small, which don't affect the flow field but on the other hand it gives rise to buoyancy forces. In more practical terms, this approximation is typically used to model liquids around room temperature. If compressible inertial effects cannot be neglected, then in that case density becomes dependent on temperature and pressure in that case the Boussinesq approximation would not be appropriate or needed. Moreover, more efficient exploration of the space of parameters is obtained by putting such equations in non-dimensional form, that is, length, time and the primitive variables (velocity V, pressure p and temperature T) are scaled here by relevant reference quantities. In particular, the following compact form:

$$\underline{\nabla}\cdot\underline{V}=0 \tag{1}$$

$$\frac{\partial \underline{V}}{\partial t}=-\underline{\nabla}p-\underline{\nabla}\cdot\left[\underline{V}\underline{V}\right]+\mathrm{Pr}\,\nabla^2\underline{V}+\mathrm{Pr}\,RaT\ \ \hat{\underline{n}}\,, \tag{2}$$

$$\frac{\partial T}{\partial t}+\underline{\nabla}\cdot\left[\underline{V}T\right]=\nabla^2 T \tag{3}$$

corresponds to the following choices: Cartesian coordinates (x, y, z), time (t), velocity ($\underline{V}$), pressure (p) scaled by the reference quantities d, d^2/α, α/d and $\rho\alpha^2/d^2$, respectively (where α is the liquid thermal diffusivity). Moreover, the temperature (T) is scaled by ΔT, that is, the difference between the temperature of the hot solid elements and the ambient temperature T_{ref} (temperature of the external gas).

Obviously, Pr is the well-known Prandtl number (defined as ratio of the fluid kinematic viscosity $\nu=\mu/\rho$ and the aforementioned thermal diffusivity α which is the thermal conductivity divided by density and specific heat at constant pressure $\frac{k}{\rho c_p}$), and $Ra=g\beta_T\Delta T d^3/\nu\alpha$ is the standard Rayleigh number. By setting Ra to 0, obviously, excluded are any processes that depend on buoyancy effects. In the present circumstances, fluid convection is also produced by gradients of surface tension, that is, thermocapillary effects. The related driving force can be accounted for through a dedicated equation, which expresses separately the balance of shear

stresses at the free surface of the layer. Neglecting the shear stress in the external gas, such relationship in non-dimensional form simply reads:

$$\frac{\partial \underline{V}_S}{\partial n} = -Ma \ \underline{\nabla}_S T \tag{4}$$

where $\underline{n}$ is the direction perpendicular to the free interface (planar in this case), $\underline{\nabla}_S$ is the derivative tangential to the interface and $\underline{V}_S$ is the surface velocity vector. Moreover, Ma is the Marangoni number defined as $Ma = \sigma_T \Delta T d/\mu\alpha$. A related number, measuring the relative importance of buoyancy and Marangoni effects, is the so-called dynamic Bond number, namely, $Bo_{dyn}=Ra/Ma$.

An adequate characterization of the overall problem also requires the introduction of proper non-dimensional geometrical parameters to be used to account for the spatial distribution of the cubic elements and their aspect ratio. These are:

$$\delta_x = \frac{\ell_x}{d}, \ \delta_y = \frac{\ell_y}{d}, \ \delta_z = \frac{\ell_z}{d}, \tag{5a}$$

$$A_{xbar} = \frac{\delta_y}{\delta_x}, \ A_{zbar} = \frac{\delta_y}{\delta_z} \tag{5b}$$

Similarly, the aspect ratios of the entire fluid domain are defined as:

$$A_x = \frac{L_x}{d}, \ A_z = \frac{L_z}{d} \tag{6}$$

where L_x and L_z are the related (dimensional) horizontal extensions. Indicating by N the number of elements along z and by M the corresponding number along x, the nondimensional distance between adjoining elements can therefore be expressed as

$$\xi_x = \frac{L_x - M\ell_x}{Md} = \frac{A_x}{M} - \delta_x, \ \xi_z = \frac{L_z - N\ell_z}{Nd} = \frac{A_z}{N} - \delta_z \tag{7}$$

Accordingly, each element indexed as (i, k) can be mathematically represented in the physical (non-dimensional) space as:

$$\begin{cases} (i-1)\delta_x + \left(i-\frac{1}{2}\right)\xi_x \le x \le (i)\delta_x + \left(i-\frac{1}{2}\right)\xi_x \ \ for\ 1 \le i \le M \\ 0 \le y \le \delta_y \\ (k-1)\delta_z + \left(k-\frac{1}{2}\right)\xi_z \le z \le (k)\delta_z + \left(k-\frac{1}{2}\right)\xi_z \ \ for\ 1 \le k \le N \end{cases} \quad (8)$$

and on its boundary with the fluid, after assuming.

$\underline{V}$ =0 (no slip conditions) and T=1 (9)

Along the portions of floor (at y = 0) separating adjoining elements, as anticipated in Sect. 2.1, adiabatic or constant temperature conditions are set, i.e.

$$\frac{\partial T}{\partial y} = 0 \quad (10a)$$

or

T=1 (10b)

Biot number which determines how quickly the heat is transferred from the surface of the body to its interiors is defined by the ratios of interparticle diffusional resistance to the convective mass transfer resistance ($Bi = \frac{h}{k}L$). In this studies, Heat exchange of the liquid with the external gaseous environment at the free surface is modeled through the classical Biot number, i.e.:

$$\frac{\partial T}{\partial y} = -BiT \quad (11)$$

The lateral boundaries of the fluid domain are considered no-slip and adiabatic or periodic boundary conditions (PBC) are assumed there. At the initial time t=0, the flow is quiescent and at the same temperature as the ambient, i.e., T=0. As time increases its temperature rises as a result of the heat being exchanged with the heated elements until equilibrium conditions are reached.

In the present work, such heat exchange is quantified through the 'ad hoc' introduction of different versions of the Nusselt numbers tailored to account separately for the thermal behavior of the lateral, top or total surface of each heated element, i.e.

$$Nu^{ik}_{barlateralsurface} = \frac{1}{(2\delta_x\delta_y + 2\delta_z\delta_y)}\left[\int_0^{\delta_y}\int_{x_i}^{x_i+\delta_x} \left.\frac{\partial T}{\partial z}\right|_{z=z_k} dxdy - \int_0^{\delta_y}\int_{x_i}^{x_i+\delta_x} \left.\frac{\partial T}{\partial z}\right|_{z=z_k+\delta_z} dxdy + \int_0^{\delta_y}\int_{z_k}^{z_k+\delta_z} \left.\frac{\partial T}{\partial x}\right|_{x=x_i} dzdy - \int_0^{\delta_y}\int_{z_k}^{z_k+\delta_z} \left.\frac{\partial T}{\partial x}\right|_{x=x_i+\delta_x} dzdy\right] \quad (12)$$

$$Nu^{ik}_{bartop} = -\frac{1}{\delta_x\delta_z}\int_{z_k}^{z_k+\delta_z}\int_{x_i}^{x_i+\delta_x} \left.\frac{\partial T}{\partial y}\right|_{y=\delta_y} dxdz \quad (13)$$

$$Nu^{ik}_{bar} = \frac{Nu^{ik}_{barlateralsurface}(2\delta_x\delta_y + 2\delta_z\delta_y) + Nu^{ik}_{bartop}\delta_x\delta_z}{(2\delta_x\delta_y + 2\delta_z\delta_y) + \delta_x\delta_z} \quad (14)$$

where $x_i = (i-1)\delta_x + \left(i - \frac{1}{2}\right)\xi_x$ and $z_k = (k-1)\delta_z + \left(k - \frac{1}{2}\right)\xi_z$

Accordingly, space averaged values are introduced as:

$$Nu^{average}_{side} = \frac{1}{NM}\sum_{k=1}^{N}\sum_{i=1}^{M} Nu^{ik}_{barlateralsurface} \quad (15)$$

$$Nu^{average}_{top} = \frac{1}{NM}\sum_{k=1}^{N}\sum_{i=1}^{M} Nu^{ik}_{bartop} \quad (16)$$

$$Nu^{average}_{bar} = \frac{1}{NM}\sum_{k=1}^{N}\sum_{i=1}^{M} Nu^{ik}_{bar} \quad (17)$$

Chapter 4:

4.1 The projection method:

The set of equations (1)-(3) with the related boundary conditions (eqs. (4) and (8)-(11)) have been solved numerically using a primitive-variable technique pertaining to the general category of "projection" or "fractional-step" methods. This class of techniques rests on the specific interrelation that is established in incompressible flows between pressure and velocity. Unlike compressible flow where pressure is generally determined using the gas state equation (and therefore it depends on density and temperature determined solving the continuity and energy equations, respectively), for incompressible flow p is only a function of another varying physical quantity, i.e., the fluid velocity $\underline{V}$. In order to understand how this apparently innocuous observation can be used to develop an effective time–marching procedure for the determination of both p and $\underline{V}$, it is worth starting from the simple realization that both unknowns appear in the momentum equation (which can therefore be taken as the starting point for the illustration of the methodology). This equation can be manipulated and split into sub-equations, which combined with the incompressibility constraint can lead to 'new' mathematical entities do not present in the original formulation, particularly suitable for the definition of a 'working' algorithm. The first step along this logical process consists of neglecting the pressure term in the momentum equation:

$$\frac{\partial \underline{V}^*}{\partial t} = \left[-\underline{\nabla} \cdot \left[\underline{V}\underline{V} \right] + \mathrm{Pr}\,\nabla^2 \underline{V} + \mathrm{Pr}\,Ra T \underline{i}_g \right] \tag{18a}$$

$$\frac{\underline{V}^* - \underline{V}^n}{\Delta t} = \left[-\underline{\nabla} \cdot \left[\underline{V}\underline{V} \right] + \mathrm{Pr}\,\nabla^2 \underline{V} \right]^n + \mathrm{Pr}\,Ra T \underline{i}_g \tag{18b}$$

where Δt is the time integration step. Although affected by this severe approximation, notably this equation expresses indirectly the conservation of vorticity. Indeed, there would be no difference in the derived equation obtained by taking the curl of either eq. (2) or eq. (18a) because, by definition, the curl of the gradient of a function is always zero. Put differently, this means that the vorticity associated with $\underline{V}^*$ is identical to the vorticity that the effective (complete) field would possess. This observation naturally leads to introduce the next step, which is the stage where $\underline{V}^*$ is made 'complete' by enriching it with the previously neglected gradient of pressure, i.e.

$$\underline{V} = \underline{V}^* - \xi \underline{\nabla} p \tag{19}$$

where ξ is a constant. This second step is needed on the one hand to make $\underline{V}^*$ 'physical' (reintroducing the effect of the gradient of pressure), and on the other hand to force the final (complete) velocity to satisfy the continuity equation (not yet involved in the algorithm). This final stage is accomplished by substituting the formally corrected velocity through eq. (19) into eq. (1). If ξ is set equal to $1/\Delta t$, this operation formally closes the problem from a numerical point of view as an additional mathematical identity is obtained by which the (otherwise unknown) pressure can be obtained:

$$\nabla^2 p = \frac{1}{\Delta t} \underline{\nabla} \cdot \underline{V}^* \tag{20}$$

If the physical boundary conditions expressed by eqs. (4) and (8)-(9) are used for eq. (18), the resulting velocity $\underline{V}$ needs not to be corrected on the boundaries, which means that eq. (2) can be solved with homogeneous Neumann conditions for the pressure (leading to the so-called CPPE Consistent Pressure Poisson Equation approach, (Gresho, 1991)). The logical sequence of steps is therefore: solution of eq. (18) with the physical boundary conditions for the velocity, solution of eq. (20) with Neumann homogeneous conditions for the pressure, and final determination of the velocity field exploiting eq. (19).

It is also worth recalling that the elegant compactness of these equations and the related algorithm relies on some well-known theorems, which make sure the problem is well-posed from a mathematical point of view. According to the so-called "theorem of the inverse calculus", in a simple connected domain a vector field can be made uniquely determined (fixed) by assigning its divergence, curl (its 'vorticity' if the considered vector is the fluid velocity) and normal component at the boundary (Ladyzhenskaya, 1969). Equations (18)-(20) guarantee that $\underline{\nabla} \cdot \underline{V}^{n+1} = 0$ and $\underline{\nabla} \wedge \underline{V}^{n+1} = \underline{\nabla} \wedge \underline{V}^*$, i.e. the divergence and curl of the velocity field are the same that would be obtained through solution of the original set of equations, making this theorem implicitly satisfied (along these lines it is also worth recalling that the boundary conditions set for the velocity in this work always imply that the component of the velocity perpendicular to the boundary is assigned, i.e. it is zero). The decomposition of the velocity field implemented through eq. (19) may also be regarded as a spin-off of the *Hodge or Helmholtz decomposition theorem* (Helmholtz, 1858), which states that any vector field ($\underline{V}^*$ in the present case) can always be decomposed into the gradient of a scalar function ($\underline{\nabla} p$) and a solenoidal part, i.e., $\underline{V}^{n+1}$. Additional information on this class of methods can be found in Refs (Guermond, 1996; Guermond and Quartapelle, 1998; Strikwerda, Lee, and Numer, 1999; Guermond, Minev, and Shen, 2006).

Using a time explicit approach like that indicated in eqs. (18)-(20), the energy equation can be integrated in a segregated manner just after the velocity field has been determined, which means that the buoyancy term at the right-hand side of eq. (19) is also implemented in an explicit way (i.e., it must be evaluated at the time n). In the present work, convective terms have been treated using the QUICK scheme while standard central differences have been used

to discretize the diffusive terms. Given the delicate role played by the coupling between pressure and velocity (see, e.g. (Choi, Nam, and Cho, 1994;)) a staggered arrangement has been used for the primitive variables, that is, while pressure occupies the center of each computational cells, the components of velocity are located at the center of the cell face perpendicular to the x and y axes, respectively (see, e.g., Lappa, 1997).

4.2 Validation:

The validation has been articulated into distinct stages of verification. More precisely, the coherence of the model has been verified through comparison with existing linear stability analyses (LSA) and earlier non-linear calculations conducted by other authors. Given the nature of the specific subject being addressed, both the classical problems of Marangoni-Bénard and buoyancy convection have been considered.

The outcomes of the validation exercise based on the comparison with the LSA for the classical MB problem are summarized in Fig. 35. In particular, Fig. 35a shows the evolution in time of the maximum velocity of the fluid for different values of the Marangoni number, while the corresponding 'growth rate' (determined as the logarithm of the slope of the branch of the velocity profile with constant inclination) is reported in Fig. 35b. The latter also includes the value of the critical Marangoni number (for the onset of convection from the initially thermally diffusive and quiescent state) determined through extrapolation to zero of the disturbance growth rates. As the reader will easily realize, this value matches with a reasonable approximation (less than 1.5%) that obtained with the LSA approach (Pearson, 1958). The 3D pattern emerging for a value of the Marangoni number slightly larger than the critical one is shown in Fig. 36 (presenting the classical honeycomb structure of MB convection).

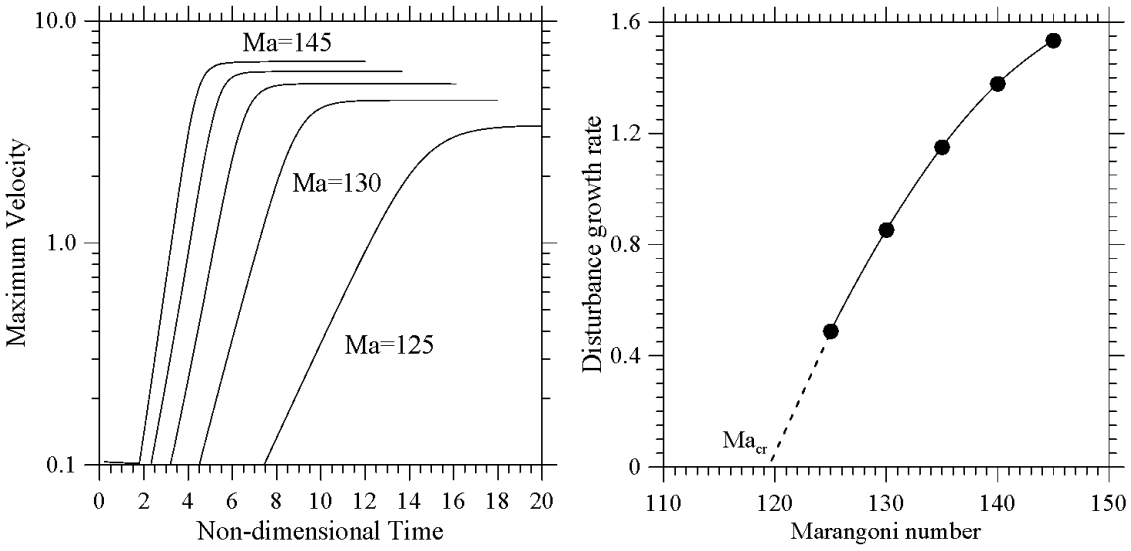

Figure 35*:* Profile of maximum velocity as a function of time (a) and related growth rate (b) as a function of the Marangoni number (Pr=10, layer uniformly heated from below with aspect ratio A=11.5, Bi=1, mesh 150x25).

For the sake of precision, it should be noted that the definition of the Marangoni number used here for comparison with the LSA is slightly different with respect to that introduced in Sect. 2.2. While in the present work the ΔT appearing in the expression of Ma is the difference between the temperature of the hot surfaces and that of the 'ambient' (the gas located at a certain distance from the liquid surface, assumed not be disturbed and maintain a constant temperature in time), the LSA considers the effective temperature difference which would be established in the absence of convective effects between the top and bottom geometrical boundaries of the liquid layer, i.e. the uniformly heated bottom wall and the free interface. Therefore, the Marangoni number shown in Fig. 35 is related to that defined in Sect. 2 through a scaling factor, which in the current theoretical framework is $(T_{hot}-S_{urface})/(T_{hot}-T_{ref})$, i.e., in non-dimensional form $Bi/(Bi+1)$ (Eckert, Bestehorn, and Thess, 1998).

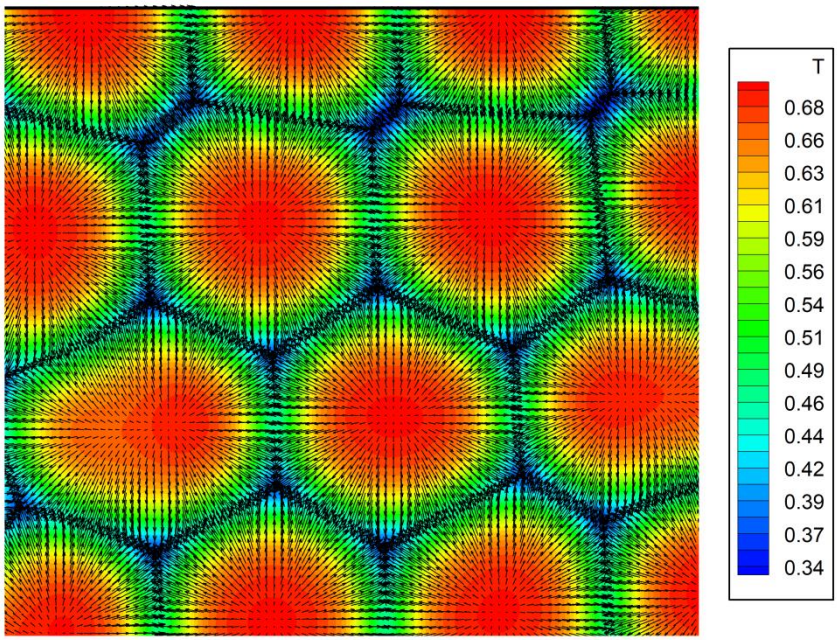

Figure 36*:* Temperature and velocity pattern on the free surface (Pr=10, layer aspect ratio $A_x= A_z=11.5$, Ma=125, Bi=1, mesh 150x25x150, PBC).

These simulations confirm that (as expected) the only effect of a $Bi\neq0$ is to shift the critical Marangoni number ($Ma_{LSA}\cong80$ for $Bi=0$) and change the growth rates of unstable modes, while the hexagonal planform (Fig. 36) is still a stable attractor for the nonlinear governing equations.

As a second step of code verification, pure buoyancy convection examined which originates from a heated element with rectangular shape encapsulated in (located on the bottom of) a square cavity with adiabatic bottom boundary and cold (isothermal) top and lateral walls. Assuming the same conditions originally investigated by Biswas et al. (Biswas, Mahapatra, Manna and Roy, 2016), Four representative conditions were tackled corresponding to distinct aspect ratios of the heater and different values of the Rayleigh number (see Figs. 37 and Table I). As witnessed by these data, a very good agreement holds in terms of Nusselt number.

As a concluding remark for this section, it's helpful to recall that the computational kernels underpinning the present algorithm have already been used extensively in earlier studies of the present authors (concerned with various realizations of buoyancy and surface-tension driven convection, see, e.g., Lappa, 2019bc). Accordingly, they were also validated through comparison with other relevant benchmarks and test cases (this information is not duplicated here for the sake of brevity).

Table 1: Comparison with the results by Biswas et al. (2016) (see Fig. 7 in their work), square cavity with heater located on adiabatic bottom and other (lateral and top) walls at constant (cold) temperature (Pr=25.83, different values of Ra and the heated element aspect ratio).

δ_{horiz}	$A_{bar}=\frac{\delta_{vert}}{\delta_{horiz}}$	Ra	$Nu_{side}^{average}$ (present)	$Nu_{top}^{average}$ (present)	$Nu_{bar}^{average}$ (present)	$Nu_{bar}^{average}$ Biswas et al.
0.64	0.3	10^4	5.56593	4.2414	4.8381	≅4.8
0.33	1.0	10^4	4.8209	3.8613	4.5010	≅4.5
0.64	0.3	10^5	10.0709	7.7318	8.6032	≅8.65
0.33	1.0	10^5	10.5065	6.0701	9.0277	≅9.1

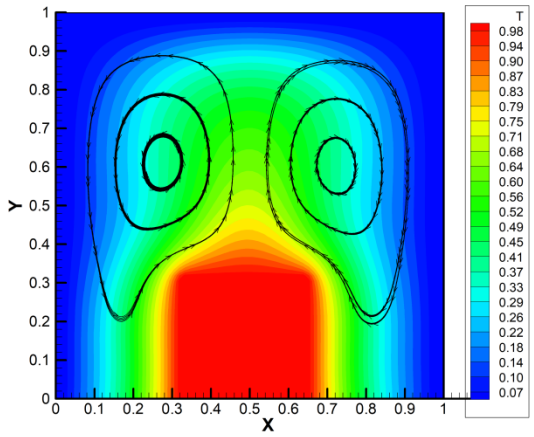

a)

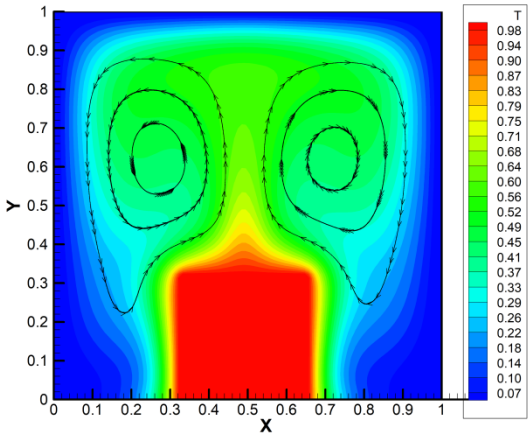

b)

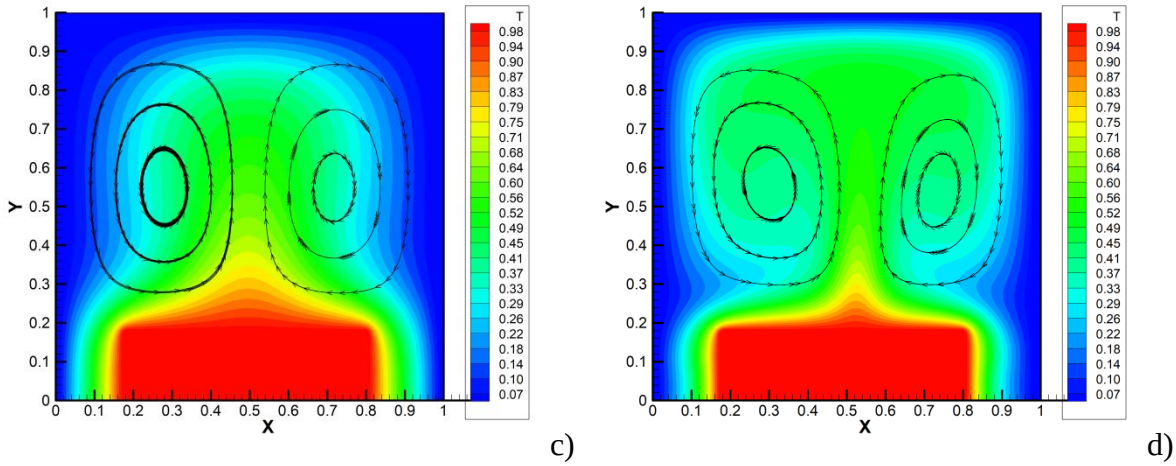

c) d)

Figure 37*:* Temperature and streamlines in a square cavity with heater located on adiabatic bottom and other (lateral and top) walls at constant (cold) temperature (Pr=25.83, different values of Ra and the heated element aspect ratio); a) δ_{horiz} =0.33, A_{bar}=1.0, Ra=10^4 (grid 70x70); b) δ_{horiz} =0.33, A_{bar}=1.0, Ra=10^5 (grid 100x100); c) δ_{horiz} =0.64, A_{bar}=0.3, Ra=10^4 (grid 70x70); d) δ_{horiz} =0.64, A_{bar}=0.3, Ra=10^5 (grid 100x100).

4.3 Mesh refinement and related criteria:

In order to ensure the judicious use of the available computational resources and, at the same time, produce results which can be trusted, it is known that good practice consists of conducting a thorough and extensive analysis of the sensitivity of the emerging solutions to the used mesh.

Towards the end to reduce the computational cost of the grid independence study itself, in particular, here such a parametric assessment has been initially conducted considering the equivalent 2D configuration (assumed to have infinite extension along the third direction z) for the same parameters investigated in Sect. 4. Such a strategy rests on the realization that since the 3D geometry illustrated in Fig 34 consists of periodically positioned items along both the x and z directions (i.e., a rotation by 90° would not change the physics of the problem), a 2D framework should be regarded as a relevant approach for a preliminary estimation of the needed numerical resolution. As sensitive parameters for such investigation, in particular, both kinematic and thermal quantities were considered, namely, the maximum of the velocity components along x and y, and the spatially averaged (over the considered set of blocks) Nusselt number defined through eq. (15) and (16). The outcomes of such a parametric investigation for a representative case (Pr=10, N=3, Ma=5000, *Ra*=10000, *Bi*=1.0, δ_{horiz}=1.0, δ_{vert}=0.3) are summarized in Table II.

Table 2: Grid independence study (2D configuration, aspect ratio=horizontal length/depth=10, Pr=10, N=3, Ma=5000,Ra=10000,Bi=1.0).

Grid	u_{max}	v_{max}	$Nu_{side}^{average}$	$Nu_{top}^{average}$
77x18	90.2574	53.7327	2.0597	1.3410
100x23	96.5027	53.6714	2.0018	1.2998
130x31	96.5020	53.6701	2.0015	1.2998
169x39	97.2471	53.5684	2.0003	1.2901

As a fleeting glimpse into a such a table would confirm, a resolution with ≅30 points along the vertical direction and 130 points along the horizontal one can be considered more than enough for the considered combination of Ma, *Ra* and Bi for Pr=10 (all the percentage variations falling below 1% for a further increase in the mesh density).

To double-check that such a resolution can also capture properly the small-scale details of surface-tension driven convection at high values of the Marangoni number (known for its ability to give rise to "high-wavenumber excitations", (Thess and Orszag, 1995); see also Sects. 4.2 and 4.3), dedicated 3D simulations have been performed considering MB and mixed Marangoni-Rayleigh-Bénard convection for resolution exceeding the 130 points in the horizontal direction. Given the disordered nature of the convective structures emerging in this case, a quantitative assessment of the pattern (on increasing the number of points) has been conducted in terms of (spatial) spectrum of the surface temperature distribution.

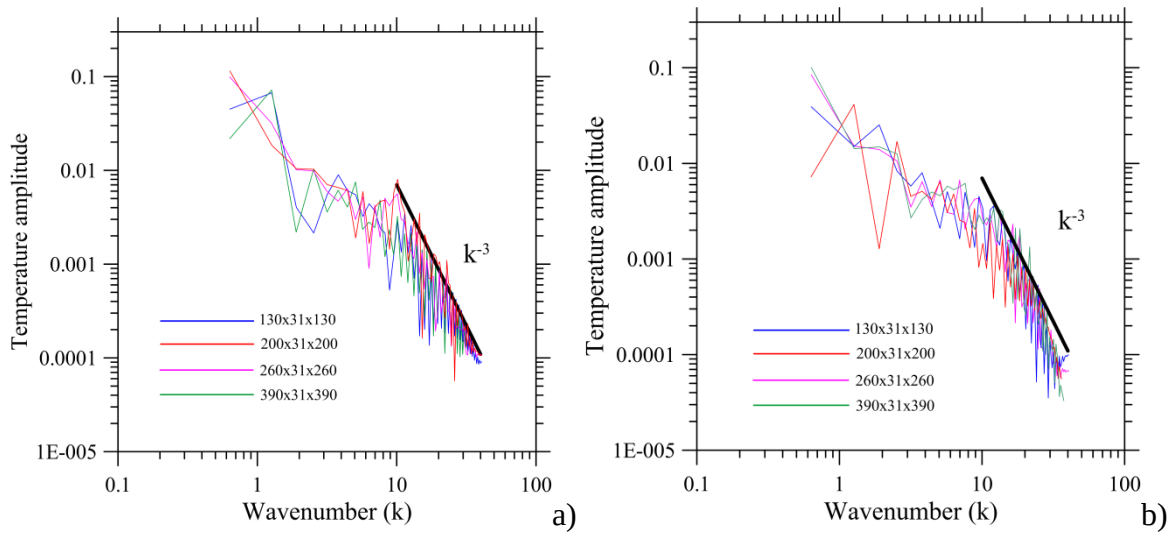

Figure 38*:* Spectrum of the surface temperature distribution for increasing number of grid points in the horizontal direction (Pr=10, A_x=A_z=10, Bi=1.0, solid lateral walls, spectrum for a temperature profile at x=5): a) Pure MB flow (Ma=5x10^3), b) Hybrid convection (Ma=5x10^3, Ra=10^4).

The related results shown in Fig. 38a and 38b for the pure MB and hybrid convection cases, respectively, confirm that, although a variation can be detected in the shape of the spectrum for small wavenumbers (this depending on the specific line along which the temperature profile is measured and on the random position where extended convective structure are formed in the fluid domain when a new simulation is run), all the spectra align perfectly in the range of high values of the wavenumber. Most importantly, the extension of the spectrum does not change on increasing the density of the mesh, neither in terms of amplitude distribution (vertical coordinate), nor in terms of horizontal extension (i.e., the maximum value of k). These observations give us confidence that a resolution of $5x10^5$ nodes is also sufficient to avoid unresolved regions in the 3D fluid domain, i.e., it is enough to capture the non-trivial small-scale behavior of surface-tension-driven convection for the considered value of the Marangoni number (a denser mesh does not result in the realization of smaller scale kinematic or thermal features).

Chapter 5: Topographically Controlled Marangoni–Rayleigh–Bénard Convection in Liquid Metals:

5.1 Thermal convection in liquid metals:

This chapter is entirely dedicated to a specific problem, that is, the numerical simulation of convection generated by a discrete set of heat sources in liquid metals. This initial section explains why this category of liquids has also been considered in this thesis. Liquid metals can be used in place of water to cool nuclear reactors given their high thermal conductivity. Thereby they are another example of the various technological cooling problems discussed in Chapter 1. However, there is also another important reason for which they are considered in this thesis.

Before being solid, many materials pass through a liquid state and the properties that they display in the final solid state often depend on the convective phenomena that are established in their liquid state. This concept applies to a variety of manufacturing and materials science applications. Whilst there is a plethora of materials that are of industrial relevance and importance due to the related technological applications and impact on world's societies, silicon and other semiconductor materials have attracted a significant increasing interest especially during the late 20th and early 21st century. This interest partly stems from the abundance of these materials (especially silicon) on the surface of our planet. However, it also originates from some of the remarkable physical properties that these substances display, through which over the last 50 years specific technological applications have been enabled (leading to what nowadays is often referred to as the 'silicon age').

Single crystals of these substances are of great importance in the electrical and op-to-electronic industries due to their 'purity'. A single crystal, often also referred to as a mono-crystalline material is a pure crystal lattice. The purity of these mono-crystalline materials is essential in electronics applications as the purer the material, the better its performances will be. Vice versa, for the use of semiconductors in microprocessors, which operate on the quantum scale, the presence structural or chemical defects in the crystal lattice can prevent these materials from reaching the expected targets in terms of electronic performances.

These simple arguments explain why the convective processes that dictate the crystalline evolution of these substances have become a subject of great interest from both the engineering and physics standpoints. Convection within the melt can deeply influence microstructure formation in solidifying materials through its intrinsic transportation mechanisms of heat, mass and momentum and related studies show no obvious sign of reaching a limit yet. Given the difficulties in observing directly semiconductor melts and liquid metals due to their opacity, most of such studies are being based on alternate methods such as theoretical analysis and numerical simulations (Kaddeche, Henry, Putelat, and Hadid, 2002) . By virtue of them, it has been clarified that the branch of convection known as natural (buoyancy) convection, which is driven by gravity as a result of thermally induced density inhomogeneities in the liquid, plays a crucial role in such dynamics.

Landmark fundamental studies on the behaviour of buoyancy convection in liquid metals date back to 1981 when this subject was investigated given its relevance to other (natural) problems such as the motion of liquid iron in Earth's core and the ensuing generation of a magnetic field. Considering a physical domain as simple as an infinite layer of liquid metal uniformly heated at the bottom and cooled at the top, (Busse and Clever, 1981), (Clever and Busse, 1981) revealed that Rayleigh-Bénard (RB) convection in such systems is initially steady and then it undergoes bifurcation to an oscillatory flow as the Rayleigh number is increased. It was shown that the instability leads to the emergence of waves that travel in the fluid along a horizontal direction. These waves were also found numerically by (McLaughlin and Orszag, 1982 and Lappa, 2005). It has been shown that superposition of these waves can also produce peculiar states known as 'standing waves', i.e., solutions where the disturbances do not travel in the fluid but grow and shrink in time at fixed spatial positions.

Another line of inquiry has originated from the realization that if the fluid is not de-limited by a solid wall at the top, i.e., it displays a free liquid-gas interface (which is often the case in most of the technological processes used for the production of the aforementioned single crystals, Lappa, 2005), another source of convection is represented by surface tension and related gradients. Surface tension of many liquids (including semiconductor melts and liquid metals) depends on temperature. If the fluid is subjected to a temperature difference, this results in fluid motion, generally referred to as Marangoni-Bénard (MB) convection when the fluid is uniformly heated at the bottom. Unlike RB flow, which typically manifests in the form of parallel rolls extended in the horizontal direction (playing the role of substrate for the propagation of the aforementioned waves when a certain temperature difference is exceeded), Marangoni-Bénard convection is known for its ability to produce patterns with the hexagonal symmetry. In the case of liquid metals, these hexagonal cells are featured by rising currents along their boundary and a central column of descending fluid (a structure known as an "inverted hexagon" to distinguish it from the companion case in which these cells form in oils and display fluid rising at the center, see, e.g., Thess and Bestehorn, 1995; Parmentier, Regnier, Lebon and Legros, 1996; Boeck and Thess, 1999. On increasing the related characteristic (Marangoni) number, this topology can be taken over by different patterns, such as stationary two-dimensional rolls either with the roll axes parallel to the short domain boundary or in two different oblique orientations. Time-dependent solutions are also possible, namely three-dimensional (3D) travelling waves.

All of these phenomena can have a detrimental impact on the quality and purity of the crystalline materials discussed before. That is why, in general, attempts are made to control these flows and the related hierarchy of bifurcations through magnetic fields or other methods such as the application of vibrations (and all references therein).

Most surprisingly, despite all these valuable studies, very few pieces of literature have appeared where an attempt has been made to 'control' these forms of convection through alteration of their 'boundary conditions', i.e., by using containers with walls that display a given topography and/or a structured thermal inhomogeneity. The problem of planform selection in such conditions has long been a theoretical puzzle.

As a first step in this direction, the present chapter is devoted to the numerical investigation of hybrid buoyancy-Marangoni convection in a layer of liquid metal cooled at the top by an adjoining gas phase and heated at the bottom by a discrete distribution of heating elements (cubic blocks). The main objective is an understanding of the relationships existing between the imposed thermal forcing and the properties of the emerging flow.

Not to increase excessively the dimensionality of the space of parameters (but without loss of generality) a fixed horizontal extension of the fluid domain is considered (assumed to be a layer with identical length along x and z, namely $A_x=A_z=10$). As the blocks have a square cross-section ($\delta_{horiz}=1$), this naturally implies that the discrete distribution of blocks can be directly mapped into a square matrix having dimensions NxN where N can be set as an input parameter for the simulations. As another degree of freedom, a variable thickness has been considered for the blocks, with δ_{vert} spanning the range $0.5\leq\delta_{vert}\leq0.7$.
Moreover, the response of these systems has been examined for three distinct values of the Prandtl number Pr≤1, namely Pr=0.01, 0.1 and 1 (the first two being representative of liquid metals or semiconductor melts, the last one corresponding to the companion case of molten salts).
With the selected number of points, each simulation has taken a time ranging between one and four weeks.
In the following, for the sake of clarity, the results are presented in three segregated sections, where the influence of each of the considered degrees of freedom is examined while keeping all the other parameters fixed. Accordingly, starting with the default case corresponding to pure silicon (Pr=0.01) with a 3 × 3 distribution of elements (N=3), the variations are induced by a change in the height of the blocks and/or a variation in the considered boundary conditions. As illustrated in Section 2, the floor can be adiabatic or set at the same temperature of the blocks (hot floor), the lateral boundary can be solid and adiabatic or treated as a cyclic (or periodic) boundary condition (PBC).

5.2 Silicon Melt with Variable Block Height:

Figure 39 provide a first glimpse of the related patterning behavior in terms of 3D structure of the temperature field. It can be seen that, in general, regardless of the considered boundary conditions at the bottom and at the domain side, a distribution of hot spots can be identified at the free surface. Comparison of the results for a fixed value of δ_{vert} (aligned along columns in Figure 39) is instrumental in showing that a replacement of the adiabatic condition at the bottom with a hot floor generally leads (as expected) to an increase in the average temperature of the system and the temperature of the surface spots. Replacement of the solid lateral wall with PBC does not seem to have a big influence if the floor is adiabatic, whereas it can lead to a slightly more disordered pattern if PBCs are considered.

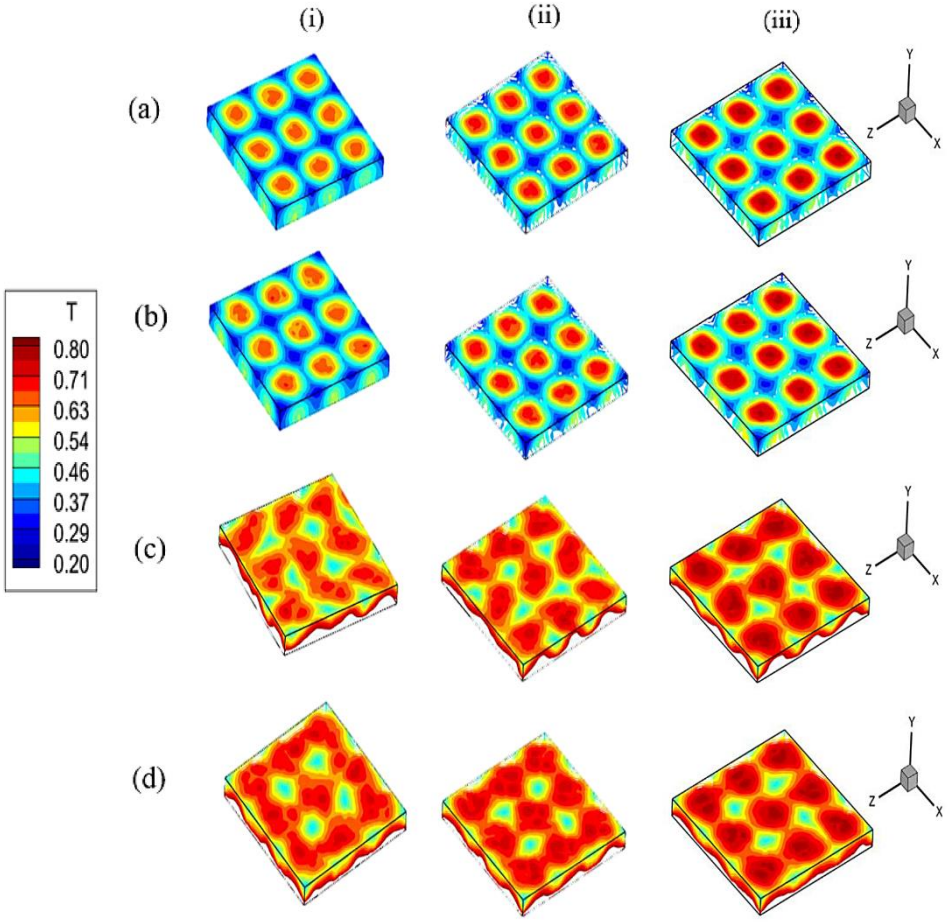

Figure 39: Three-dimensional (3D) Temperature snapshots (Pr=0.01, 3 × 3 configuration): (a) adiabatic floor with PBC, (b) adiabatic floor with lateral SW, (c) hot floor with lateral PBC, (d) hot floor with lateral SW; (i) δ_{vert}=0.5, (ii) δ_{vert}=0.6, (iii) δ_{vert}=0.7.

An increase in the vertical block extension, obviously makes the temperature of the surface spots higher as the distance between the top of the blocks and the free interface becomes smaller (see the results aligned along rows in Figure 39).

These results are naturally complemented by those reported in Figures 40 and 41. The former shows the corresponding temperature maps in a transversal section (plane xy), the latter concerns the velocity field. These confirm the trends discussed before in terms of expected rise in the temperature when the hot floor is considered, or the height of the blocks is increased.

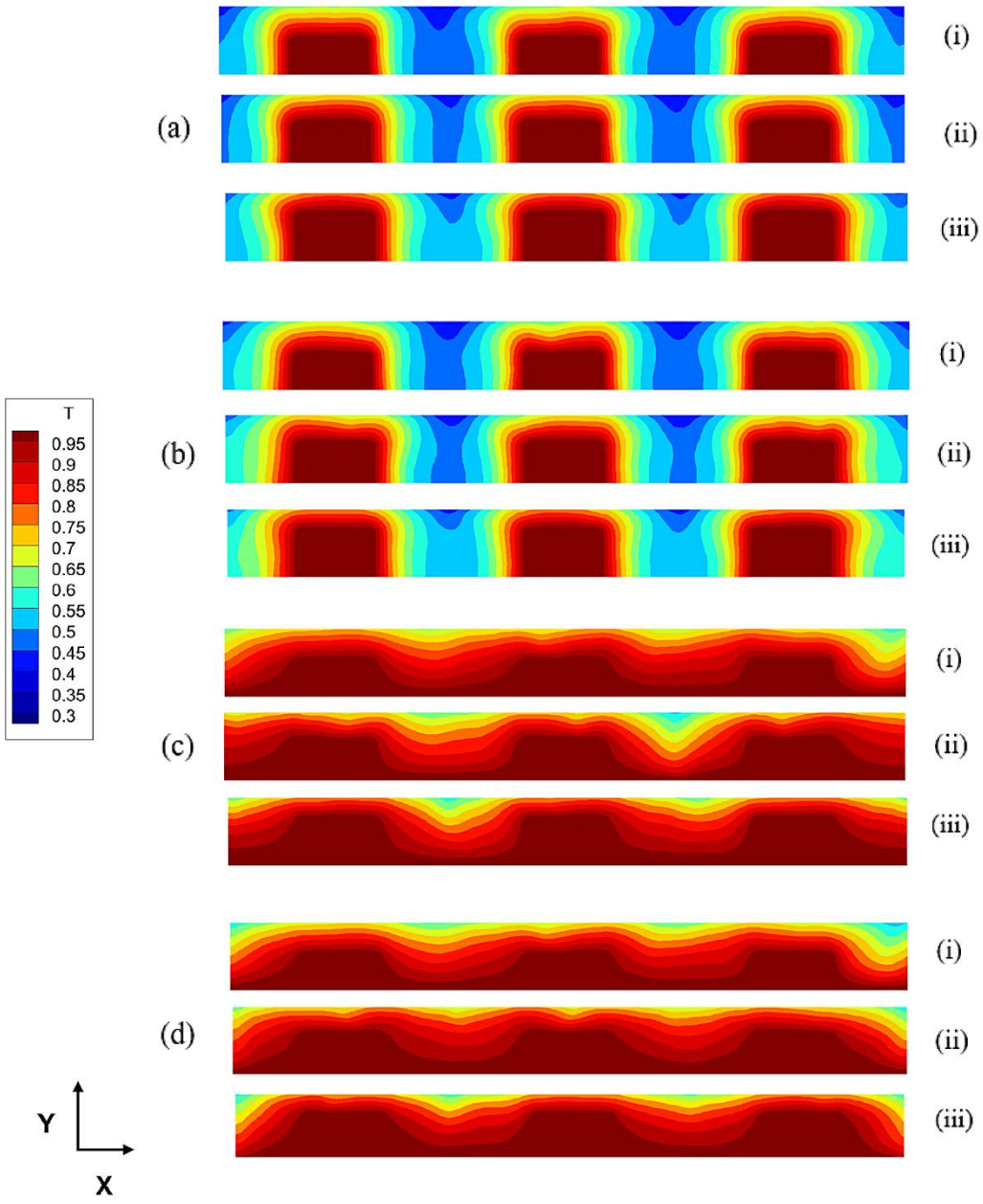

Figure 40. Temperature distribution snapshots in the plane z=5 (Pr=0.01, 3 × 3 configuration): (a) adiabatic floor with PBC, (b) adiabatic floor with lateral SW, (c) hot floor with lateral PBC, (d) hot floor with lateral SW; (i) δ_{vert}=0.5, (ii) δ_{vert}=0.6, (iii) δ_{vert}=0.7.

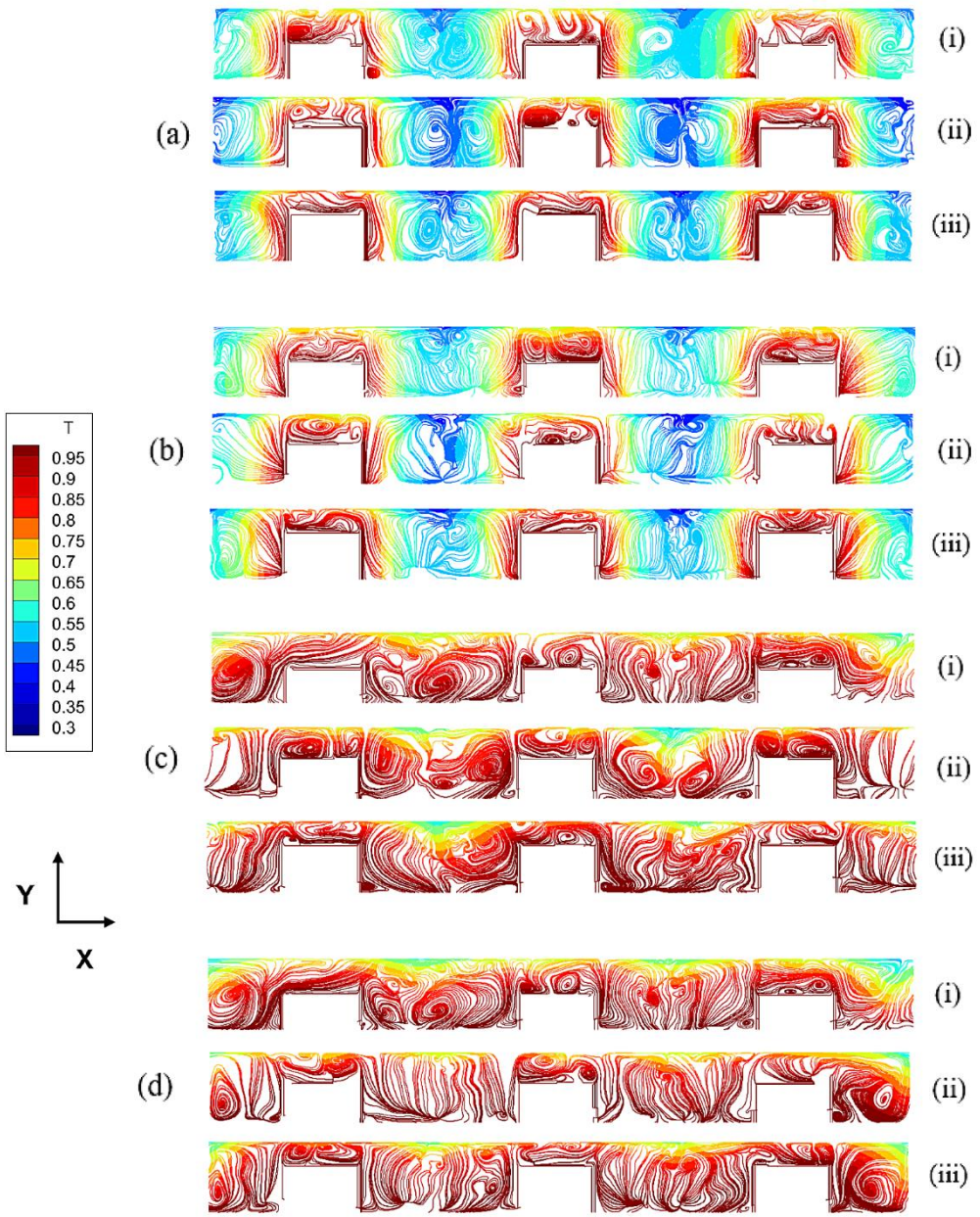

Figure 41. Snapshots of the streamlines of the velocity field projected on the z=5 plane, colored according to the corresponding distribution of temperature (Pr=0.01, 3 × 3 configuration): (a) adiabatic floor with PBC, (b) adiabatic floor with lateral SW, (c) hot floor with lateral PBC, (d) hot floor with lateral SW; (i) δ_{vert}=0.5, (ii) δ_{vert}=0.6, (iii) δ_{vert}=0.7.

In particular, as qualitatively substantiated by Figure 41, the velocity field can be more complex than the corresponding temperature distribution. As the reader will realize by inspecting this figure (showing the lines tangent to the projection of the instantaneous velocity field on the $z=A_z/2$ midplane, colored according to the corresponding distribution of temperature), the topology of such streamlines is quite intricate with vorticity being present in the form of more or less extended eddies both in the regions above the blocks and in the space between them (the former being reduced as δ_{vert} is increased).

5.3 Silicon Melt with Variable Number of Blocks

The next figure of the sequence (Figure 42) shows the 3D structures obtained when the number of blocks is increased from 3 × 3 to 5 × 5 while keeping their height fixed to 0.6.

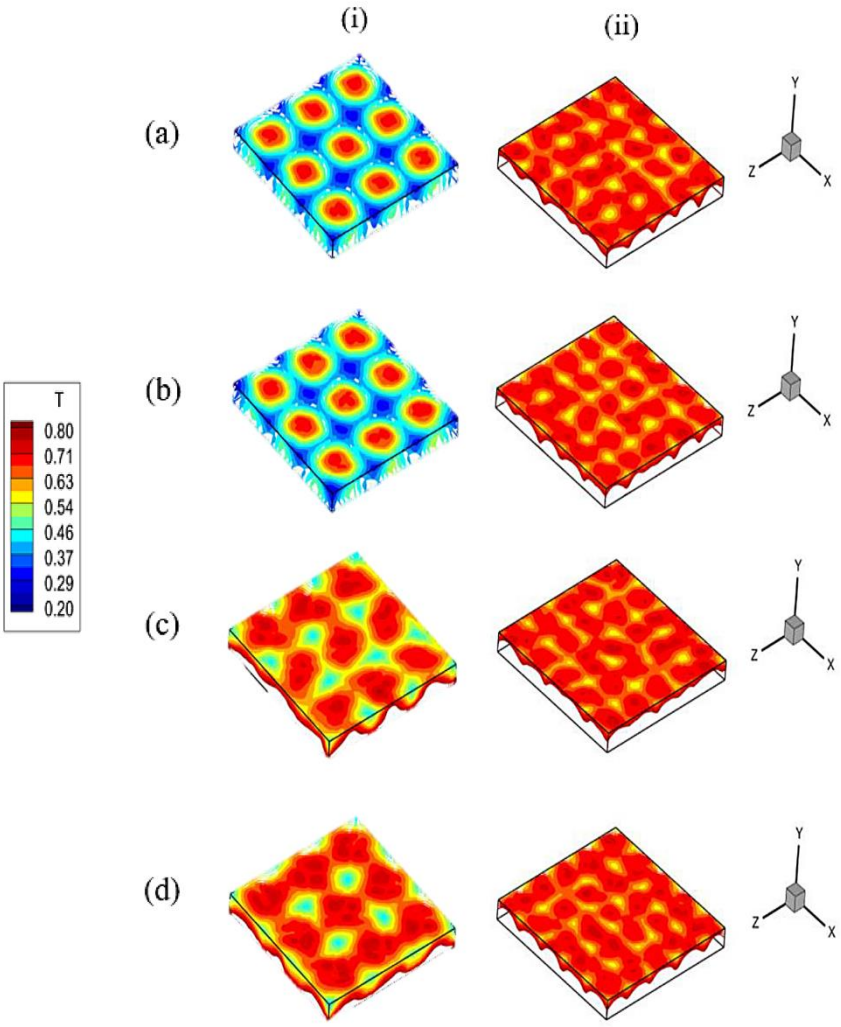

Figure 42. 3D Temperature snapshots (Pr=0.01, δ_{vert} =0.6): (a) adiabatic floor with PBC, (b) adiabatic floor with lateral SW, (c) hot floor with lateral PBC, (d) hot floor with lateral SW; (i) 3 × 3 array (ii) 5 × 5 array.

The most remarkable change clearly occurs in terms of multiplicity of the surface spots. However, significant modifications can also be detected in the distribution of temperature in the transversal sections (Figure 43). When the number of blocks is increased, the amount of heat being released in the fluid per unit time clearly increases causing an ensuing rise in the average system temperature. Along these lines, it can be seen that when the configuration with 5 × 5 blocks is considered, the differences between the cases with adiabatic and hot floor become less evident.

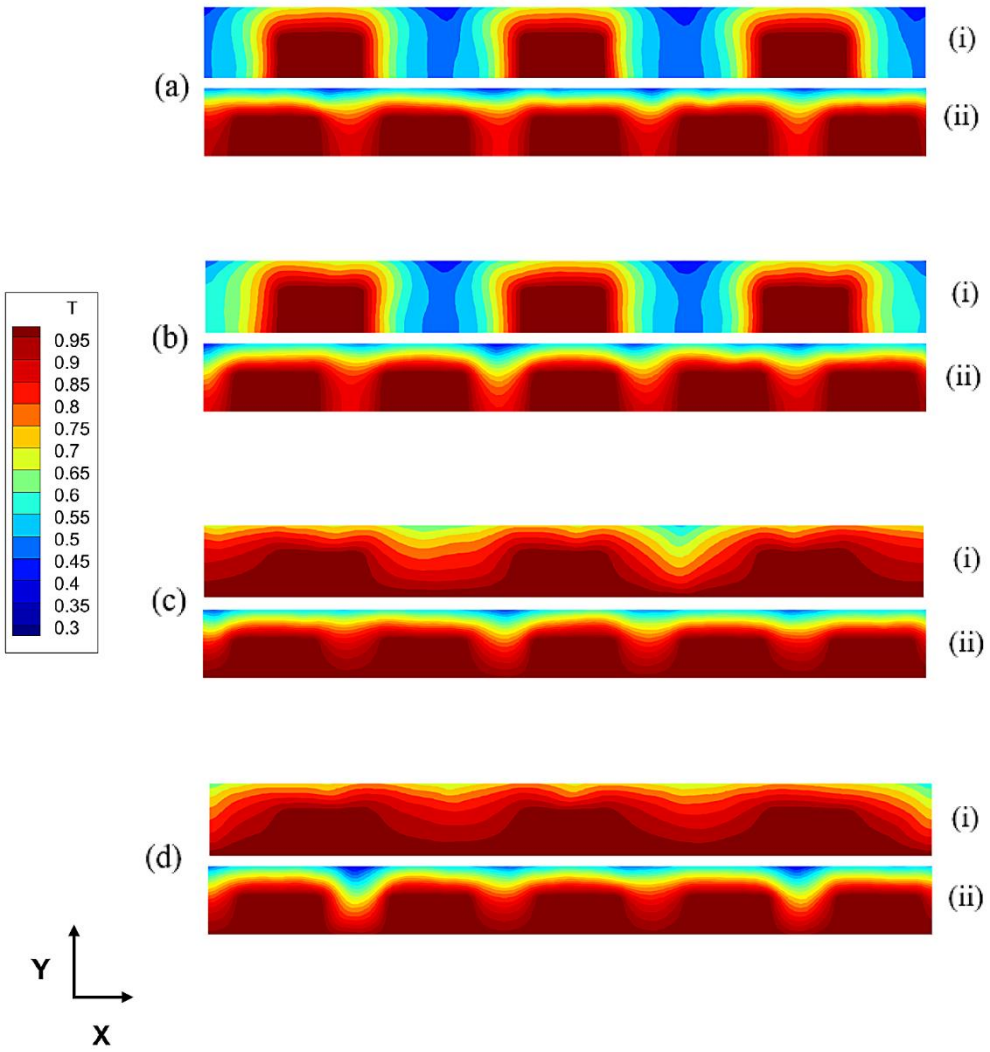

Figure 43. Temperature distribution snapshots in the plane z=5 (Pr=0.01, δ_{vert} =0.6): (a) adiabatic floor with PBC, (b) adiabatic floor with lateral SW, (c) hot floor with lateral PBC, (d) hot floor with lateral SW; (i) 3 × 3 array (ii) 5 × 5 array.

Finally, Figure 44 shows that an increase in the number of blocks also affects the topology of the streamlines; nevertheless, these retain their behavior with fluid rising from the top of the blocks towards the free interface and moving down in the regions between the blocks.

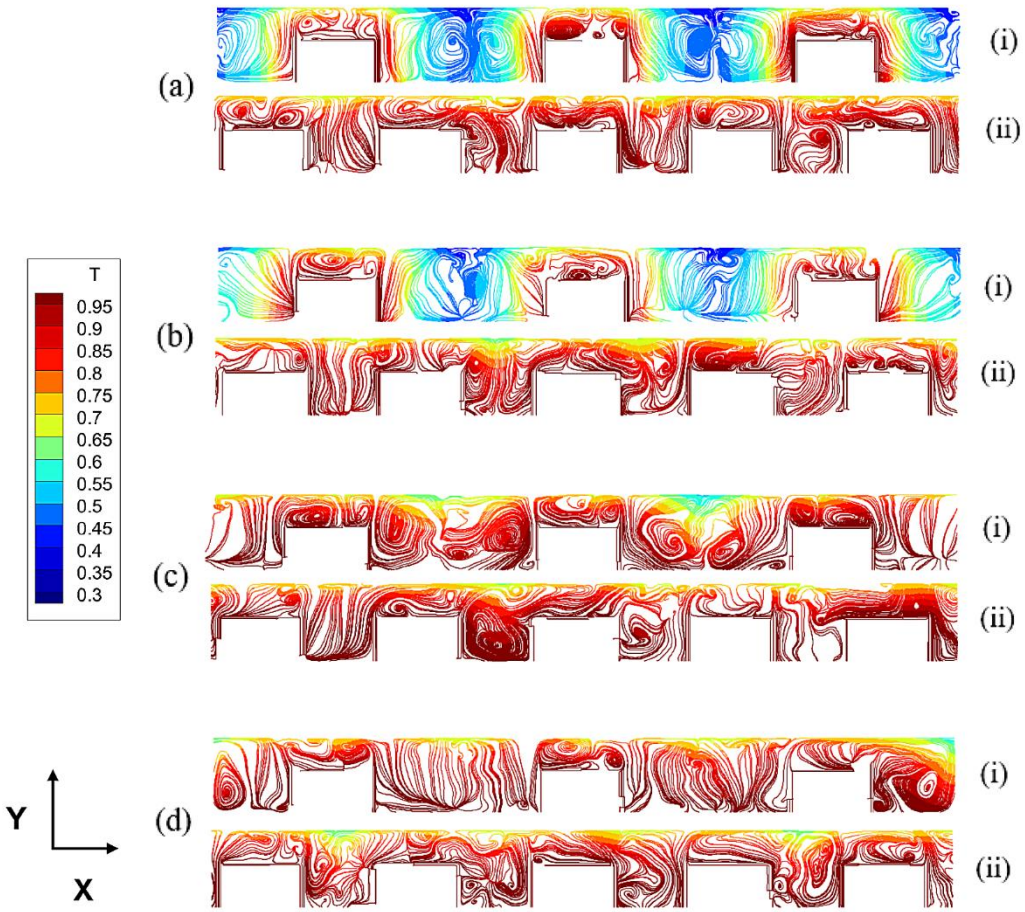

Figure 44. Snapshots of the streamlines of the velocity field projected on the z=5 plane, colored according to the corresponding temperature distribution (Pr=0.01, δ_{vert} =0.6): (a) adiabatic floor with PBC, (b) adiabatic floor with lateral SW, (c) hot floor with lateral PBC, (d) hot floor with lateral SW; (i) 3 × 3 array (ii) 5 × 5 array.

Most remarkably, taken together all these figures also lead to the conclusion that (in terms of patterning behavior) in the presence of a distribution of cubic blocks, thermal convection in a small-Pr fluid can retain neither the classical structure with elongated two-dimensional rolls typical of RB convection, nor the hexagonal-cell based topology of classical MB convection. Regardless of whether the floor is adiabatic or set at the same temperature of the blocks, the blocks create a kind of 'blockage' or act as barriers (or perturbing elements) that can break the two-dimensional rolls and prevent the system from developing a pattern with the honeycomb symmetry. On the other hand, varying the number of blocks can also have a non-negligible impact on the temporal response (time-dependence) of the flow. Before treating this specific aspect, the next sub-section is concerned with the influence of another significant parameter, i.e., the Prandtl number itself.

5.4 Effect of the Prandtl Number

As witnessed by Figure 45, on varying the Prandtl number for a fixed number (N=3 in this case) and given height of the blocks (δ_{vert} =0.6), significant changes can be induced in the system in terms of patterning behavior. This is more evident when the configuration with hot floor is considered and/or the Prandtl number is increased.

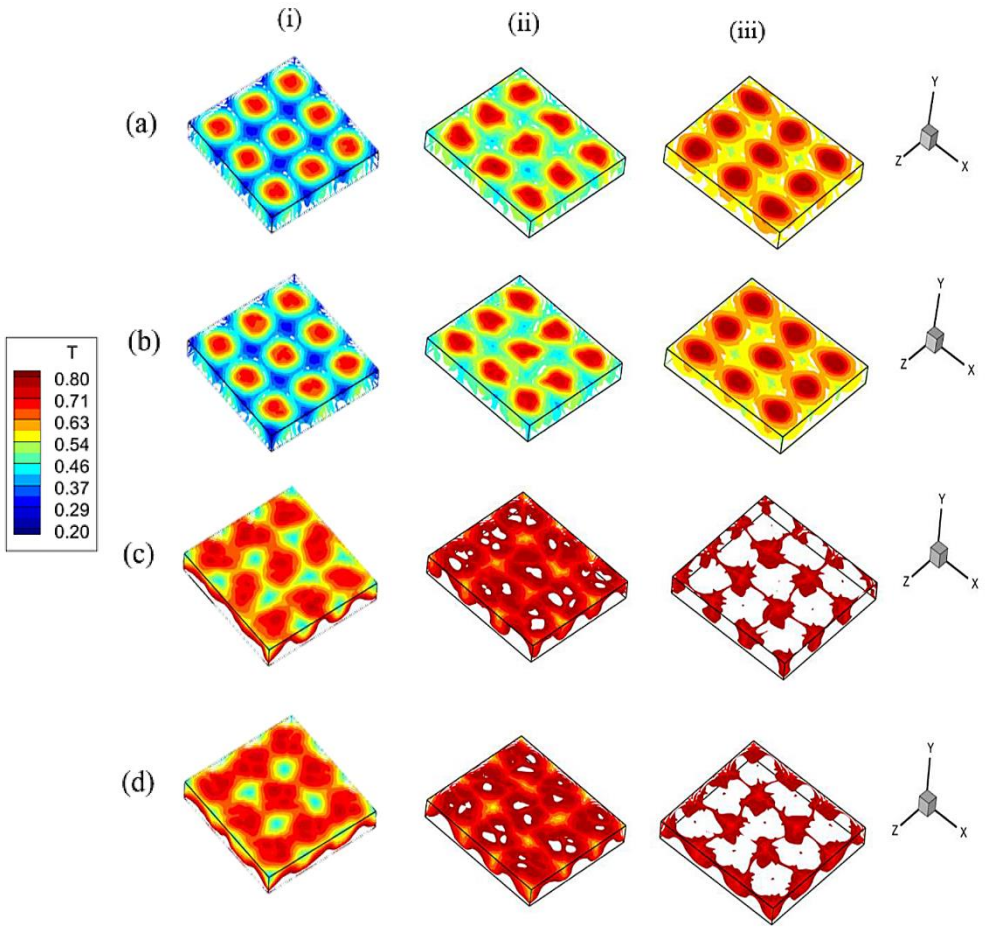

Figure 45. 3D Temperature snapshots (δ_{vert} =0.6): (a) adiabatic floor with PBC, (b) adiabatic floor with lateral SW, (c) hot floor with lateral PBC, (d) hot floor with lateral SW; (i) Pr=0.01 (ii) Pr=0.1 (iii) Pr=1.

For both Pr=0.1 and Pr=1 and hot floor condition (Figure 45(c, ii), (c, iii), (d,ii) and (d,iii)), the rising columns of hot fluid inside the layer no longer simply reflect the underlying distribution of hot blocks. In place of nine plumes evenly spaced along the x and z axes, a set of 4 × 4 thermal pillars are obtained.

As the reader will realize by taking a look at Figures 46 and 47, the increase in the visible number of columns of rising hot fluid (the aforementioned pillars) is due to a change in the process leading to plume formation. When the floor is hot and the Prandtl number is 0.1 or 1, plumes originate from the top corners of each block rather than from its center as it was for Pr=0.01. This should be ascribed to the increased ability of the vertical walls of the blocks to produce convection in such conditions.

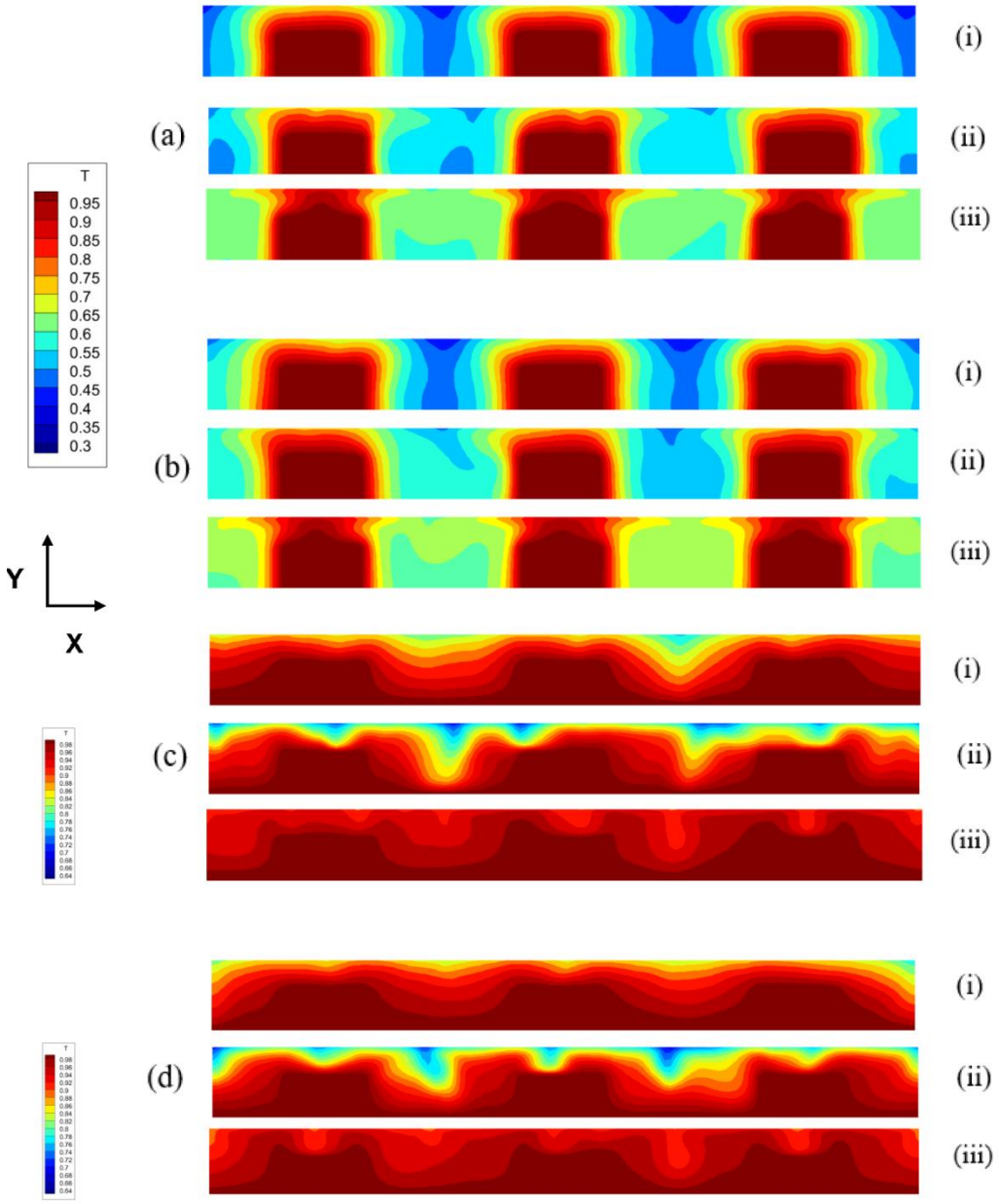

Figure 46. Temperature distribution snapshots in the plane z=5 (δ_{vert} =0.6): (a) adiabatic floor with PBC, (b) adiabatic floor with lateral SW, (c) hot floor with lateral PBC, (d) hot floor with lateral SW; (i) Pr=0.01 (ii) Pr=0.1 (iii) Pr=1.

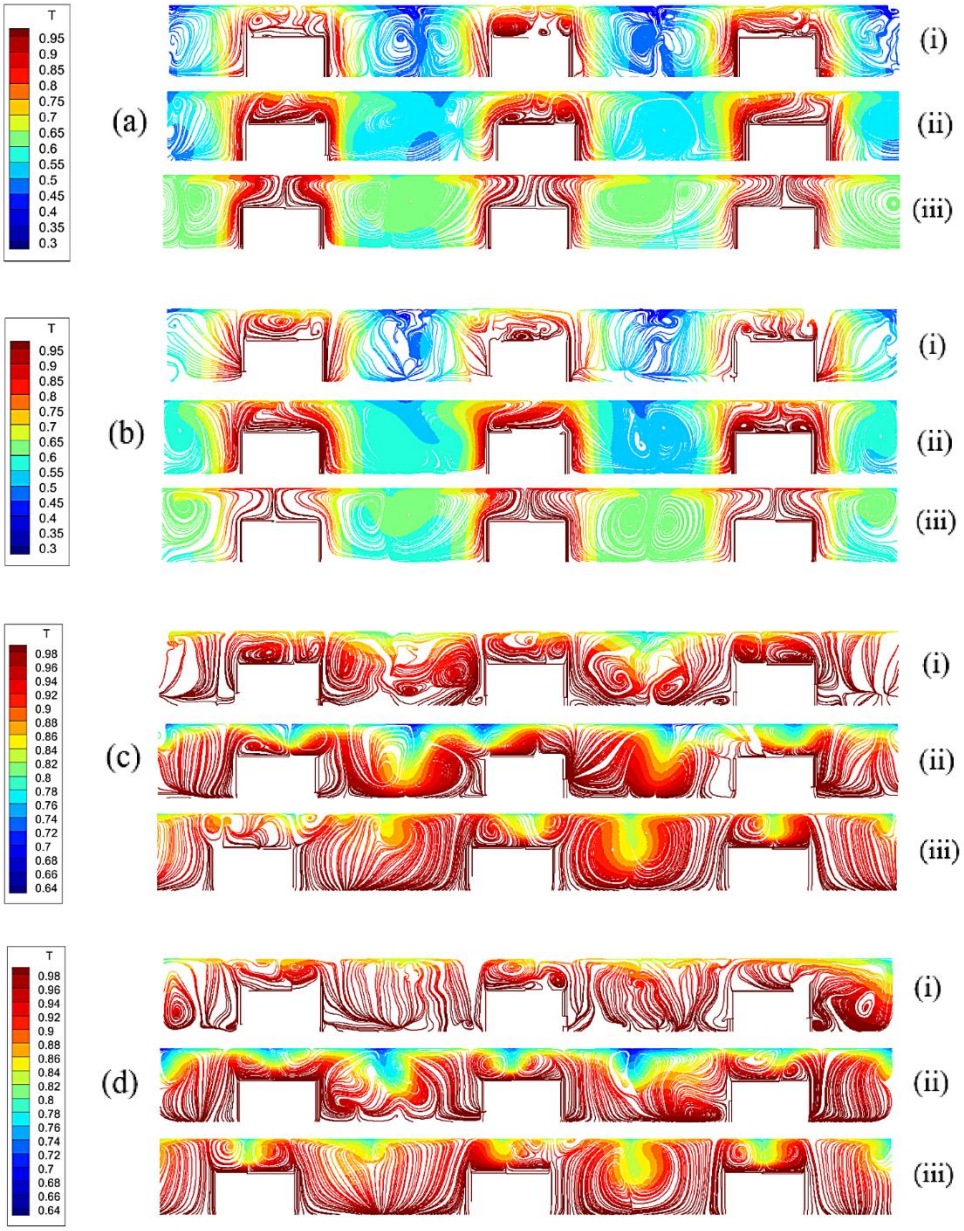

Figure 47. Snapshots of the streamlines of the velocity field projected on the z=5 plane, colored according to the corresponding temperature distribution (δ_{vert} =0.6): (a) adiabatic floor with PBC, (b) adiabatic floor with lateral SW, (c) hot floor with lateral PBC, (d) hot floor with lateral SW; (i) Pr=0.01 (ii) Pr=0.1 (iii) Pr=1.

5.5 Time-Dependence and Related Effects

This section is dedicated to treat an aspect that has been glossed over until now, namely the behavior of these systems from a temporal point of view.

In this regard, it is worth starting from the simple remark that, in all cases relatively similar dynamics have been observed, namely a flickering behavior of the plumes or 'pillars' discussed before due to localized oscillations of the vortical structures supporting them. In general, these localized oscillations have been observed to be relatively chaotic for the considered values of the Rayleigh and Marangoni number. The related spectra for Pr=0.01 can be seen in Figure 48.

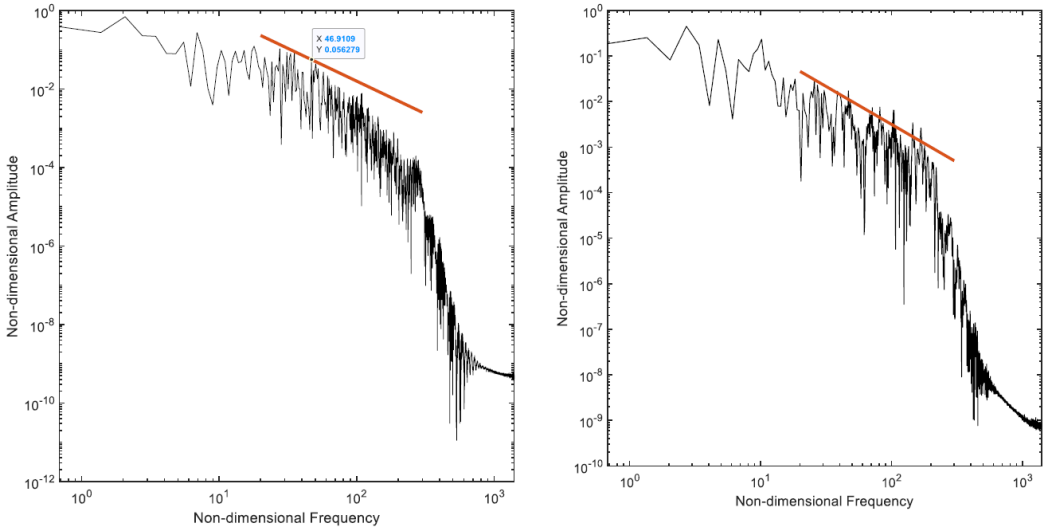

Figure 48. Frequency spectra for 3 × 3 (left) and 5 × 5 array (right) for adiabatic floor with lateral SW and δ_{vert} =0.6 (the red straight line indicates the Kolmogorov scaling; the spectra refer to the temperature signal measured by a probe located above one of the heated blocks, at y=0.8).

Some meaningful information can be gathered from this figure as follows.

A range of frequencies can be identified where the spectrum follows the so-called Kolmogorov law (highlighted using a red straight line in the figure). Roughly speaking, this law states that a range of wavenumbers exists in space [k_1, k_2], where the energy density of the flow E scales as $k^{-5/3}$ (where k denotes the wavenumber). In a completely equivalent way (because in terms of vorticity the local flow velocity turnover cycle depends on the length scale) the same law can be formulated stating that a range of frequencies exist in time where the energy density of the flow E scales as $\omega^{-5/3}$ (where ω denotes the angular frequency, see, e.g., (De, Eswaran and Mishra, 2017)). This is a well-known outcome of a theory originally elaborated by Kolmogorov, 1942; where it was postulated that, while the large scales of a flow are not isotropic because they are influenced by the specific geometry of the considered domain and the nature of the forces driving it, the memory of this geometrical and directional information is progressively lost while energy cascades from large to smaller scales. In other words, a range of scales should exist where small-scale turbulent motions are statistically isotropic (i.e., no preferential spatial direction can be identified) before the kinetic energy reaches a scale where it is finally converted into internal energy (heat) due to dissipative (frictional) effects.

Cross comparison of Figure 48a,b leads to the conclusion that if the number of blocks is increased, the spectra are very similar, although, the latter seems to align with the Kolmogorov law over a slightly larger interval.

Along these lines, Figure 49 reveals that an increase in the Prandtl number can make the spectrum slightly more energetic in the range of high frequencies, which, in agreement with the observations reported in the earlier sections, can be explained considering the excitation of smaller scale features in the flow.

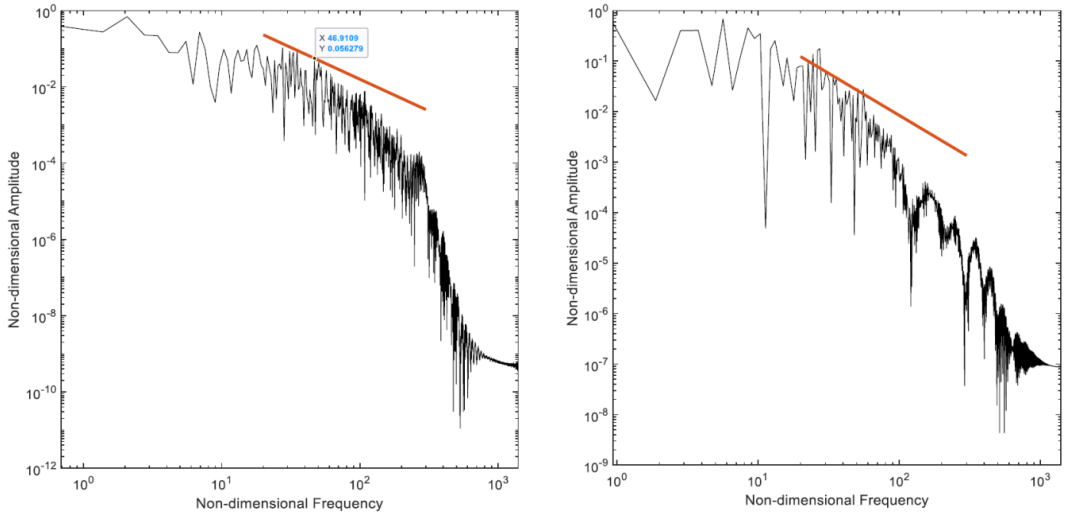

Figure 49. Frequency spectra for Pr=0.01 (left), Pr=0.1 (right) for adiabatic floor with lateral SW and δ_{vert} =0.6 (the red straight line indicates the Kolmogorov scaling; the spectra refer to the temperature signal measured by a probe located above one of the heated blocks, at y=0.8).

5.6 Heat Exchange Effects

In line with the approach implemented by Biswas (Biswas, Mahapatra, Manna, and Roy, 2016) and other authors, further characterization of these systems can be obtained through evaluation of the Nusselt number on the basis of Equations (13) – (18).

Relevant information about the dependence of $Nu_{side}^{average}$, $Nu_{top}^{average}$ and $Nu_{bar}^{average}$ on Pr, N and δ_{vert}, has been summarized in Tables 3–5, respectively.

Table 3 . As a function of Pr, N, δ_{vert} and the considered boundary conditions.

Pr	N	δ_{vert}	Adiabatic Floor, Lateral PBC	Adiabatic Floor, Lateral SW	Hot Floor, Lateral PBC	Hot Floor, Lateral SW
0.01	3	0.5	1.9812	2.0203	0.3864	0.2839
0.01	3	0.6	1.7447	1.7915	0.3351	0.2613
0.01	3	0.7	1.6406	1.6601	0.3313	0.3038
0.01	5	0.6	0.6150	0.6175	0.3691	0.3662
0.1	3	0.6	2.2188	2.1873	0.2822	0.2850
1.0	3	0.6	2.4194	2.4497	0.3880	0.4203

Table 4. As a function of Pr, N, δvert and the considered boundary conditions.

Pr	N	δ_{vert}	Adiabatic Floor, Lateral PBC	Adiabatic Floor, Lateral SW	Hot Floor, Lateral PBC	Hot Floor, Lateral SW
0.01	3	0.5	1.5137	1.5138	1.0898	0.9938
0.01	3	0.6	1.5025	1.4941	1.1511	1.1057
0.01	3	0.7	1.4867	1.4908	1.2336	1.2357
0.01	5	0.6	1.2531	1.2374	1.2176	1.2283
0.1	3	0.6	1.3962	1.4032	1.0314	1.0317
1.0	3	0.6	1.5760	1.5952	0.8291	0.9107

Table 5: $Nu_{bar}^{average}$ as a function of Pr, N, δvert and the considered boundary conditions.

Pr	N	δ_{vert}	Adiabatic Floor, Lateral PBC	Adiabatic Floor, Lateral SW	Hot Floor, Lateral PBC	Hot Floor, Lateral SW
0.01	3	0.5	1.8254	1.8514	0.62085	0.5205
0.01	3	0.6	1.6735	1.7041	0.5751	0.5096
0.01	3	0.7	1.6001	1.6155	0.5688	0.5491
0.01	5	0.6	0.8027	0.800	0.6187	0.6198
0.1	3	0.6	1.9768	1.9567	0.5026	0.5046
1.0	3	0.6	2.1714	2.1984	0.5178	0.5645

The most striking effect that can be seen in these tables concerns the weakening of heat exchange when the adiabatic floor is replaced with a (hot) isothermal boundary. This change, which occurs regardless of the considered value of Pr, *N* or δ_{vert}, can be ascribed to the rise in the average temperature of the liquid when the floor is hot (clearly visible in Figures 40, 43 and 46). As a result of such an increase, the difference between the temperature of the liquid and the top or lateral surfaces of the blocks becomes smaller, thereby lowering the related Nusselt numbers. As similar mechanism is responsible for the decrease in $Nu_{bar}^{average}$ when δ_{vert} is increased for fixed Pr, *N* and assuming the adiabatic floor. Although $Nu_{top}^{average}$ does not change much, making the blocks taller leads to an appreciable shrinkage in the values of $Nu_{side}^{average}$ owing to the larger amount of heat that is released accordingly in the surrounding fluid and the ensuing increase in temperature. The same arguments also apply to the cases with a larger number of *N*. Yet for the case with adiabatic floor, if *N* is increased from 3 to 5 while keeping the other parameters unchanged, the Nusselt numbers become smaller and approach the values obtained in the corresponding situations with the hot floor. This is due to a three-fold effect, namely the increase in the average temperature of the system, the weakening of temperature gradients present in the liquid and the ensuing damping of convection driven by such gradients.

As a concluding remark for this section, it is also worth noting that, on increasing the Prandtl number, the average heat exchange occurring between the blocks and the surrounding fluid (as quantified by $Nu_{bar}^{average}$) becomes more intense, and the simplest way to justify this dependence is to consider a decrease in the thickness of the thermal boundary layers formed along the horizontal and vertical surfaces of the hot blocks.

5.7 Discussion and Conclusions

In this section some additional insights into the considered problem are sought through comparison with 'companion problems', not necessarily linked to thermal convection driven by buoyancy of Marangoni effects.

As already discussed in the introduction of this thesis, a first quite relevant exemplar can be found in the field concerned with the cooling of printed circuit boards and the assessment of the related thermal performances (Liu and Phan-Thien, 2000; Chuang, Chiang and Kuo, 2003; Rahman, Alim S. Saha and Chowdhury, 1970; Tyacke and Tucker, 2012). These problems are generally modeled considering the horizontal flow over a matrix of wall-mounted 'cubes', some of which behave as heat-producing sources. The professional and researchers involved in this field are typically interested in evaluating the local heat transfer coefficients owing to their strong connection with the lifespan and reliability of microprocessors and memories. In turn, these coefficients are highly dependent on geometrical factors such as the size of the considered chip, its relative position with respect to other electronic components, and the 'channel height' (i.e., the distance between the upper and lower printed circuit boards). Models based on a staggered arrangement of finite-size squared elements, however, are not an exclusive prerogative of this specific area. Parallelepipedic items fully submerged in a (mathematically reconstructed) urban atmospheric boundary layer, can also be used to model the interaction of wind with an array of buildings (Nakayama, Takemi and Nagai, 2011) or with a set of power generators (power plants, (Lappa, 2019a)). In these cases, the elements are typically staggered in the downstream direction and periodically arranged in the streamwise and/or spanwise directions. Taken together, all these efforts have shown that flow interruptions created in flow passages at periodic intervals can result in a variety of fluid-dynamic effects. These include flow separation at the sharp leading top of each element, flow recirculation originating from side edges with subsequent flow reattachment along these faces, arc-type vortices formed in the wake of any upstream cube, horseshoe-type vortices in front of the downstream cubes and other flow instabilities causing vortex shedding at the side faces of the elements (and ensuing small-scale turbulence in the near wake region (Meinders and Hanjali, 1999).

Although the physics of the problem examined in the present chapter is quite different, referring to this companion category of phenomena is useful because such studies have shown that a variation in the gap between two items can produce significant changes in the heat transfer process. In those cases such modifications are essentially due to the different 'level of blockage' that is induced in the flow when the spacing among the protuberances is altered. The resulting flow physics is made extremely complex by the interplay of the horizontal flow with the related solid boundaries and the ensuing generation of a large number of (mutually interacting) vortex systems, and regions of relatively stagnant fluid. This complex physics, in turn, significantly affects the heat transfer mechanisms.

Obviously, the concept of blockage is not applicable directly to the present conditions, where the heated elements (regardless of whether the dominant driving force is buoyancy or thermocapillary) represent the source of convection rather than factors hindering it. Moreover, the role of the cold 'wind' entering the domain hosting the hot elements is taken on by the heat exchange with the external gaseous environment through the top free liquid/gas interface (which acts as an extended heat sink for the entire system). Another interesting observation is

that, despite these differences in the characteristic directions of fluid flow and heat transfer, some useful similarities can still be identified by simply replacing the notion of blockage with that of 'heat island' (visible in Figure 43). Just like portions of stagnant fluid can contribute to weaken heat exchange effects in a fluid blowing through a set of warm solid blocks, regions of stagnant heat (due to the excessive proximity of adjoining hot elements) can hamper the mechanism producing natural convection thereby causing a decrease in the Nusselt number.

Additional affinity can also be identified in the tendency of both categories of systems to develop turbulence or relatively chaotic solutions in some circumstances, i.e., large values of the Reynolds and Marangoni numbers, respectively (both account for the strength of horizontally directed flow). In the wind-obstacles problem, such complex states are essentially the outcome of purely hydrodynamic effects and related bifurcations (Lappa, 2019a; Yaghoubi and Velayati, 2005; Coceal, Dobre, Thomas and Belcher, 2007; Leonardi and Castro, 2010; Basara, 2015; Saeedi and Wang, 2015; Blackman and Perret, 2016 and Khan and Saha, 2021).In addition, if hybrid buoyancy-Marangoni convection induced by hot blocks in liquid metals is considered, the frequency spectra still align with the Kolmogorov law in a certain range of frequencies.

Some general conclusions on the basis of the findings presented in Sections 5.2-5.5 and the analogy with the companion category of phenomena discussed in the present section, can therefore be drawn as follows. Though quite limited in terms of depth and scope due to the extremely long time required by the simulations, the present work has shown that a topography at the bottom of a layer of liquid metal coupled with a thermal inhomogeneity can deeply alter the flow with respect to the patterns which would be produced in the equivalent conditions without blocks. The presence of obstructions prevents the layer from forming the horizontally extended rolls or the hexagonal cells, which would be typical of RB and MB convection, respectively.

While the outcomes of an increase in the height of the blocks are generally limited to a rise in the temperature of the hot spots produced by rising thermal currents that meet the free surface, an increase in their numbers can make the average temperature of the entire fluid layer much higher. As a result, the difference between the configuration with adiabatic and isothermal (at the same temperature of the blocks) floor becomes less evident.

On increasing the Prandtl number in the range from 0.01 to 1 even more interesting phenomenon are enabled. Owing to a shift in the location of the regions from which thermal plumes originate (from the center of the top surface of blocks to their edges), the perfect correspondence between the disposition of hot blocks at the bottom and the set of hot spots on the free surface is lost. In such conditions the multiplicity of surface spots overcomes that of the underlying matrix of heat sources.

Regardless of the considered value of the Prandtl number or the boundary conditions at the bottom and at the lateral boundary, in place of the traveling waves known to be the typical outcome of the first Hopf bifurcation for both RM and MB classical forms of convection in liquid metals, unsteadiness is due to small oscillations in time of the thermal pillars. Analysis of the related frequency spectra has revealed that a range of frequencies exists where the spectrum aligns with the prediction of the Kolmogorov theory for isotropic homogeneous turbulence and that the extension of such a range depends on the specific conditions considered.

Future studies shall be devoted to determine the minimum height of the blocks for which the formation of classical hexagonal cells or traveling waves is prevented, assess the system response when the horizontal size of the blocks is varied continuously in a given range, analyze all these behaviors also for other values of the Marangoni and Rayleigh numbers, and eventually exploit relevant turbulence models (such as those elaborated by De, Eswaran and Mishra, 2017) to reduce the otherwise prohibitive computational times required by DNS).

Chapter 6: Topographically Controlled Marangoni–Rayleigh–Bénard Convection in Oil:

Having completed the treatment for small values of the Prandtl number ($0.01 \leq Pr \leq 1$) in Chapter 5, in this chapter the case of a high-Pr fluid is considered, that is a transparent oil. Without loss of generality the analysis is restricted to Pr=10 (a value representative of a vast category of high-Prandtl number fluids) and unit Biot number (Bi=1). Moreover, a square layer with relatively large aspect ratio (horizontal extension/depth) is considered, i.e., $A_x=A_z=A_{horiz}=10$; accordingly set $\delta_x=\delta_z$ (hereafter simply referred to as δ_{horiz}, i.e. the heated solid elements have a square basis) and N=M (i.e. the number of elements along x reflects the corresponding distribution of elements along the z direction, and vice versa).

As a key to unlocking the puzzle about the relationship between the emerging pattern and the imposed boundary conditions, it was decided to vary parametrically the number of square rods present in the regular array (NxN from 3x3 to 9x9 passing through intermediate states 5x5 and 7x7). Not to increase excessively the dimensionality of the space of parameters, the vertical extension of the rods is fixed to δ_y=0.3 (hereafter simply referred to as δ_{vert}, corresponding to 30% of the overall depth of the liquid layer), while three distinct values are selected for δ_{horiz} (namely, 0.1, 0.55 and 1.0). This allows us to change the spacing among the elements while retaining the same overall number NxN. As anticipated in Sect. 3.1 (Chapter#3), as an additional degree of freedom, the portions of flat surface (at the bottom) separating adjoining elements are considered adiabatic (thermally insulated) or isothermal (at the same temperature as the heated elements). Moreover, no-slip conditions (finite-size horizontal extension) or periodic boundary conditions (to mimic an infinite layer) are imposed at the lateral boundaries.

Since in the absence of observational information to properly constrain the model parameters, considering asymptotic conditions in which a new problem reduces to already known paradigms is beneficial, this chapter also examines the cases with uniform heating, or a single heat source (heated bar) located in the geometric center of the physical domain (these two models being obviously opposite extremes with respect to the situations mathematically described by eq. (8) (Sect. 3.2). Moreover, towards the end to assess the separate influence of buoyancy and Marangoni effects, the simulations are conducted by setting Ma and Ra to their intended values and 'switching off' alternately one of them (the complementary situations with Ma=0 or Ra=0 being obviously instrumental in discerning the pure gravitational or surface-tension driven phenomena). To limit the otherwise prohibitive scale of the problem thus defined, the ratio of the Rayleigh and Marangoni numbers (Bo_{dyn}) is fixed to 2, i.e. $Ra=10^4$ and $Ma=5\times10^3$ (assuming a realistic Pr=10 oil with kinematic viscosity $\nu=6.5\times10^{-7}$ m^2/s, thermal diffusivity $\alpha=6.5\times10^{-6}$ m^2/s, density $\rho\cong0.97\times10^3$ kg/m^3, thermal expansion coefficient $\beta_T=10^{-3}$ K^{-1}, surface tension derivative $\sigma_T = 6\times10^{-5}$ N/mK, this would correspond to a layer with depth d≅3.5 mm and a $\Delta T\cong$1 K).

In the present thesis ΔT accounts for the temperature difference between the bottom plate and the 'ambient' (gas) temperature (see Chapter 4). Using the same definition of the Marangoni number traditionally adopted in the frame of LSA and similar studies on MB convection, the Ma_{LSA} corresponding to the present value 5000 would be 2500, which is very close to the case that (Thess, 1995; Thess and Orszag, 1995) examined in the limit as $Pr \to \infty$ (this interesting observation will be further developed later).

All the simulations have been run for a time sufficiently long to allow the Nusselt number to reach asymptotic (time-independent) values for the cases where the flow is stationary (generally a period corresponding to 4 times the thermally diffusive time based on the depth of the layer, i.e., $t_\alpha = d^2/\alpha$). The equations have been integrated with a non-dimensional time step 2.5×10^{-6} (therefore requiring more than one million of steps for each case). For time-dependent solutions, the simulations have been extended to a non-dimensional time t=10. Given the density of the mesh (5×10^5 grid points), three continuous months of calculations have been required using an 8-core workstation to produce all the results reported in the following subsections.

6.1 The purely buoyant case:

Following the approach outlined above, a first sub-set of numerical findings for the purely gravitational situation (no surface tension effects being considered) are presented in Figs. 50-52. These refer to the situation with adiabatic floor. In particular, Fig. 50 relates to the simplest possible case, i.e., the configuration with a single block located at the center.

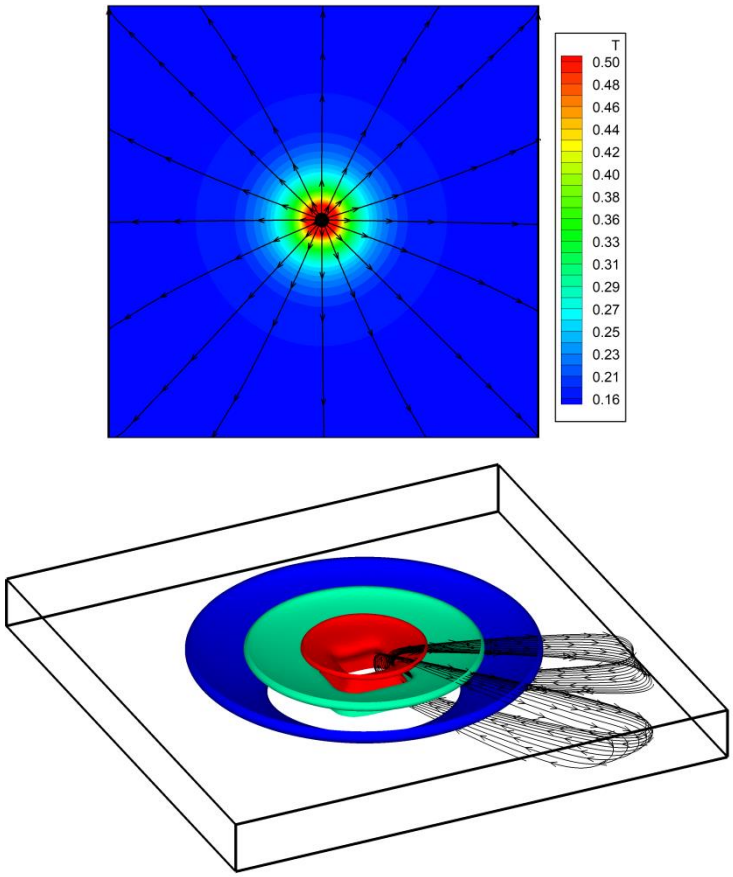

Figure 50: Temperature and velocity fields for pure buoyancy convection ($Ra=10^4$, Ma=0, Bi=1) and single block with $\delta_{horiz}=1$ (otherwise adiabatic floor): temperature and streamlines distribution at the free interface (left); and Isosurfaces of temperature (blue=0.11, green=0.22, red=0.41) shown in combination with two representative bundles of streamlines (right). The bowl shape of the temperature Isosurfaces reflects the toroidal structure of the single annular roll established in the cavity; hot fluid is transported from the center towards the lateral walls at the interface, while relatively cold fluid moves in the opposite direction along the bottom wall. $Nu_{side} \cong 6.32$, $Nu_{top} \cong 5.12$ and $Nu_{bar} \cong 5.78$.

In agreement with the observations reported in earlier works (see, e.g., the numerical investigation by Sezai, 2000), the reader will recognize in this figure the classical convective structure with hot fluid rising just above the top surface of the heated block, reaching the top of the boundary (the free surface exchanging heat with the external gas in present case, as opposed to the solid cold wall considered by Sezai, 2000), then spreading radially outward towards the sidewalls where it finally turns downward and moves back in the radial direction towards the source where it was generated.

Following up on the previous point, Fig. 51 provides a first glimpse of all the considered geometrical configurations and the related (surface temperature) patterns after transients have decayed away when the number of blocks is increased from one to larger numbers.

As a property common to many different cases, it can be noticed that for a relatively 'dilute' distribution of blocks (i.e., a not too high value of N), each of them contributes to the emergence of a well-defined plume similar to that obtained for N=1. This is witnessed by the visible presence of a 'set' of distinguishable approximately circular spots on the free surface. Each of these warm areas corresponds to the localized region where a current of rising hot fluid meets the liquid/gas interface (where heat exchange with the external environment takes place).

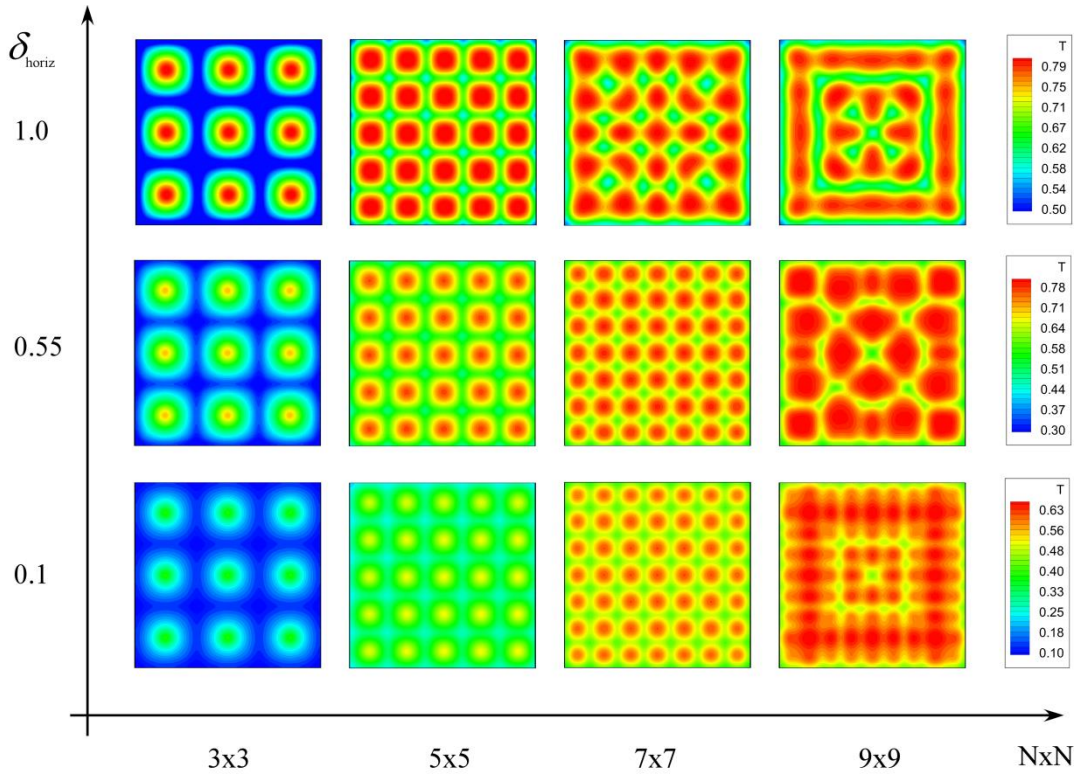

Figure 51: Survey of patterns (surface temperature distribution) obtained by varying N in the range between 3 and 9 for δ_{horiz}=1, 0.55 and 0.1 (pure buoyancy convection, adiabatic floor).

The significance of these figures primarily resides in their ability to make evident that for relatively large spacing of the heated elements, the plumes are independent, i.e., they do not interact and do not coalescence. However, they also reveal that if the spacing is reduced (by increasing N), at a certain stage, non-trivial planforms are produced, i.e. patterns with well-defined properties which do not simply reflect the (a-priori-set) order of the underlying grid of hot blocks.

In particular, for δ_{horiz}=1, i.e., unit horizontal extension of the element side (first row of Fig. 51), a perfect *1:1 correspondence* can be established between sources and plumes for both N=3 and N=5. The change from these obvious behaviors to more interesting ones occurs for N=7. For this value of N, as a result of plume interaction the number of recognizable hot spots at the free surface decreases. More precisely, as opposed to situations with smaller N, for which the location of rising currents is simply consistent with the related distribution of heat sources, an external observer looking at the free surface of the configuration with N=7 would naturally be induced to map the set of plumes into an array with lower dimensions, i.e., a 5x5 matrix.

When N is finally increased to N=9, the percentage decrease in the number of plumes is even larger in comparison to the multiplicity of the underlying (9x9) grid of sources. In fact, only five plumes can be detected along each sidewall parallel to the x or the z axes (Fig. 51, first row, last panel). In the central area, the patterning behavior is slightly more complex than in other cases as some plumes undergo complete coalescence resulting in a kind of (hot) circuit embracing the aforementioned central cold plume. In turn, this plume is surrounded by a set of other four descending currents slightly displaced in the radial direction along the main diagonals of the domain (Fig. 52a).

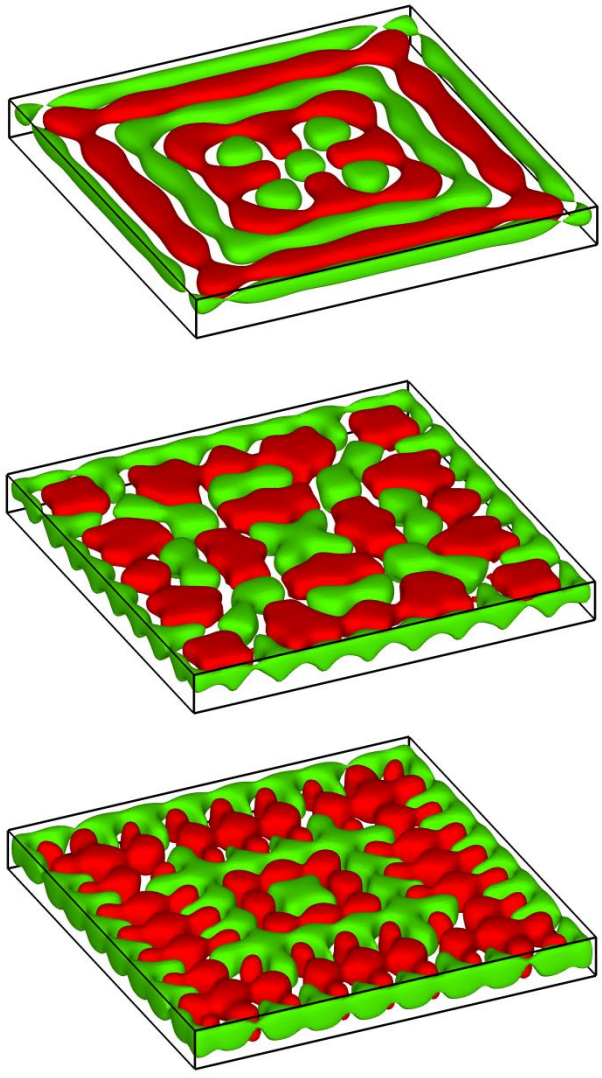

Figure 52: Isosurfaces of vertical velocity component (green=-3,5, red=3.5, pure buoyancy convection, adiabatic floor, N=9): a) δ_{horiz}=1; b) δ_{horiz}=0.55; c) δ_{horiz}=0.1.

A similar scenario still holds when elements with a different (smaller) transverse extension are considered (i.e., situations for which δ_{horiz} <1). As yet made evident by Fig. 51 (second row), on increasing N, coalescence of vertical (rising) currents is still enabled as a given threshold is exceeded. Thereby there is evidence that, just like the parent form of convection with uniform heating at the bottom (Rayleigh-Bénard convection), these systems still contain their own capacity for transformation, which requires only the right conditions for activation (in particular, the smaller δ_{horiz}, the higher the required value of N to make this ability effective). Along these lines, Fig. 52b illustrates in detail the 3D structure of the emerging pattern for a 9x9 grid of elements and δ_{horiz}=0.55. Such a figure is useful as it clearly shows that, once plume merging mechanisms are excited, the effective topology of the thermal plumes sensitively depends on δ_{horiz}.

For N=9 and δ_{horiz}=0.55, a single cross-shaped cold current pops up in the center of the domain. It is surrounded by four thermal pillars. These four hot 'blobs', in turn, are encapsulated in a polygonal circulation system consisting of a discrete set of cold (descending) currents. Along each sidewall, a total of 5 well-defined hot plumes can be discerned, which may be regarded as another distinguishing mark with respect to the pattern reported in Fig. 52a.

When δ_{horiz} is finally reduced to 0.1, the morphology of the 3D pattern becomes even more intricate. In this case, seven rising plumes are established along each wall (in such a way that by looking at the pattern from above, an observer would get the illusion of a 'square' circuit). A more internal ring (yet with square shape) of descending plumes (4 along each direction) separates the external hot circuit from a more internal (yet hot) one with three plumes along each side and an embedded (central) single descending current.

Following up on these observations, very interesting aspects concern the symmetries, which are broken or retained. In such a context it is worth recalling briefly that the considered square configuration with a free surface has the symmetries of the dihedral group D_4, that is, the group of symmetries of a regular polygon with 4 vertices. These include the reflections S_0, S_1, S_2, and S_3 (where the generic S_k is the reflection about the line through the center of the square making an angle of $\pi k/4$ with one of its sides, e.g., the x axis in this case). The chosen disposition of the blocks allows to keep these symmetries, whereas the up-down symmetry is not valid because of the free upper surface and the presence of blocks.

It is interesting to see that all the buoyant cases (Fig. 51) keep all the symmetries of the D_4 group. The related patterns are also all steady. This suggests that no bifurcation occurs in this case when the size of the blocks is increased and that there is a continuous evolution between the cases with different sizes of blocks, even when the correspondence between the blocks and the surface distribution of hot spots is lost, for example for the 7 × 7 case when δ_{horiz} is changed from 0.55 to 1. In terms of wavenumbers of the dominant structures in the flow, while for the trivial cases it can be simply expressed as $2\pi N/A_{horiz}$, the wavenumbers present in the pattern for the other cases (determined through analysis of the surface temperature distribution) are k≅2.5 and k≅3.14 for N=9 and δ_{horiz}=1 (also for δ_{horiz}=0.55), k≅1.88 and k≅5.65 for N=9 and δ_{horiz}=0.1.

Having completed a description of the emerging patterns in terms of spatial features, next step involves characterization of these solutions in terms of heat exchange (for which the parameters introduced 'ad hoc' in Sect. 3.1 were used here). These are reported in an ordered way as a function of N in Figs. 53a, 53b and 53c for δ_{horiz} =1.0, 0.55 and 0.1, respectively.

As a fleeting glimpse into these figures would confirm, though the trends are all monotonic, swaps are possible in the relative importance of nusselt numbers $Nu_{side}^{average}$ and $Nu_{top}^{average}$, which require some proper explanations or interpretations. In this regard it is convenient to start from the simple remark that the decreasing behavior of the different curves (being perfectly monotonic for all cases) should be regarded as a consequence of a *thermal saturation effect*, i.e. the obvious tendency of the fluid to acquire (on average) an increasingly larger temperature as the number of heating elements ('heaters') grows (Figs. 54). Such an increase obviously tends to weaken the temperature gradients between the elements and the fluid, thereby causing a general decrease in the magnitude of the Nusselt number.

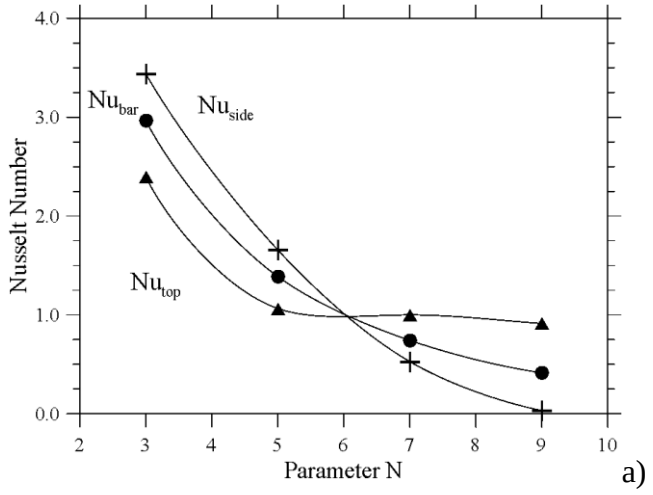

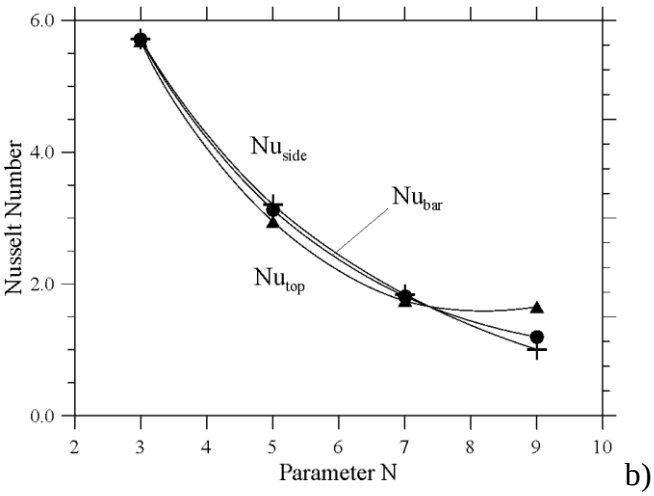

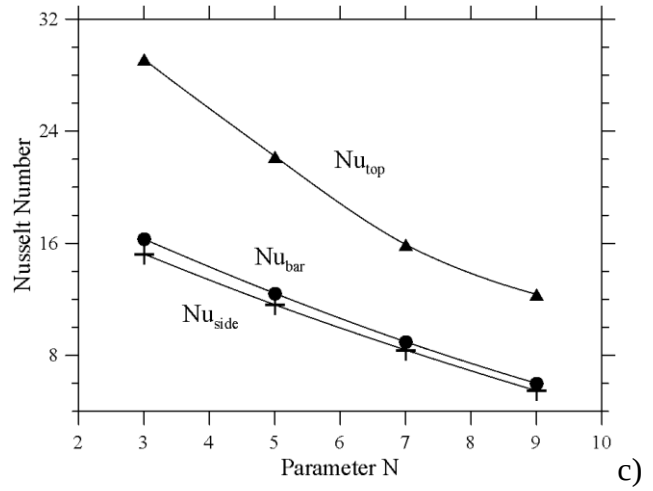

Figure 53: Nusselt number as a function of N for the configurations with adiabatic floor and adiabatic lateral solid walls (pure buoyancy convection, the splines are used to guide the eye): a) δ_{horiz} =1; b) δ_{horiz} =0.55; c) δ_{horiz} =0.1.

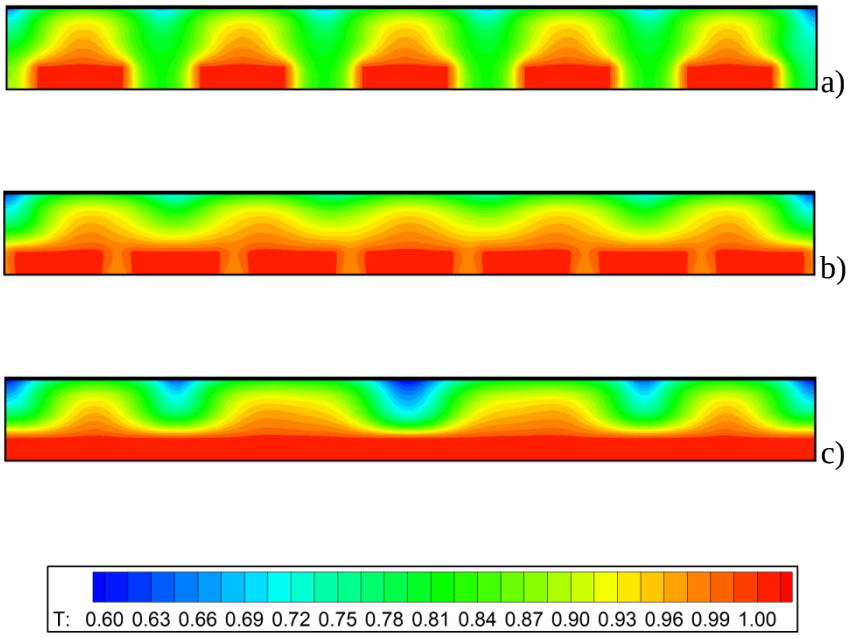

Figure 54: Lateral view (plane xy) for δ_{horiz} =1 and different values of N (pure buoyancy convection, adiabatic floor and adiabatic lateral solid walls): a) N=5; b) N=7; c) N=9.

This mechanism is also responsible for the inversion in the relative importance of $Nu_{side}^{average}$ and $Nu_{top}^{average}$ for δ_{horiz} = 1.0 as N exceeds a given threshold (in Fig. 53a, $Nu_{top}^{average} < Nu_{side}^{average}$ or $Nu_{side}^{average} < Nu_{top}^{average}$ for N ≤ 5 or N >5 , respectively). The simplest way to elaborate a relevant interpretation is to consider the emergence of 'heat islands', which for δ_{horiz} =1 tend to be formed in the thin (interstitial) regions located between adjoining elements as N is increased. As an example, see Fig. 54c, for N=9 the temperature in these regions becomes almost identical to that of the elements. In other words, for these specific conditions, the entire set of rods (though physically disjoint) formally behave as they were a single uniformly heated block (having constant thickness and the same horizontal extension of the entire liquid domain). Accordingly, $Nu_{side}^{average}$ drops to a value that is almost negligible.

Although the condition with unit horizontal extension of the elements (δ_{horiz} =1) is the only one for which $Nu_{side}^{average}$ becomes almost zero for N=9 (Fig. 53a), a similar justification can be invoked for the inversion in the relative importance of $Nu_{top}^{average}$ and $Nu_{side}^{average}$ in the range N≤5 when δ_{horiz} is decreased ($Nu_{top}^{average} < Nu_{side}^{average}$ or $Nu_{side}^{average} < Nu_{top}^{average}$ for $\delta_{horiz} \geq 0.55$ or δ_{horiz} <0.55 , respectively). A rationale for this trend can directly be rooted in the realization that while for $\delta_{horiz} \geq 0.55$ large thermal plumes *originate from the top of the heated elements* giving rise to vertically extended regions of fluids (Figs.55ab) where the temperature is relatively uniform and close to that of the heat sources (causing a significant weakening of $Nu_{top}^{average}$ with respect to $Nu_{side}^{average}$), for δ_{horiz} =0.1, such 'heat islands' are weaker and, accordingly, the gradient between the top surface of the elements and the overlying fluid is higher (Fig. 55c).

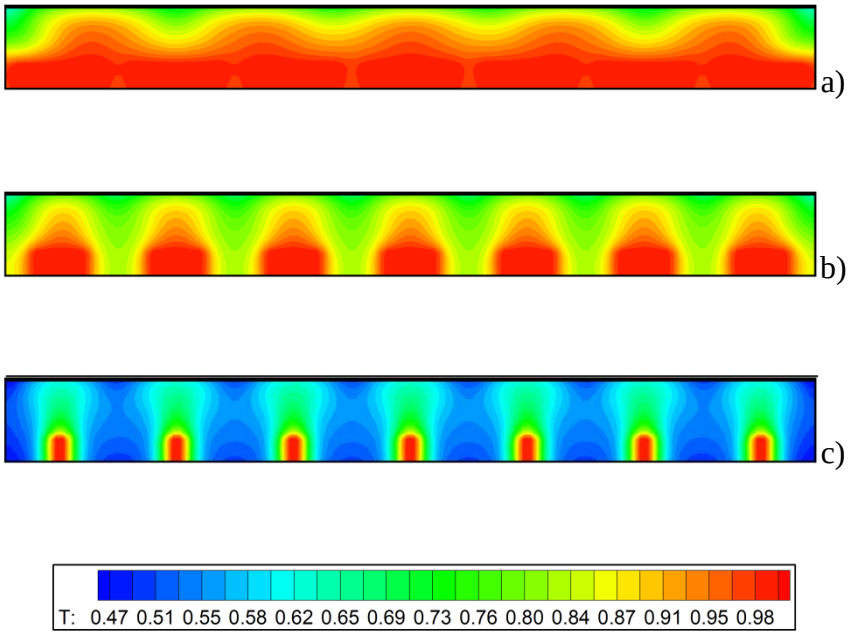

Figure 55: Lateral view (plane xy) for N=7 and different values of δ_{horiz} (pure buoyancy convection, adiabatic floor and adiabatic lateral solid walls): a) δ_{horiz} =1; b) δ_{horiz} =0.55; c) δ_{horiz} =0.1.

Obviously the aforementioned thermal saturation effect is enhanced if the portions of adiabatic floor located among adjoining elements are replaced with equivalent portions of isothermal (hot) wall. Such a swap in the thermal boundary condition at the bottom causes an appreciable decrease in the block Nusselt number (this being quantitatively substantiated by the data summarized in Table 6, where the values of *Nu* can be compared for different thermal behaviors of the floor and equivalent geometrical conditions, i.e. same values of N and δ_{horiz} for some representative cases).

Table 6: Comparison between the Nusselt number obtained for configurations with adiabatic and hot bottom wall ($Ra=10^4$, Ma=0).

N	δ_{horiz}	Floor	$Nu_{side}^{average}$	$Nu_{top}^{average}$	$Nu_{bar}^{average}$
3	1	Adiabatic	3.436	2.394	2.963
3	1	Isothermal	0.331	0.403	0.364
7	0.1	Adiabatic	8.390	15.915	8.968
7	0.1	Isothermal	1.158	6.49	1.568

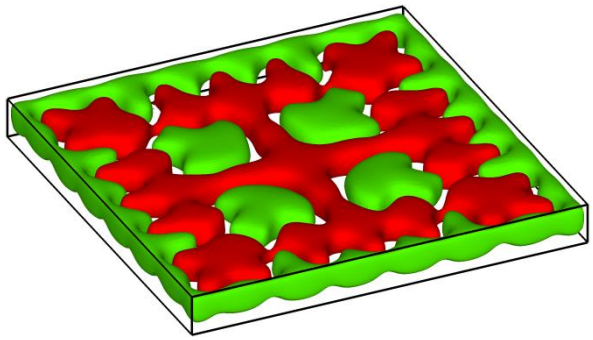

a)

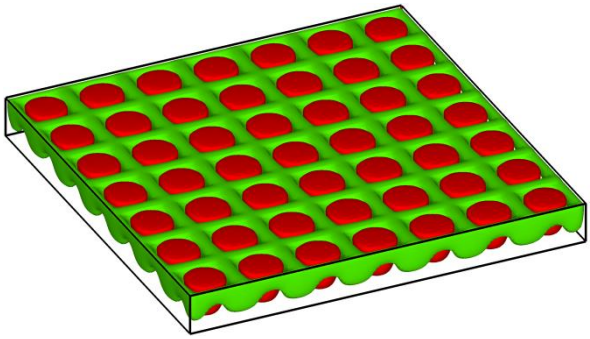

b)

Figure 56: Isosurfaces of vertical velocity component (green=-3,5, red=3.5, pure buoyancy convection, adiabatic lateral solid walls): a) N=7, δ_{horiz} =0.1 hot floor, b) N=7, δ_{horiz} =0.1, adiabatic floor.

Notably, the differences are not limited to a variation in the magnitude of the heat exchange taking place between the elements and the fluid. The changes can be substantial and affect the entire structure of the flow especially if one considers configurations with *small* δ_{horiz}. This conclusion is supported by cross-comparison of the patterns in Figs. 56. Moving on from the case with adiabatic floor to that with hot floor, it can be seen that, although some localized plumes originating from the hot blocks still manifest as independent flow features, in the latter case the overall pattern tends to take a configuration very similar to that with three main plumes along each wall, which is obtained when the equivalent (classical) RB configuration is considered (this being shown in Fig. 57). Although the shape of the plumes in Fig. 56a is less regular (their border is relatively jagged), they occupy the same positions shown in Fig. 57d.

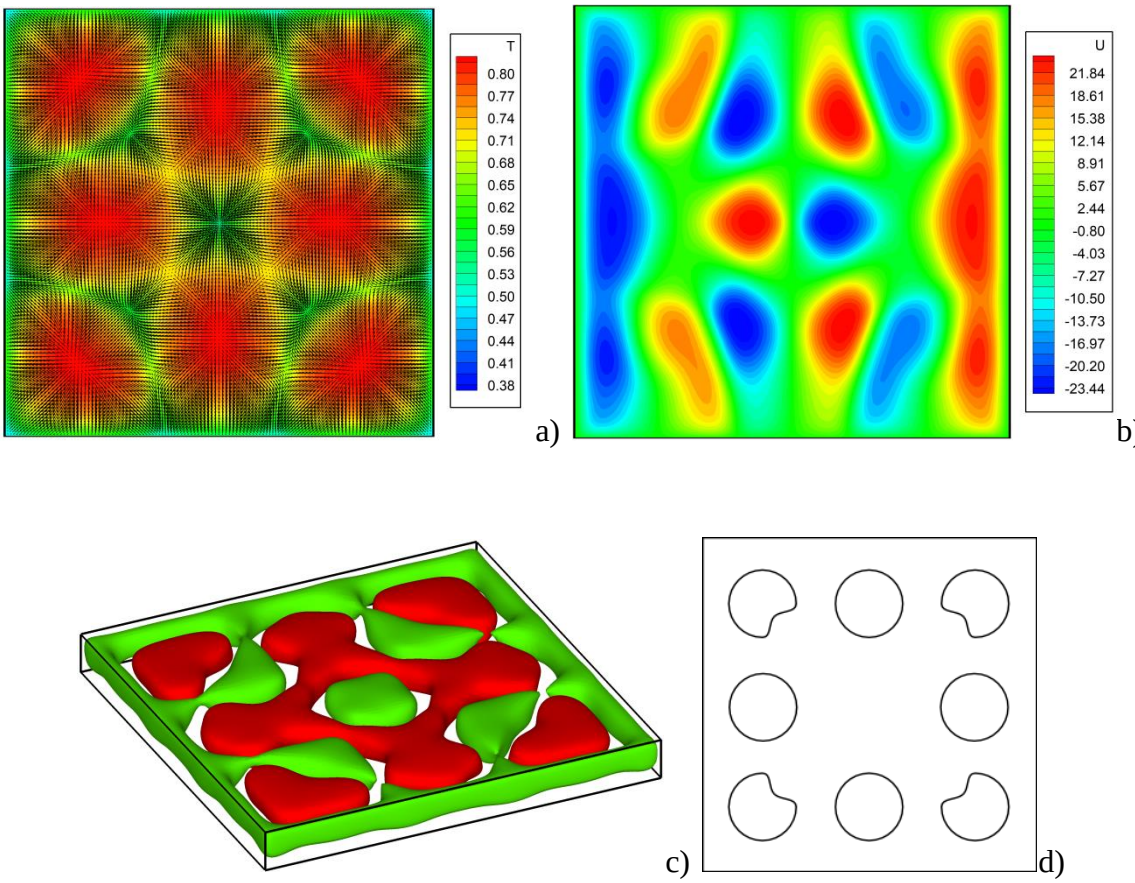

Figure 57: Classical Rayleigh-Bénard convection (Ra=10^4, Ma=0, Bi=1, adiabatic lateral solid walls, no blocks along the bottom): a) combined view of surface temperature and velocity distribution; b) surface distribution of velocity component along x; c) Isosurfaces of vertical velocity (green=-3,5, red=3.5), d) sketch showing the location of the main plumes, to be compared with Fig. 56a.

6.2 Mixed convection with Marangoni effects

The present section continues the previous investigation by probing the additional role played by surface tension and related gradients induced by temperature differences at the liquid/gas interface (i.e., cases with *Ra*≠0 and Ma ≠0 are examined).

As a first meaningful example of these results, Fig. 58 immediately leads to an important finding or observation, which needs to be highlighted suitably here. It shows the increased complexity of Marangoni-Rayleigh-Bénard convection with respect to the equivalent purely buoyant counterpart. Three main surface spots relatively extended in the horizontal direction play a dominant role in the temperature field (resembling a flower with three large ‘petals’, see Fig. 58a).

Most importantly, unlike the regular convective structure depicted in Fig. 57, the flow is no longer steady and regularly organized. Rather it is relatively disordered in space with many ‘spokes’ (loci of points where the surface velocity undergoes a kind of ‘discontinuity’, which manifest as ‘folds in the fabric of the petals’, see Fig. 58b). The spokes apparently emanate from the hot spots and move irregularly in space as time passes. The more involved nature of the flow can also be gathered from the surface temperature spectrum (at a fixed time) presented in Fig. 58c, where alignment with a k^{-3} law can be noticed in a certain range of wavenumbers (This interesting aspect will be discussed in Sect. 6.3 when dealing with the case of pure Marangoni convection).

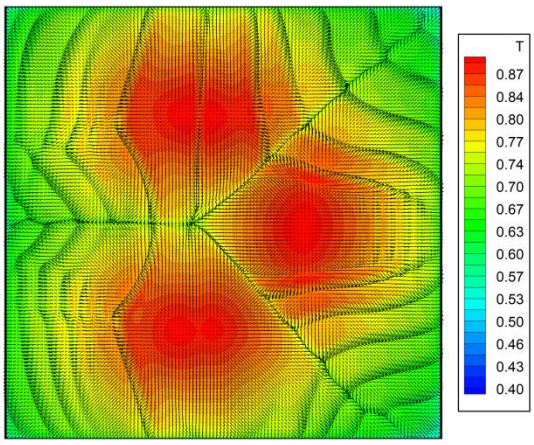

a)

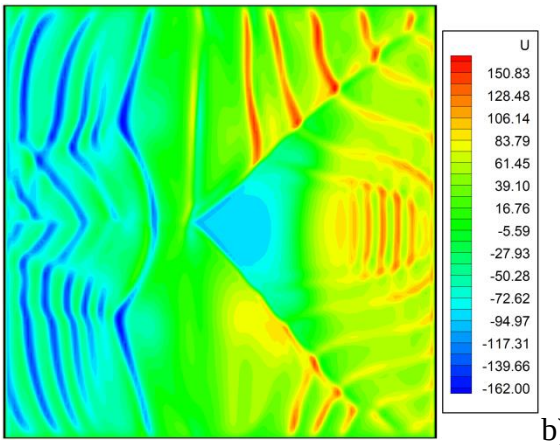

b)

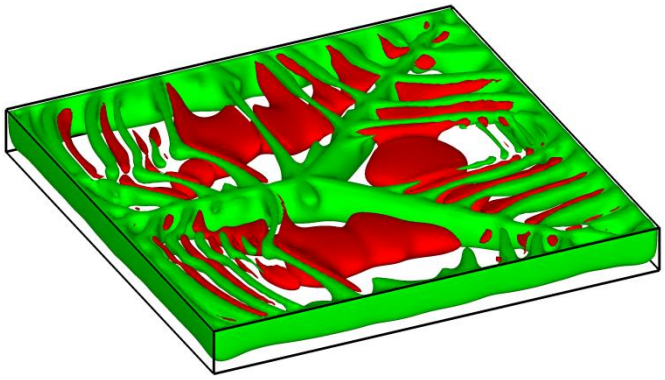

c)

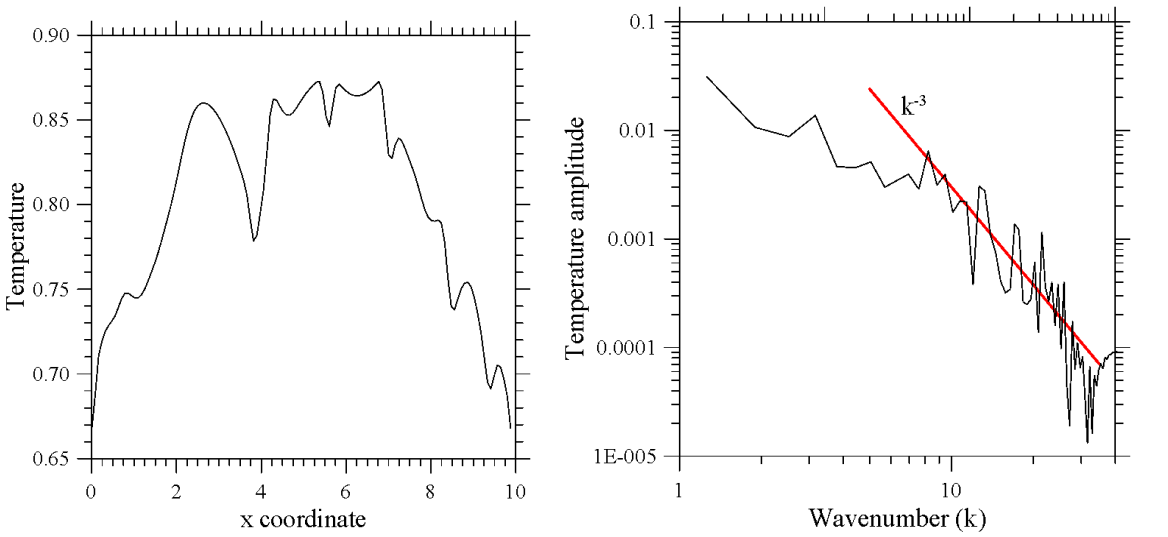

d) e)

Figure 58: Marangoni-Rayleigh-Bénard convection (Bo_{dyn}= 2, adiabatic lateral solid walls, no blocks along the bottom, t=4.8): a) combined view of surface temperature and velocity distribution; b) surface distribution of velocity component along x; c) Isosurfaces of vertical velocity component (green=-3,2, red=11.3); d) profile of temperature along x for z=6.57; e) Surface temperature spectrum (z=6.57).

Figure 58 (placed just after Fig. 57 to make evident the striking differences with respect to the equivalent RB convection) logically paves the way for the next analysis, which goes back to the situation with adiabatic bottom wall and an increasing number of evenly spaced heated elements (still for Bo_{dyn} fixed to 2). In this regard, the same deductive approach followed, which already has undertaken in Sect. 6.1 allowing both N and δ_{horiz} to span relatively wide ranges.

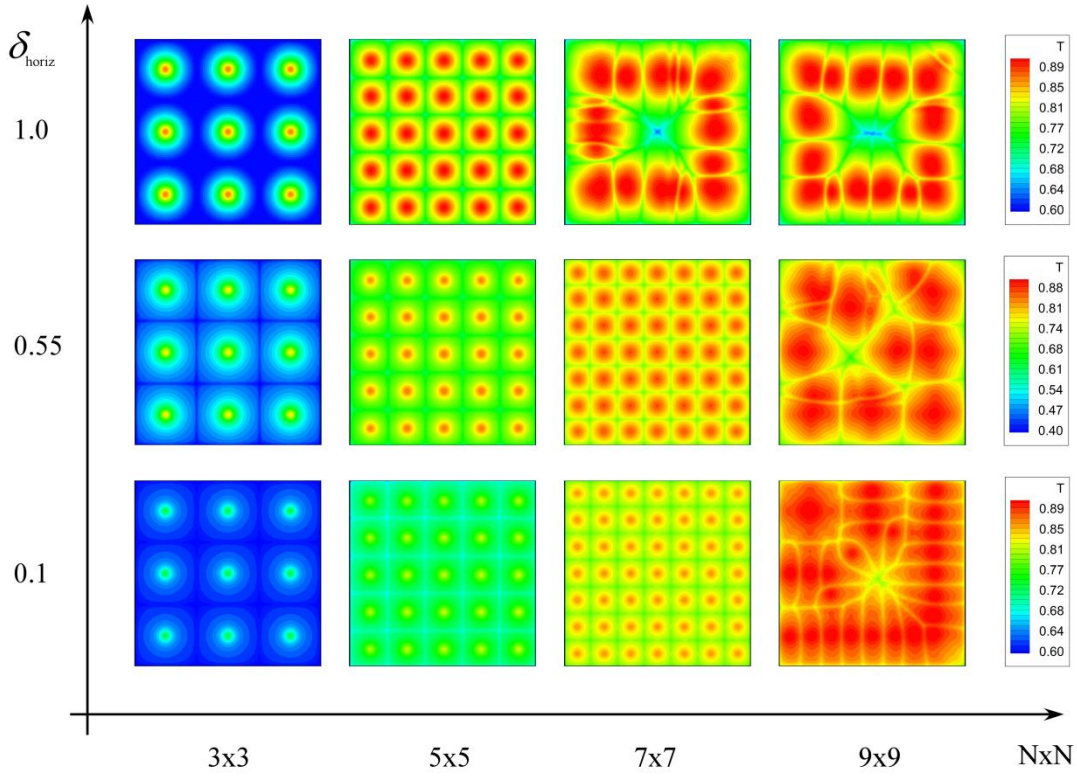

Figure 59: Survey of patterns (surface temperature distribution) obtained by varying N in the range between 3 and 9 for δ_{horiz}=1, 0.55 and 0.1 (mixed convection, adiabatic floor).

The case with N=1 is not discussed given its analogy with the convective structure already described for pure buoyancy flow. The reader specifically interested in the mixed Marangoni-buoyancy flow generated by a single source may consider some relevant works in the literature (e.g., Bratukhin et al., 2000) [88]. Here results were limited to reporting the values for Nu_{side}, Nu_{top} and Nu_{bar} which for N=1 read 7.38, 7.31 and 7.35, respectively (as expected, these values are slightly larger than those reported in the caption of Fig. 50).

The results for N≠1 is collected in Fig. 59 (the analogue of Fig. 51). By inspecting this figure, one may say (in a broad outline) that the observable trend is formally similar to that already seen for pure buoyant convection (from a spatial point of view). Put simply, for relatively small values of N, the flow still manifests itself in the form of separate convective cells at the free surface. However, some non-negligible distinguishing marks can be identified. Although these cells resemble those obtained in the pure buoyant case, their shape becomes 'square' (as opposed to the more rounded morphology seen in Fig. 51). Notably, for relatively small N these patterns are *steady* just like those found for pure buoyancy; nevertheless, on decreasing the space between the elements, at a certain stage, more complex spatio-temporal phenomena are enabled.

Interestingly, these emerge as fascinating ordered flows, where, in analogy with the purely buoyant situation, a direct connection between the heat sources at the bottom and planform visible at the top *can no longer be recognized*. At the same time, like the flow reported in Fig. 58, however, these convective structures also display an appreciable time dependence (this aspect will be described later however the reader being also referred to the extended discussion reported in Sect. 5).

Interestingly, the D_4 symmetries, i.e., the mirror reflections with respect to the middle and diagonal vertical planes can still be recognized for the smallest number of blocks (for all the cases with 3 × 3 and 5 × 5 blocks and even for cases with 7 × 7 blocks for δ_{horiz} = 0.1 and 0.55), and these cases are steady. For larger numbers of blocks, the underlying block pattern is no longer visible, but, unlike the buoyant cases, these cases have also lost the D_4 symmetries, and they are oscillatory, which imply that a Hopf bifurcation has occurred.

Again, the relationship between the pattern and the multiplicity of heated elements sensitively depends on the horizontal extension of the elements (δ_{horiz}) as further illustrated in the following.

In particular, as shown in Fig. 60 for δ_{horiz} = 1.0, the steady and very ordered distribution of small surface square cells for N=5 (simply reflecting the underlying 5x5 matrix of elements periodically positioned on the bottom, Fig. 60 (left)), is taken over for N=7 (central panel of Fig. 60) by an aesthetically appealing convective configuration with four large approximately square cells located in the corners of the domain and a more complex internal circulation structure where the surface fluid is driven towards a central sink (this being witnessed by the distribution of the surface velocity component along x in the second row of Fig. 60). This special point (knot) with four-fold topology corresponds to a kind of 'singular' vertex where the fluid (reaching it along different horizontal directions) is finally pushed towards the bottom of the layer. As yet visible in Fig. 60(center), all the other knots have a smaller topological order p=3. The corresponding surface temperature distribution (reported in the third panel of the first row of Fig. 59) essentially consists of a single thermal loop formed by many plumes surrounding a central colder region that culminates in a central peak where the surface temperature attains its smallest possible value (this point occupies the same position of the aforementioned knot with topological order 4). This flow is weakly unsteady.

On increasing N to 9 (Fig. 60 (right panel)), the dynamics are still unsteady and, most interestingly, besides a few minor differences, significant changes can be noticed neither in the topological properties of the velocity field, nor in the temperature distribution; importantly, this indicates that a kind of *saturation* has been enabled by which the flow is no longer sensitive to the multiplicity of the sources at the bottom.

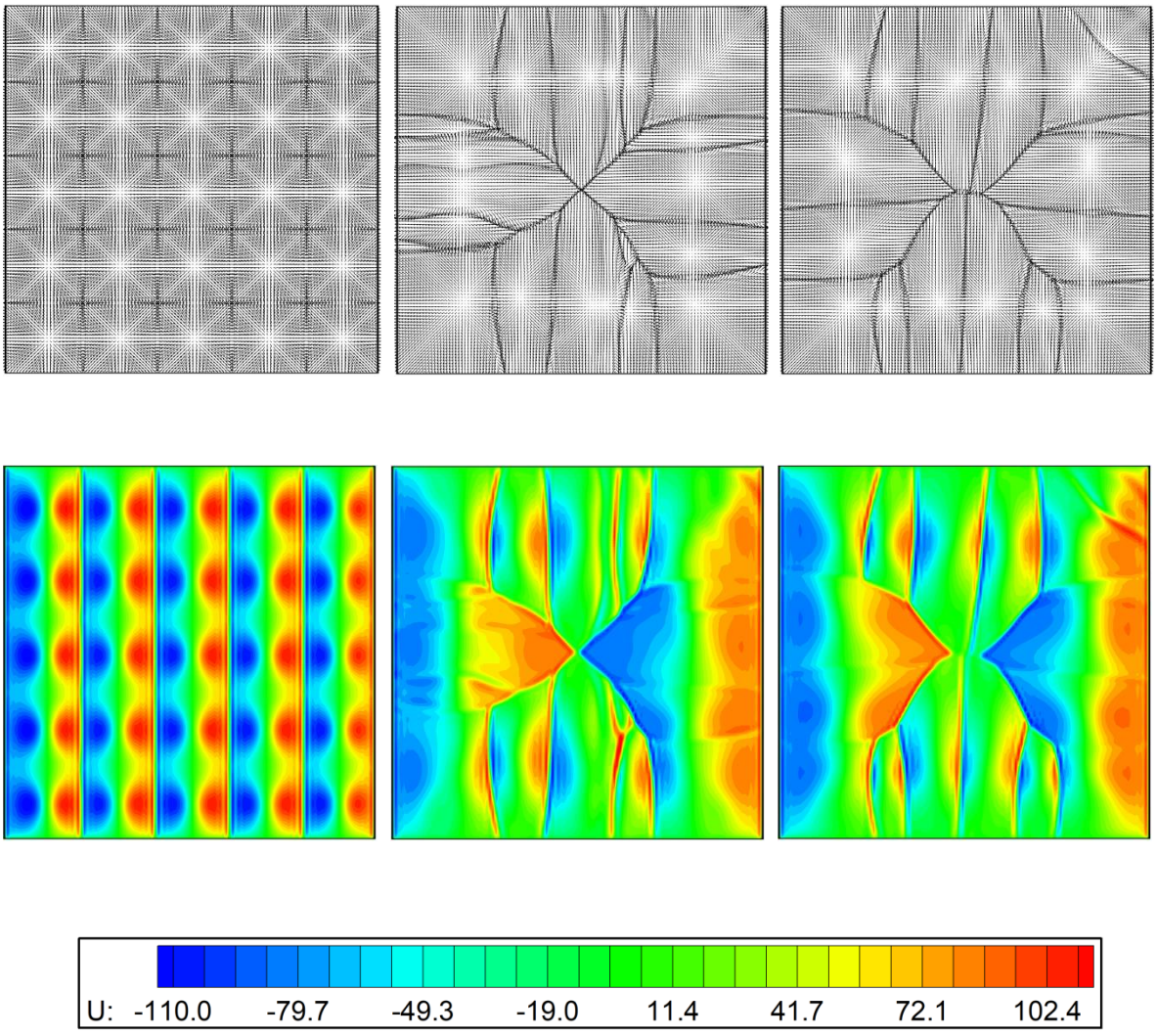

Figure 60: Surface vector plot (first row) and distribution of velocity component along x (second row) for δ_{horiz} =1 and different values of N (mixed convection, adiabatic floor and adiabatic lateral solid walls): (left) N=5 (steady flow); (center) N=7 (unsteady flow); (right) N=9 (unsteady flow).

These results obviously further support the realization that once a certain value of N is exceeded, these systems contain their own capacity for transformation, which can promote the emergence of planforms with well-defined (non-trivial) features. However, comparison with the classical case with uniform heating at the bottom (Fig. 60) also leads to the remarkable conclusion that, although at a certain stage a kind of asymptotic condition or regime is attained in terms of textural behavior, localized heating at fixed positions can contribute to make the emerging flow more regular (from both spatial and temporal points of view) with respect to the pure Marangoni-Rayleigh-Bénard paradigm.

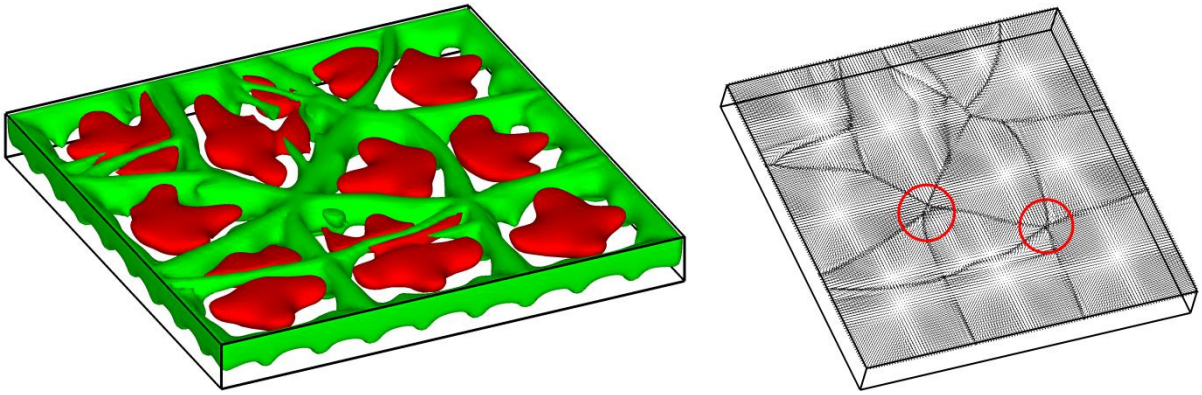

a)

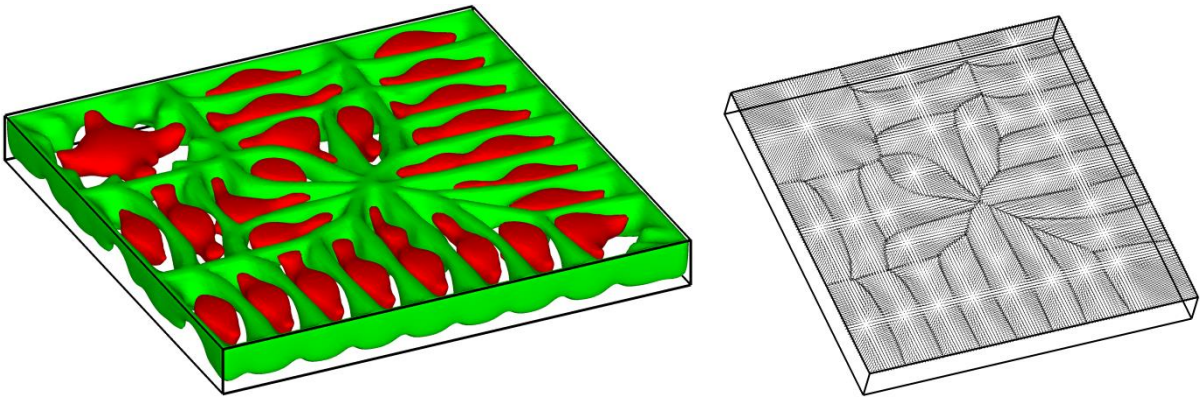

b)

Figure 61: Isosurfaces of vertical velocity component (left, green=-3,2, red=11.3) and surface vector plot (right) for N=9 and different values of δ_{horiz} (mixed convection, adiabatic floor and adiabatic lateral solid walls): a) δ_{horiz} =0.55 (unsteady flow, k≅1.88); b) δ_{horiz} =0.1 (unsteady flow, k≅5.66).

The next figure of the sequence (Fig. 61a and 61b) simply indicates that, like the purely thermogravitational case discussed in Sect. 6.1, the threshold to trigger flow self-organization is shifted to higher values of N as δ_{horiz} becomes smaller. The factor N must indeed be increased to N=9 for δ_{horiz}=0.55 and 0.1 to see again interesting dynamics. In these cases, the lines bounding the convective cells visible on the free surface yet organize themselves to form fascinating networks.

In line with earlier observations about the topological order of the central vertex for the configurations with δ_{horiz}=1.0, it is worth noticing that many of these lines originate from some special knots which behave as the centers of closed polygonal multi-cell structures that resemble the shape of a "flower". As an example, two of such structures can be recognized in Fig. 61a (highlighted by the red rings).

Although partial overlap among these sub-patterns is possible, the above-mentioned special knots can be uniquely identified through the topological order p of the radial spokes which emanate from them. For δ_{horiz} =0.55 this order is p_{max} = 5 (in such a context it's important to recall that for standard MB patterns with the classical hexagonal or square cells, p_{max} would take values p_{max} = 3 or p_{max} = 4, respectively, see, e.g., Nitschke and Thess, 1995; Bestehorn, 1996; Eckert et al., 1998; Kvarving et al., 2012). The dominant wavenumber (yet determined through analysis of the surface temperature distribution) in this case is k≅1.88.

From a temporal point of view, the flow unsteadiness essentially stems from localized effects, which consist of a 'flickering' (back and forth) motion of the spokes along directions approximately *perpendicular to them*; this is shown by the sequence of snapshots contained in Fig. 62. However, this is not the only mechanism responsible for the unsteady nature of convection. The overall time-dependent behavior is characterized by two apparently disjoint temporal scales, one related to the just-mentioned localized oscillation of the spokes (which display slightly different scales according to the considered cell, refer to the figure caption) and another due to a more general process by which all the cells undergo a slow adjustment in time. The latter results in minor changes in cell position and shape, which leads to a displacement of the aforementioned knots (the centers of the 'flowers').

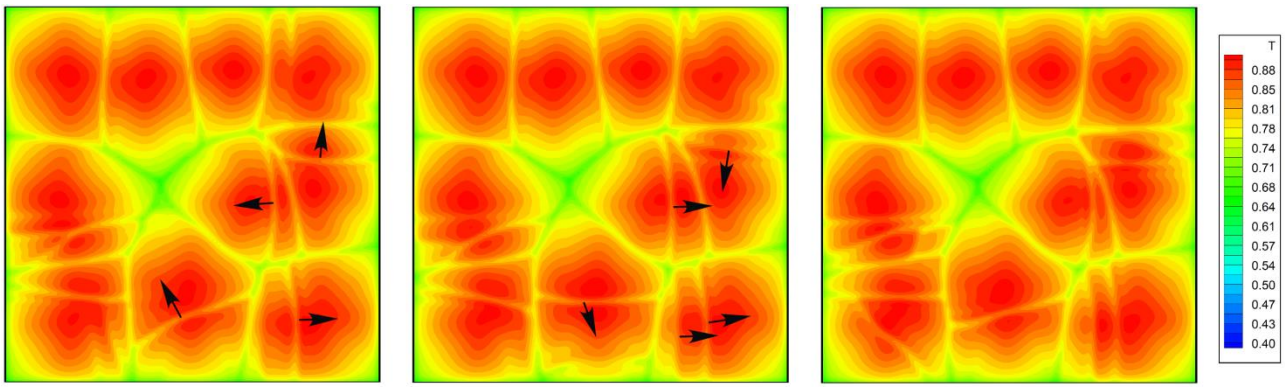

Figure 62: Snapshots of surface temperature for N=9 and δ_{horiz} =0.55 (mixed convection, adiabatic floor and adiabatic lateral solid walls): $t=t_o$, $+\tau$, $t_o+2\tau$ (τ=0.05, t_o=5.65). The black arrows indicate the istantaneous direction of motion of the spokes. Some cells are arrow-free (e.g., those located in the lower-left corner) as the related spokes evolve over timescales slightly larger (their displacement being not appreciable in the shown timeframe).

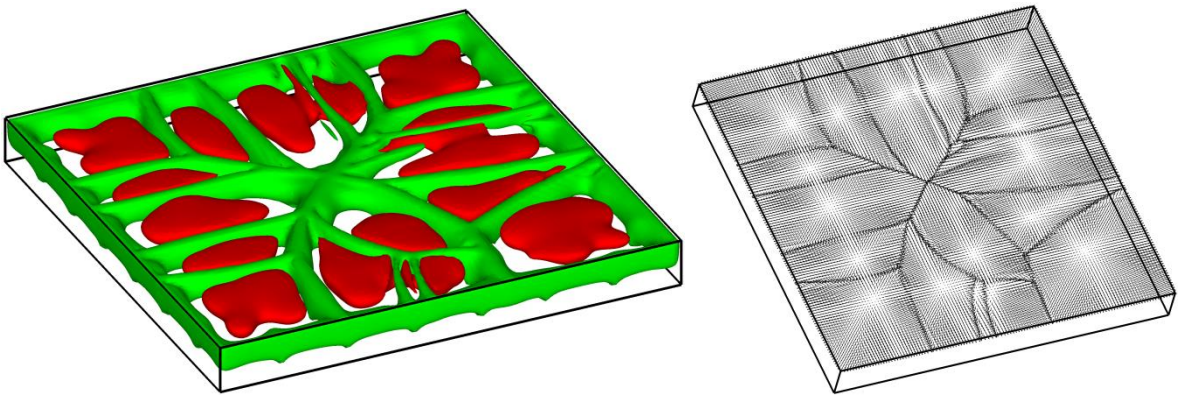

Figure 63: Isosurfaces of vertical velocity component (left, green=-3,2, red=11.3) and surface vector plot (right) for the hot floor case (mixed convection, adiabatic lateral solid walls), N=7 and δ_{horiz} =1 (unsteady flow, $Nu_{side}^{average} \cong 0.329$, $Nu_{top}^{average} \cong 1.154$, $Nu_{bar}^{average} \cong 0.704$).

Notably, when the system has entered the specific regime where the surface pattern is no longer a trivial (1:1) manifestation of the underlying topography, a switch in the thermal boundary condition at the bottom (from adiabatic to isothermal) has a weak impact. These observations are quantitatively substantiated by Fig. 63 (N=7 and δ_{horiz} =1); apart from some minor modification (compare Fig. 66 with Fig. 60(center)), the flow has the same structure and topology.

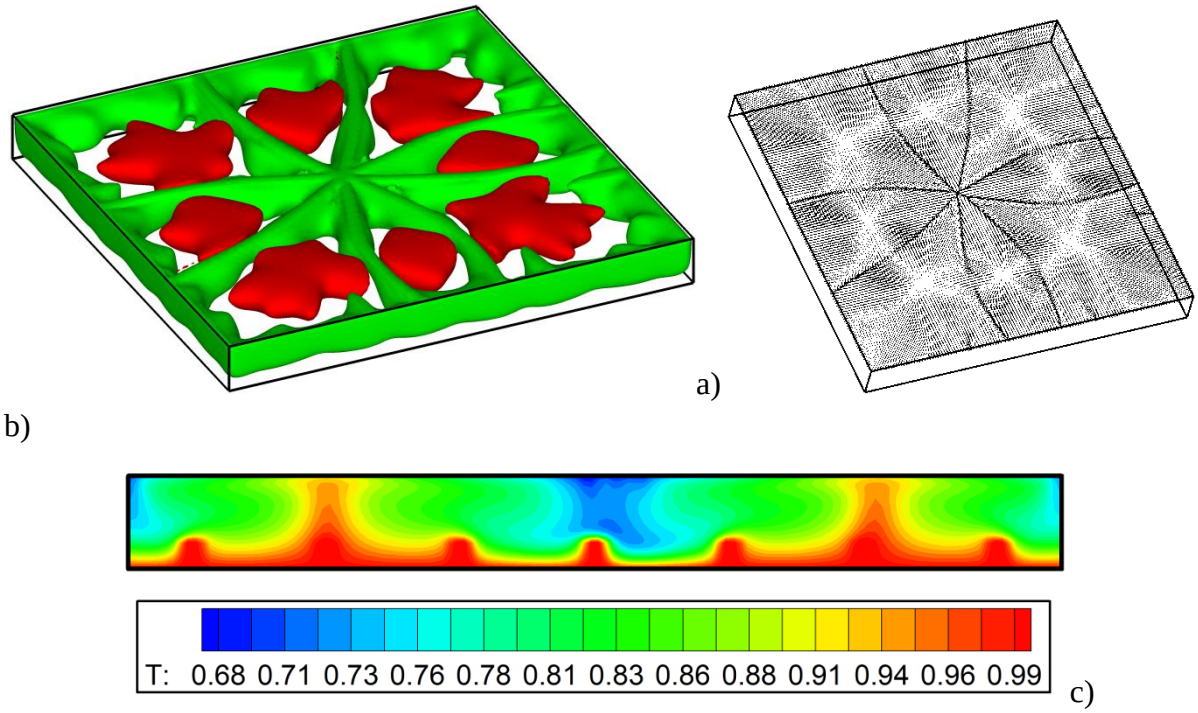

Figure 64: Isosurfaces of vertical velocity (green=-3,2, red=11.3) component (a), surface vector plot (b) and temperature distribution in the xy midplane (c) for the hot floor case (mixed convection, adiabatic lateral solid walls), N=7 and δ_{horiz} =0.1 (steady flow, $Nu_{side}^{average}$ ≅1.398, $Nu_{top}^{average}$ ≅8.525, $Nu_{bar}^{average}$ ≅1.947).

Vice versa, the variation is dramatic if the swap in the thermal boundary condition is implemented for systems which have not entered yet the self-organization regime, see Fig. 64 (N=7 and δ_{horiz} =0.1). As implicitly revealed by this figure, in place of the trivial array of perfectly aligned spots which would be obtained for N=7 with the adiabatic floor condition (Fig. 59, third row, third panel), a planform with well-defined properties is produced. Notably, it possesses all of the symmetries pertaining to the aforementioned D_4 group, i.e., the mirror reflections with respect to the vertical planes $x=A_{horiz}/2$, $z=A_{horiz}/2$, x=z and $z=A_{horiz}$-x and related combinations.

In this regard, some additional insights follow naturally from a cross-comparison of Fig. 64 with Fig. 58, i.e., the case with uniform heating at the bottom and no rods. It can be argued that the utilization of a discrete and ordered set of relatively small protuberances at the bottom would still be effective in turning otherwise disordered and unsteady Marangoni-Rayleigh-Bénard convection into a spatially regular and steady flow. Notably, in this case the topological order of the central knot is even increased with respect to the preceding cases (p_{max}=8), while other knots do not exist at all. Figures 64a and 64b are naturally complemented by Fig. 64c, where evidence is provided that the perfect symmetry of the flow (and the ensuing increase in the topological order of the central knot) is supported by a kind of synchronization between specific heated blocks and the location of the dominant thermal plumes.

Apparently, specific blocks play the role of 'catalysts' in generating rising currents, thereby stabilizing the flow, which becomes essentially steady. A further understanding of all these modes of convection can be gained by considering the related behavior in terms of heat exchange between the hot elements and the fluid. Following the same approach implemented in Sect. 6.1, this subject is further developed solely for the situations with adiabatic floor and solid sidewalls for which the majority of the present results have been obtained (Fig. 65).

Correlation of Fig. 65a and 53a (δ_{horiz}=1.0 cases) is instrumental in revealing that (as expected) the presence of an additional mechanism of convection *located at the free surface* causes an appreciable rise in the values of $Nu_{top}^{average}$. Vice versa, no significant variations can be seen in $Nu_{side}^{average}$ both in terms of magnitude and trend (compare again Fig. 53a and 65a).

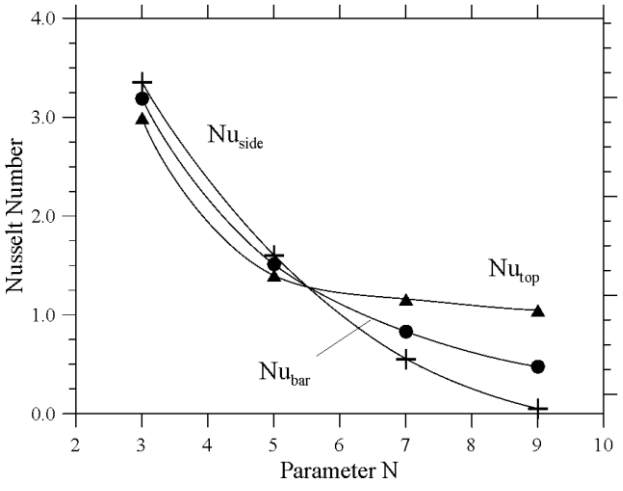

a)

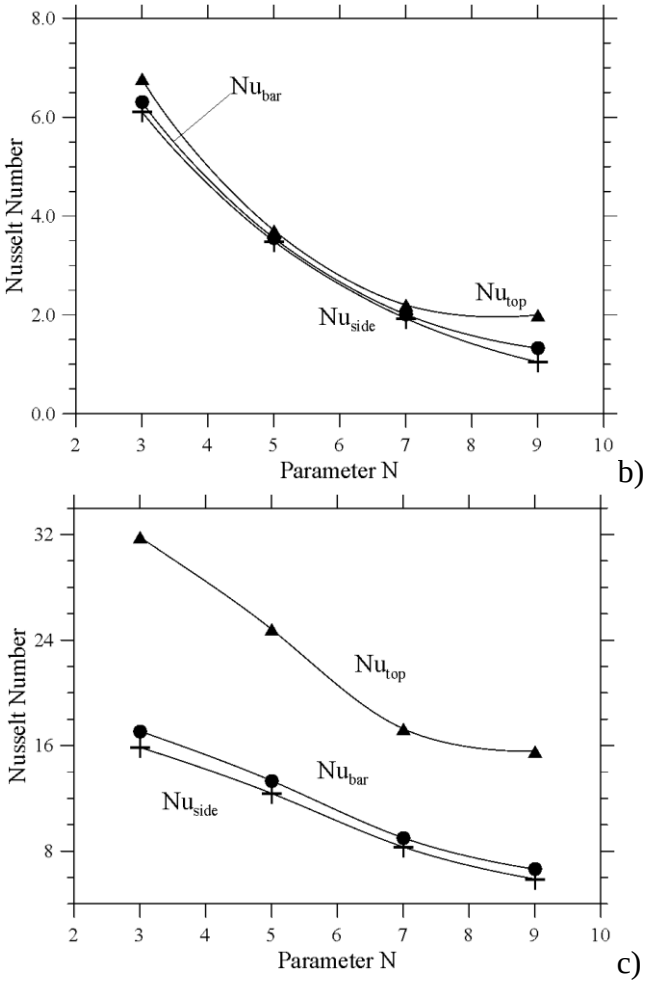

Figure 65: Nusselt number as a function of N for the configurations with adiabatic floor and adiabatic lateral solid walls (Mixed convection, the splines are used to guide the eye): a) δhoriz =1; b) δhoriz =0.55; c) δhoriz =0.1.

The increase in $Nu_{top}^{average}$ is still appreciable for smaller values of δ_{horiz}. For δ_{horiz} =0.55 (Fig. 65b), $Nu_{top}^{average}$ is now located above the corresponding $Nu_{side}^{average}$ line as opposed to the situation seen in Fig. 53b. For δ_{horiz} =0.1 (Fig. 65c) a big gap separates $Nu_{top}^{average}$ and $Nu_{side}^{average}$. Like the equivalent situation with only buoyancy flow (Fig. 53c), the reason for the proximity $Nu_{bar}^{average}$ to $Nu_{side}^{average}$ resides in the fact that the top area of each element is very small with respect to its total lateral area (which, as made evident by eq. (14) contributes to make $Nu_{bar}^{average} \cong Nu_{side}^{average}$).

6.3 Microgravity Conditions

A separate discussion is needed for the Ra=0 circumstances, the surface expression of which in the classical situation with uniform heating (and no topography) would be the canonical Marangoni-Bénard (MB) convection. It is worth recalling that, strictly speaking, this kind of flow can be obtained only in microgravity conditions (where the influence of buoyancy forces can be completely filtered out). In normal gravity, situations approaching those for which pure MB convection is obtained can be mimicked by reducing the ratio Ra/Ma as much as possible (typically by decreasing the depth of the considered layer), i.e., if $Bo_{dyn} \cong 0$. The results presented in this section could therefore be applied in principle to experiment performed on an orbiting platform (such as the International Space Station) or on Earth in 'microscale' conditions (layer depth significantly smaller than 1 mm). This subject has received significant attention over the years (though not being comparable to that attracted by the companion problem represented by RB convection). Other studies worthy of mention in addition to those reported in the introduction and the book by Colinet et al. (2001) are those by Thess and Bestehorn, 1995 and Bestehorn, 1996) , who concentrated on the evolution of the emerging planforms, showing that the well-known hexagonal symmetry of the cells (underpinned by a threefold organization of the vertices, i.e. p=3) is spontaneously taken over for larger values of Ma by a fourfold vertex topology (p=4) resulting in square-shaped convective cells. Given the amount of literature available on this specific subject, these references are obviously selective samples of existing valuable investigations. However, studies concerned with the regime where this form of convection becomes disordered in both time and space are relatively rare (Thess and Orszag, 1994 and 1995; Thess et al., 1995 and 1996) and used for some conclusive arguments elaborated in Sect. 6.4. In the present section, focus would be on describing the dynamics found in the present conditions by setting Ra=0, a first example of which can be seen in Fig. 66.

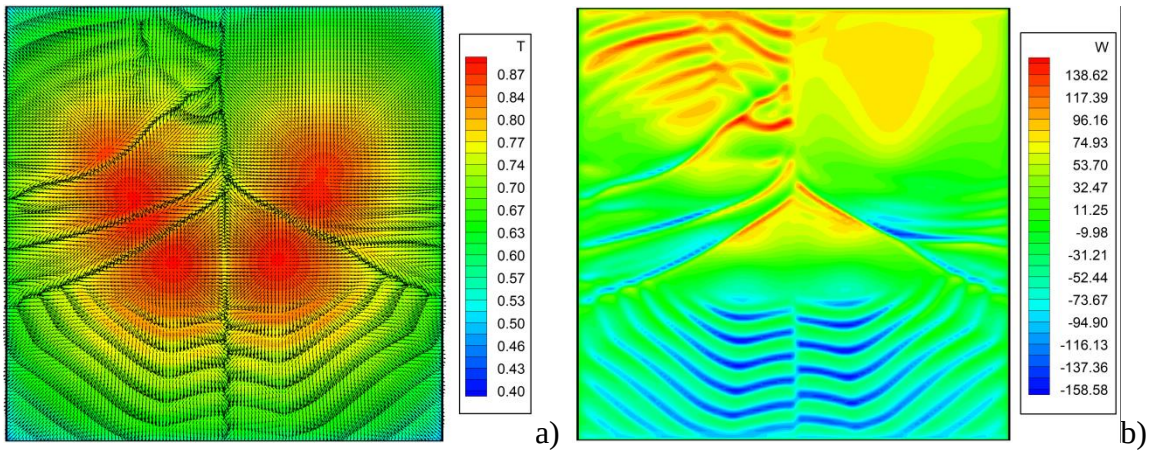

a) b)

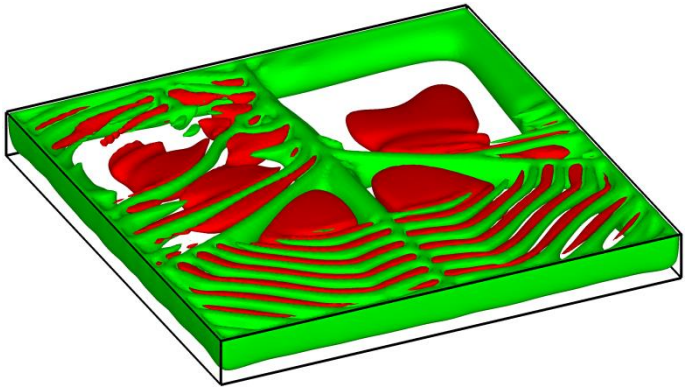

c)

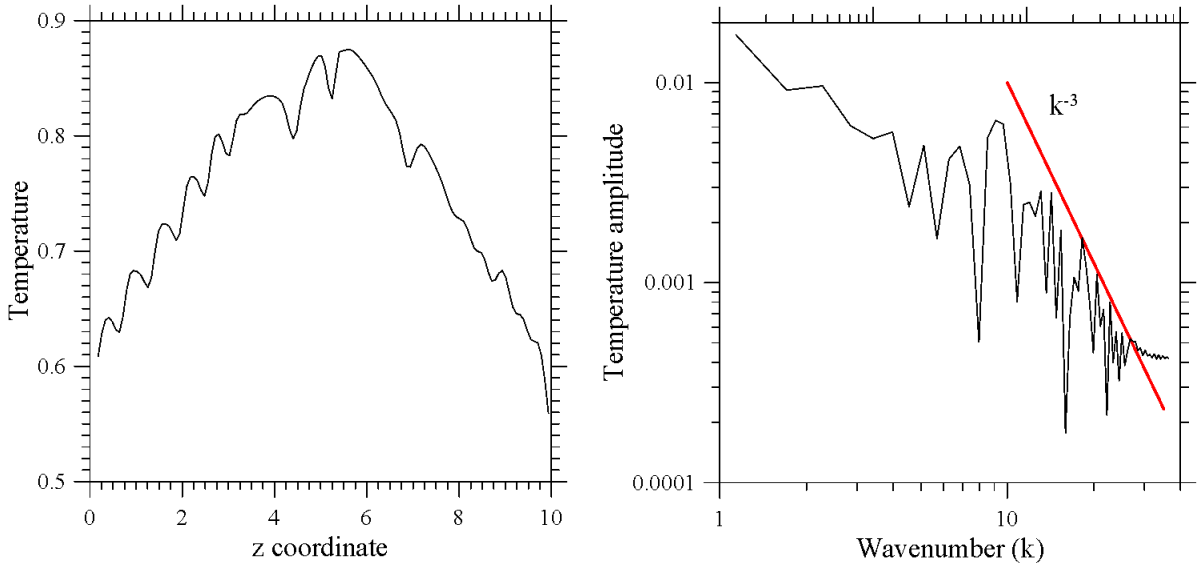

d)

e)

Figure 66: Marangoni-Bénard convection (Ra=0, Ma=5x10^3, Bi=1, adiabatic lateral solid walls, no blocks along the bottom, t=6.42): a) combined view of surface temperature and velocity distribution; b) surface distribution of velocity component along z; c) Isosurfaces of vertical velocity component (green=-3,2, red=9.2); d) profile of temperature along z for x=7.0; e) Surface temperature spectrum (line x=7.0).

This figure naturally complements Fig. 58 by revealing that the thermal structure with three main hot spots (the three-lobe windmill) seen for the Marangoni-Rayleigh-Bénard system (uniform heating at the bottom) is taken over for pure Marangoni-Bénard convection by a slightly different pattern with four main spots arranged in a butterfly-like configuration. It is also worth noticing that the flow retains its unsteady nature (as it was in the presence of buoyancy) and many spokes can yet be detected in the velocity field (their number largely exceeding that seen in the presence of buoyancy, Fig. 66b). Despite these topological differences, however, the surface (spatial) temperature spectrum still aligns perfectly with the aforementioned k^{-3} law (see Sect. 6.2).

Selected examples of the dynamics obtained with discrete distribution of blocks on an adiabatic floor are collected in Figs. 67 and 68. In particular, the former refers to the results for δ_{horiz} =1 for which the trend is relatively similar to that already reported for mixed flow. As a given N is exceeded, the flow self-organizes in a peculiar pattern that does not change (in terms of topology of the network of spokes) if N is further increased.

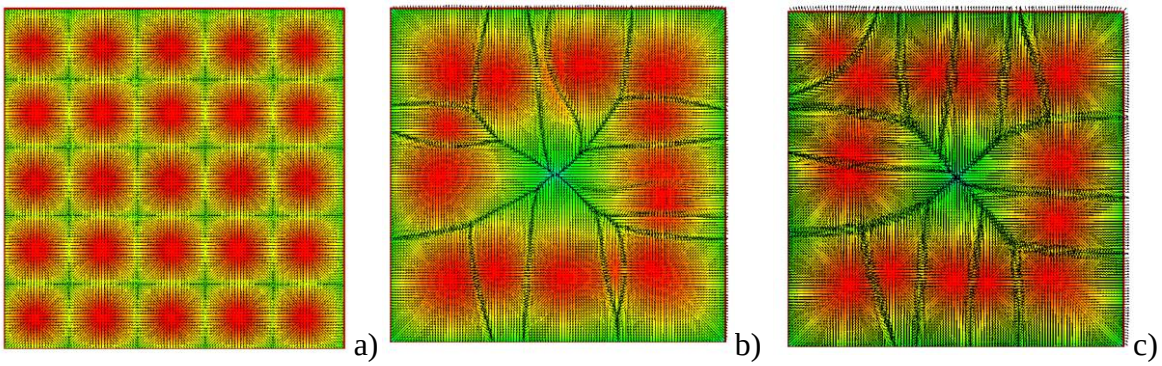

Figure 67: Combined view of surface temperature and velocity distribution for δ_{horiz} =1 and different values of N (microgravity conditions, adiabatic floor and adiabatic lateral solid walls): a) N=5 (steady flow); b) N=7 (unsteady flow); c) N=9 (unsteady flow).

In terms of symmetries, considerations very similar to those already developed in Sect. 6.2 could be given. For the sake of brevity, re-emphasizing that the loss of symmetry with respect to the aforementioned D_4 group still manifest itself in conjunction with transition to time-dependent convection, which indicates that this should be seen as a bifurcation of the flow.

Once again, the non-trivial states are somehow ‘quantized’, in the sense that they do not depend on the multiplicity of wall-mounted elements. Moreover they are rather similar to those collected in the first row of Fig. 59 and this apparently innocuous observation goes some way to reinforce the idea (already supported by correlation of the results discussed in Sect. 6.1 and 6.2) that for these circumstances the main pattern-controlling factor is transferred from the number of elements mounted on the bottom wall to intrinsic convective disturbance amplification mechanisms of the Marangoni flow.

Comparison with the equivalent cases in the presence of buoyancy (Sect. 6.2), however, also leads to the remarkable realization that buoyancy does play a non-negligible (important) role in some cases, especially when the horizontal size of the elements is decreased (compare, e.g., Fig 68a with Fig. 61a and Fig. 68b with Fig. 61b). In particular, for δ_{horiz} =0.55, the number and extension of spokes (and cells) undergoes a remarkable increase in the absence of buoyancy. Vice versa, for δ_{horiz} =0.1 in place of the complex network visible in Fig. 61b, one gets a relatively simple pattern with 5 triangular cells concurring in a single central knot (with topological order p=5, Fig. 68b).

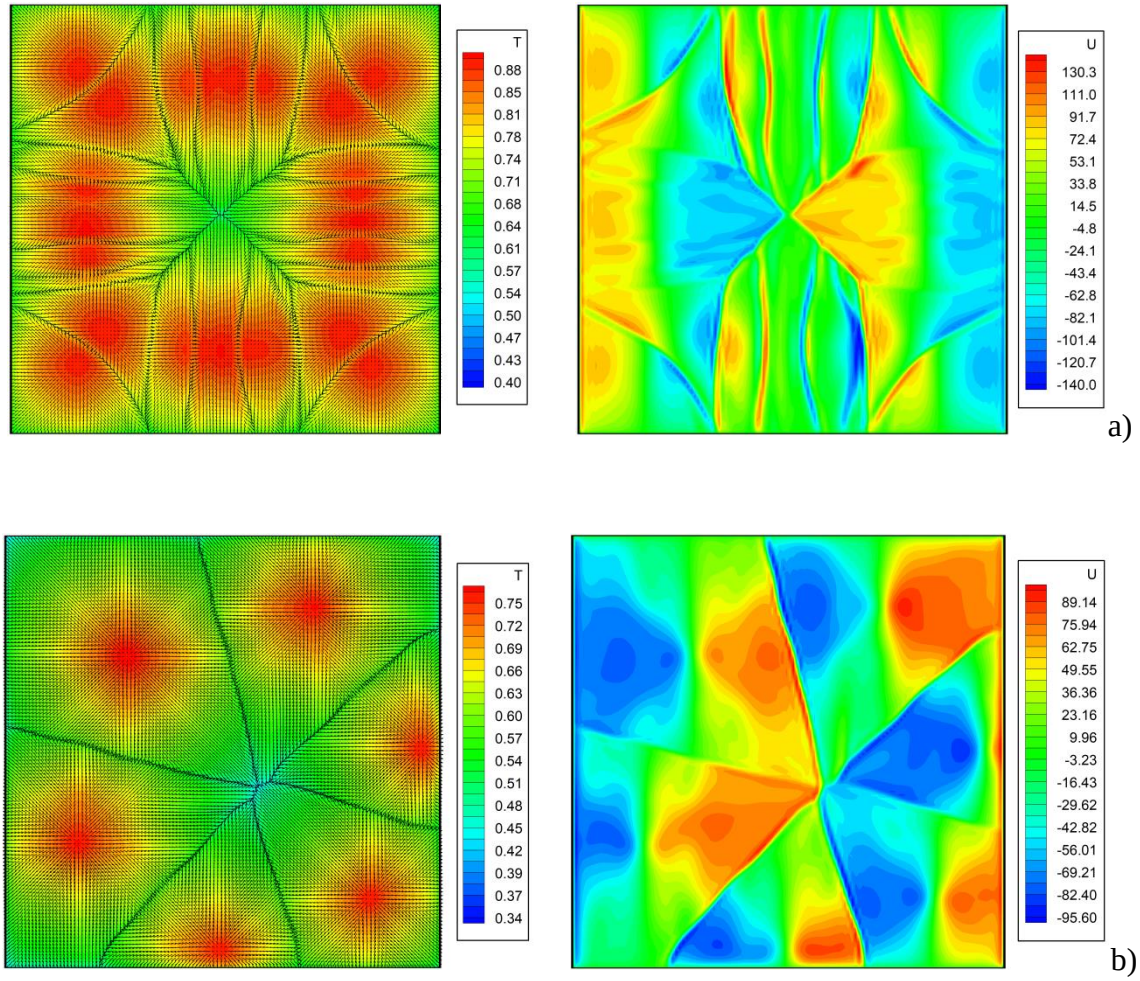

Figure 68: Combined view of surface temperature (left) and surface distribution of velocity component along x for N=9 (pure surface-tension-driven convection, adiabatic floor and adiabatic lateral solid walls): a) δ_{horiz}=0.55 ($Nu_{side}^{average} \cong 0.756$, $Nu_{top}^{average} \cong 2.205$, $Nu_{bar}^{average} \cong 1.182$), b) δ_{horiz}=0.1 ($Nu_{side}^{average} \cong 5.359$, $Nu_{top}^{average} \cong 18.253$, $Nu_{bar}^{average} \cong 6.351$).

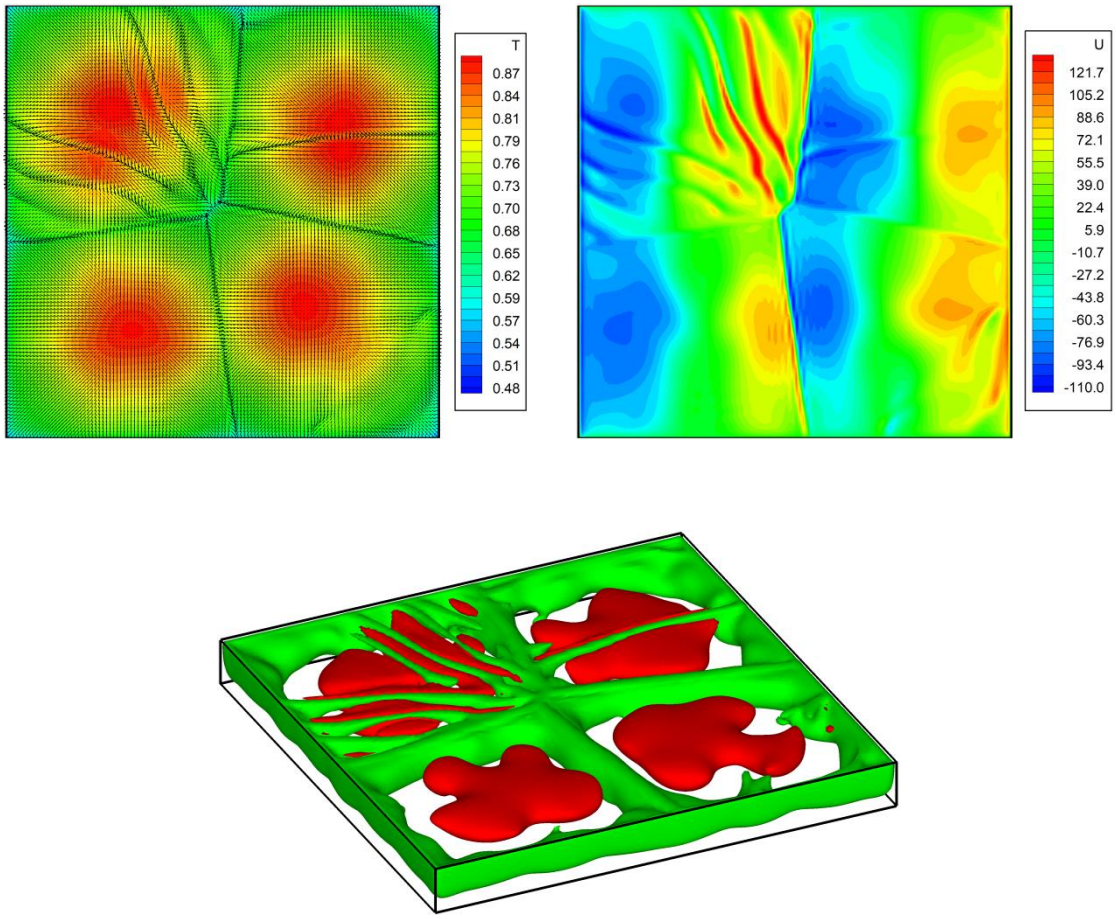

Figure 69: Temperature distribution for N=7 and δ_{horiz}=0.1 (pure surface-tension-driven convection, hot floor and adiabatic lateral solid walls, unsteady flow with a localized oscillon, $Nu_{side}^{average} \cong 1.578$, $Nu_{top}^{average} \cong 10.517$, $Nu_{bar}^{average} \cong 2.265$). (green=-3,2, red=9.2).

Consideration of a representative hot floor case is also instructive (Fig. 69). *Without buoyancy*, the ability of the heated protuberances with small transverse extension (δ_{horiz}) to exert an influence on the emerging pattern and its spatio-temporal behavior is relatively limited. In place of the perfect (and steady) arrangement of cells observed in Fig. 64 for N=7, δ_{horiz}=0.1 and Bo_{dyn}=2, the pattern with four large thermal spots found for MB flow is recovered when Bo_{dyn}=0 (Fig. 69). It is evident, however, that despite the number of spots is identical to that obtained in the classical case with smooth and uniformly heated boundary (Fig. 66), the presence of blocks on the bottom can still exert a certain influence by making the pattern more regular with respect to that seen in Fig. 66 (a smaller number of spokes or discontinuities can be detected in Fig. 69).

Continuing with a focused review of the literature on classical MB convection, it's worthy to remark that oscillatory behaviors relatively similar to that shown in Fig. 69 have also been observed in other studies dealing with classical MB convection. As an example, while investigating the possible existence of multiple solutions (states which depend on the initial

conditions) for slightly supercritical conditions, Kvarving et al., 2012) found that the final state of MB convection may be dominated by a steady convection pattern with a fixed number of cells, or the same system may occasionally end up in a steady pattern involving a slightly different number of cells, or it may display a peculiar convective configuration where most of the cells are stationary, while one or more cells undergo a localized oscillatory behavior (a cell being continuously destroyed and re-formed as time passes).

This is what can also be seen in Fig. 69, where the oscillations display a strongly confined nature. In line with the dynamics visible in Fig. 66 and 68a, the cell does not disappear. Rather it apparently undergoes a localized instability, which results in a series of ripples originating from the central segment where the two cells aligned along the NW-SE diagonal meet. All these spokes are embedded inside a single cell, while the rest of the pattern is seemingly not affected by them.

These observations can be used as a cue to recall another related concept, that is, the notion of 'oscillon', already used in previous works. In Lappa and Ferialdi (2018) , it was loosely defined as the spontaneous localization or confinement of oscillatory phenomena to a limited subregion of an otherwise stationary pattern in a translationally invariant system. Although the present system is no longer perfectly isotropic like the classical MB, the present results show that in the presence of a repetitive topography or thermal forcing, this definition or concept can still be considered relevant.

As a concluding remark for this section, in line with similar considerations elaborated for the companion circumstances with pure buoyancy or mixed buoyancy-Marangoni convection, next step focuses on the heat exchange behavior. Along these lines, for the purpose of quantifying the variation undergone by such effects, Fig. 70 and Tables 7, 8 and 9 show the behavior of the related Nusselt number for various cases. The major outcome of Fig. 70 (through critical comparison with the equivalent Figs 53a and 65a) resides in the indirect confirmation that most of the increase of $Nu_{top}^{average}$ for δ_{horiz} =1 (adiabatic floor case) and relatively small values of N when surface-tension effects are added to buoyancy (by which $Nu_{top}^{average}$ becomes almost equal to $Nu_{side}^{average}$), essentially stems from the Marangoni effect itself.

Table 7: Comparison between the Nusselt number obtained for configurations with adiabatic bottom wall in different circumstances (N=9, δ_{horiz} =0.55).

Ra	Ma	$Nu_{side}^{average}$	$Nu_{top}^{average}$	$Nu_{bar}^{average}$
10^4	0	1.008	1.655	1.198
10^4	$5x10^3$	1.051	2.004	1.331
0	$5x10^3$	0.756	2.205	1.182

Table 8: Comparison between the Nusselt number obtained for configurations with adiabatic bottom wall in different circumstances (N=9, δ_{horiz} =0.1).

Ra	Ma	$Nu_{side}^{average}$	$Nu_{top}^{average}$	$Nu_{bar}^{average}$
10^4	0	5.479	12.361	6.009
10^4	$5x10^3$	5.887	15.587	6.634
0	$5x10^3$	5.359	18.253	6.351

Tables 7 and 8 indicate that in the absence of buoyancy-induced plumes, i.e. for *Ra*=0, a significant increase in $Nu_{top}^{average}$ takes place also for other values of δ_{horiz}. This can be ascribed to the absence of the heat islands, which buoyancy would otherwise induce above the hot blocks. Table 9 finally confirms that, though heat exchange is weakened with respect to the equivalent configuration with the adiabatic floor, such enhancement still holds if an isothermal floor is considered.

Table 9: Comparison between the Nusselt number obtained for configurations with hot bottom wall in different circumstances (N=7, δ_{horiz} =0.1).

Ra	Ma	$Nu_{side}^{average}$	$Nu_{top}^{average}$	$Nu_{bar}^{average}$
10^4	0	1.158	6.49	1.568
10^4	$5x10^3$	1.398	8.525	1.947
0	$5x10^3$	1.578	10.517	2.265

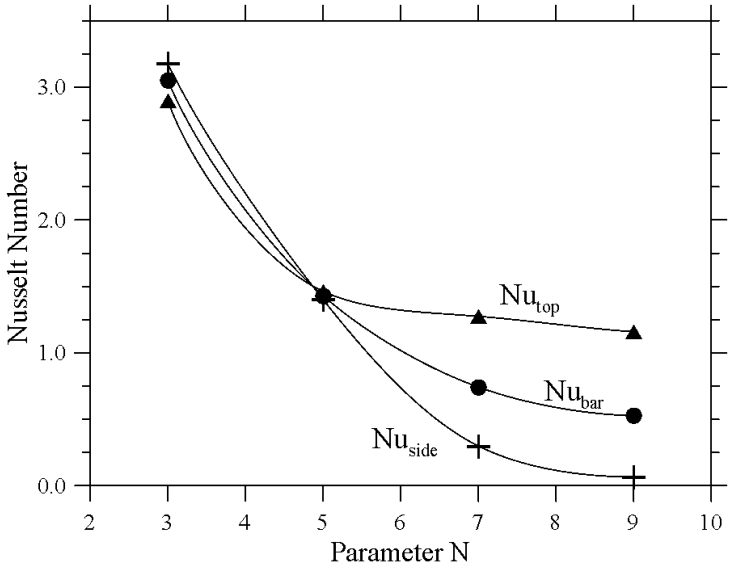

Figure 70: Nusselt number as a function of N for the configurations with pure surface-tension-driven convection, δ_{horiz} =1, adiabatic floor and adiabatic lateral solid walls (the splines are used to guide the eye).

6.4. Discussion

6.4.1 The strongly non-linear regime of MB flow

A critical discussion of earlier studies in companion fields (and related theoretical outcomes) is used in this section to elaborate some additional arguments for the interpretation of the observed dynamics.

In particular, as a first level of this specific abstraction hierarchy, the main outcomes of the existing literature were considered where models were specifically introduced to characterize chaos in MB systems. More specifically it's useful to consider the line of inquiry originating from the studies by Thess and Orszag, 1994 and 1995, where the so-called 'strongly nonlinear regime' of MB flow was examined (enabled when the Marangoni number based on the temperature difference between the bottom wall and the free surface exceeds a value of 2000). These authors studied this problem under the assumption of infinite value of the Prandtl number (because it leads to convenient simplifications in the governing equations) and revealed that the dynamics typical of this regime have a 'signature' that makes them very peculiar even when they are compared with akin phenomena such as turbulence in buoyancy flow (i.e. notable differences also exist with regard to the "hard Rayleigh-Bénard turbulence" originally analyzed by Castaing et al. 1989).

As assumed by this model, MB flows in high-Pr fluids are dominated by viscous effects, while the temperature isolines become strongly deformed. Moreover, it considers the thermal diffusivity everywhere negligible with the exception of *thin thermal layers*.

In agreement with the numerical results presented in Sects. 6.2 and 6.3 (see, e.g., Fig. 58d and 66d), earlier simulations based on such approach have shown that the temperature field consists of parabolic regions separated by increasingly sharp transition layers at the cell boundary, where the temperature gradient *experiences a discontinuity* (as an example, Thess and Orszag, 1994, 1995 could reveal such discontinuities through evaluation of the second derivative of the surface temperature).

The existence of such discontinuities also led researchers to naturally identify an analogy with the slow dynamics of the Burgers equation; in this regard, it's necessary to recall that the specific mathematical properties of this equation are known to produce shock discontinuities (as shown by Figs. 58, 60, 66, 68 and 69, such discontinuities also manifest in the present results, where they appear in the form of spokes emanating from specific points).

Some variants have also been elaborated where in place of an infinite Prandtl number, investigators considered the $Ma \rightarrow \infty$ idealized asymptotic state. Also, this condition was found to be advantageous because in this limit the thickness of the surface Marangoni layer tends to zero, thereby allowing for two-dimensional models to be developed. Notably, in such a theoretical/mathematical context, (Thess et al. 1995,1996) and Colinet et al. (2001) could reduce the original 3D problem to a 2D nonlinear evolution equation involving only free surface quantities "under the perspective that any statistical quantity related to the three-dimensional velocity field could be considered a function of the two-dimensional surface temperature only".

The most important outcome of all this focused theoretical effort resides in the connection that has been established between the formation of the discontinuities of the temperature gradient (that emerge in a random way causing the splitting of large convective cells into smaller ones) and the instability of the surface thermal boundary-layer.

The present results obtained through solution of the original equations in their complete form essentially demonstrate that these concepts are also applicable to situations where the Prandtl number takes a finite value. The discontinuities manifest as spokes in the velocity field, corresponding to the presence of ripples in the temperature distribution, which, in turn, are produced as a result of instability of the surface temperature boundary layer. The adherence of the present results to this interpretation is further witnessed by the peculiar scaling (in terms of wavenumbers) displayed by the surface temperature distribution, which in these cases (see Figs. 58e, and 66e) follows the same universal spectrum $E(k) \propto k^{-3}$ predicted by Thess et al. (1995, 1996) and Colinet et al. (2001).

Notably, the spatial surface spectrum of temperature for layers uniformly heated from below aligns very well with that predicted by such models not only in the circumstances where flow is produced by surface tension alone, but also in the cases where buoyancy is significant (which leads to the conclusion that for Bo_{dyn} =2 and Bo_{dyn} =0, the (spatial) scaling properties of the surface turbulence are essentially the same).

6.4.2 Quantized states and Buoyancy effects

Although comparison with other existing numerical simulations for high values of Ma conducted in the limit as the Prandtl number tends to infinite or assuming an infinite value of the Marangoni number (boundary-layer model) shows that the related dynamics are in good agreement with those depicted in Sect 6.2 and 6.3, however, it should not be forgotten that the present problem is different, in the sense that while in some circumstances 'quantized' states are produced (i.e. 'typical' solutions where the pattern becomes independent from the properties of the bottom), in other cases non-trivial states emerge which *do depend on the underlying morphologically and thermally textured wall* (i.e. the size and spacing of the blocks).

The present dynamics are made more complex or intriguing by the existence of what in this thesis has been called *self-organization regime*. Again, comparison with the literature can help to shed some additional lights on such behaviors. In this regard, it is certainly worth considering the earlier experimental investigation by Ismagilov et al. (2001).

As outlined in the introduction, by means of infrared imaging, Ismagilov et al. (2001) revealed that when the convective cells typical of MB convection form under the same conditions that would produce 'standard' MB convection, but over a periodically patterned surface (uniformly heated), a specific kind of complexity is produced that is not possible when the bottom wall is perfectly planar and with no corrugations. More precisely, they found a kind of competition between the 'intrinsic spatial periodicity' of the flow (i.e., the wavelength of the planform that would be produced in the absence of topography) and the geometrical properties of the considered wall. This was found to result in a non-smooth (jerky) behavior consisting of a set of discrete states, i.e., the ability of the fluid system to undergo abrupt transitions between different planforms (commensurate with the imposed shape of the bottom boundary) as the ratio of the intrinsic (wavelength) and perturbing length scales (size and morphology of the bulges) was changed.

This trend is consistent with that which have been observed in the present study (where the same pattern has been found for conditions differing in terms of number and spacing of elements, Figs. 60 center and right panels, 63, 67 center and right panels and 68a). Here, however, the patterned nature of the bottom wall has not been limited to the presence of bulges (the cubic elements in present case). Some control on the flow has also been exerted through the related thermal properties (i.e., through thermal forcing). Assuming the portion of floor between adjoining elements to be adiabatic, it has been observed that new types of planforms can be produced which reflect neither the ordered distribution of elements at the bottom (through a trivial 1:1 correspondence), nor states which would be typical of standard MB convection.

In this regard, comparison of mixed buoyancy/Marangoni (Sect 6.2) and pure MB flow (Sect. 6.3) has proved effective in allowing discerning the role played by buoyancy in such processes. This adds new information to the study by Ismagilov et al. (2001) where, owing the small thickness of the layer (100 cSt silicone oil with depth ≅0.8 mm), buoyancy was almost negligible ($Bo_{dyn} = \rho g \beta_T d^2/\sigma_T \cong 0.1$).

Another important difference concerns the degree of supercriticality. In Ismagilov et al. (2001) circumstances were considered for which the emerging planform of standard MB convection would correspond to the classical pattern with the honeycomb symmetry. Here, conditions enabling the so-called 'strongly nonlinear dynamics', originally examined by Thess and Orszag (1994 and 1995), have been investigated.

As widely illustrated in Sects. 6.1 and 6.2, for Ma= $5x10^3$ and Bo_{dyn} =2, buoyancy enhances the role of thermal forcing through the generation of warm plumes that originate from the top surface of the heated elements. With a few exceptions (Fig. 68b), this effect contributes to make the emerging unsteady solutions and related pattern more regular than the corresponding flow in the absence of buoyancy. As a result, buoyancy can strengthen the system abilities to produce a new zoo of patterns.

6.4.3 Temporal scaling laws and Confinement effects

This final subsection is dedicated to a couple of aspects that have been glossed over until now, namely, the spatio-temporal behavior of the flow and the influence of the lateral confinement (the sidewalls, which, as already shown in earlier valuable fundamental studies, can play a non-negligible role in the dynamics of Marangoni-Rayleigh-Bénard convection, see, e.g., Dauby and Lebon, 1996; Medale and Cerisier, 2002). As further developed in the following, these two features are intimately connected in the present problem.

In order to implement such discussion and obtain some statistically meaningful data (i.e., insights which display a sufficiently high level of generality), three representative cases were considered, all pertaining to the sub-region of the space of parameters where self-organization is effective. These are the two configurations with adiabatic boundary (N=7, δ_{horiz}=1) and (N=9, δ_{horiz}=0.55), respectively and the one with isothermal floor (N=7, δ_{horiz}=0.1). The analysis is developed considering the temporal evolution of the Nusselt numbers $Nu_{side}^{average}$, $Nu_{top}^{average}$ and velocity signals (velocity component along the horizontal direction u as a function of time) provided by numerical probes located above the heated blocks (at an intermediate position between the top of the block and the free surface of the layer). In particular, the Nusselt number is characterized in terms of FFT (i.e., frequency spectrum), that is, a further understanding of the observed phenomena is gained by considering a fine-grained micromechanical perspective able to provide information on the small spatial scales of the flow. In addition, an explicit strategy was used to uncover features that could not be revealed by the macrophysical approach (based only on the spatial properties of the patterns) developed in Sect. 6.4. As a first example of this inquiry, Fig. 71 shows the FFTs of the Nusselt number for the mixed and Marangoni (microgravity) convection cases with N=9, δ_{horiz}=0.55 whose patterns have been reported in Figs 61a and 68a, respectively.

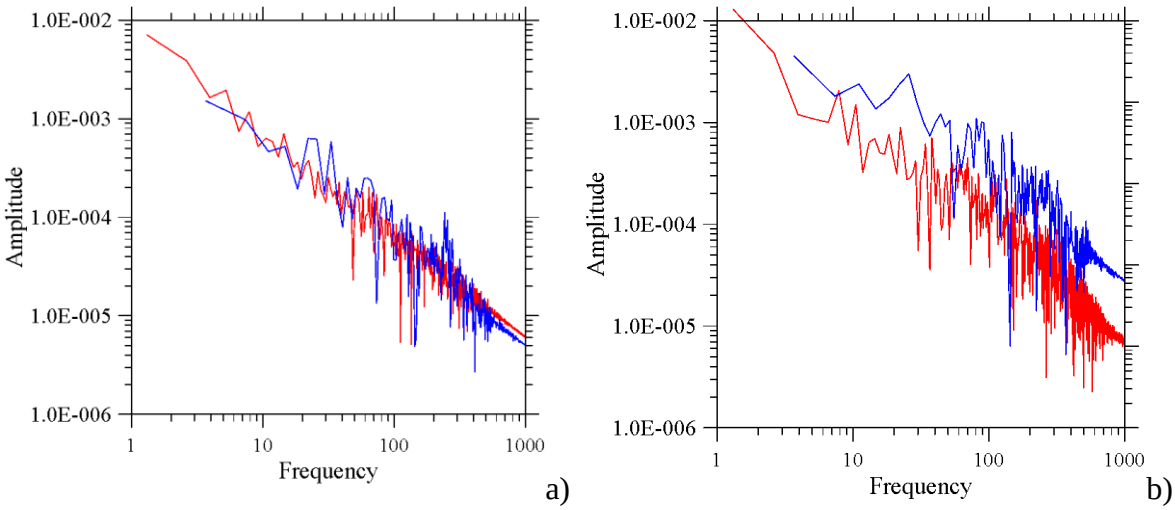

Figure 71: Frequency spectrum for the Nusselt number (Bi=1, adiabatic floor, solid sidewalls, N=9 and δ_{horiz} =0.55): a) $Nu_{side}^{average}$ b) $Nu_{top}^{average}$ [Mixed flow (red line), Pure Marangoni flow (blue line)].

It can be seen that, despite the differences in the patterning scenario (see again Figs. 61a and 68a), the spectra of the Nusselt numbers for Ra=0 (blue line) and Ra≠0 (red line) are relatively similar, a minor difference being evident only for $Nu_{top}^{average}$ (the spectrum being less energetic for the mixed flow case in line with the arguments developed before about the stabilizing role played by the thermal plumes generated by the different heated elements). Another key observation concerns the presence of peaks in the spectra of both $Nu_{side}^{average}$ and $Nu_{top}^{average}$ in the very low frequency range only for the case of mixed convection. This apparently innocuous difference reflects an important feature that have not been discussed so far, i.e., the slow re-adjustment in time, in terms of shape and position of the cells, which takes place in the presence of gravity (i.e., it is no longer a typical feature of the pure Marangoni flow for which the main source of unsteadiness is represented by the emergence of spokes and their flickering behavior).

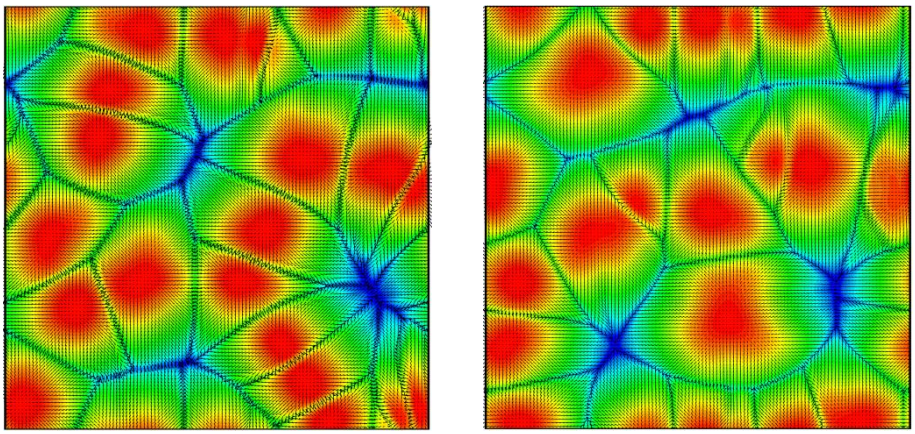

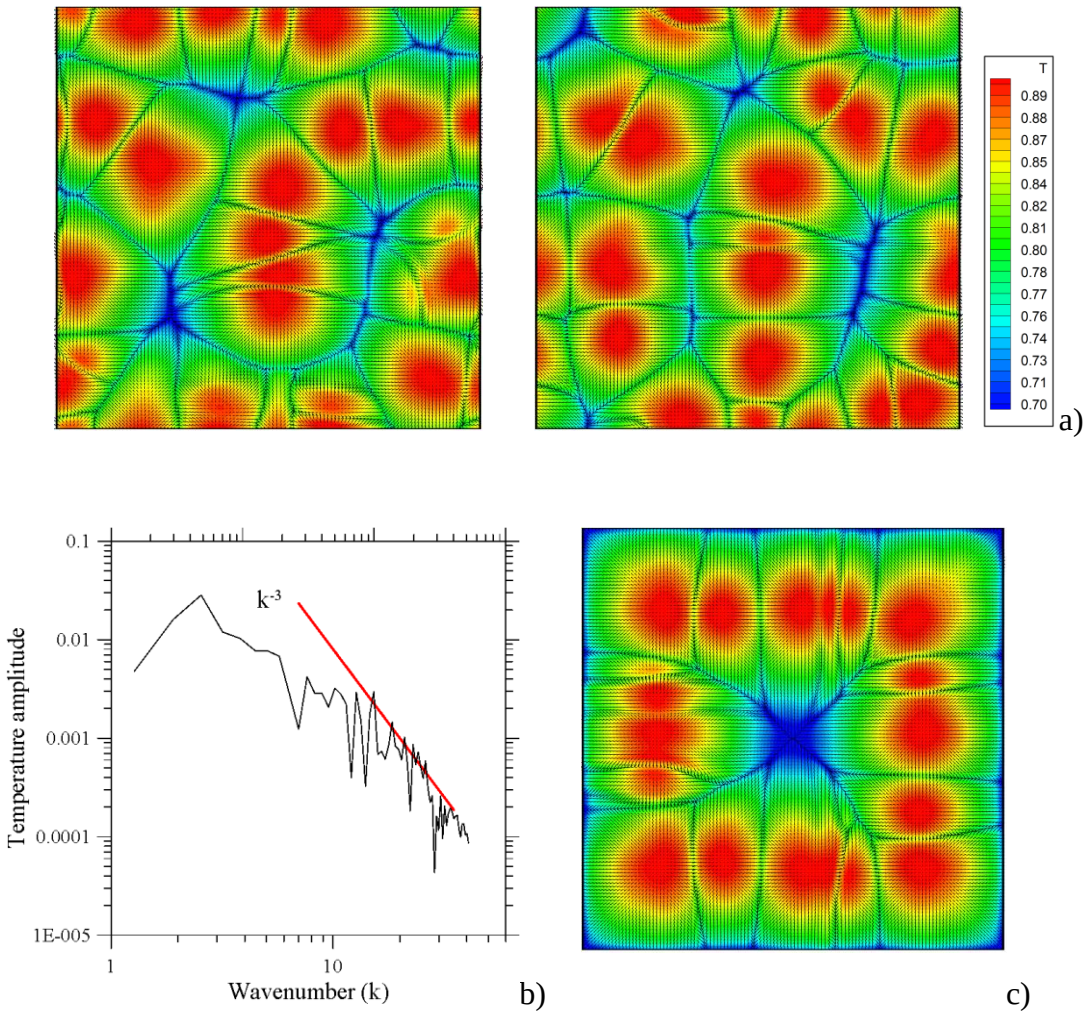

Figure 72: Mixed convection for N=7, δ_{horiz} =1 and adiabatic floor: a) combined view of surface temperature and velocity distribution for the case with periodic lateral boundary conditions (four snapshots equally spaced in time, $\Delta\tau$=1.0); b) related surface temperature spectrum (line x=3.55 at t≅6); c) combined view of surface temperature and velocity distribution for the case with solid sidewalls (snapshot at t=5.25).

As anticipated at the beginning of this discussion, at this stage, it is also worth highlighting that an additional important factor influencing the considered phenomena is represented by the solid sidewalls. Simulations conducted replacing the solid vertical boundaries with PBC have indeed confirmed that the lateral confinement contributes significantly to the perfection of some of the stable and highly ordered structures reported in Sects. 6.2 and 6.3.

As a first example of this influence, Figs. 72ab (N=7, δ_{horiz} =1, adiabatic floor, see also Movie 1) immediately reveals that, if the no-slip lateral walls are replaced by periodic boundary conditions (PBC), the pattern takes a relatively disordered spatio-temporal organization with respect to that obtained under confinement (reported for the convenience of the reader in Fig. 72c). The well-defined ring of hot spots (cell) surrounding a central knot with topological order p=4 (clearly visible in Fig. 72c) can no longer be recognized in Fig. 72a. In place of a structure dominated by p=3 knots (and a single central p=4 point), a much more complex network of spokes is produced, with cells having a number of sides ranging between 3 and 6 (from triangles

to irregular hexagons) and knots with topological order much larger than that seen for the configuration with solid walls (increasing up to p=9 as witnessed by the presence of one or more flower-like structures with many petals).

On a separate note, it is also worth highlighting that correlation of the related surface temperature (spatial) spectrum (Fig. 72b) with that obtained for the Marangoni-Rayleigh-Bénard convection (Fig. 58c) indicates that, despite the larger number of spots and the dominant polygonal structure of the cells emerging in the discrete sources case with PBC, the two surface patterns follow essentially the same k^{-3} scaling predicted by the models for highly supercritical MB convection discussed in Sect. 6.4.1.

As the same conclusions can be applied to the case N=9, δ_{horiz} =0.55 with adiabatic floor, for the sake of brevity, it was decided to pass over the description of the related details (Movie 2). The next figure of the sequence (Fig. 73), however, refers to a case where the floor is not adiabatic (hot bottom wall). As the reader will easily realize by inspecting it (see also Movie 3), in such a situation, the changes induced by a swap in the lateral boundary conditions are even more dramatic. While the flow arising with solid sidewalls was essentially steady (Fig. 73c), when PBC are applied, this is taken over by completely different spatial and temporal convective mechanism. The p=8 multiplicity of the central knot is lost (a central knot even does no longer exist or make sense). The cross-shaped network formed by cell boundaries (Fig. 73c) is replaced by a much more complex topology (Fig. 73a). An interesting (peculiar) behavior can be seen where the fluid is pushed down (blue regions). These are characterized by the presence of several ripples.

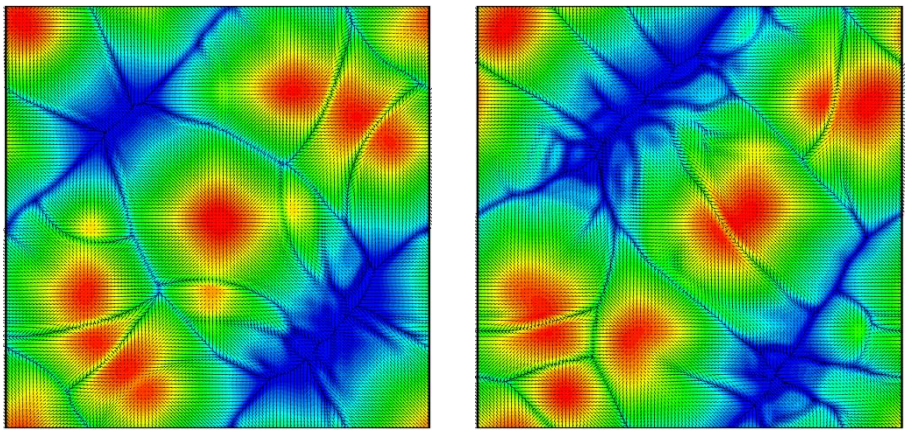

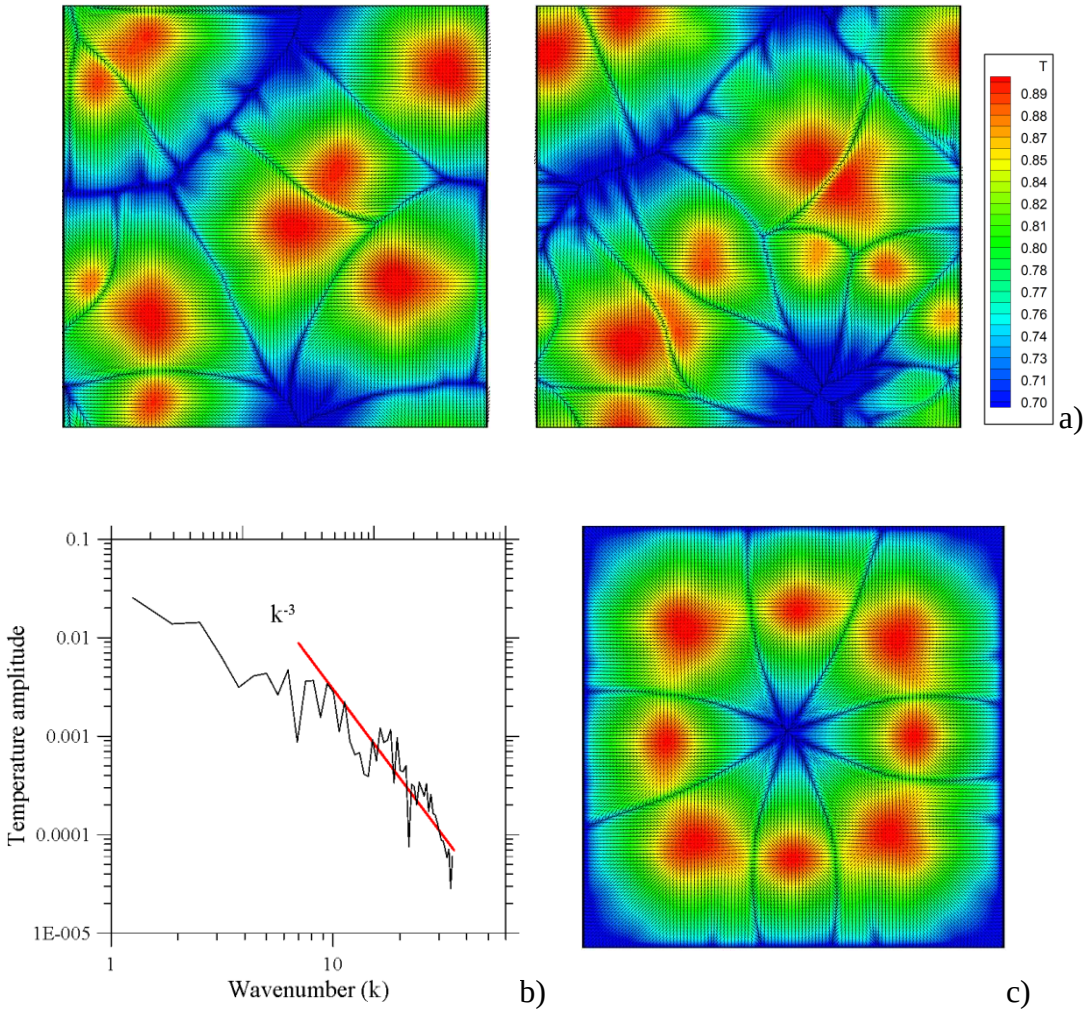

Figure 73: Mixed convection for N=7, δ_{horiz} =0.1 and hot floor: a) combined view of surface temperature and velocity distribution for the case with periodic lateral boundary conditions (four snapshots equally spaced in time, $\Delta\tau$=1.0); b) surface temperature spectrum (line x=3.52 at t=6); c) combined view of surface temperature and velocity distribution for the case with solid sidewalls (snapshot at t=3.44).

Notably, the surface temperature distribution (Fig. 73b) still obeys the k^{-3} scaling found for the other cases.

On the other hand, besides the spatial scaling law for the surface temperature spectrum (distribution of wavenumbers), all these cases with PBC also share another remarkable property, which needs to be pinpointed suitably here. Although, thermal ripples leading to localized splitting of cells are present in almost all cases (just like for the cases with solid sidewalls), the most significant contribution to time-dependence now comes from the continuous modification in the size, shape and positions of the cells.

Unlike the discretely heated configurations under lateral confinement shown in Fig. 72c, where time-dependence occasionally manifests as defects that travel slowly in the pattern along the horizontal direction or localized 'vibrating' spokes that cause breaking of cells into two or more

parts, with PBC, the temporal behavior consists of cells that, ‘like boats drifting in open water’, continuously wander in an endless process. This peculiar motion, which closely resembles that found by Lappa and Ferialdi (2018) for slightly supercritical MB convection in viscoelastic fluids, affects the entire physical domain (Figs. 72a and 73a). The characteristic time with which cells move is smaller than the equivalent one corresponding to the aforementioned slow re-adjustment process induced by gravity in the presence of sidewalls. This observation is qualitatively and quantitatively substantiated by the velocity signals reported in Fig. 74a and 74b for a sample case.

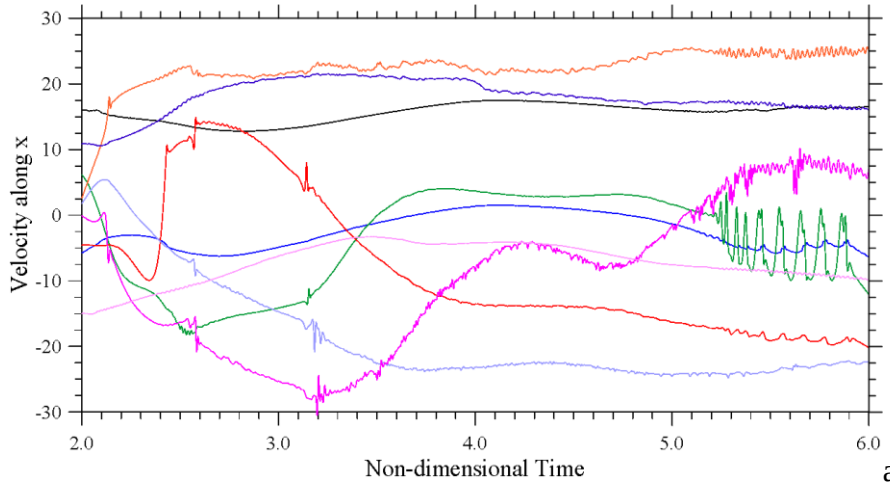

a)

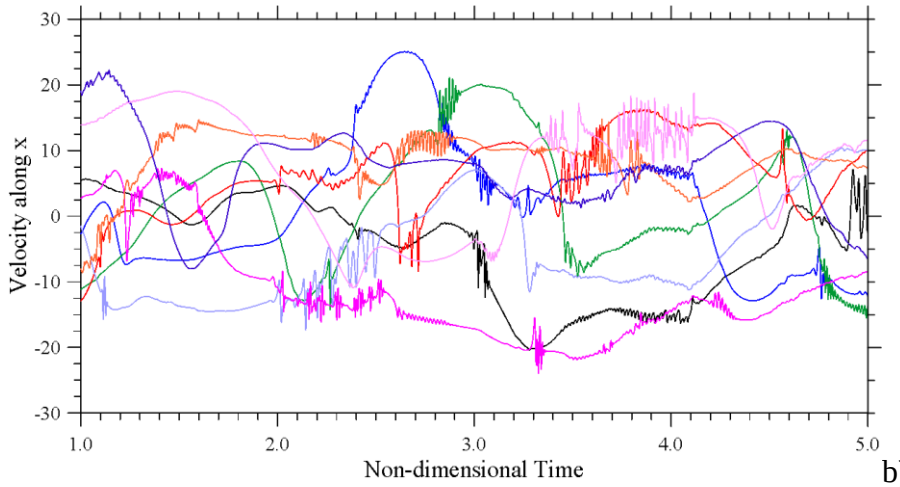

b)

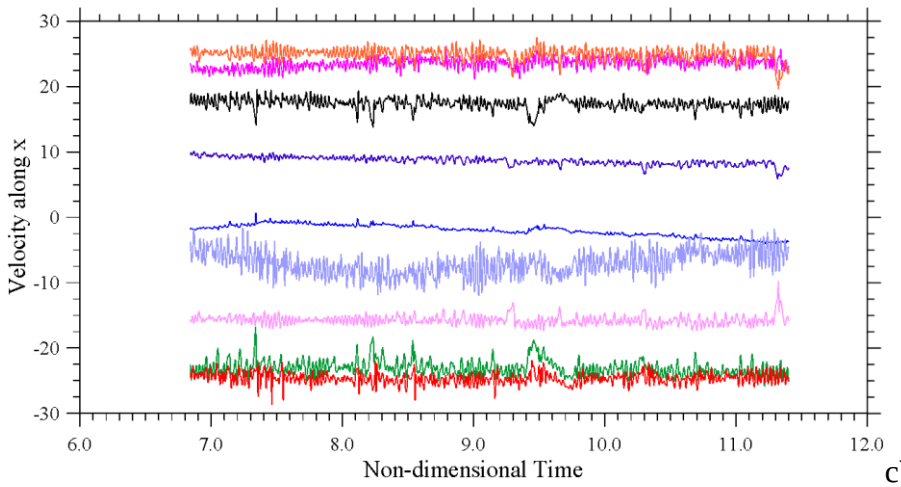

c)

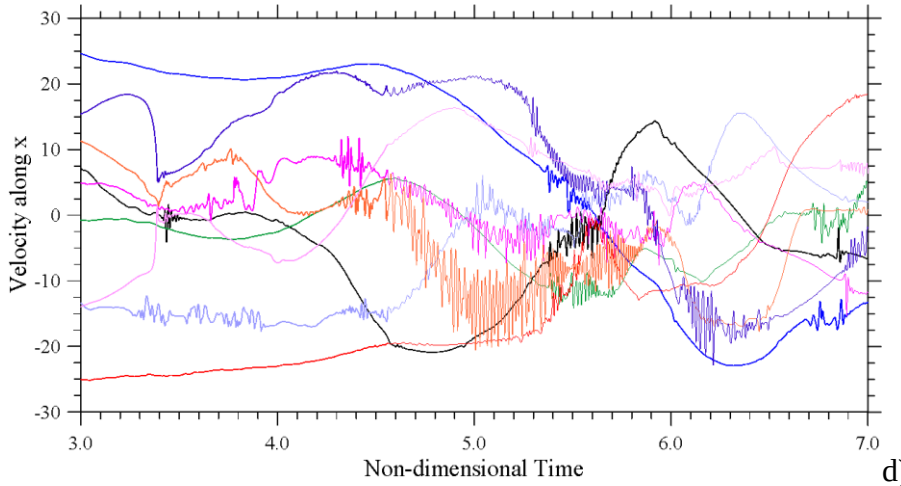

Figure 74: Signals provided by probes located above the heated blocks (y=0.65) for N=9, δ_{horiz} =0.55 and adiabatic floor: a) Solid lateral walls (mixed convection); b) PBC (mixed convection), c) Solid lateral walls in microgravity conditions (Ra=0) , d) PBC in microgravity conditions (Ra=0).

Following up on the previous point, this figure immediately shows that the simple (slow) adjustment of the cells on a relatively long time scale (Fig. 74a) for solid sidewalls is taken over for PBC by a faster process made visible by the increased number of valleys and mountains in the velocity signals (Fig. 74b). Localized (high frequency) oscillations superimposed on an otheriwse smaller-frequency signal are present in both cases. Obviously these correspond to the flickering of spokes repeatedly discussed before, which exists independently of the motion of cells. Most remarkably, the vibrating spokes are the only source of unsteadiness when pure Marangoni flow limited by sidewalls is considered (Fig. 74c). The last figure of the sequence (Fig. 74d) naturally complements the earlier observations by making evident that, even in the absence of buoyancy, pure Marangoni flow with PBC can yet display a progressive cell repositioning mechanism (which however occurs on a time scale larger than that visible in Fig. 74b).

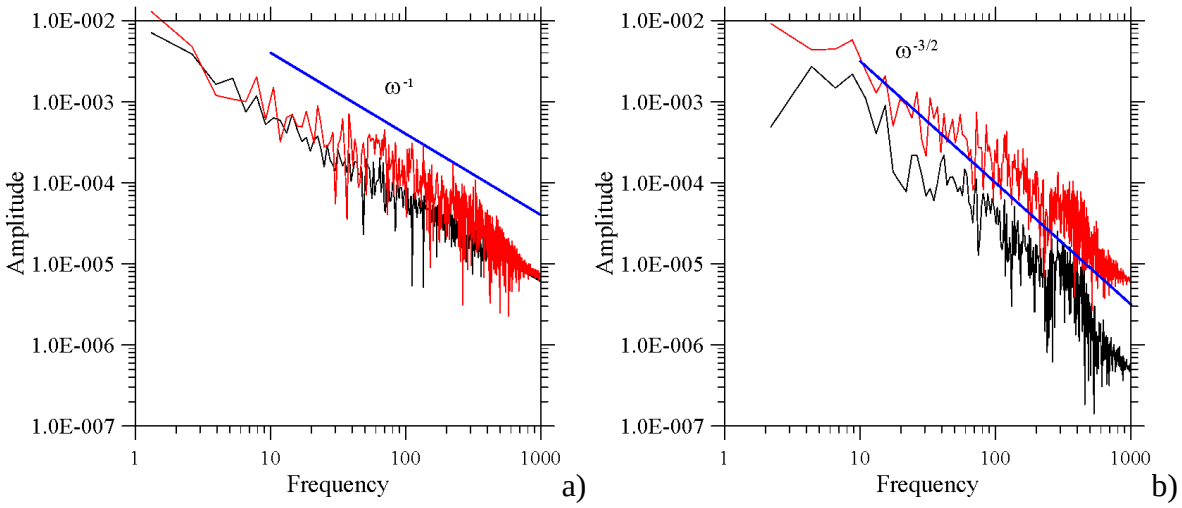

Figure 75: Frequency spectrum for the Nusselt number (mixed convection, N=9, δ_{horiz} =0.55 and adiabatic floor): a) Solid lateral walls; b) PBC [$Nu_{side}^{average}$ (black line), $Nu_{top}^{average}$ (red line), related scaling law (blue line)]. The corresponding case for pure Marangoni flow (Ra=0) and solid sidewalls (not shown) displays a scaling behavior identical to that obtained for Ra=10^4.

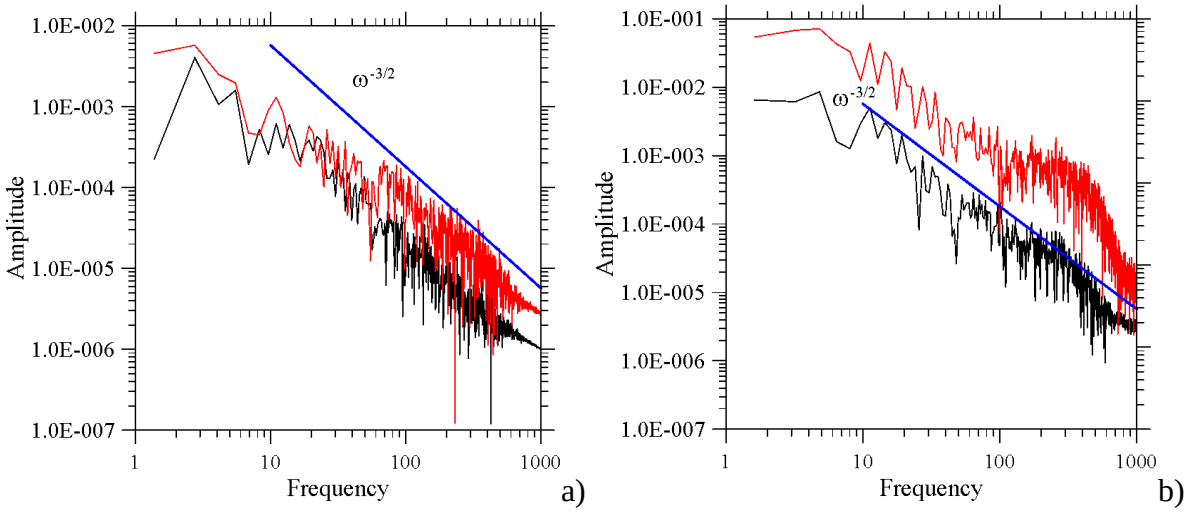

Figure 76: Frequency spectrum for the Nusselt number (mixed convection, PBC at the lateral boundaries): a) adiabatic floor, N=7, δ_{horiz} =1; b) hot floor, N=7 and δ_{horiz} =0.1 [$Nu_{side}^{average}$ (black line), $Nu_{top}^{average}$ (red line), related scaling law (blue line)].

To elucidate further the significance and implications of these findings, Fig. 75 reports the amplitudes of the different modes that contribute to the frequency spectrum of the element Nusselt numbers for the flows with both buoyancy and Marangoni effects (i.e., those corresponding to Figs. 74a and 74b, respectively).

Cross comparison of the numerical results with physical lateral boundaries and PBC indicates that these obey different scaling laws. It can be seen that the continuous and relatively fast cell wandering allowed by the lack of sidewalls causes a switch from a ω^{-1} to a $\omega^{-3/2}$ dependence. Notably, both scaling laws can be considered universal, as witnessed by Fig. 76 where the spectra for different values of N, δ_{horiz} and thermal boundary condition at the bottom wall have been reported for the cases with PBC.

6.5 Conclusions

This chapter focused on investigations of the peculiar dynamics that a morphological alteration (topography) of the bottom wall consisting of periodically positioned cubic (hot) blocks can induce in an overlying layer of a high-Pr liquid (Pr=10) with an upper free surface.

In articulating this problem, specific aim was to move beyond the idealized limitations of the classical RB and MB paradigms, which so much attention have attracted over several decades in terms of hierarchy of bifurcations and patterning behavior (up to the onset of chaos). In order to identify the correspondence between the geometrical and thermal characteristics of the bottom wall and the emerging flow in terms of textural, temporal and heat exchange properties, a systematic effort has been provided to map the complexity of such conditions into a corresponding zoo of patterns.

Given the intrinsic nature of thermal convection induced by gravity, surface tension or both driving forces, fulfilling such objective has required a fully 3D approach based on the integration of the non-linear and time-dependent governing equations.

Taking advantage of this framework, it also has been observed that the connection between the flow structure and the underlying structure is not as straightforward as one would imagine since a variety of factors can contribute to determine the related non-linear feed-back or coupling mechanisms. The relationship between a patterned boundary (intended as as repetition of sudden variations in its shape and related thermal attributes) and the flow field induced accordingly is just like the interrelation between two fundamental types of properties of any system in nature: characteristics that appear as a consequence of the interaction of the system with its environment (the larger system of which it is a part) through all its ‘boundaries’ and features that emerge as a result of mechanisms inherent within the system itself (its sensitivity to certain categories of fluid-dynamic disturbances).

Put together these aspects determine how the behavior of the considered system arises from detailed structures and interdependencies on a smaller scale. In particular, three distinct regimes, have been identified for the situation considered in the present work: trivial modes of convection where the surface pattern simply reflects (through a 1:1 correspondence) the ordered distribution of the underlying hot elements, states that display a notable degree of analogy with the 'parent' convective mechanisms (classical RB and MB flow) and a third category of flows represented by a kaleidoscope of possible solutions driven by intrinsic self-organization abilities of the considered system (enabled when a given threshold in terms of number or horizontal size of the elements is exceeded).
Although such a general classification has been found to hold for all the considered combinations of characteristic numbers (Ra≠0, Ma=0), (Ra=0, Ma≠0) and (Ra≠0, Ma≠0), significant differences have been observed depending on the involved driving forces. For pure buoyancy convection, transition from trivial patterns to more complex ones are essentially driven by thermal plume interaction mechanisms. Such processes result in shrinkage of the dimension of the matrix that can be used to map the distribution of surface spots, in comparison to the size of the underlying grid of hot elements. For $Ra=10^4$, only steady solutions exist. With the addition of surface tension effects ($Bo_{dyn}=2$), the complexity of the problem increases as unsteadiness enters the dynamics and points (vertices) with relatively high topological order pop up in the spatial network of surface spokes. These 'knots' behave as the centers of closed polygonal multi-cellular structures. Due to their existence, in general, the flow is more ordered (both in time and space) than the corresponding convective state that would be obtained assuming a flat and isothermal floor (Marangoni-Rayleigh-Bénard flow).

Although surface-tension effects become dominant, buoyancy does still play a role in such phenomena. This has been revealed through direct comparison of microgravity and terrestrial conditions, leading to the realization that the hot blocks evenly spaced along the bottom can contribute to the regularity of the flow spatial organization through the creation of thermal pillars at fixed positions (still able to influence accordingly surface flow).

The involved driving forces, however, are not the only influential factor driving the outcomes of the fluid-bottom-wall interaction. This process is also mediated by apparently secondary details such as the thermal behavior of the portion of floor between adjoining elements and (especially) the kinematic condition at the system side (its outer rim).

If the adiabatic bottom wall (on which the hot blocks are placed) is replaced with an isothermal floor (at the same temperature as the blocks) and the distribution of elements is dilute and/or their horizontal extension is small, the intrinsic mechanisms of the parent forms (MB, RB) of convection tend to become dominant in determining the emerging planform. However, this is not a general rule, as in some cases the separated elements can still serve as 'catalysts' for the formation of well-defined and stable plumes.

Replacement of the solid lateral wall with periodic boundary conditions has even more significant consequences, especially in terms of temporal dynamics. The triadic relationship between the hierarchy of involved driving forces, the lateral confinement and the system temporal response can be summarized as follows. For pure Marangoni convection (microgravity conditions) and solid lateral walls, unsteadiness essentially manifests itself in the

form of high frequency oscillations physically corresponding to the existence of vibrating spokes in the pattern, which cause localized cell breaking or coalescence effects. If buoyancy is also present, these high-frequency modes are complemented by long-period disturbances corresponding to the slow propagation of defects through the pattern (a slow displacement of the cell centers occurring on time scale comparable to the thermal diffusion time). For periodic boundary conditions, this slow process is taken over by a different phenomenon by which cells undergo a faster relocation in time, accompanied by significant changes in their size and shape. Moreover, the continuous and relatively fast cell wandering enabled in these cases causes a switch from the ω^{-1} law for the block Nusselt number frequency spectrum seen for solid lateral walls to a $\omega^{-3/2}$ dependence (in turn, both dependences seem to be universal as witnessed by the simulations conducted for different conditions, i.e. distinct values of N, δ_{horiz} and thermal boundary condition at the bottom wall).

In order to interpret this kaleidoscope of possible variants, a concerted approach has been implemented using the tools of computational fluid dynamics in synergy with existing models on the evolution of MB convection for highly supercritical Ma. Interestingly, it has shown that the pattern of surface temperature is forced to follow the k^{-3} spatial scaling originally identified by other authors (Thess and co-workers) regardless of the amplitude of buoyancy flow for Bo_{dyn} up to 2.

Chapter 7: Experimental facilities and tools:

7.1 Geometrical Model:

A sketch of the considered experimental setup used to produce the experimental results reported in this thesis is shown in Fig. 77. The fluid container consists of a square metal plate of aluminium having a size of 10 x 10 cm, on which solid walls of Perspex (1 cm tick and 2 cm tall) have been mounted along the boundary, thereby leaving 8 x 8 cm of internal space to be occupied by the considered liquid (up to a total volume of 1.28×10^{-4} m^3, corresponding to 128 ml, in the absence of obstructions at the bottom).

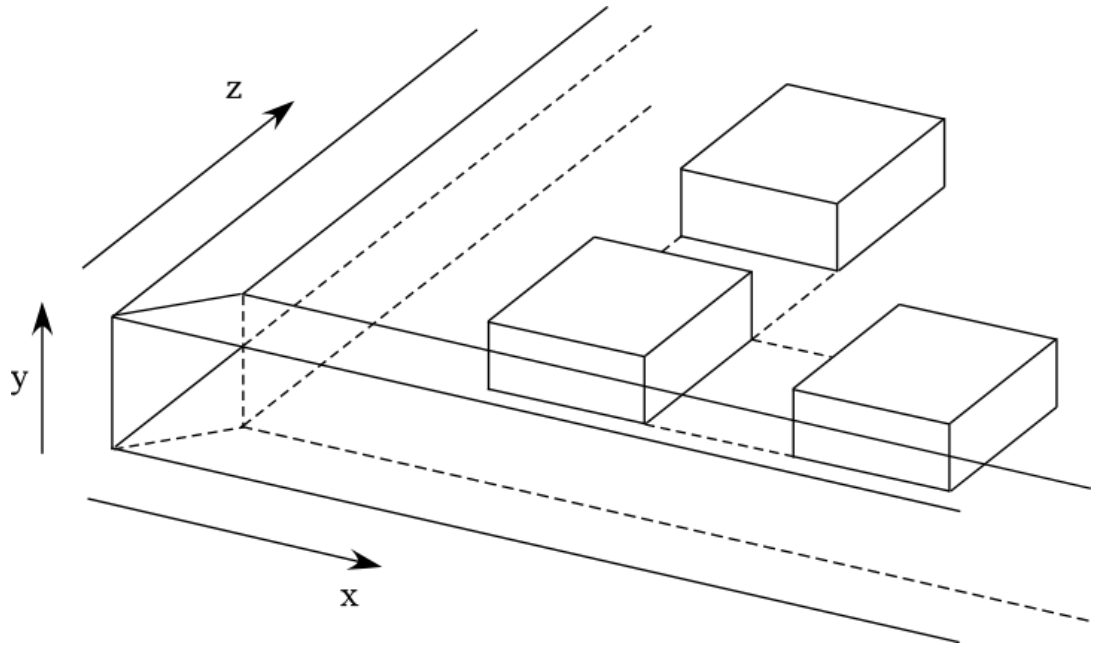

Figure 77*:* Three-dimensional view of the fluid container delimited by sidewalls of Perspex with series of bottom wall-mounted square elements evenly positioned along the sidewall directions (spacing, width and height can be systematically varied).

The blocks are also made of aluminium (same material used for the bottom plate) and are mounted along the bottom wall in such a way to maintain their spacing regular along both the x and z horizontal directions. They are available with different horizontal and vertical sizes as follows:

Table 10: Block families

Family	Horizontal size	Vertical size	Volume
1a	8 mm	10 mm	640 mm^3
1b	8 mm	5 mm	320 mm^3
1c	8 mm	3 mm	192 mm^3
2a	10 mm	10 mm	1000 mm^3
2b	10 mm	5 mm	500 mm^3
2c	10 mm	3 mm	300 mm^3

7.2 Heating system :

Figure 78*:* MS-H280-Pro Round ceramic coated Steel Hotplate.

A commercial component is used to produce the required uniform heating at the bottom of the aforementioned fluid container, namely, a MS-H280-Pro Round ceramic coated Steel Hotplate/Stirrer by which the heating temperature can be increased up to 280 °C in precise 1 °C increments, other specifications being reported in Table 11.

Table 11: Specifications of MS-H280-Pro Round ceramic coated Steel Hotplate/Stirrer

Parameter	Value/range
Work plate Dimension	Φ 135 mm
Work plate material	stainless steel cover with ceramic
Motor type	Brushless DC motor
Motor rating input	5 W
Motor rating output	3 W
Power	515 W
Heating output	500 W
Voltage	100-120/200-240V 50/60Hz
Heating temperature range	Room temp.-280, increment 1°C
Control accuracy of work plate	±1 °C (<100°C) ±1%(>100 °C)
External temperature sensor	PT1000 (accuracy ±0.5 °C)
Dimension [W x D x H]	150×260×80 mm
Weight	1.8 kg

7.3 Thermographic Camera:

The distribution of temperature on the free surface of the considered liquid is observed using a FLIR C3-X Compact Thermal Imaging Camera (the related IR sensor has a resolution of 128 x 96 px and thermal sensitivity of 70mK; moreover, it can detect and measure temperatures between -20°C and +300°C to an accuracy of ±3%). The overall inclination of the system is measured using a digital inclinometer with an accuracy of 0.01° (Neoteck NTK033-V). the following ranges are investigated: $0.5 \leq d \leq 0.75$ cm corresponding to $0.86 \leq Bo_{dyn} \leq 1.94$, moreover, $T_{air} \cong 21 \pm 1$°C.

Figure 79*:* The distribution of temperature on the free surface is obtained using a FLIR C3-X Compact Thermal Imaging. The FLIR C3-X Compact Thermal Imaging Camera's IR sensor has a resolution of 128 x 96px and thermal sensitivity of 70mK. It can detect and measure temperatures between -20°C and +300°C to an accuracy of ±3°C/3%.

In Figure 78, you can see that hot plate is placed on a solid wooden board which has screws on each corner. For flat fluid surfaces, screws were totally inside the board to provide plane surface to the hot plate. In case of inclined fluid layers, screws were moved out from one end of the board to produce inclination in fluid layer. Then inclinometer was used to measure the angle of inclination. For that, process was quite simple. Digital inclinometer provides accurate angle of inclination when it is placed on an inclined surface.

Container was placed over the hot plate where you can see that hot blocks are perfectly placed and organized on the bottom surface of the fluid layer. Regarding measurement of the depth of fluid layer, Glass graduated measuring beaker was used. For example, for depth of 1cm the required volume of fluid layer should be $64cm^3$. By using measuring beaker exact fluid was measured and then poured into the container to provide accurate required depth of fluid layer. Finally thermographic camera was used to capture the convective pattern over free surface of the fluid layer.

Chapter#8: Thermographic Analysis of Topographically Controlled Thermal Convection in a Fluid with Temperature-dependent Properties

In the present chapter, thermal convection in a shallow layer of liquid with an array of metallic (aluminium) cubic elements evenly spaced along the bottom is investigated experimentally. The blocks protrude upwards and, although they are prevented from reaching the free surface, their vertical thickness, horizontal size and overall number can be varied parametrically. As a continuation of the studies presented in preceding chapters, this configuration is used with the two-fold intention to produce a kind of obstruction or blockage in the flow and, at the same time, to feed thermal convection with heat directly injected into the fluid at a certain distance from the (hot) floor.

The present chapter takes inspiration from the earlier experimental investigation (based on a thermographic technique) by Ismagilov (Ismagilov, Rosmarin, Gracias, Stroock and Whitesides, 2001). Their simple and elegant analysis of MB convection (buoyancy effects being negligible in their study) revealed the existence of a non-trivial connection between a physical modulation of the bottom hot wall (implemented as bulges having various polygonal shapes or corrugations developing continuously along a fixed direction) and the symmetry properties of the emerging flow. On varying these features, the latter was found to undergo sudden transitions between different planforms, which were commensurate with the physical topography at the bottom but were differing in terms of ratio of the intrinsic flow wavelength and length scale of the bulges (this ratio being constrained to remain an integer number).

This causality has been further explored in the preceding chapters of this thesis where the attention has been concentrated on bulges (blocks) having a cubic shape. Moreover, as a distinguishing mark with respect to (Ismagilov, Rosmarin, Gracias, Stroock and Whitesides, 2001) much thicker layers of liquid have been considered, thereby allowing buoyancy to play a significant role. In these circumstances, solid protuberances have been found to prevent the flows from developing the classical rolls or inverted hexagonal cells typical of RB and MB convection in liquid metals (Chapter 6) and, similarly, to produce vigorous thermal plumes (thermals) able to interfere with classical surface-tension driven effects in silicone oils (Chapter 7). Accordingly, it has been clarified that due to the presence of blocks, the set of possible solutions can be significantly modified, resulting in a zoo of possible behaviours, which seem to escape a possible simple definition or classification in the light of the exiting literature. In In the abovementioned studies, a possible classification has been attempted as follows: trivial modes of convection where the surface temperature distribution simply reflects (through a 1:1 correspondence) the ordered arrangement of the underlying hot protuberances, patterns that display a notable degree of analogy with the ‘parent’ convective mechanisms (classical RB and

MB flow) and a third category of flows represented by a kaleidoscope of previously unknown states driven by intrinsic self-organization abilities of the considered system.

The experimental investigation presented in this chapter builds on, but also tries to extend those chapters by expanding the set of non-dimensional parameters in terms of values of the Prandtl, Rayleigh and Marangoni numbers. In particular, given the intrinsic nature of the considered problem, a thermographic technique is used to visualize directly the thermally induced fluid currents originating from the top of the considered (disjoint) solid blocks with finite-size and study their influence of the emerging (spatially varying) patterns. Furthermore, different fluid depths are examined in order to change the relative importance of the buoyancy and Marangoni effects for a fixed geometry and temperature difference. Specific insights into the results are obtained using typical tools for the analysis of planform formation in non-linear systems and, accordingly, some effort is provided to interpret them, whenever possible, in the light of existing theories for pattern selection in canonical thermal convection systems.

The blocks are also made of aluminium (same material used for the bottom plate) and are mounted along the bottom wall in such a way to maintain their spacing regular along both the x and z horizontal directions. They are available with different horizontal and vertical sizes as indicated in Table 12.

Table 12: Block families

Horizontal size	Vertical size
10 mm	10 mm
10 mm	5 mm
10 mm	3 mm

The physical properties of the used fluid (Emkarate RL22H oil) as a function of the temperature are summarized in Fig. 80 (these figures also include the related fitting laws in the form of polynomial expressions).

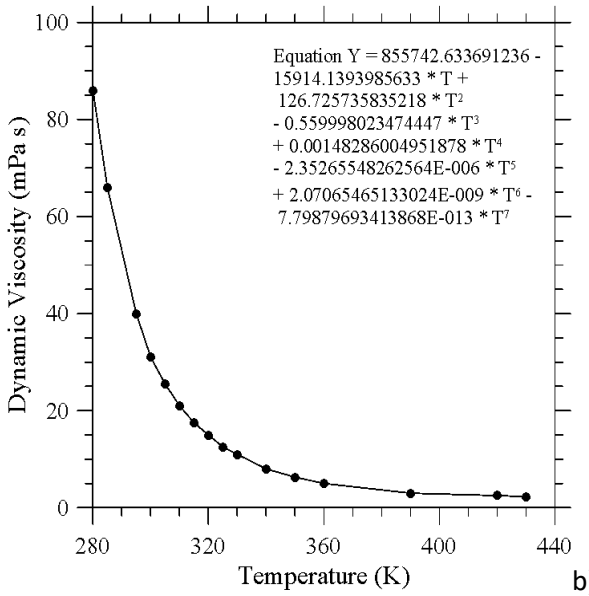
Equation Y = 855742.633691236 -
15914.1393985633 * T +
126.725735835218 * T²
- 0.559998023474447 * T³
+ 0.00148286004951878 * T⁴
- 2.35265548262564E-006 * T⁵
+ 2.07065465133024E-009 * T⁶ -
7.79879693413868E-013 * T⁷
Dynamic Viscosity (mPa s)
Temperature (K)

a)

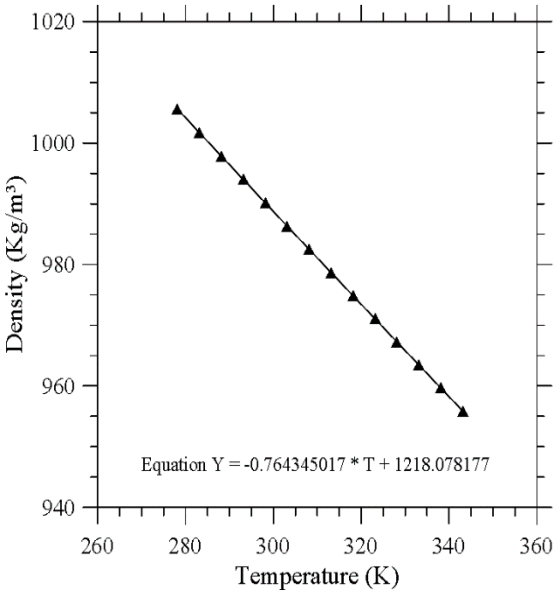
Equation Y = -0.764345017 * T + 1218.078177
Density (Kg/m³)
Temperature (K)

b)

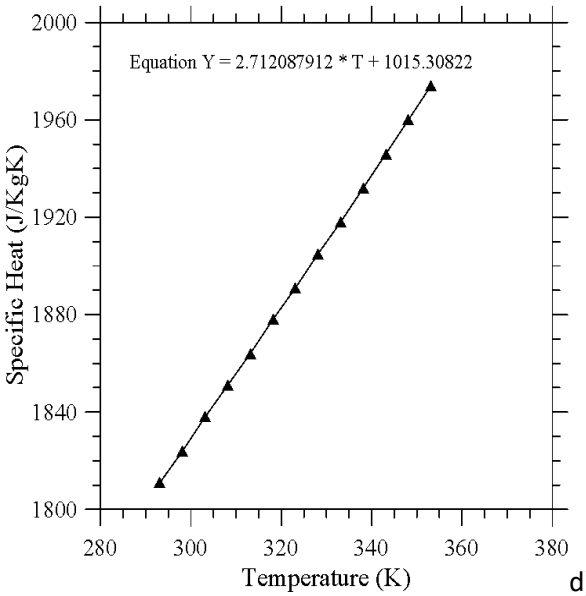
Equation Y = 2.712087912 * T + 1015.30822
Specific Heat (J/KgK)
Temperature (K)

c)

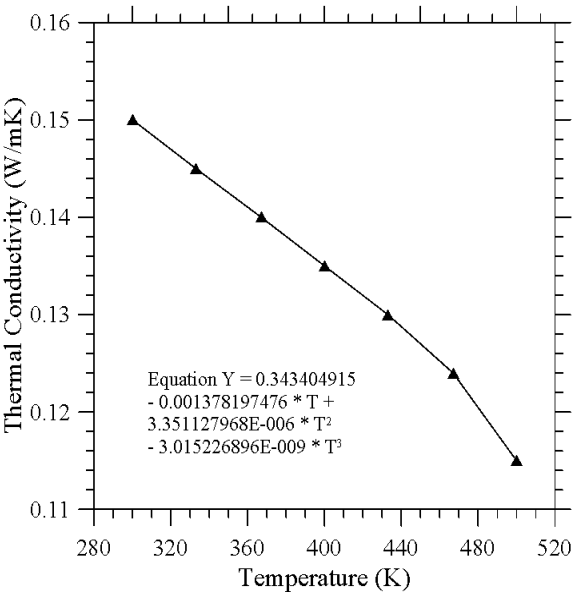
Equation Y = 0.343404915
- 0.001378197476 * T +
3.351127968E-006 * T²
- 3.015226896E-009 * T³
Thermal Conductivity (W/mK)
Temperature (K)

d)

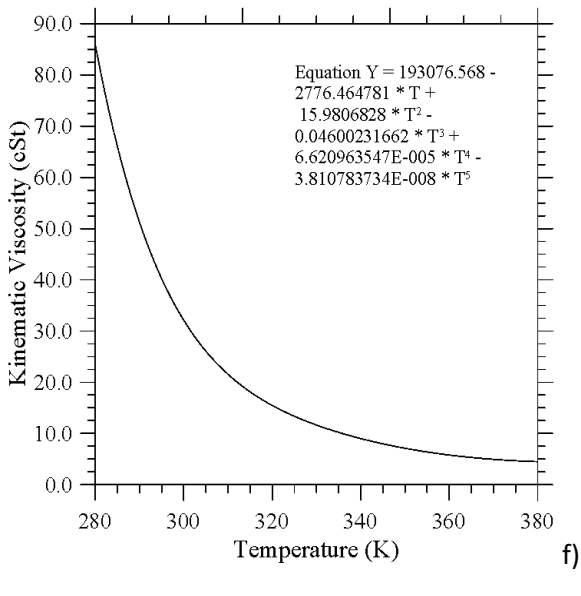
Equation Y = 193076.568 -
2776.464781 * T +
15.9806828 * T² -
0.04600231662 * T³ +
6.620963547E-005 * T⁴ -
3.810783734E-008 * T⁵
Kinematic Viscosity (cSt)
Temperature (K)

e)

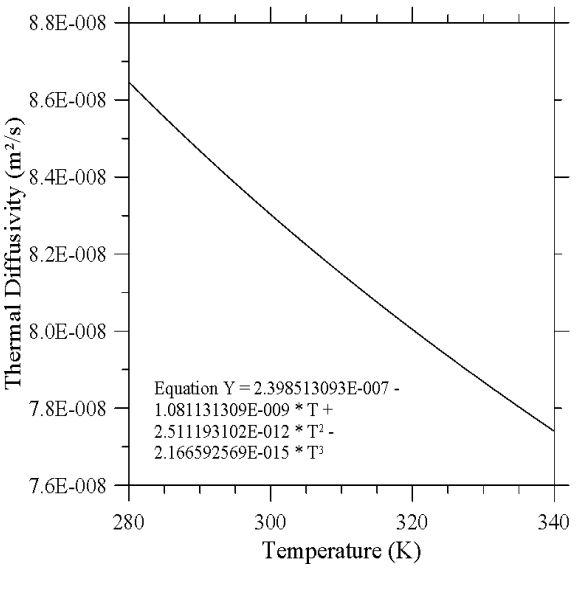
Equation Y = 2.398513093E-007 -
1.081131309E-009 * T +
2.511193102E-012 * T² -
2.166592569E-015 * T³
Thermal Diffusivity (m²/s)
Temperature (K)

f)

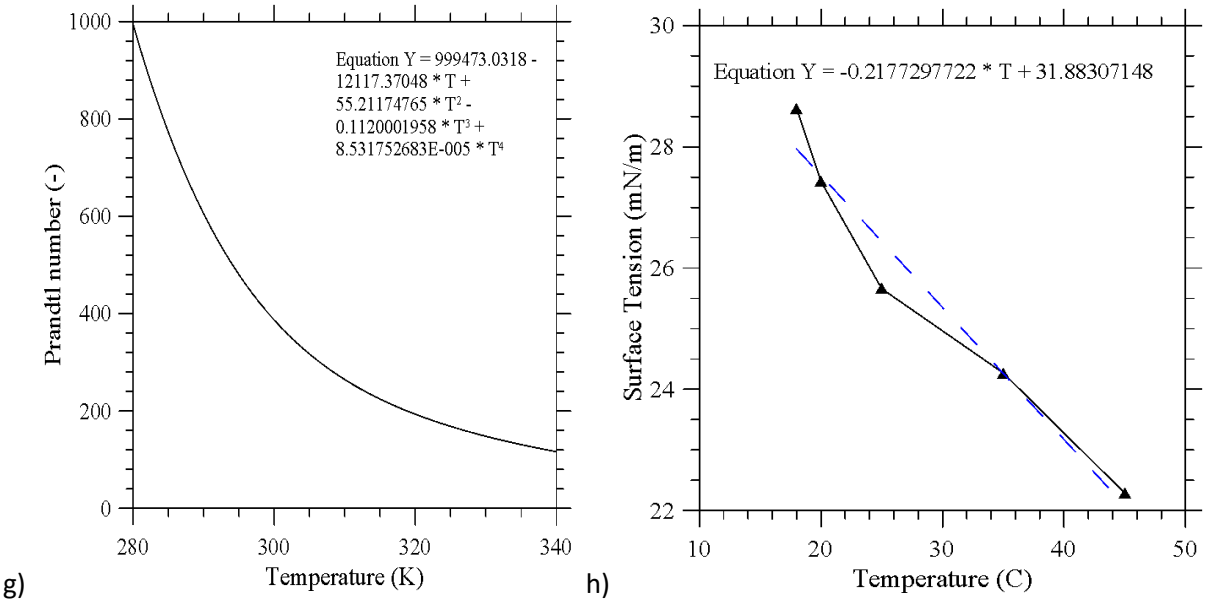

Figure 80: Physical Properties of Emkarate RL22H as a function of temperature as provided by the manufacturer: a) Dynamic viscosity μ (exp. measurements); b) Density ρ (exp. measurements); c) Specific Heat at constant pressure C_p (exp. measurements); d) Thermal conductivity λ (exp. measurements); e) Kinematic viscosity ν (derived quantity, ν=μ/ρ, 1 cSt=10^{-6} m^2/s); f) Thermal diffusivity α (derived quantity, α=λ/ρC_p); g) Prandtl number (derived quantity, Pr= $\frac{v}{\alpha}$) , h) Surface tension σ (exp measurements).

These figures are instrumental in showing that the physical properties of the considered fluid display a variable degree of sensitivity on temperature depending on the considered property. Density, specific heat, thermal conductivity, and thermal diffusivity (Fig. 80b, 80c, 80d and 80f, respectively) undergo a 10% percentage variation (or even smaller) over a range of 100 K. Nevertheless, the corresponding change in terms of viscosity is much more significant (see Fig. 80a and 80e for the dynamic and kinematic viscosity, respectively).

$$Pr = \frac{v}{\alpha} \qquad (21)$$

Where v and α are the liquid kinematic viscosity and thermal diffusivity, respectively. The dependence of this parameter on temperature can be gathered from Fig. 80g where it is shown that for the considered oil a relatively high increase in the average temperature is equivalent to considering a fluid with a much smaller value of the Prandtl number (e.g., a value of the Prandtl Pr≅520 for T≅ 20°C is reduced to a value as small as Pr≅170 for T≅50°C).

8.1 Shallow Blocks in shallow layer:

As already explained to a certain extent before, the present chapter should be regarded as a sequel to the two earlier chapters based on numerical simulations, where the ability of an increasing number of blocks to induce multicellular states with varying degrees of complexity and self-organization was investigated for a fixed aspect ratio of the blocks, fixed values of the Prandtl, Marangoni and Rayleigh numbers and fixed layer thickness. Moreover, the physical properties of the liquid were assumed constant. Here, all these constraints are removed through a four-fold approach relying on a liquid with temperature-dependent physical properties (Fig. 80), blocks with variable height (as shown in Table 12), increasing values of the temperature of the bottom plate (for a fixed value of the ambient gas temperature) and different liquid depths.

In doing so, a logical process is implemented by which one influential factor is varied at a time, while the others are kept fixed. Such a specific hierarchy is obviously instrumental in the selective identification of specific system trends, which would remain otherwise out of reach due to the intertwined nature of many of these dependences. For the convenience of the reader, some of these can be briefly illustrated as follows. While a larger temperature difference contribute to increase directly (through a direct linear proportionality law) and indirectly (through the dependence of viscosity on temperature) both the Marangoni and Rayleigh number by a similar percentage (in such a way that their ratio, i.e. the dynamic Bond number remains almost constant), an increase in the liquid depth can cause a mismatch or disparity in the ensuing increase of these non-dimensional parameters (which display a linear and cubic dependence on the system size, respectively) thereby causing a significant variation of Bo_{dyn}.

Also, the block size and aspect ratio have obviously an impact on the possible emerging solutions.

In order to clarify these dynamics, in the following, an extensive parametric investigation is carried out. In particular, the following ranges are investigated: $15 \le \Delta T \le 30$°C, $0.75 \le d \le 1.5$ cm and $3 \le \ell_y \le 10$ mm (see again Table 12), corresponding to $O(1) \le Bo_{dyn} \le O(10)$, $5.3 \le A \le 10.6$, $0.3 \le A_{bar} \le 1.0$, $0.2 \le \delta_y \le 0.66$ in terms of non-dimensional parameters. The temperature field is obtained from the infrared radiation emitted by the oil-gas interface. Moreover, the resulting images are digitized in order to allow the extraction of some relevant (quantitative) data using an appropriate Matlab based software.

In particular, the discussion begins with the simplest possible situation, that is, the case with a shallow single block located in the center of the domain. Moreover, layers with the role of buoyancy increasing are considered as the discussion progresses, that is, the analysis starts from the layer with thickness 0.75 cm.

Shallow Blocks in shallow layer

Figure 81 provides a first glimpse of the dynamics observed for the block with height 3 mm located at the bottom of a layer with thickness 0.75 (Bo_{dyn}≅1.93) and increasing values of the temperature set for the bottom hot plate.

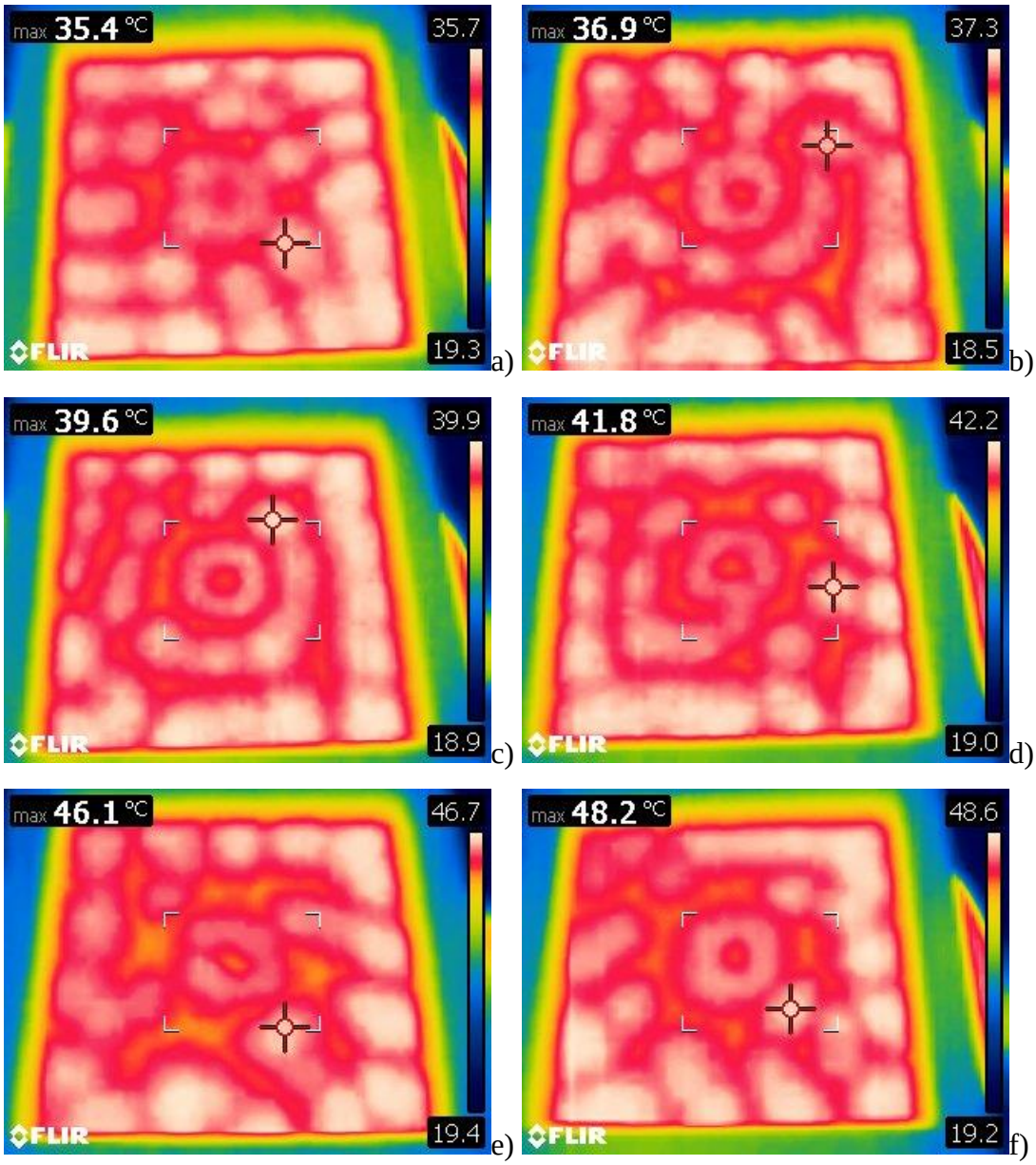

Figure 81: depth of the layer 0.75 cm (A=10.6, Bo_{dyn}≅1.93), N=1, block thickness 3 mm (δ_y=0.4, A_{bar}=0.3), variable temperature difference (Ra≅8.6x10^2xΔT, Ma≅4.4x10^2xΔT): a) ΔT=15°C, b) ΔT=18°C, c) ΔT=21°C, d) ΔT=24°C, e) ΔT=27°C, f) ΔT=30°C. Temperature maps show the descending currents as lines of colder (dark) material.

It can be seen that for the smallest value of ΔT considered (Fig. 81a), a multicellular configuration is obtained. This is indirectly proven by the distribution of hot spots visible along the free surface, each reflecting the presence of a convective structure with fluid rising

(vertically) at the center and descending at the lateral boundary of the cell (after it has exchanged heat with the external environment). Another key observation concerns the number and distribution of such cells. At first glance, indeed, the overall pattern might resemble that typical of classical MB convection. However, upon closer analysis, this figure also reveals that the influence of the central block is not negligible. This is qualitatively witnessed by the specific arrangement of spots visible in the central part of the domain. While five distinct cells/hot spots can be distinguished along each sidewall, a larger thermal feature occupies the geometrical center of the domain. The hallmark of this specific localized structure is not limited to its (slightly) larger size. Unlike all the other spots, a smaller concentric area is visible. It displays a temperature identical to that of the other regions separating adjoining spots (which, as explained before, correspond to the presence of fluids that after being cooled due to its interaction with the external environment tends to sink), which leads to the straightforward conclusion that a current of descending fluid is created just above the single block mounted on the bottom, i.e. a toroidal roll is formed just over the top surface of the block (see the sketch in Fig. 82).

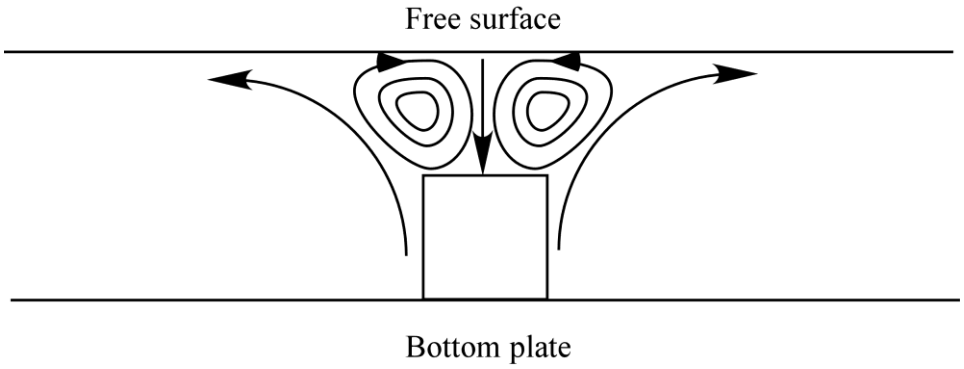

Figure 82: Sketch of the toroidal roll formed above the top surface of blocks.

The next panel of Fig. 81 reveals that the symmetry of the arrangement of spots in Fig. 81a is lost as the temperature difference is increased. Although the central donut-like thermal feature is maintained, the surrounding pattern undergoes strong modifications. Initially, these consist of spot coalescence phenomena (Fig. 81b), which cause a decrease in the number of spots aligned along the external sidewalls and the formation of an almost circular circuit or ‘ring’ of spots encapsulating the central thermal feature. On a further increase of the temperature difference, also this specific scheme is lost in favour of a more disordered patterning behaviour (Figs. 81 c-f).

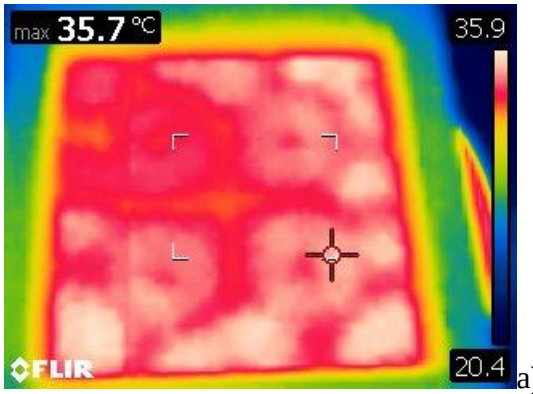

a)
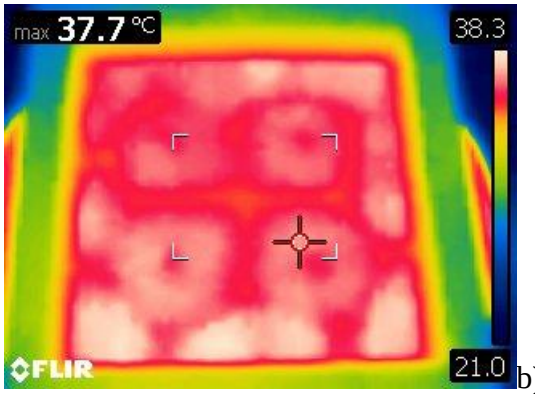

b)
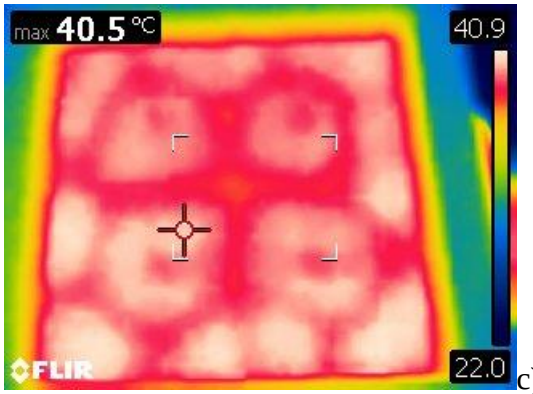

c)
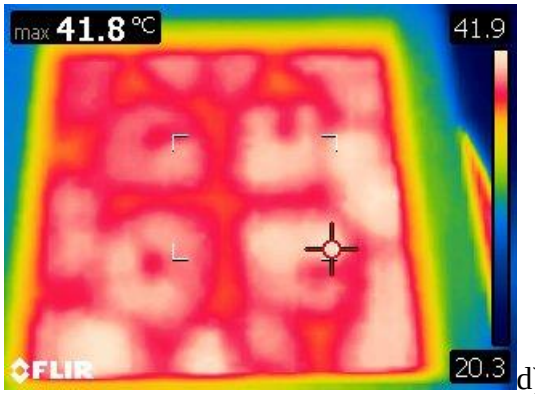

d)
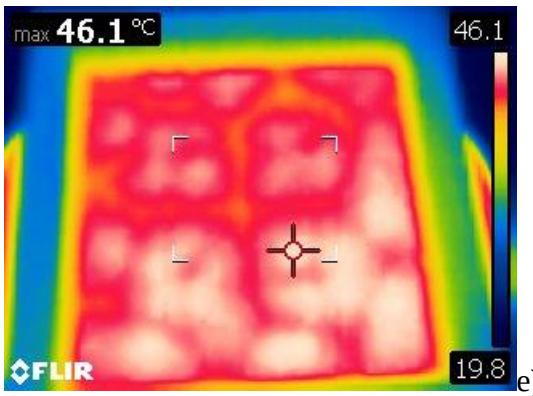

e)
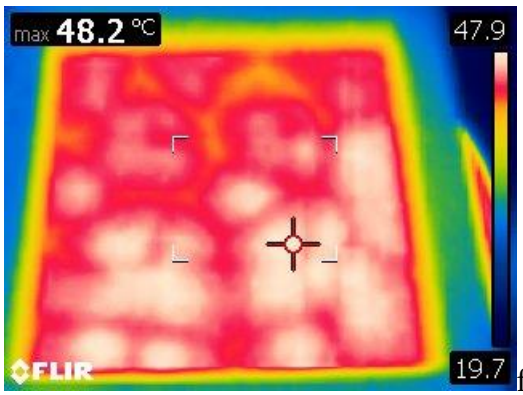

f)

Figure 83: depth of the layer 0.75 cm, (A=10.6, $Bo_{dyn}\cong 1.93$), N=2, block thickness 3 mm ($\delta_y=0.4$, $A_{bar}=0.3$), variable temperature difference ($Ra\cong 8.6x10^2x\Delta T$, $Ma\cong 4.4x10^2x\Delta T$): a) $\Delta T=15°C$, b) $\Delta T=18°C$, c) $\Delta T=21°C$, d) $\Delta T=24°C$, e) $\Delta T=27°C$, f) $\Delta T=30°C$.

On increasing N to 2 (Fig. 83), the ability of the topography to influence the pattern strengthens as witnessed by the multiplicity of the thermal features linked to the underlying blocks by a 1:1 correspondence.

The thermal inhomogeneities induced at the free surface by the cubic elements at the bottom always manifest as warmer regions with a relatively large spatial extension in comparison to the other minor spots located in proximity to the walls. In turn, the number of these (see, e.g., Fig. 82a) is smaller than that visible in Fig. 81 for N=1 (3 spots aligned along each sidewall in place of 4).

Overall, for not too high values of ΔT, the pattern for N=2 obeys the D_4 symmetry group (Chapter 6), that is, the set of reflections applicable to a regular polygon with 4 vertices. These include mirroring with respect to the lines perpendicular to the container sidewalls (parallel to the x and z axes shown in Fig. 81), which pass through the geometrical center of the domain and the analogous property with respect to the diagonal directions, i.e., the lines passing through diametrically opposite vertices. As a result, the center of the domain behaves as a special point (knot) with four-fold topology where the fluid (reaching it along four different horizontal directions) is finally pushed towards the bottom of the layer. The chosen disposition of the blocks within the container is compatible with these symmetries, which are retained by the emerging flow. Obviously, this concept cannot be extended to the up-down reflection, which is broken in any case because of the free upper surface and the presence of blocks (Chapter 7).

Apart from interesting information about the symmetries which are retained or violated, the major significance of these findings resides in the confirmation they provide about the ability of hot protuberances to behave as ‘catalysts’, by forcing thermal plumes of buoyant nature to form at fixed positions. These behave as ‘pillars’, which can somehow ‘stabilize’ the pattern, i.e. make it much more regular with respect to those which would be produced with no topography. Suffice to recall that in the absence of topography, the pattern would be characterized by a disordered distribution of rolls with different orientations and/or convective cells emerging at different positions. Moreover, such a distribution would change on repeating the experiments in identical conditions.

Along the same lines, frame-by-frame comparison of Figs. 83 and 81 also indicates that as N is increased, the transition to a disordered pattern is delayed to larger values of the ΔT, which may be regarded as a further demonstration or verification of the stabilizing role that the bottom hot blocks can have on the emerging dynamics. This realization indeed finds its ultimate verification in the dynamics shown in Figs. 84, yet for a layer with depth 0.75 cm for N=3.

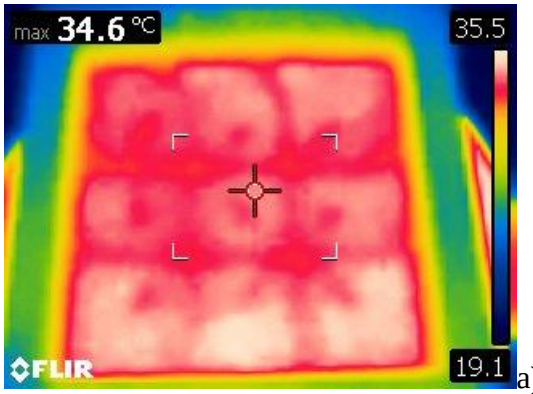

a)
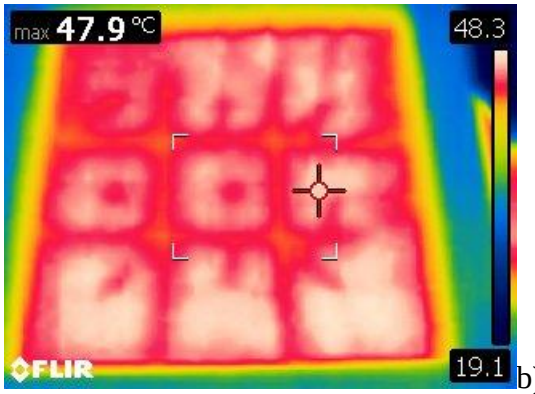

b)

Figure 84: Depth of the layer 0.75 cm, (A=10.6, $Bo_{dyn}\cong 1.93$), N=3, block thickness 3 mm ($\delta_y=0.4$, $A_{bar}=0.3$) , variable temperature difference ($Ra\cong 8.6x10^2x\Delta T$, $Ma\cong 4.4x10^2x\Delta T$): a) $\Delta T=15°C$, b) $\Delta T=30°C$.

Regardless of the considered value of ΔT, a total of nine spots with well-defined square shape and highly ordered arrangement can be distinguished in this figure. This means that conditions are attained for which the features of the surface temperature field can be directly mapped into the topography at the bottom, i.e. they simply reflect the (a-priori-set) order of the underlying grid of hot blocks (while all the other minor spots are suppressed, a solution hereafter simply referred to as 'saturated state'). However, a closer inspection of these figures also reveals that, although disordered patterns are no longer possible, on increasing the ΔT, the D4 symmetry can still be broken due to some 'localized effects'. These manifest as localized star-shaped patterns (Fig. 84b).

8.2 Tall Blocks in shallow layer

A replacement of the blocks having thickness 3 mm with the 5 mm ones has a two-fold effect. For N=1, the central thermal feature that was displaying a donut shape in Fig. 81 (descending flow at the center) is replaced by a full spot (rising fluid at the center, Fig. 85). Moreover, (given the proximity of the top surface of protuberances to the free surface) the size of this central spot is appreciably larger (it can be argued that due to the limited space between the top surface of the block and the free liquid-gas interface the central toroidal roll described in Sect. 8.1 is no longer formed).

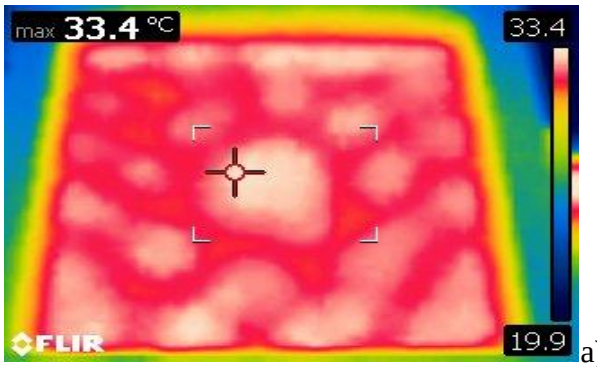

a)
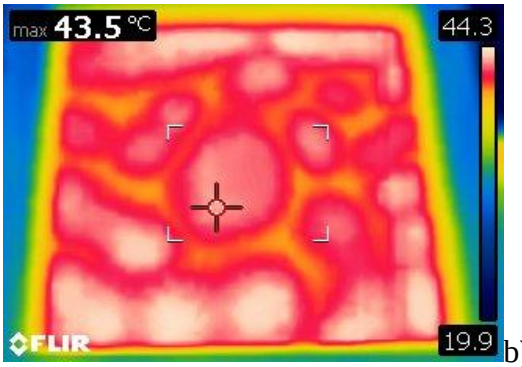

b)

Figure 85: Depth of the layer 0.75 cm, (A=10.6, $Bo_{dyn}\cong 1.93$), N=1, block thickness 5 mm ($\delta_y=0.66$, $A_{bar}=0.5$), variable temperature difference ($Ra\cong 8.6x10^2x\Delta T$, $Ma\cong 4.4x10^2x\Delta T$): a) $\Delta T=15°C$, b) $\Delta T=30°C$.

For ΔT =15 °C (Fig. 85a), the ring of spots surrounding the central one displays 8 distinct features in place of the 6 observed in Fig. 81a. For larger ΔT (Fig. 85b), this ordered arrangement is taken over by a relatively disordered distribution of rolls with inclined orientation, which tend to break into separated spots.

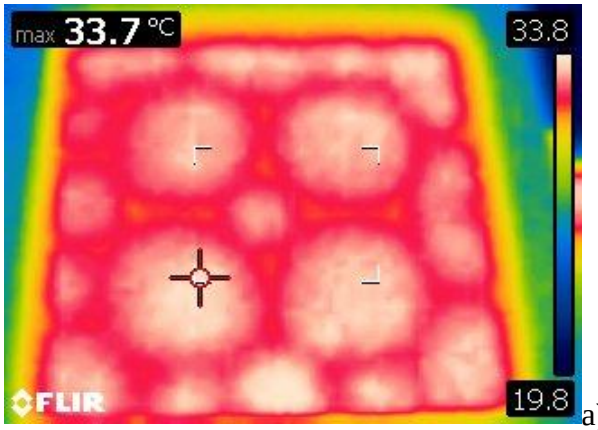

a)
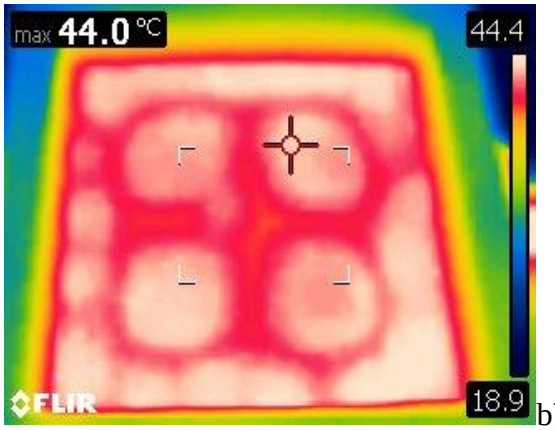

b)

Figure 86: Depth of the layer 0.75 cm (A=10.6, $Bo_{dyn}\cong 1.93$), N=2, block thickness 5 mm ($\delta_y=0.66$, $A_{bar}=0.5$), variable temperature difference ($Ra\cong 8.6x10^2x\Delta T$, $Ma\cong 4.4x10^2x\Delta T$): a) $\Delta T=15°C$, b) $\Delta T=30°C$.

The next figure of the sequence (Fig. 86) is instrumental in showing that, moving on to the case with N=2, a stable pattern preserving the D_4 symmetries is established over the entire interval of temperature differences considered. As a minor difference with respect to the equivalent dynamics depicted in Fig. 6, the aforementioned central 'singular' vertex with four-fold topology (collecting fluid moving horizontally towards it along the free surface, as explained in Sect. 4.1) is taken over by a small spot emerging at the center of the domain.

Additional insights follow naturally from a comparison of Figs.86b and 83f. The flow for a block thickness of 5 mm is much more regular and ordered at the same ΔT, which indicates that for a fixed layer depth the stabilizing role played by the topography strengthens as the thickness of the blocks is increased. The same concept also applies to N=3 (Fig. 87). The location of spots is simply consistent with the related distribution of protuberances, and an external observer looking at the free surface in this case would naturally be induced to map the set of spots into an array having the same dimensions of the underling matrix of blocks (once again a saturated state condition).

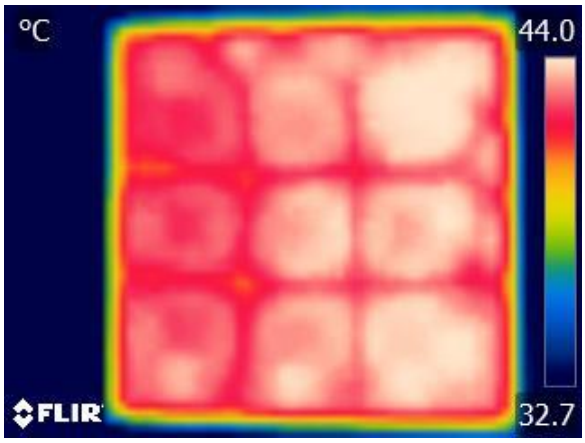

Figure 87: Depth of the layer 0.75 cm (A=10.6, $Bo_{dyn}\cong 1.93$), N=3, block thickness 5 mm ($\delta_y=0.66$, $A_{bar}=0.5$), $\Delta T=30°C$ ($Ra\cong 8.6x10^2x\Delta T$, $Ma\cong 4.4x10^2x\Delta T$).

8.3 Shallow Blocks in intermediate-depth layer

Having completed a description of the emerging patterns in terms of spatial features for the shallow layer case, now the companion situations with thicker layer are considered, these experiments being instrumental in clarifying the nonlinear processes of wavenumber selection at play in these systems**.** Along these lines, Fig. 88 refers once again to the archetypal N=1 case. As the reader will realize by inspecting this figure, the most striking difference with respect to the analogous dynamics depicted in Figs. 81 and 85, for relatively small values of the ΔT concern the size of the emerging thermal features, which increases considerably (compare e.g., Fig. 88a and 81a). Moreover, for small ΔT the D4 symmetry is no longer a property of the pattern, this being replaced by a smaller degree of symmetry, namely, the reflectional invariance with respect to a line parallel to the z axis passing through the center of the domain (Fig. 88a). The significance of this figure, however, primarily resides in its ability to make evident that the distribution of wavenumbers is not independent from the ΔT. As the vertical temperature difference grows, the number of convective becomes higher and accordingly the size shrinks (thereby indicating that an increase in ΔT can cause a rise in the wavenumber, this concept will be re-examined later).

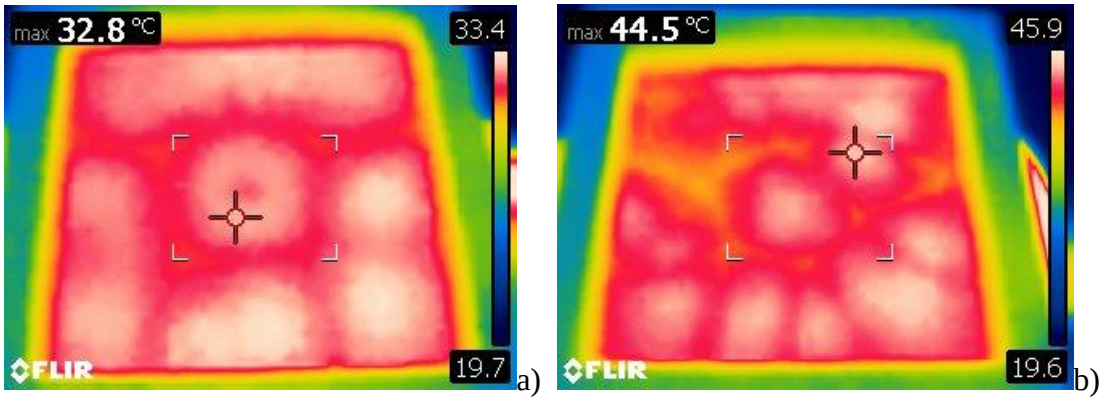

a) b)

Figure 88: Depth of the layer 1 cm (A=8, $Bo_{dyn}\cong3.44$), N=1, block thickness 3 mm (δ_y=0.3, A_{bar}=0.3), variable temperature difference ($Ra\cong2.0x10^3x\Delta T$, $Ma\cong5.9x10^2x\Delta T$): a) ΔT=15°C, b) ΔT=30°C.

For N=2, the pattern is very ordered (Fig. 89a), with four central spots encapsulated into an external ordered arrangement displaying 3 spots along each side. On increasing the ΔT, however, the symmetry is broken (Figs. 89b). Finally, for N=3, the trivial aforementioned "saturated state" is recovered (simply reflecting the underlying distribution of elements, not shown).

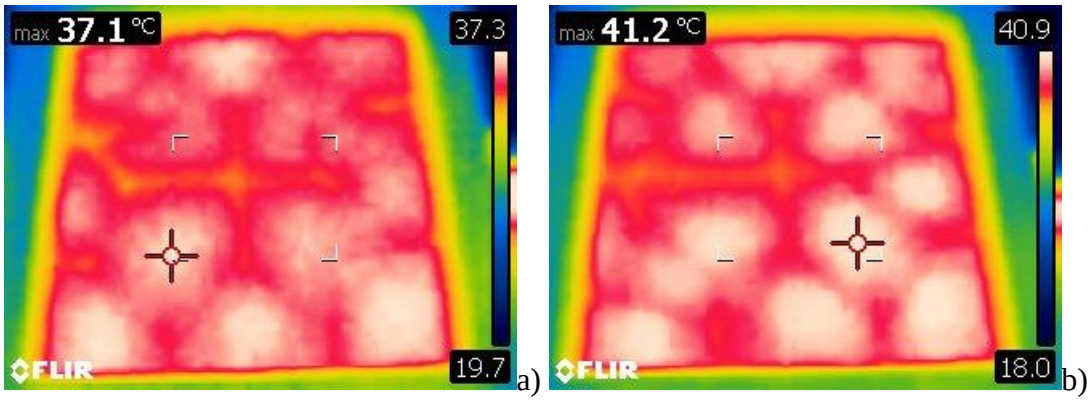

a) b)

Figure 89: Depth of the layer 1 cm (A=8, $Bo_{dyn}\cong3.44$), N=2, block thickness 3 mm (δ_y=0.3, A_{bar}=0.3), variable temperature difference ($Ra\cong2.0x10^3x\Delta T$, $Ma\cong5.9x10^2x\Delta T$): a) ΔT=21°C, b) ΔT=27°C (topological order of central knot p=4).

8.4 Tall Blocks in intermediate-depth layer

As the next logical step, in this section the focus is shifted to the scenario where the vertical size of the blocks is increased while retaining the same layer depth considered in Sect. 4.3. In such a treatment, however, the case N=1 is skipped as the related patterns are almost identical to that already shown in Fig. 88, which leads to the conclusions that for this depth the ability of a single block to influence the overall pattern is relatively limited.

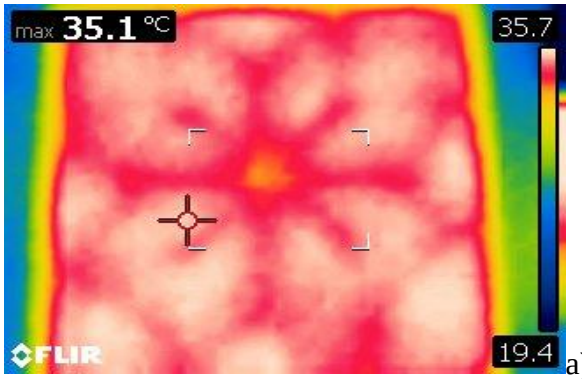

a)
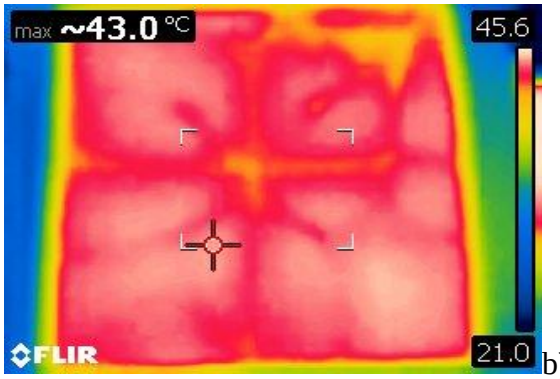

b)

Figure 90: Depth of the layer 1 cm (A=8, $Bo_{dyn}\cong 3.44$), N=2, block thickness 5 mm ($\delta_y=0.5$, $A_{bar}=0.5$), variable temperature difference ($Ra\cong 2.0x10^3x\Delta T$, $Ma\cong 5.9x10^2x\Delta T$): a) $\Delta T=21°C$, b) $\Delta T=30°C$.

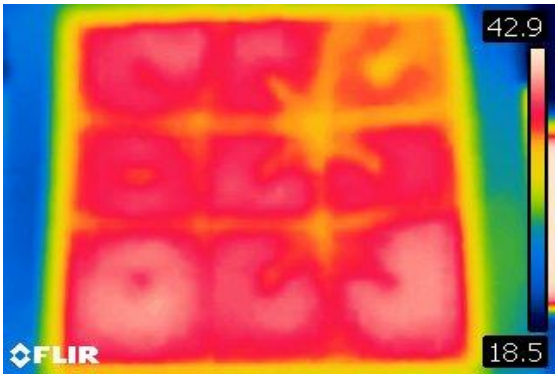

Figure 91: Depth of the layer 1 cm (A=8, $Bo_{dyn}\cong 3.44$), N=3, block thickness 5 mm ($\delta_y=0.5$, $A_{bar}=0.5$), $\Delta T=27°C$ ($Ra\cong 2.0x10^3x\Delta T$, $Ma\cong 5.9x10^2x\Delta T$).

On considering values of N larger than 1, however, some interesting, localized effects become evident (Figs. 90 and 91). The phenomena originally seen in Fig. 84 for a depth 0.75 cm, N=3 and block thickness 3 mm also manifest in this case. In particular, as a result of an instability affecting the position of the inner colder spot located at the center of any square hot spot, some special knots appear in the domain, which can be uniquely identified through the topological order p of the radial spokes that emanate from them. For N=2, notably, one of these special points is located just in the center of the domain (Fig. 90) and its topological order is p = 8. Remarkably, the p=8 multiplicity is still present for N=3 (Fig. 91), although the related knot no longer occupies the center of the domain. Owing to this asymmetry, knots with topological order p=6 are also present in addition to the standard one with p=4 (a similar effect can also be noticed in Fig. 84).

8.5 Shallow Blocks in thick layer

This section and the next one (Sect. 8.6) are finally used to describe the dynamics for a layer with thickness 1.5 cm (doubled with respect to that considered in Sects. 8.1 and 8.2).

In line with the trends highlighted in the earlier sections, by which an increase in the layer depth and or temperature difference causes a breakdown in the symmetry of the emerging pattern, Fig. 92 clearly shows that for a single block (N=1) with height 3 mm in a layer with depth 5 times this height, no specific spatial order exists over the entire range of ΔTs considered.

As the vertical temperature difference is increased, the wavenumber becomes higher and some "spokes" separating spots having asymmetric square or hexagonal shape appear, thereby making the pattern similar to those reported by other authors for the case of pure buoyancy convection (see Sect. 5).

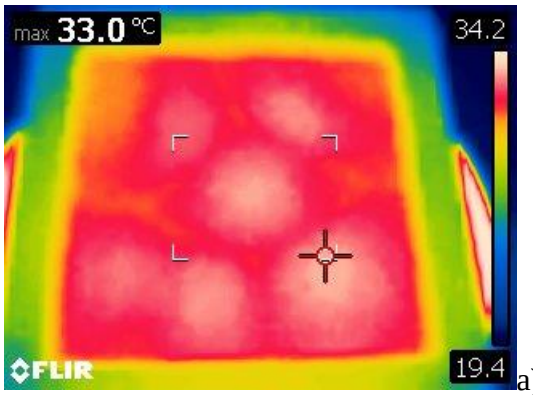

a)

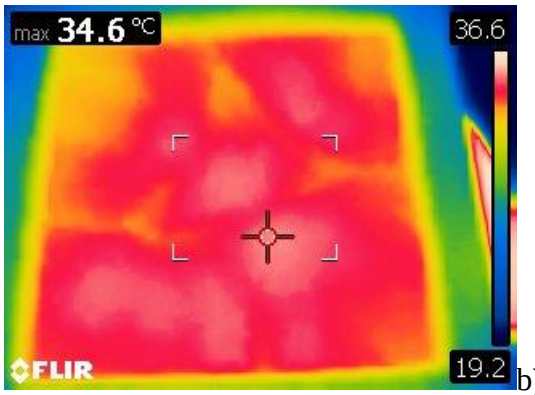

b)

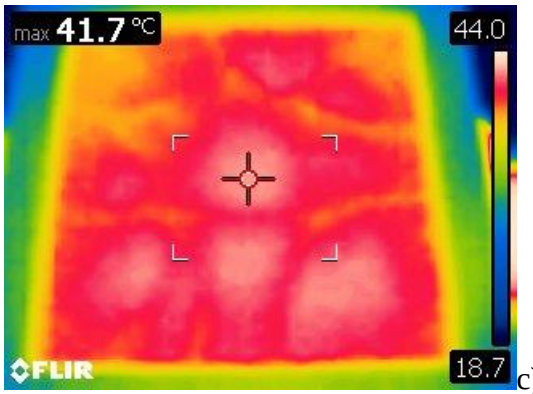

c)

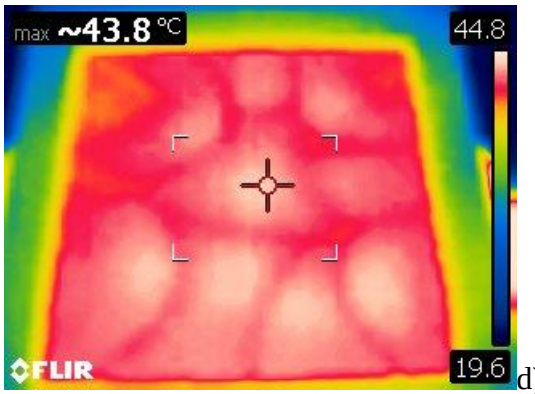

d)

Figure 92: Depth of the layer 1.5 cm (A=5.3, $Bo_{dyn}\cong 7.75$), N=1, block thickness 3 mm (δ_y=0.2, A_{bar}=0.3), variable temperature difference ($Ra\cong 6.85x10^3x\Delta T$, $Ma\cong 8.8x10^2x\Delta T$): a) ΔT=15°C, b) ΔT=18°C, c) ΔT=27°C, d) ΔT=30°C.

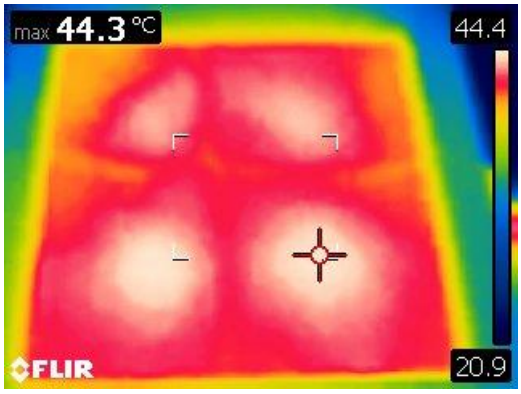

Figure 93: Depth of the layer 1.5 cm (A=5.3, $Bo_{dyn}\cong 7.75$), N=2, block thickness 3 mm ($\delta_y=0.2$, $A_{bar}=0.3$), $\Delta T=30°C$ ($Ra\cong 6.85\times10^3\times\Delta T$, $Ma\cong 8.8\times10^2\times\Delta T$).

For N=2 (Fig. 93) a trivial pattern with four large spots is obtained over the entire range of ΔT considered, which leads to the conclusion that for this layer depth the system enters the saturated state condition for a smaller value of N (compare with Figs. 83 and 89).

8.6 Tall Blocks in thick layer

A scenario similar to that described in Sect. 8.5 still holds when the height of the block is increased.

While Figs. 94 and 95 provide a glimpse of the more complex dynamics that are enabled when N=1 regardless of the thickness of the considered block (this being 5 mm and 10 mm in Figs. 94 and 95, respectively), a saturated state is recovered as soon as N is increased to 2 (not shown).

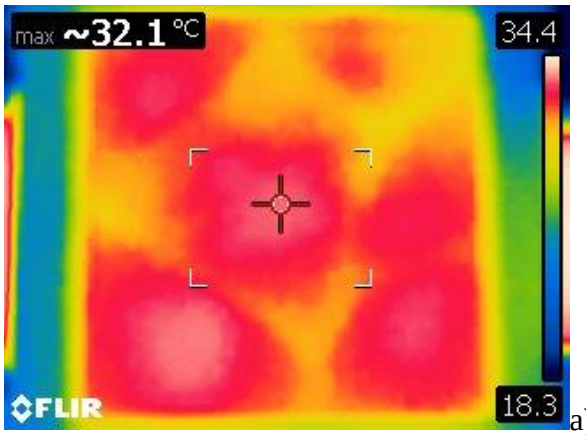

a)
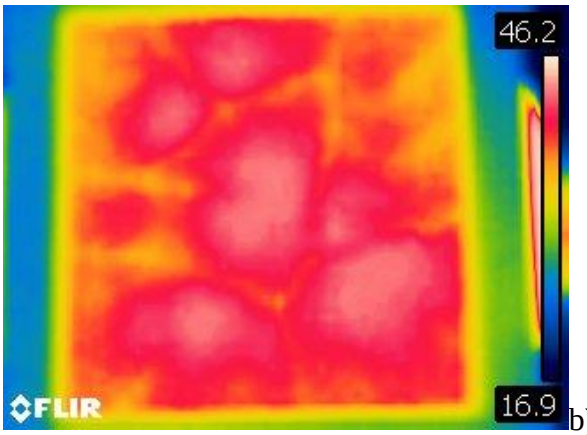

b)

Figure 94: depth of the layer 1.5 cm (A=5.3, $Bo_{dyn}\cong 7.75$), N=1, block thickness 5 mm ($\delta_y=0.33$, $A_{bar}=0.5$), variable temperature difference ($Ra\cong 6.85\times10^3\times\Delta T$, $Ma\cong 8.8\times10^2\times\Delta T$): a) $\Delta T=15°C$, b) $\Delta T=30°C$.

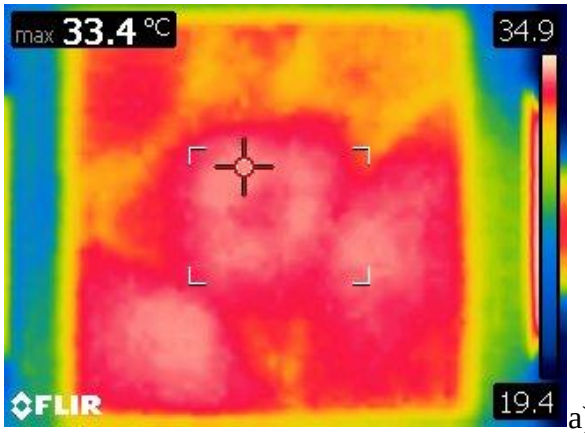

a)
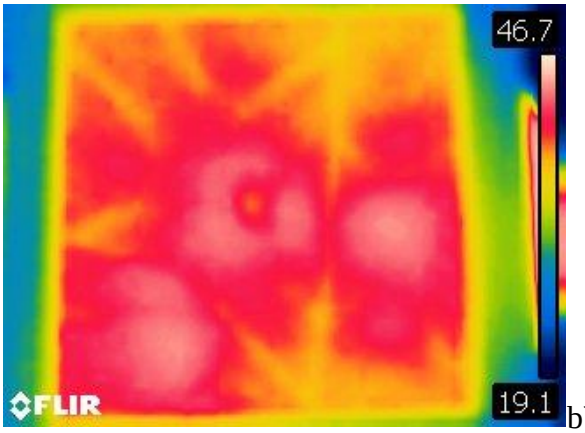

b)

Figure 95: Depth of the layer 1.5 cm (A=5.3, $Bo_{dyn}\cong 7.75$), N=1, block thickness 10 mm ($\delta_y=0.66$, $A_{bar}=1$), variable temperature difference ($Ra\cong 6.85x10^3x\Delta T$, $Ma\cong 8.8x10^2x\Delta T$): a) $\Delta T=15°C$, b) $\Delta T=30°C$.

8.7 Discussion

In order to interpret the present findings, a more detailed review of certain results appearing in the literature is beneficial (in addition to the information already reported in Chapter 2), in particular, a short excursus into the peculiar properties of RB convection in problems that lack the up-down reflection property may help to filter out those aspects which are typical of this form of convection with respect to those induced by the presence of blocks.

As the reader will have realized at this stage, in the present case, such the up-down symmetry is broken due to the contribution of three independent factors, namely, 1) the strong dependence of some fluid properties on the temperature (as quantitatively substantiated in Fig. 3), 2) the presence of a free surface (as opposed to the no-slip conditions at the bottom) and 3) the existence of hot protuberances along the floor (the topography).

Often hexagonal and asymmetric square convective cells have been observed in the literature even in circumstances where no topography was present in conditions where the first or the second factors were at play, relevant examples being the works by (Palm, 1960) and (Golubitsky, 1984) for the situation with temperature-dependent viscosity and by (Demircan and Seehafer, 2001) for the case of RB convection in layer with a free surface. In this regard it is also worth citing (Clever and Busse, 1996) , who found a pattern resembling that shown in Fig. 15b for a fluid layer delimited by solid walls both from above and from below (see Fig. 4.25 in Lappa, 2009).

Most interestingly, (Demircan and Seehafer, 2001) demonstrated by means of numerical simulations that, if stress-free conditions are considered at the horizontal boundaries in place of no-slip ones, square patterns appear in RB convection via the Skewed Varicose instability of rolls. In particular, square cells are made possible by the nonlinear interaction of modes with two different wavenumbers that are excited at the same time. These interacting modes can produce bifurcations leading to periodic alternation between a non-equilateral hexagonal

pattern and a square pattern or to different kinds of standing oscillations (Demircan and Seehafer, 2001). It is also worth recalling that this oscillatory behaviour of dynamical side swapping in square convection can also be found in Marangoni-Bénard convection (see, e.g., Ondarcuhu, 1993) and (Krmpotic et al., 1996), where it was still described as the nonlinear interaction between different critical modes). Re-examination of the present results in the light of this knowledge seems to indicate that, although the tendency to square convection is indeed present in some circumstances (the reader being referred once again to the saturated states shown in Figs, 84, 87 and 93), in general, the considered cases display the ability to give rise to more complex states or behaviours.

As indicated by the present findings, on the one hand, thermals developing in the fluid due to the presence of blocks can dramatically limit the tendency of these systems to produce disordered patterns and multiple solutions, i.e., solutions that coexist in the space of phases and are selected depending on the initial conditions. On the other hand, however, features can be produced, which would not be a solution in the classical situation with no topography. In order to clarify this second aspect, in the following, in particular, the case N=1 is considered for which, as illustrated in Sect. 4, the influence of the topography on the resulting pattern is mediated by the depth of the layer, the height of the blocks and the temperature difference (i.e. the central block displays a variable degree of success in influencing the overall dynamics depending on d, ℓ_y and ΔT, which provides a hint for the existence of interesting scaling laws).

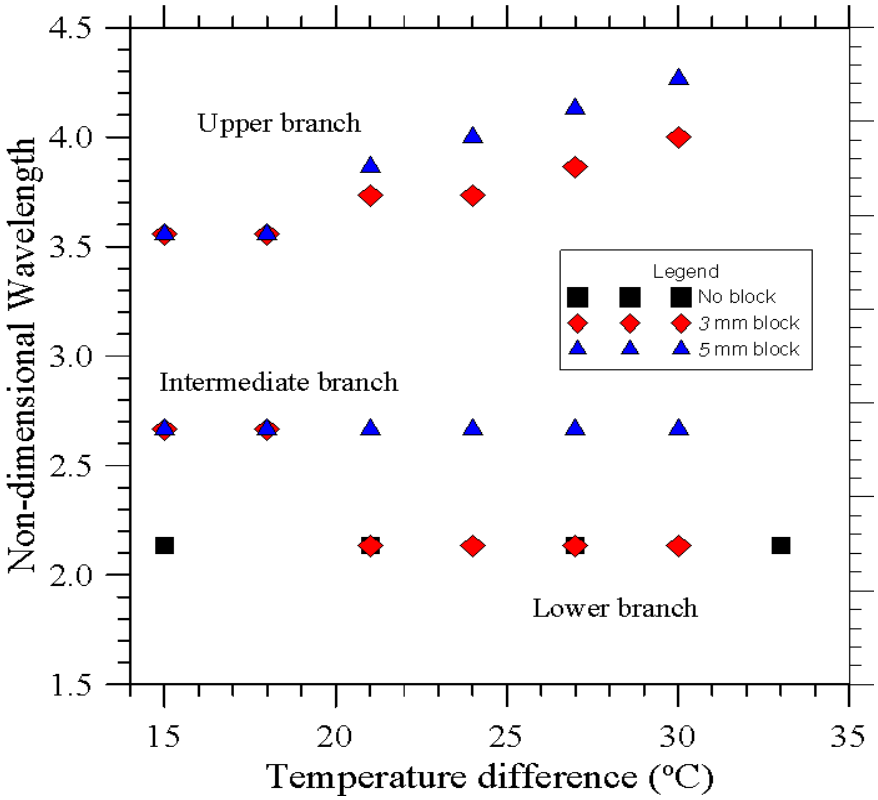

Figure 96: Wavelength as a function of the temperature difference between the bottom plate and the ambient for the layer with depth 7.5 mm ($Bo_{dyn} \cong 1.93$).

The impact of a single block on the distribution of non-dimensional wavelengths (made non-dimensional using the layer depth) is quantitatively substantiated in the next three maps obtained for d = 0.75,1 and 1.5 cm (Figs. 96, 97 and 98 for $Bo_{dyn} \cong 1.93$, 3.44 and 7.75, respectively). These figures are used to reveal the non-trivial correspondence between the topography and the pattern; in particular, multiple occurrences of the same symbol for a fixed value of the temperature difference (e.g., along the vertical direction in Fig. 96) indicate the presence of coexisting convective structures with different horizontal extension. For completeness, quantitative data about the unobstructed layer are also included (the reader being referred to the "no block" symbol).

A first key observation stemming from Fig. 96 ($Bo_{dyn} \cong 1.93$) concerns the visible similarities for the layer with and without topography. Such common features (made evident by the overlapping symbols) clearly indicate that these are inherited from the parent forms of convection (the classical RMB problem).

Comparison of the results with and without blocks, however, is also instrumental in showing that an additional branch of wavelengths (representative of another class of convective features) exists for the case with blocks (upper branch in Fig. 96). Notably, in general, an increase in the temperature difference results in larger convective structures only if this branch is considered, whereas no significant dependence of the wavelength on the temperature difference can be noticed for the lower branch.

The required explanation for the perfect horizontal orientation of the lower branch can be elaborated in its simplest form on the basis of the argument that the although the aspect ratio of the fluid domain in this case is relatively large (A=10.6), it however is not infinite (which leads to the conclusion that the system is prevented from producing continuous changes in the wavelength of the modes of convection pertaining to the parent RMB flow).

Interestingly, the presence of the blocks also allows the system to develop an 'intermediate' branch of wavelengths, which does not exist in the case with no topography. The use of different colours in this figure is also instrumental in revealing that a net distinction exists between the wavelength for blocks with 3 and 5 mm (upper branch). This implies that the anisotropy introduced by the central block, not only leads to the emergence of a new branch of localized states, but it also cause some readjustments in the general ability of the system to produce other localized convective features (thereby providing a justification for the different extension of the intermediate branch for different vertical size of the block).

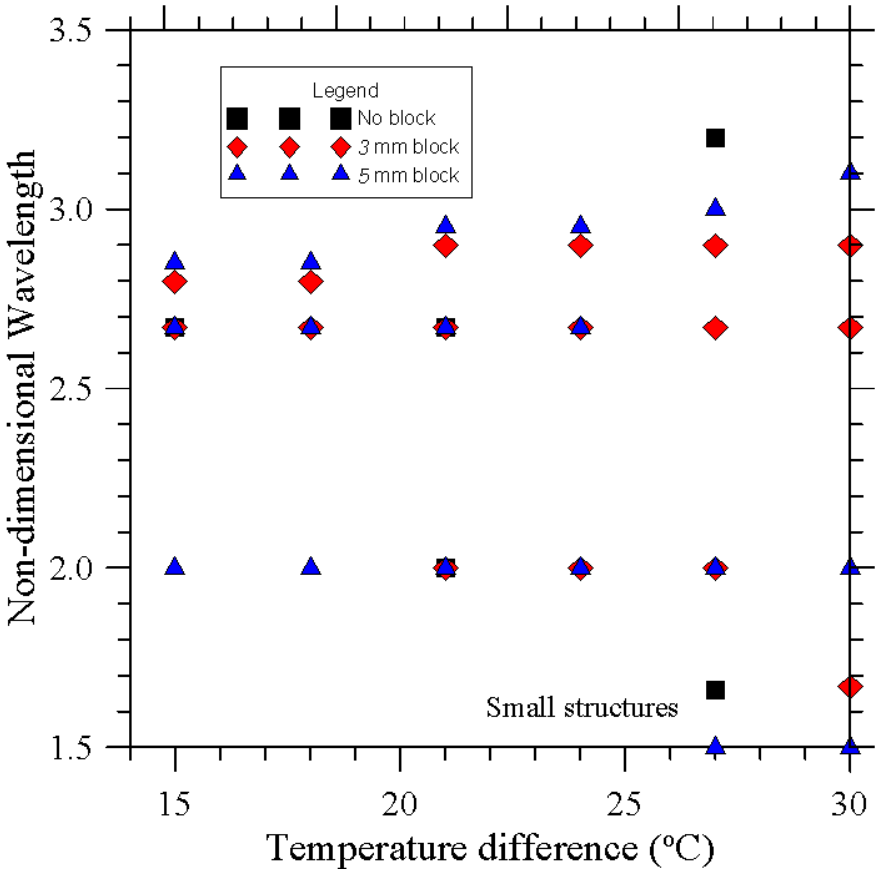

Figure 97: Wavelength as a function of the temperature difference between the bottom plate and the ambient for the layer with depth 10 mm (Bodyn≅3.44).

At first glance, when the depth of the layer is increased to 1 cm (Fig. 97, Bo_{dyn}≅3.44), the results obtained for blocks having a height of 5 mm and 3 mm are relatively close one another. Moreover, the (vertical) distance of the upper branch accounting for the presence of the central convective structure from the other branches becomes smaller. On a separate note, it is also worth highlighting that, on increasing the ΔT, the central spot displays a tendency to grow whereas the structures produced by standard RMB convection become smaller for $\Delta T \geq 27$°C (the shrinkage being even more evident for the 5 m block case).

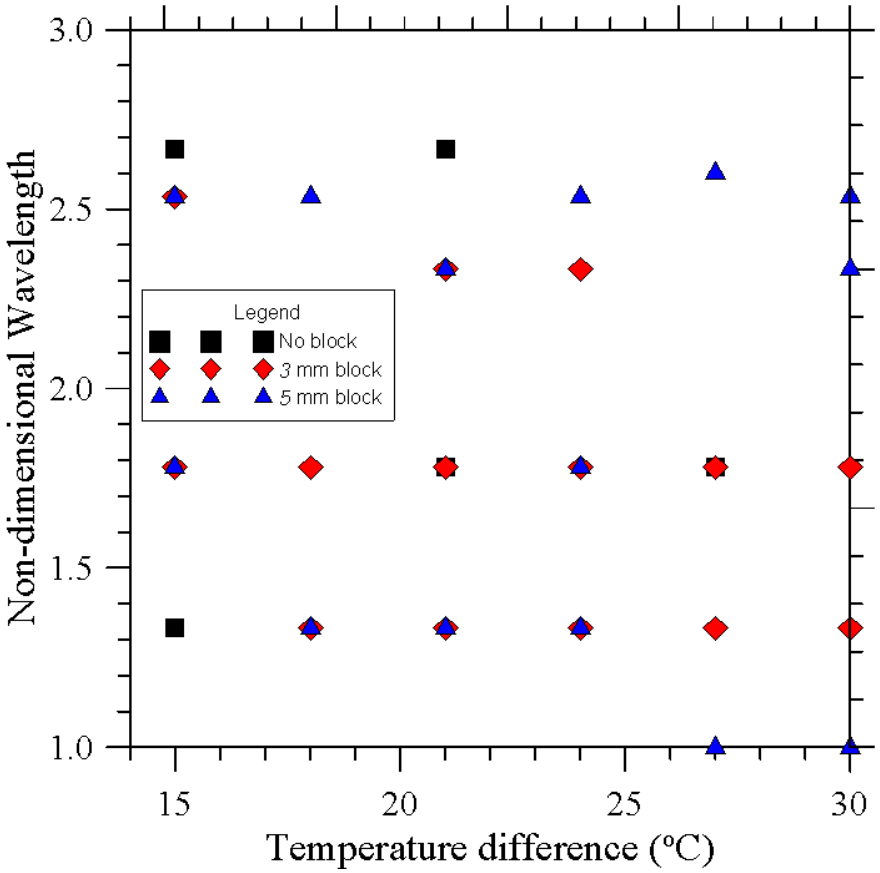

Figure 98: Wavelength as a function of the temperature difference between the bottom plate and the ambient for the layer with depth 15 mm ($Bo_{dyn}\cong 7.75$).

As the layer depth is increased to 1.5 cm (Fig. 98, $Bo_{dyn}\cong 7.75$), the branch related to the spot above the single central block is no longer present. The ability of the block to influence the overall flow is relatively limited as also witnessed by the overlap of wavelengths obtained for the cases 3 mm and 5 mm. Relatively small structures appear only for $\Delta T \geq 27$°C in the case 5mm.

As already discussed to a certain extent in Sect. 8.4, this variety of coexisting wavelengths tends to be mitigated as N is increased, until the convective features generated by the block becomes so dominant that they prevent the system from adapting to changes in the depth of the layer and/or height of the blocks, which explains why figures equivalent to Figs. 96-98 have not been produced in the present work for N=2 and N=3.

Additional insights finally stem from comparison with Chapter 7 from which it can be inferred that consideration of a fluid with variable (temperature-dependent) physical properties can promote the emergence of self-organized states such as those shown in Figs. 53,56,59 and 60 for smaller values of the parameter N. As a concluding remark, it should also be highlighted that, as in Chapter 7, time-dependent states (localized oscillations) have also occasionally been detected in the present chapter (e.g., for ΔT larger than $\cong 27$ °C and $\cong 21$ °C in the 7.5 mm and 10 mm depth cases, respectively). Although, the threshold is slightly dependent on the presence

of blocks, however only minor variations have been found in terms of patterning behaviour (consisting of minor modulations in the shape and size of the spots due to localized 'vibrating' spokes), which explains why this chapter has essentially dealt with 'spatial' rather than temporal aspects.

8.8 Conclusions

Complex patterns typical of canonical forms of convection such as MB and RB arise spontaneously as a result of the amplification (and ensuing saturation) of certain categories of disturbances which are selected out of the full spectrum of possible perturbations because of the symmetry that they satisfy and the isotropy and/or multidirectional translational invariance of the system where they are amplified. In contrast, as revealed by the present chapter, somehow 'engineered' patterns can be produced through the introduction of a given topography in the system. This can help to meet the desired objective through a two-fold influential process, namely, first (passive control) by limiting the accessibility of the flow to certain regions of the physical domain (breaking the in-plane isotropy of the fluid layer), second (active control) through the buoyancy-induced generation of thermals, which, by acting as 'pillars' can force the pattern to develop nodes with relatively high topological order at fixed points, just like atoms positioned at lattice points in a crystal.

The system response to a change in the topography (N) is mediated by a number of factors, including, the depth of the layer, the height of blocks, the temperature difference and the layer aspect ratio. By following a structured modus operandi aimed to unravel some specific interwoven aspects, in this chapter it has been shown that for N=1, features of the abovementioned classical forms of convection can still be clearly identified. For small and intermediate depths of the layer, these features correspond to the branches visible in the lower part of the figures (maps) providing the distribution of wavelength as a function of the temperature difference. In turn, the horizontal orientation of such branches indicates that, for the conditions considered in the present work, i.e. A=O(10), the layer is not sufficiently extended in the horizontal direction to allow a continuous variation of the wavelength with ΔT (in other words, the size of the emerging convective structures represented by these branches is dictated essentially by the aspect ratio of the layer).

The anisotropy introduced by the blocks leads to the emergence of another branch and some related re-adjustments in the other branches. The related ability of the wavelength to scale with the ΔT may be regarded as evidence of the different nature of this convective feature, which is not constrained to obey the rules of standard RMB convection and represents a clear departure from convection in isotropic layers (it clearly draws from fluid motion originating from the hot vertical walls of the block, which allows it to escape the abovementioned rules).

On increasing the layer depth, as expected, the pattern-forming mechanism is transferred back to the parent form of convection. Remarkably, however, an increase in N has the opposite effect, i.e., the system gradually evolves towards topography-controlled solutions, whereas the properties of the parent forms of convection tend to be suppressed in favour of more system specific ones.

For all the conditions considered in the present chapter, indeed, as N is increased from 1 to 2 the convective features induced by the blocks become dominant with respect to those of the parent RMB convection in unobstructed layers regardless of the depth of the layer. Moreover, as already explained before, the thermal plumes generated above blocks act as pillars stabilizing the flow and reducing dramatically the set of allowed wavelengths until a single possible wavelength corresponding to $L/3$, i.e. a trivial state is obtained for N=3 over a wide range of conditions.

A tendency opposing the emergence of such saturated states is represented by the ability of the planform to develop localized features, which can increase locally the topological order of certain knots and cause a breakdown in its symmetry, especially if a relatively small layer depth is considered.

Chapter#9: Patterning behavior of hybrid buoyancy-Marangoni Convection in inclined layers heated from below

Alongside the interesting effects driven by gravity or surface tension in non-isothermal fluids when blocks are installed on the bottom wall, other exotic (poorly known) modes of convection can be enabled in a fluid layer when its container is inclined to the horizontal direction. Exotic modes of convection can be excited in these circumstances even if no blocks are present, i.e. the fluid layer is delimited from below by a hot plate and unbounded from above For the sake of completeness, this specific problem is considered in the present chapter.

Apart from the fundamental importance that it has in the general kingdom of thermal convection, which naturally makes it a fundamental topic of interest to fluid physicists and other scholars, additional factors which make this problem a subject worthy of analysis are the various areas of applications it is somehow connected to. A first example is related to the field of crystals (growth from melt) where crystals of different materials are used for advanced electronic devices and typically produced through different processes (melting and re-solidification of polycrystalline materials) performed in well-known conditions. It is known that even tilt angles as small as 0.5° can cause uncontrolled non-axisymmetric growth conditions in such processes and related detrimental effects (Markham and Rosenberger, 1984; Bachran et al., 1998; Mizev and Schwabe, 2009).

Similar examples are related to the solidification of metal alloys, where inclination-induced shear flow can lead to serious morphological instabilities. In 2006 Forth and Wheeler investigated coupled convective and morphological instabilities in a simple model of the solidification of a binary alloy, which also includes shear flow mechanism (Forth and Wheeler, 2006). Another relevant case is represented by phase change materials which are typically used in ‘energy-saving’ applications. These substances actually store energy during melting process and release it during solidification and can support during these repeated cycles of solid/liquid transition which corresponds to emergence of both buoyancy and surface-tension driven convection (Lappa, 2018).

The configuration considered in this chapter is intended to mimic situations such as those occurring in the abovementioned technological applications and provide general insights into the dynamics of variable-depth systems supporting both buoyant and Marangoni effects. Such a configuration is shown in Fig. 99. In this case the closeness of free surface to the heated bottom in the areas where the depth of the fluid layer is smaller, is responsible for the emergence of a temperature inhomogeneity at the interface, thereby giving rise to fluid convection directly driven by the Marangoni effect. Fluid motion is also supported by buoyancy effects. Due to the inclination of the fluid layer, the horizontal component of gravity

can cause relatively warm fluid to flow up along the bottom wall (from left to right in Fig. 99) and in the opposite direction along the free interface.

The magnitude ratio of buoyant and surface-tension-driven effects can be varied by changing the overall amount of fluid, i.e., its average depth. The larger the depth, the higher the relative importance of gravitational effects in comparison to surface tension ones. The most important implication of this observation is that relevant links also exist between this problem and a series of problems of meteorological, oceanographic, and geophysical interest (see, e.g., Lipps, 1971 and Thorpe, 1987 for the atmosphere; Farrow and Patterson, 1993 for the hydrosphere and Richter, 1973 for analogous considerations about the mantle of our planet).

It is also worth noting that, from a purely theoretical standpoint, the considered problem may be regarded as a specific realization of a more general category of phenomena where a 'shear flow' breaks the in-plane isotropy of the system (see, e.g., Weber, 1978). This effect can cause a deviation from the known dynamics of out-of-equilibrium systems, which are invariant with respect to translations in a direction parallel to the bottom boundary such as the canonical Rayleigh-Bénard and Marangoni-Bénard flows.

In previous studies, former author considered fluid domains with uniform thickness and tilted with respect to the horizontal direction. In those cases, isotropy was lost due to the mismatch in the symmetry of the boundary conditions in relation to the applied body force (gravity). From all previous studies in last two decades, it can be concluded that depending on the inclination, the considered fluid, the size of the system and the applied temperature difference, many complexities and a rich variety of flow phenomena can take place. In addition, the emerging (gravitational) modes of convection in tilted enclosures can be broadly categorized into two groups: namely, transverse rolls and longitudinal rolls (LR).

Based on existing literature on these subjects, it becomes also evident that in comparison to gravitational convection, studies on systems driven by surface-tension-driven effects where the isotropy of the classical heated-from-below configuration is broken, are much rarer and sparse. However, some interesting efforts exist for the case where the isotropy-breaking shear flow has been obtained by inclining the temperature gradient with respect to the liquid-gas interface rather than by inclining the layer itself. In that case, the temperature gradient results from the combination of heating from below and horizontal differential heating.

As an example, after the problem's initial popularization by (Nepomnyashchy et al. 2001) and (Ueno et al. 2002), additional insights into these specific situations have been provided by Shklyaev and Nepomnyashchy, 2004), (Mizev and Schwabe, 2009) and (Patne et al. 2020). These studies showed that despite the shift in the driving force from buoyancy to Marangoni effects, the duality in terms of transverse and longitudinal modes of convection still holds in these cases.

As shown in Fig. 99, the bottom of the cavity considered in this chapter has a constant temperature higher than that of the external gaseous environment (air) while the lateral walls are thermally insulated. The inclination of the container causes the liquid to redistribute its volume in such a way that its surface remains perfectly horizontal with respect to an external observer. In other words, on tilting the system at different angles, the liquid-gas interface will adjust its orientation in order to remain perpendicular to the gravity. In this regard, it should be briefly recalled that the lack of horizontal translational invariance (due to the inclination of the heated bottom wall such as in classical studies on inclined thermal convection) is reinforced in this case by the asymmetry produced in the geometry by its spatially varying depth, i.e., the system would not be isotropic even by replacing gravity with a force perfectly perpendicular to the bottom wall. Remarkably, this is the hallmark of the present configuration, that is, the major factor expected to expand the set of possible solutions with respect to those identified in earlier chapters.

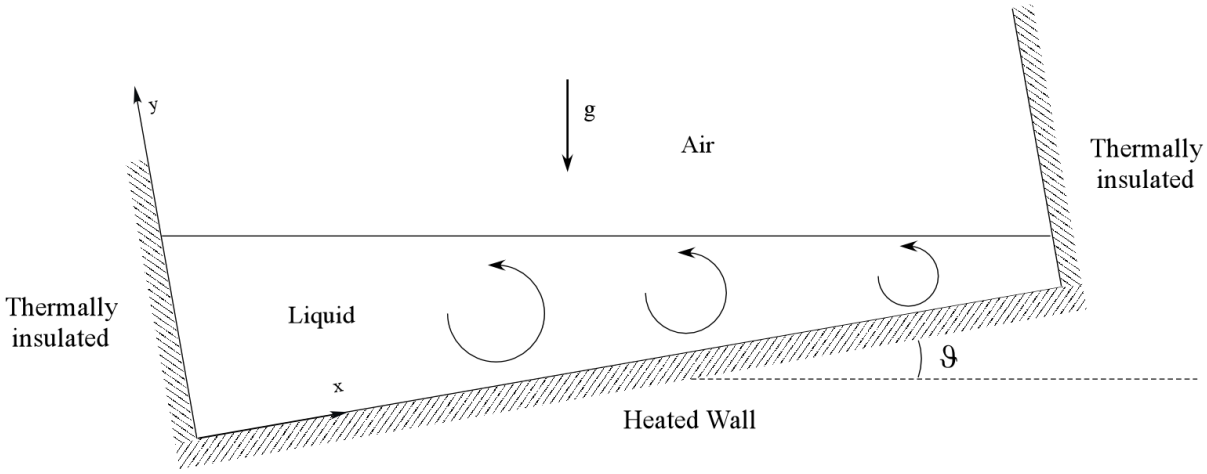

Figure 99: Sketch of the considered system.

Fig 100 shows the sketches of the containers effectively used for the experiments. While one container has the square symmetry and characteristic internal size 8 cm (Fig. 100a, already presented in Chapter 5), the other has the cylindrical symmetry and an internal diameter of 13.3 cm (Fig. 100b). While conducting experiments, the same conditions (same liquid depth, temperature of the bottom plate and overall system inclination) were applied to both containers in order to discern the role played in the considered dynamics (if any) by the solid lateral wall

and the aspect ratio of the fluid domain. The physical properties of the liquid used for the experiments (Emkarate RL22H oil) have already been provided in Chapter 8 (See Figs. 80).

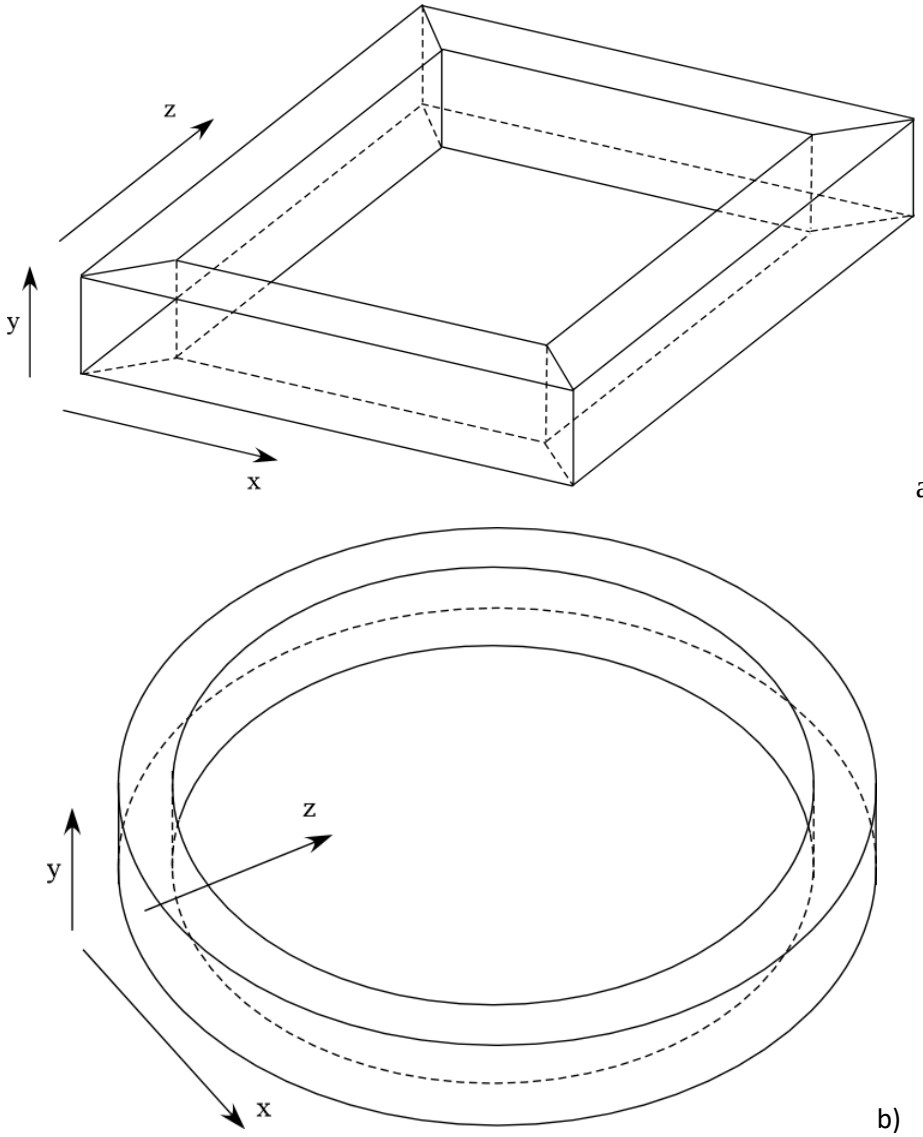

Figure 100: Three-dimensional sketch of the fluid container delimited by sidewalls of Perspex: a) square container, b) cylindrical container.

Introducing the average (or "equivalent") depth of the layer (d) as ratio between the effective volume (Ω) of liquid present in the container and the area of the container base (corresponding to constant depth of the fluid when no tilt is applied), the classical Rayleigh and Marangoni numbers can be re-defined as:

$$Ra=g\beta_T\Delta T d^3/\nu_0\alpha_0 \qquad (21)$$

$$Ma=\sigma_T \Delta T d/\mu_0\alpha_0 \quad (22)$$

where ΔT accounts for a representative temperature difference, namely, the difference between the temperature of the bottom plate (T_{plate}) and that of the ambient (T_{air}), i.e. $\Delta T = T_{plate} - T_{air}$, (this temperature difference, much higher than that effective through the liquid, is used for practical purposes as the temperature of the free liquid-gas interface is not known a priori and behaves as a spatially varying quantity in the presence of convection); moreover, g and β_T are the gravity acceleration and the thermal expansion coefficient, 9.81 ms^{-2} and $\cong 7.7x10^{-4}$ K^{-1} of the considered fluid, respectively; σ_T is the surface tension derivative coefficient ($\cong$0.218 $mNm^{-1}K^{-1}$ for the considered fluid, see Fig. 80). The subscript "0" refers to a reference temperature, which in the present thesis, for simplicity and without loss of generality, is assumed to be the temperature T_0 of the environment (i.e., T_{air}). As already discussed in Chapter 3, these two characteristic numbers can be further combined into a third non-dimensional group, generally known as the dynamic Bond number:

$$Bo_{dyn}=Ra/Ma=\rho g \beta_T d^2/\sigma_T \quad (23)$$

Although this should be regarded as a 'derived' parameter, the convenience in using it stems from its independence from the temperature difference and the immediate information it provides on the relative importance of buoyancy and surface-tension driven effects.

9.1 Canonical states of thermal convection in the horizontal case

Following a logical approach, first the simplest case is considered, i.e., the perfectly horizontal configuration (ϑ=0°) for which convection is expected to emerge in the form of rolls or hexagonal cells according to whether buoyancy or surface-tension effects are dominant, respectively (Rayleigh-Marangoni-Bénard convection). In this regard the first set of figures, collected in Fig. 101 for the case with constant liquid depth 0.5 cm, is instructive as these figures show that the pattern-less state visible in the first panel (Fig. 101a) is taken over by a recognizable distribution of rolls and localized convective cells as soon as the critical threshold for the onset of convection is exceeded (Fig. 101b-d).

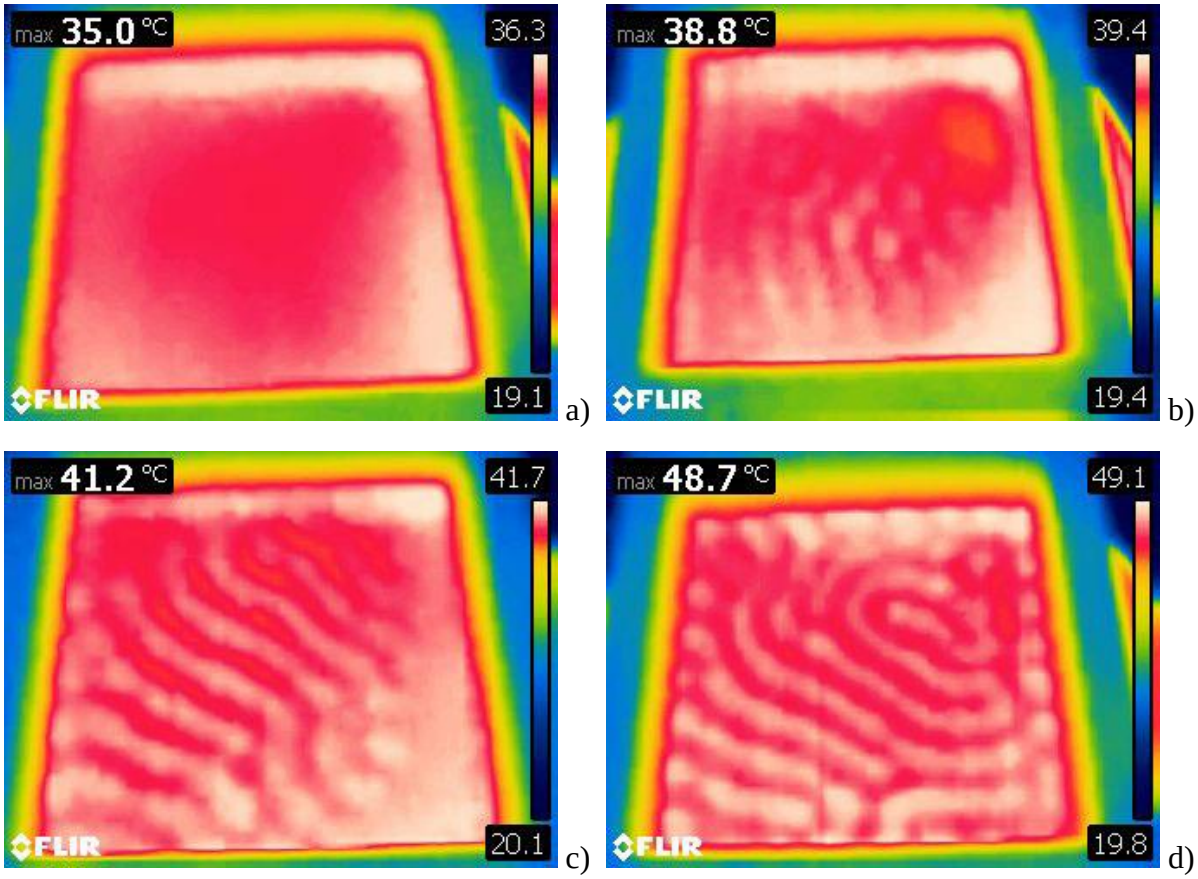

Figure 101: Surface temperature distribution for d=0.50 cm (Ω = 32 ml) and no inclination (A=16, Bo_{dyn}≅0.86, Ra≅2.5x10^{2}xΔT, Ma≅2.94x10^{2}xΔT): a) ΔT=13°C, b) ΔT=18°C, c) ΔT=21°C, d) ΔT=27°C.

These are made evident by the rising (descending) currents of hot (cold) fluid as localized spots or strips with temperature higher (smaller) than the surrounding fluid.

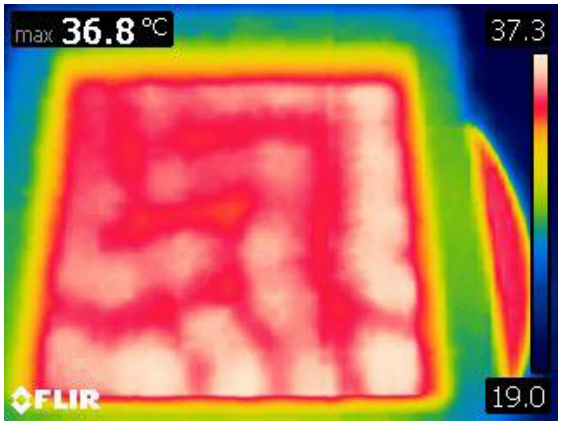

a)
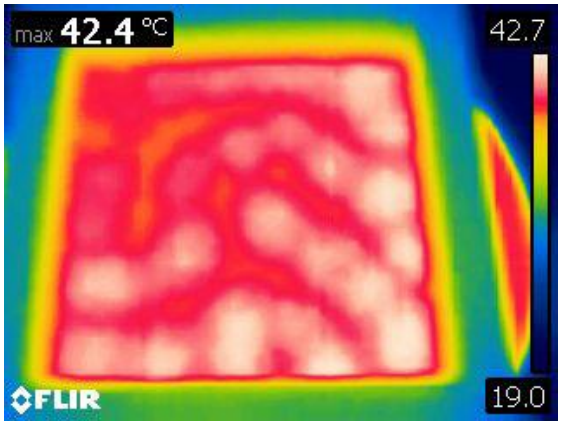

b)
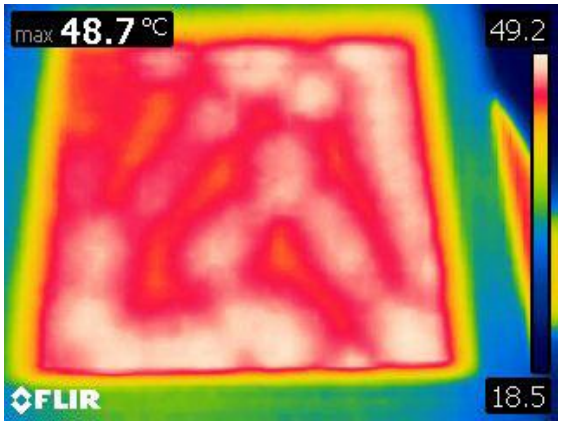

c)
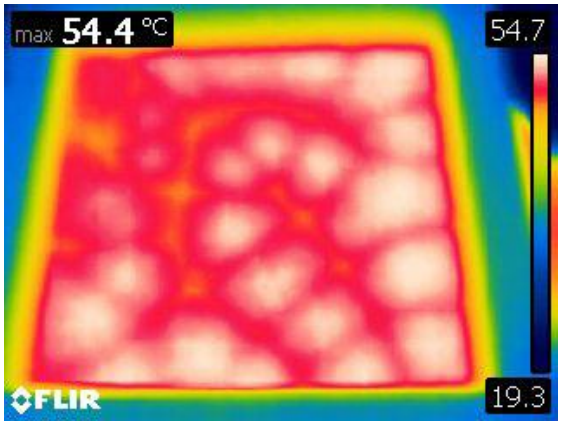

d)

Figure 102: Surface temperature distribution for d=0.75 cm (Ω = 48 ml) (A=10.6, $Bo_{dyn}\cong$1.94, $Ra\cong 8.6\text{x}10^2\text{x}\Delta T$, $\text{Ma}\cong 4.4\text{x}10^2\text{x}\Delta T$): a) ΔT=15°C, b) ΔT=21°C, c) ΔT=27°C, d) ΔT=33°C.

On increasing the depth of the layer, as expected the horizontal extension of the convective features grows accordingly (compare, e.g., each panel of Fig. 102 with the corresponding one in Fig. 101). Another key observation stemming from Fig. 102 concerns the complexity of the pattern and the number of convective features, which in qualitative agreement with other results in the literature, keep increasing with the ΔT, i.e., it grows with the distance from the critical conditions.

9.2 Convection in inclined square layer

The simplest way to undertake a discussion of the situation where the layer is inclined to the horizontal is to start from the major remark that, unlike the canonical case considered in Sect. 4.1, for $\vartheta\neq$zero the basic state is not in quiescent conditions. Rather it consists of a symmetry-breaking shear flow induced by the horizontal component of the temperature gradient (see the related discussion in the introduction).

Following up on the previous point, Fig. 103 provides a first glimpse of the patterning behavior in such conditions when $\vartheta \cong 3.5°$.

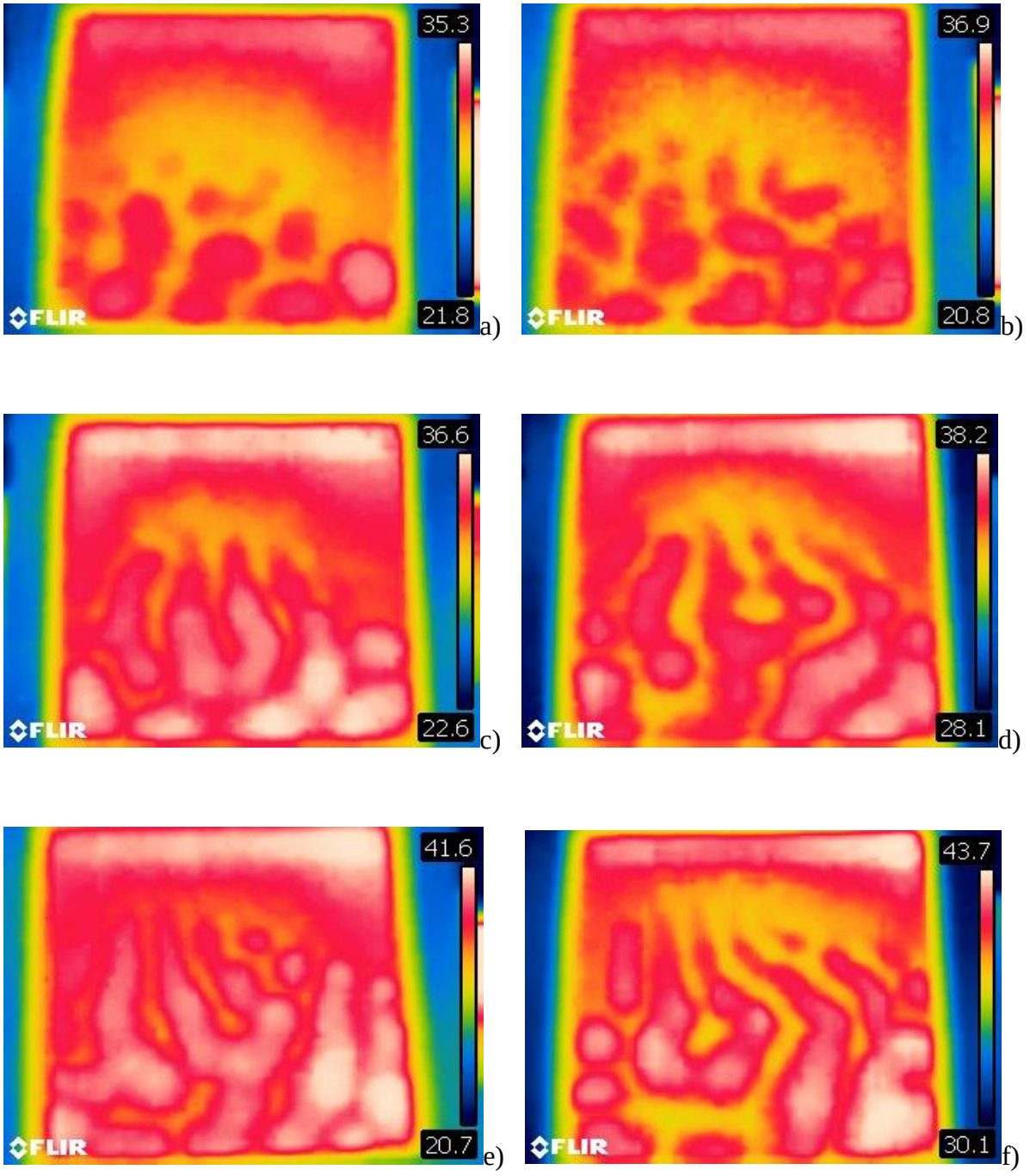

Figure 103: Surface temperature distribution for d=0.50 cm (Ω = 32 ml) and $\vartheta \cong 3.5°$ (A=16, $Bo_{dyn} \cong 0.86$, $Ra \cong 2.5 \times 10^2 \times \Delta T$, $Ma \cong 2.94 \times 10^2 \times \Delta T$): a) ΔT=15°C, b) ΔT=18°C, c) ΔT=21°C, d) ΔT=24°C, e) ΔT=27°C, f) ΔT=30°C.

The significance of this figure primarily resides in its ability to make evident that the inclination leads to two remarkable effects. The first concerns the hybrid (spatial) nature of the visible pattern. In place of the scattered distribution of spots occupying all the available space in Fig. 101, the surface temperature exhibits in this case an almost feature-free region localized in the part of the physical domain where the depth of the layer is smaller.

Moreover, the random distribution of rolls (in terms of direction in the xz plane) seen in the constant-depth case is taken over by a much more ordered arrangement where the convective features display a tendency to align with the z axis (the vertical direction in the figures, see, e.g., Fig. 103c).

Notably, although these may immediately be classified as 'longitudinal rolls' (their axes being parallel to the tilt direction), their specific spatial configuration bares characteristic ingredients, which also need to be pinpointed suitably here. Their cross-extension, i.e., the typical size in a direction perpendicular to the roll axis undergoes remarkable variations along the z (tilt) direction, which indicates that the dimensional wavelength *is not constant* in the physical domain (these behaviors being quantitatively substantiated in Fig. 104, where this quantity has been plotted as a function of the z coordinate for a representative ΔT). Moreover, as the ΔT is increased, some other interesting changes show up. The length of the rolls along the z direction grows (compare, e.g., Fig. 103a and 103f, the reader being also referred to the data reported in Fig. 105).

Superimposed on these trends, most interestingly, in some cases, in place of the striped pattern, which one would expect in the ideal situations of parallel longitudinal rolls, tree-like shapes can be distinguished in the surface temperature distribution. These give an external observed the illusion of a roll with a fork-like structure (two strips originating from a single initial strip, see, e.g., Figs. 103d-f)). Regarding wavelength measurements, in first step the images were digitized using a Matlab based software. Using this software, the surface temperature distribution acquired using the thermographic camera was turned in to a matrix of values. This matrix then further processed to extract information about the pattern wavelength along different directions. The wavelength along a given direction is usually determined by taking the distance between two adjoining peans or valleys and dividing it by the depth of the liquid layer. This software can also be used to extract the profile of temperature along a given direction.

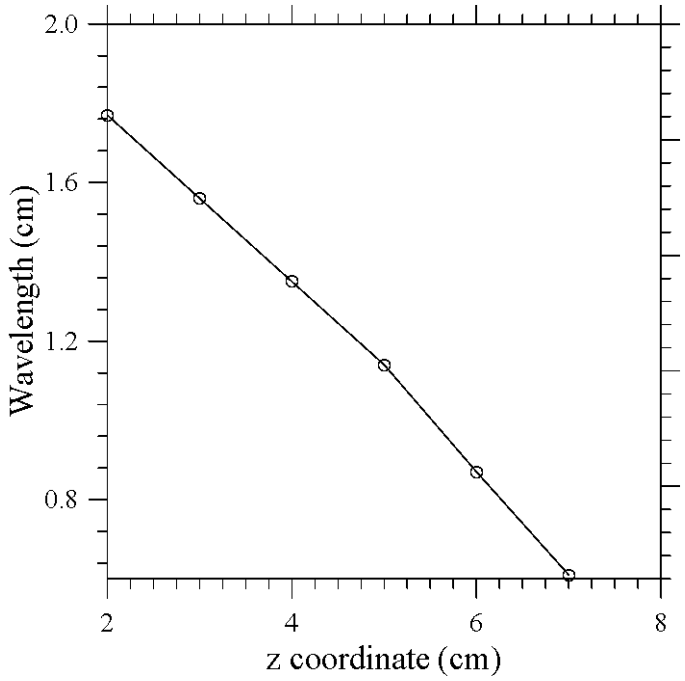

Figure 104: Transverse roll extension as a function of the longitudinal direction z for ΔT = 27°C (square container, A=16, d = 0.50 cm, Bo_{dyn}≅0.86, $\vartheta \cong 3.5°$).

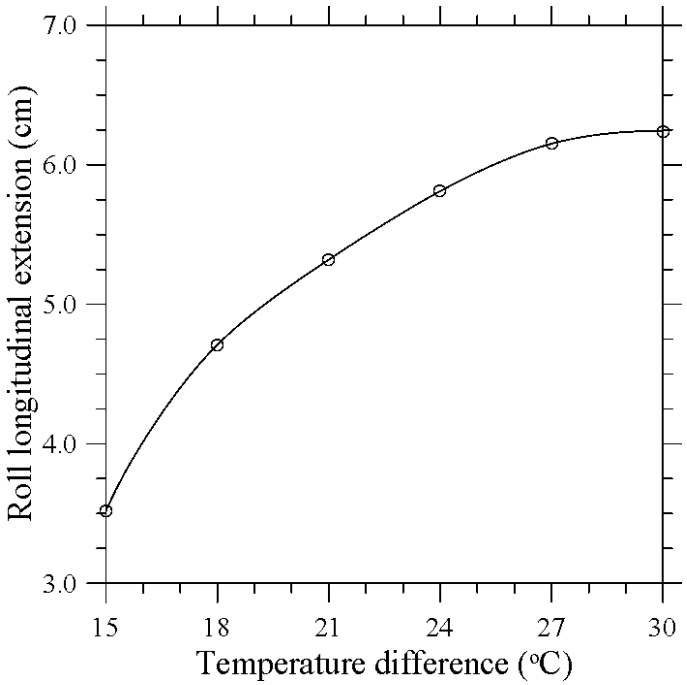

Figure 105: Longitudinal extension of the rolls as a function of ΔT (square container, A=16, d = 0.50 cm, Bo_{dyn}≅0.86, $\vartheta \cong 3.5°$).

Given the complexity of such phenomena, which seem to escape a possible simple definition or classification within the framework of the past lines of research (still retaining, however, some affinities with the typical features and salient ingredients pertaining to such categories), in the following, a peculiar modeling and analysis hierarchy is implemented in order to 'filter out' already known facts and concentrate selectively on new mechanisms. More specifically, this modus operandi is based on the step-by-step variation of the distinct (independent) parameters controlling the various degrees of freedom of the considered system, these being the characteristic temperature ΔT (whose effects have already been outlined before), the tilt angle ϑ, the volume of liquid and the shape and aspect ratio of the considered container. While the effect of the ΔT has already been outlined before (see gain Fig. 105), the overall volume of liquid is expected to influence the dynamics through related value of the dynamic Bond number based on the average depth of the liquid, which accounts for the relative importance of buoyancy and surface-tension driven effects. Similarly, the shape and aspect ratio of the considered container may influence the pattern selection mechanism through confinement and other geometrical effects

As a first step of this analysis hierarchy, a larger value of the inclination angle is considered for the same conditions of Fig. 103 (same volume of liquid and set of temperature differences).

As immediately made evident by Fig. 106, an increase in ϑ can produce a mitigation of the aforementioned roll pinching mechanism (by which a single longitudinal roll can be split into two neighboring rolls with smaller wavelength). A slightly larger values of ϑ has also another remarkable consequence; on average, it causes a small (non-negligible) growth of the transverse extension of the rolls (this effect will be clarified later in this chapter).

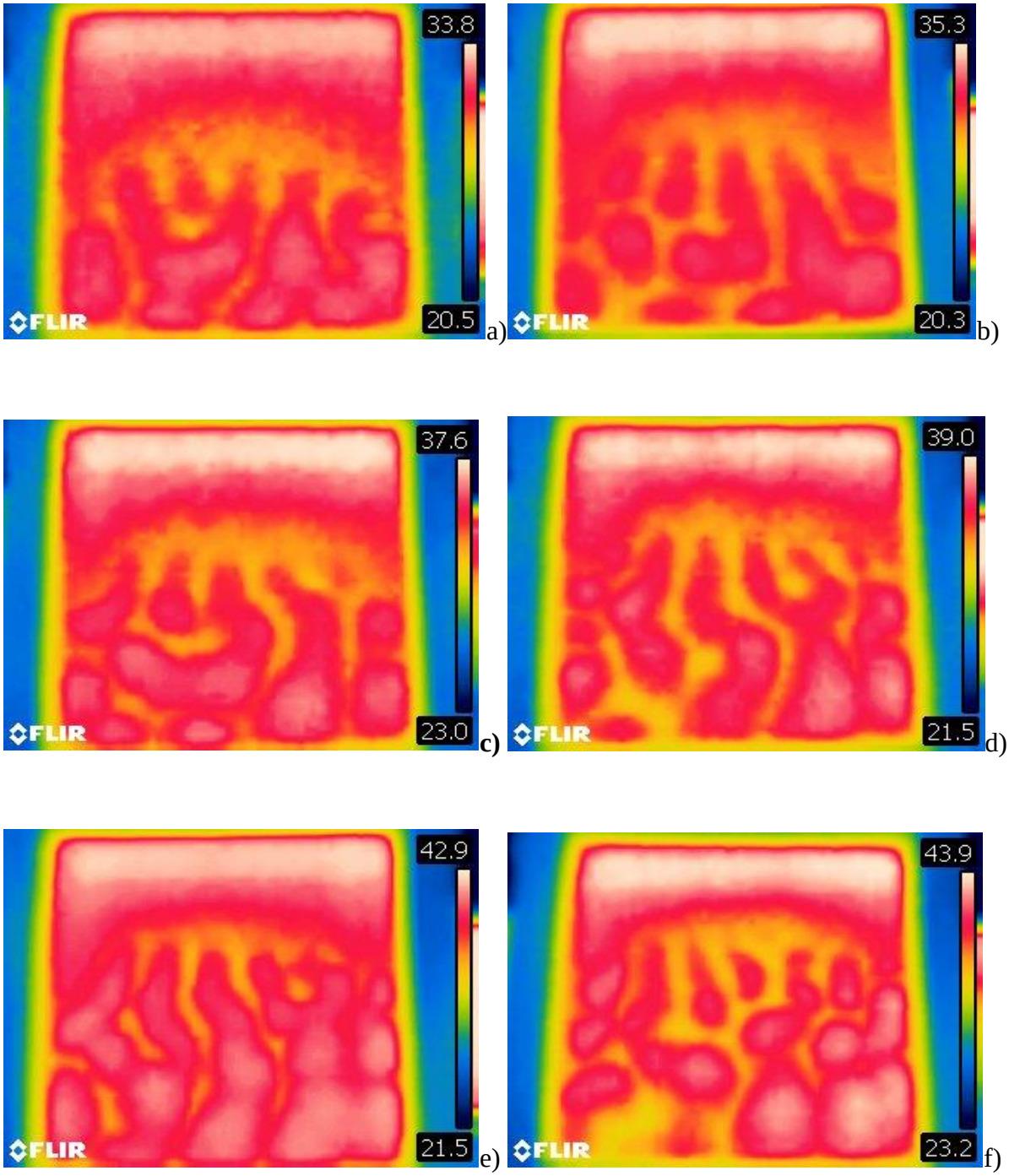

Figure 106: Surface temperature distribution for d=0.50 cm (Ω = 32 ml) and $\vartheta \cong 5°$ (A=16, Bo_{dyn}≅0.86, Ra≅2.5x10^{2}xΔT, Ma≅2.94x10^{2}xΔT): a) ΔT=15°C, b) ΔT=18°C, c) ΔT=21°C, d) ΔT=24°C, e) ΔT=27°C, f) ΔT=30°C.

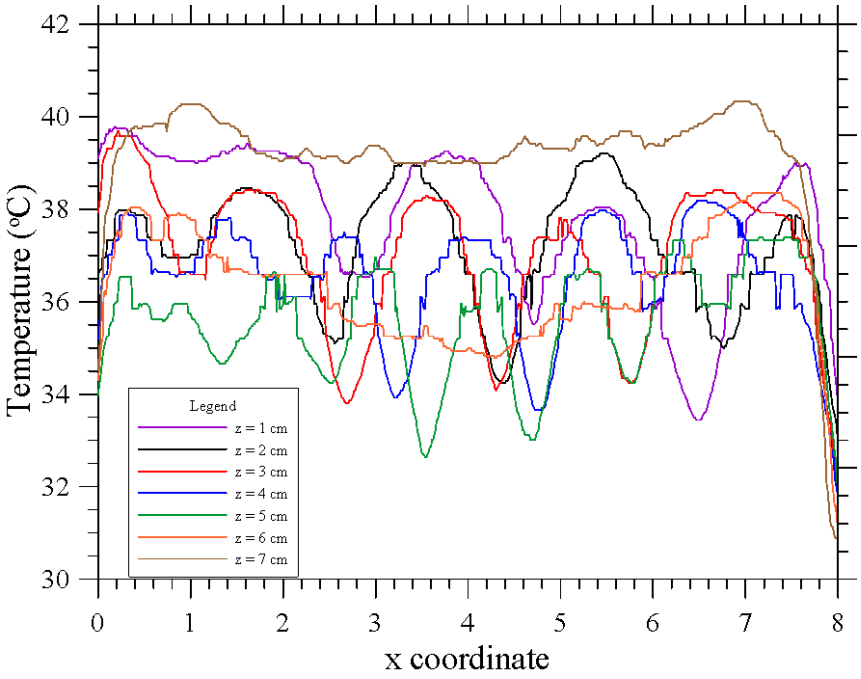

Figure 107: Profiles of temperature at different stations along the longitudinal direction z (square container, A=16, d = 0.50 cm, Bo_{dyn}≅0.86, ΔT = 27°C, $\vartheta \cong 5°$).

The reduced tendency of the system to support roll pinching mechanism is qualitatively substantiated in Fig. 107. On closer inspection, indeed, this figure reveals that the number of peaks visible at each station z remains almost constant throughout the longitudinal extension of the domain (until no well-defined peaks can be seen as a certain limiting value of z is exceeded, which corresponds to the transition from the patterned to the spot-free region).

Towards the end of getting a better grasp on how all these dynamics are affected by the depth of the layer, the next set of figures refers to the case where the average depth of the liquid is 0.75 cm (see Fig. 108, yet for $\vartheta \cong 5°$). Along these lines, taken together Fig. 108 and Fig. 106 are instrumental in showing that an increase in the relative importance of buoyancy forces with respect to surface-tension driven effects (as witnessed by the related rise in the dynamic Bond number) can help to make the roll-pinching mechanism even less frequent in favor of a more regular (parallel) distribution of longitudinal rolls. As even a fleeting glimpse into Fig. 108 would immediately reveal, in fact, the patterned surface now corresponds to the entire free liquid-gas interface of the fluid layer, i.e., no cell-free area can be identified in this case (a kind of "saturated state" is attained in terms of roll extension along the tilt direction z).

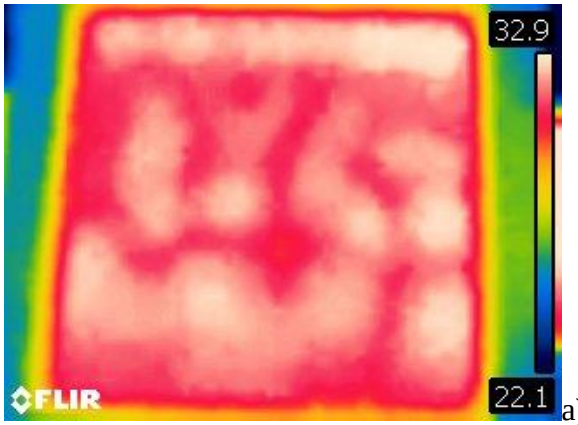

a)
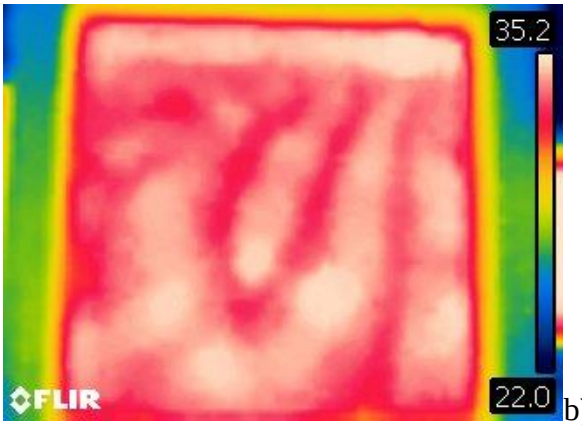

b)
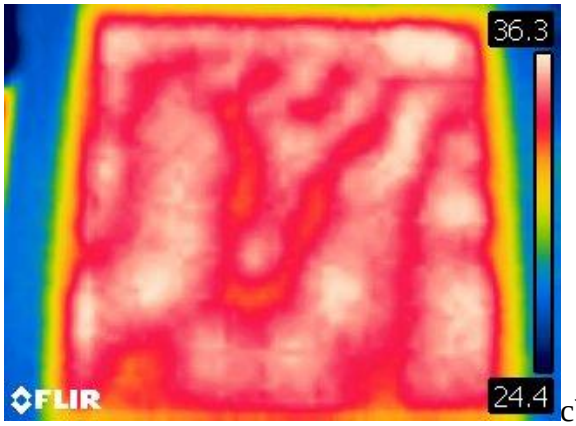

c)
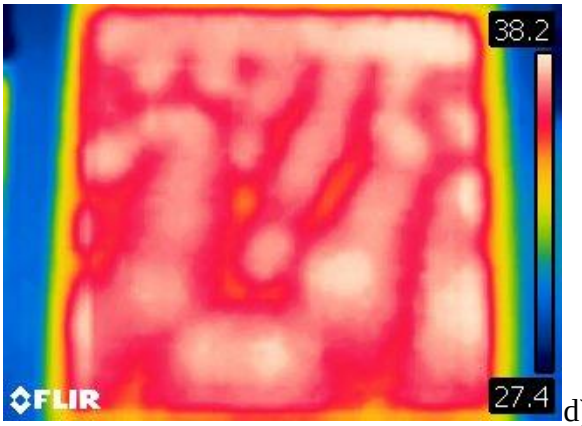

d)
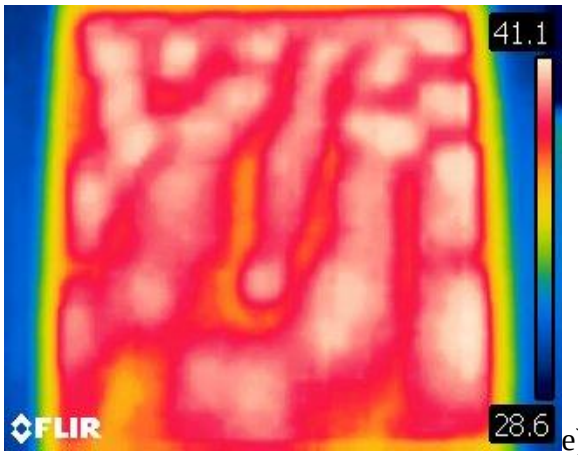

e)
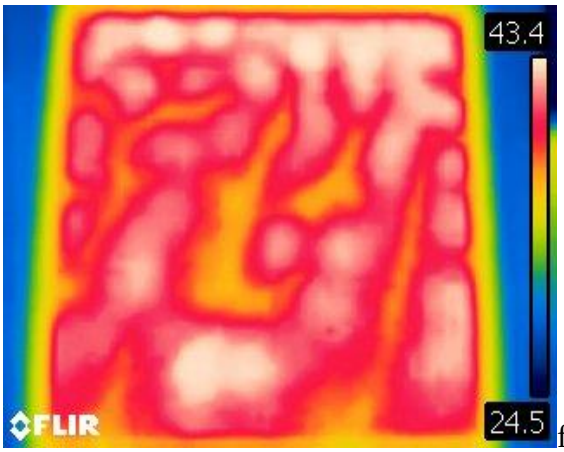

f)

Figure 108: Surface temperature distribution for d=0.75 cm (Ω = 48 ml) and $\vartheta \cong 5°$ (A=10.6, $Bo_{dyn} \cong 1.94$, $Ra \cong 8.6 \times 10^2 \times \Delta T$, $Ma \cong 4.4 \times 10^2 \times \Delta T$) a) ΔT=15°C, b) ΔT=18°C, c) ΔT=21°C, d) ΔT=24°C, e) ΔT=27°C, f) ΔT=30°C.

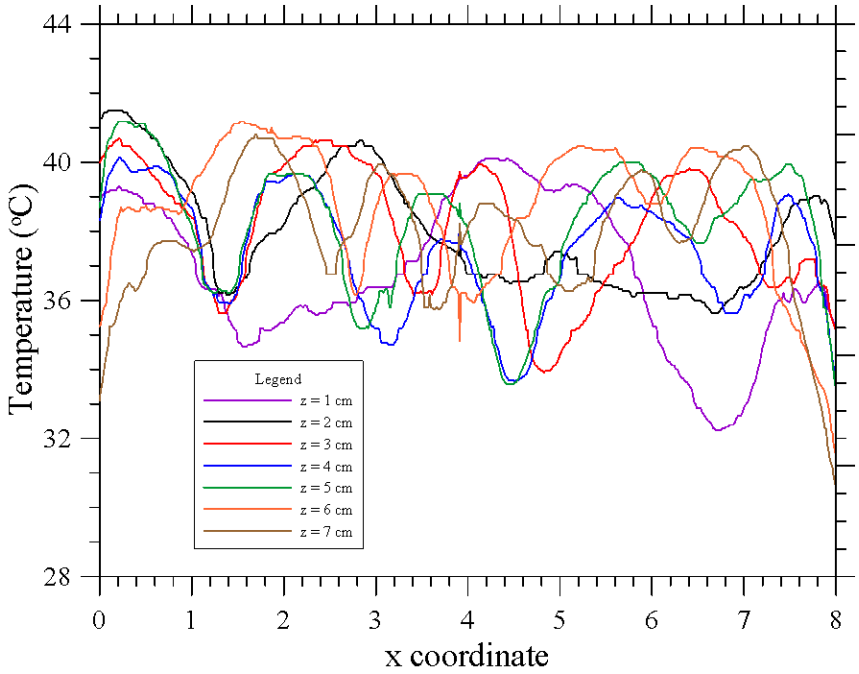

Figure 109: Profiles of temperature at different stations along the longitudinal direction z (square container, A=10.6, d = 0.75 cm, Bo_{dyn}≅1.94, ΔT = 27°C, $\vartheta \cong 5°$).

Additional insights follow naturally from a cross-comparison of Fig. 109 and 107. It can be seen that the number of rolls sitting in the cavity is reduced in the d=0.75 cm case (as clearly demonstrated by the smaller number of recognizable peaks at any given station in comparison to the equivalent ones visible in Fig. 107 for d=0.5 cm).

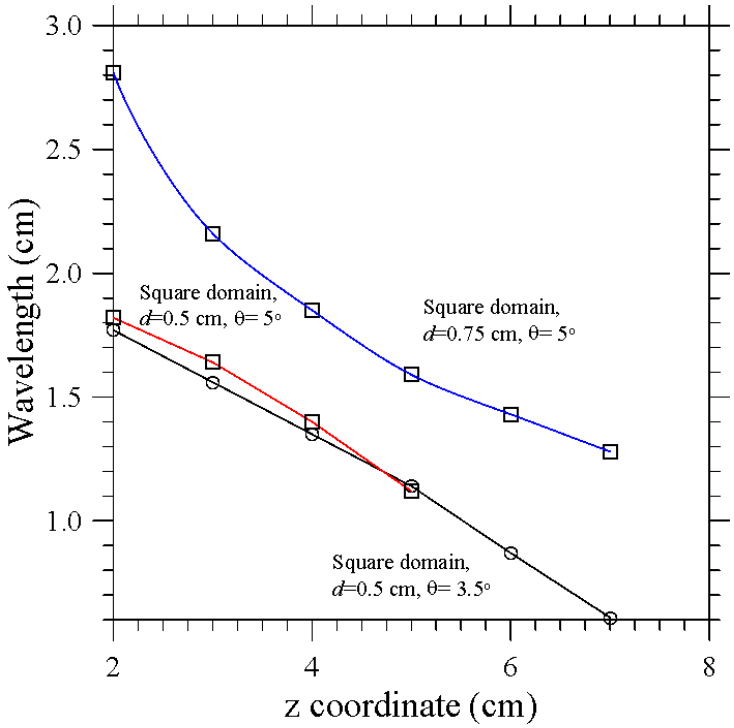

Figure 110: Transverse roll extension as a function of the longitudinal direction z for ΔT = 27°C for different average fluid depths and inclinations (square container).

All these trends are finally summarized in Fig. 110 in terms of roll extension along x as a function of the longitudinal coordinate z for different values of the layer average depth and inclination.

Having completed a description of the observed phenomena in the square geometry case, now the equivalent dynamics emerging in the cylindrical container are examined briefly. As already explained to a certain extent before, this practice finds its justification in the two-fold purpose of assessing the role played by the system aspect ratio (ratio of the horizontal and average vertical extension) and the shape of the side boundary.

9.3 Convection in inclined cylindrical layer

As the reader will immediately realize by inspecting Fig. 111, moving on from the case with square boundary to that with cylindrical sidewall (compare with Fig. 103), no significant or appreciable changes can be discerned in terms of patterning behavior. The flow still displays a set of coexisting rolls, which originate from the side where the fluid depth is larger and protrude into the pattern-less region located at the other end of the container.

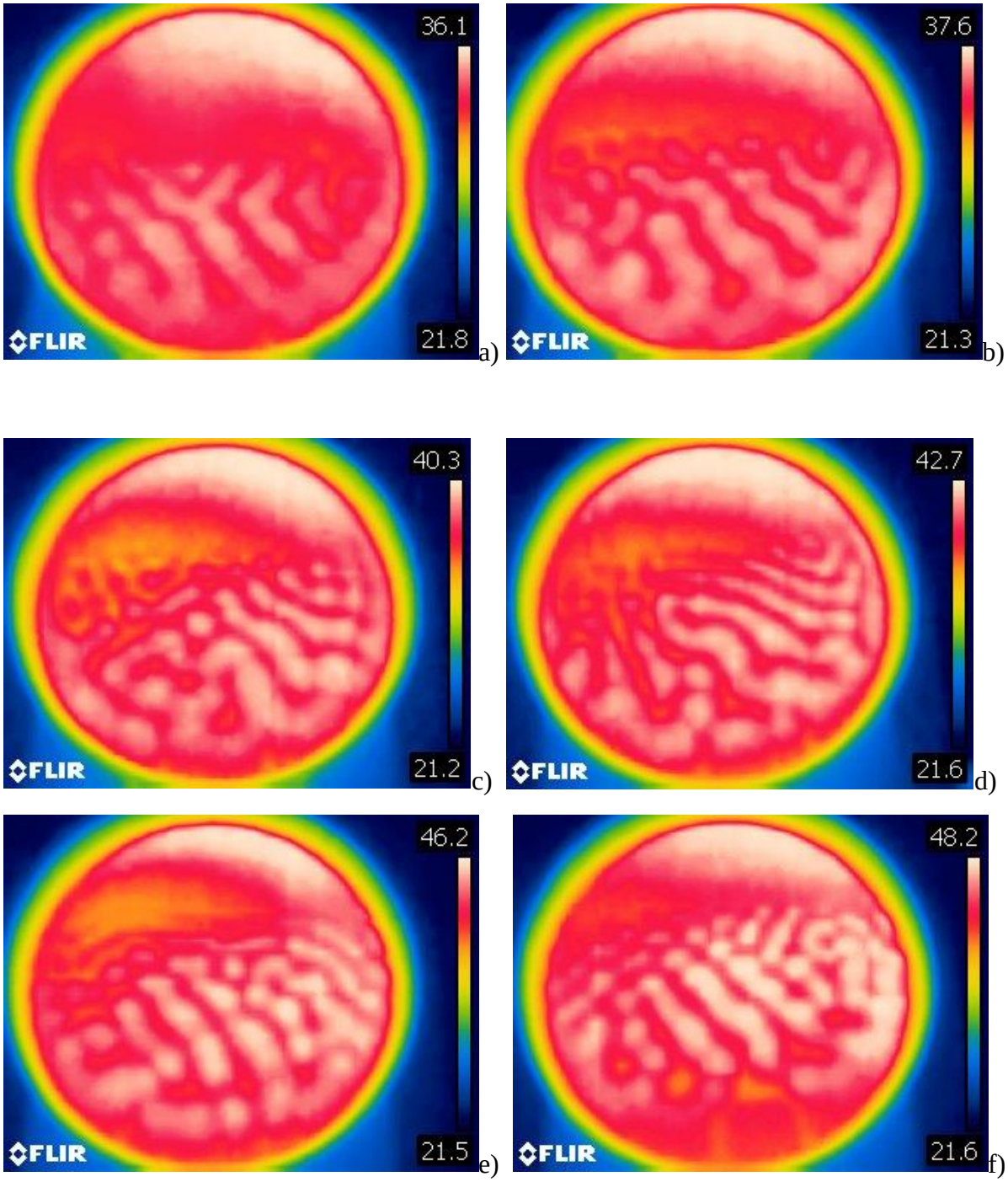

Figure 111: Surface temperature distribution for d=0.50 cm ($\Omega \cong$ 70 ml) and $\vartheta \cong 3.5°$ (A=26.6, $Bo_{dyn} \cong 0.86$, $Ra \cong 2.5 \times 10^2 \times \Delta T$, $Ma \cong 2.94 \times 10^2 \times \Delta T$): a) ΔT=15°C, b) ΔT=18°C, c) ΔT=21°C, d) ΔT=24°C, e) ΔT=27°C, f) ΔT=30°C.

Although from a qualitative standpoint, the scenario is essentially the same, however, a discrepancy or departure from the equivalent dynamics shown in Fig. 103 can be identified. It is represented by the tendency of the rolls to assume an oblique configuration with respect to the tilt direction (North-West/South-East in the different panels of Fig. 111).

Moreover, as revealed by a closer (quantitative) assessment of the pattern in terms of wavelength, this difference in the prevailing roll orientation occurs in conjunction with an appreciable increase in the roll transverse extension (Fig. 112).

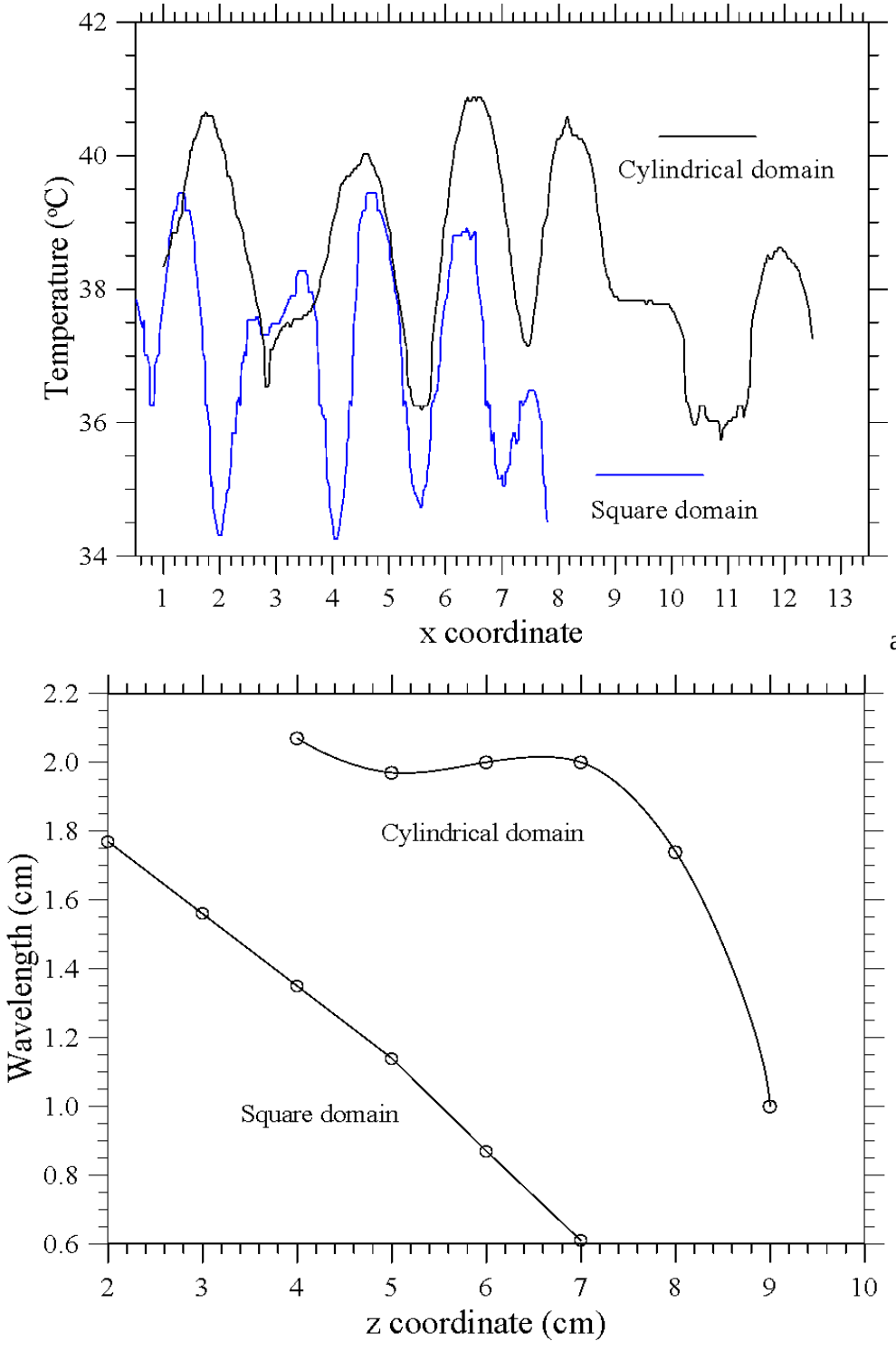

Figure 112: Transverse roll extension analysis (d= 0.50 cm, Bo_{dyn}≅0.86, ΔT = 27°C, $\vartheta \cong 3.5°$): a) Temperature as a function of the transverse coordinate x at z= 4 cm, b) Roll extension along x as a function of the longitudinal direction z.

On the one hand, these results indicate that the scenario does not depend significantly on the shape of the domain, on the other hand, they provide evidence that, if the geometrical aspect ratio is increased (A=26.6 as opposed to A=16), the pattern is allowed to "relax" in the horizontal direction, thereby causing an increase in the dimensional wavelength. Another (more obvious) outcome of the cylindrical nature of the outer solid boundary is the modulation of the longitudinal extension of the rolls along the x axis for any fixed value of ΔT (the rolls closer to left and right side of the container having smaller longitudinal extension that those located in the center, as a result of they being all terminated at the same station z).

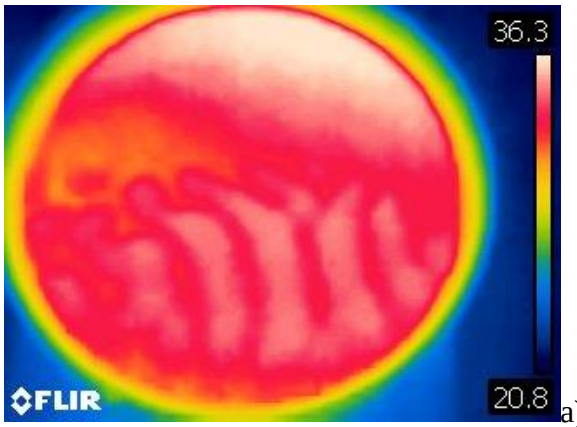

a)
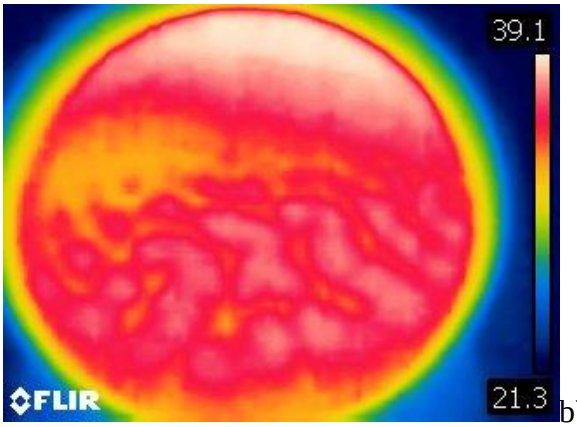

b)
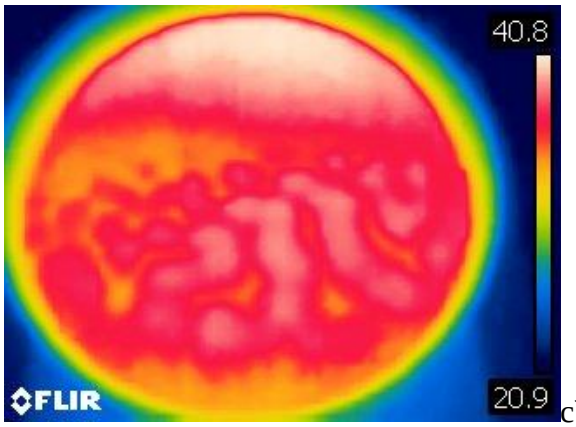

c)
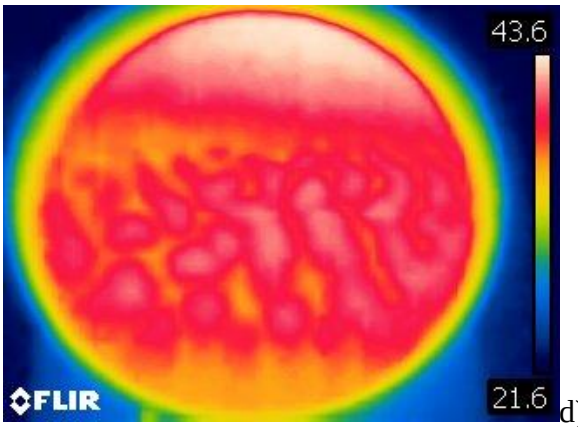

d)
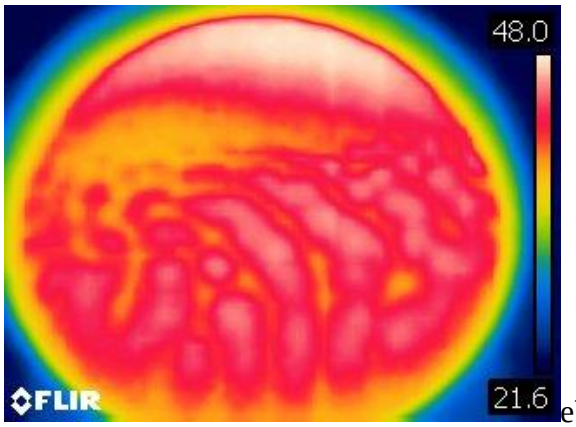

e)
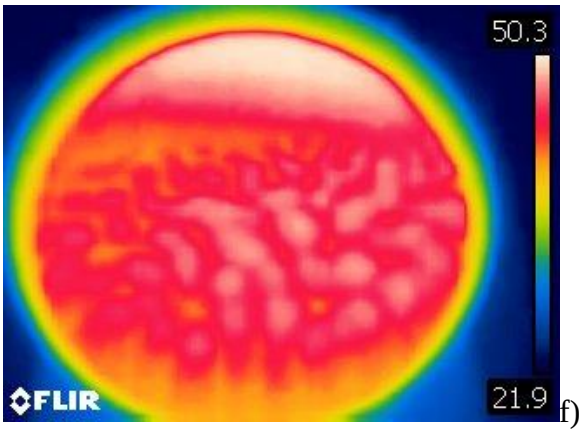

f)

Figure 113: Surface temperature distribution for d=0.50 cm ($\Omega \cong$ 70 ml) and $\vartheta \cong 5°$ (A=26.6, $Bo_{dyn} \cong 0.86$, $Ra \cong 2.5 \times 10^2 \times \Delta T$, $Ma \cong 2.94 \times 10^2 \times \Delta T$): a) ΔT=15°C, b) ΔT=18°C, c) ΔT=21°C, d) ΔT=24°C, e) ΔT=27°C, f) ΔT=30°C.

Fig. 113 naturally complements figure 111, where additional evidence is provided that, on increasing the inclination, the transverse wavelength can be made higher (especially for intermediate values of z).

Figure 114 and 115 complete this sequence by illustrating the behavior for larger average depth of the layer (Fig. 115 to be compared for analogous cicumstances with the findings about the square layer in Fig. 108).

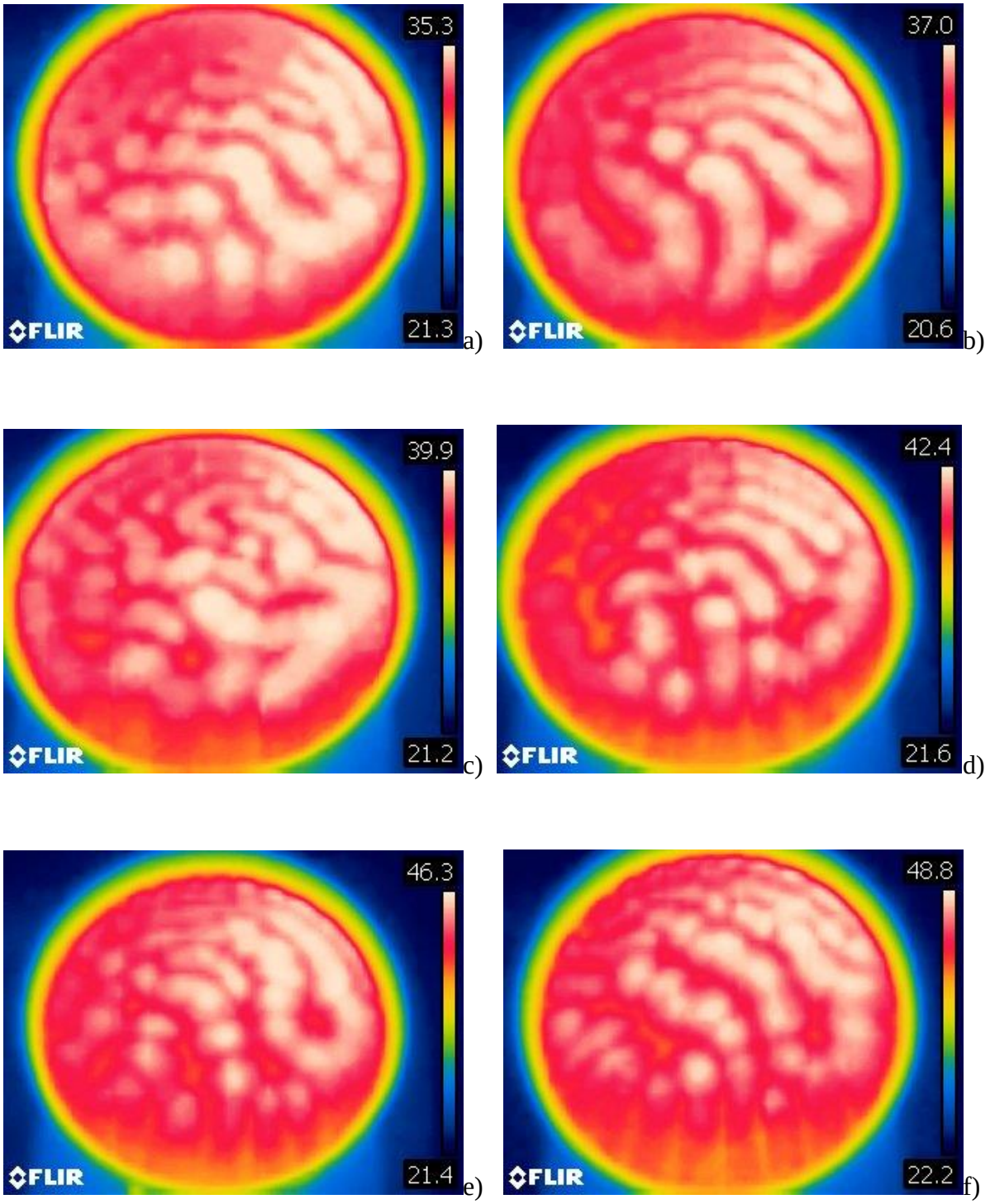

Figure 114: Surface temperature distribution for d=0.75 cm (Ω = 104 ml) and $\vartheta \cong 3.5°$ (A=17.7, $Bo_{dyn} \cong 1.94$, $Ra \cong 8.6 \times 10^2 \times \Delta T$, $Ma \cong 4.4 \times 10^2 \times \Delta T$) a) ΔT=15°C, b) ΔT=18°C, c) ΔT=21°C, d) ΔT=24°C, e) ΔT=27°C, f) ΔT=30°C.

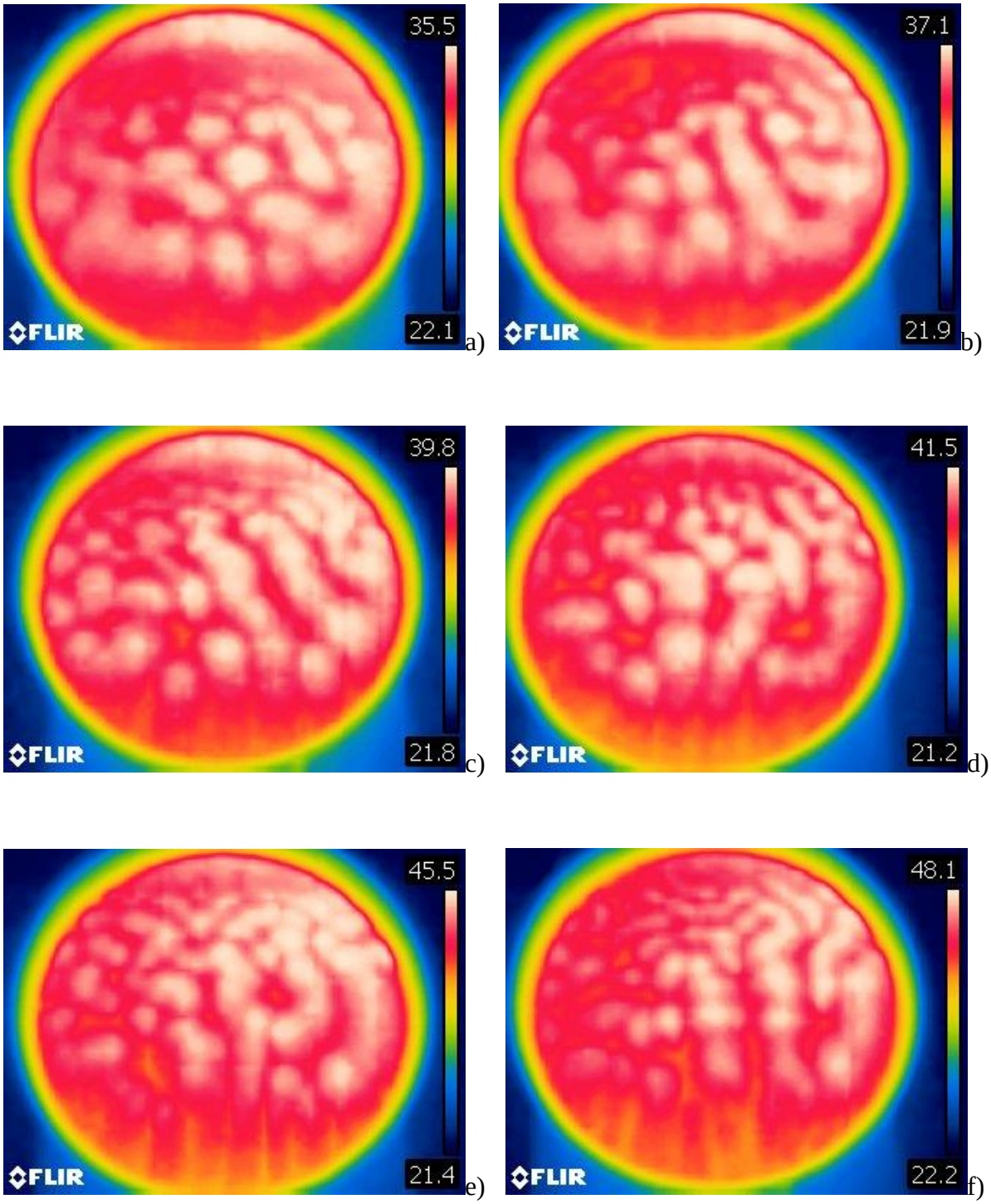

Figure 115: Surface temperature distribution for d=0.75 cm (Ω = 104 ml) and $\vartheta \cong 5°$ (A=17.7, $Bo_{dyn}\cong$1.94, $Ra\cong 8.6\text{x}10^2\text{x}\Delta T$, $\text{Ma}\cong 4.4\text{x}10^2\text{x}\Delta T$) a) ΔT=15°C, b) ΔT=18°C, c) ΔT=21°C, d) ΔT=24°C, e) ΔT=27°C, f) ΔT=30°C.

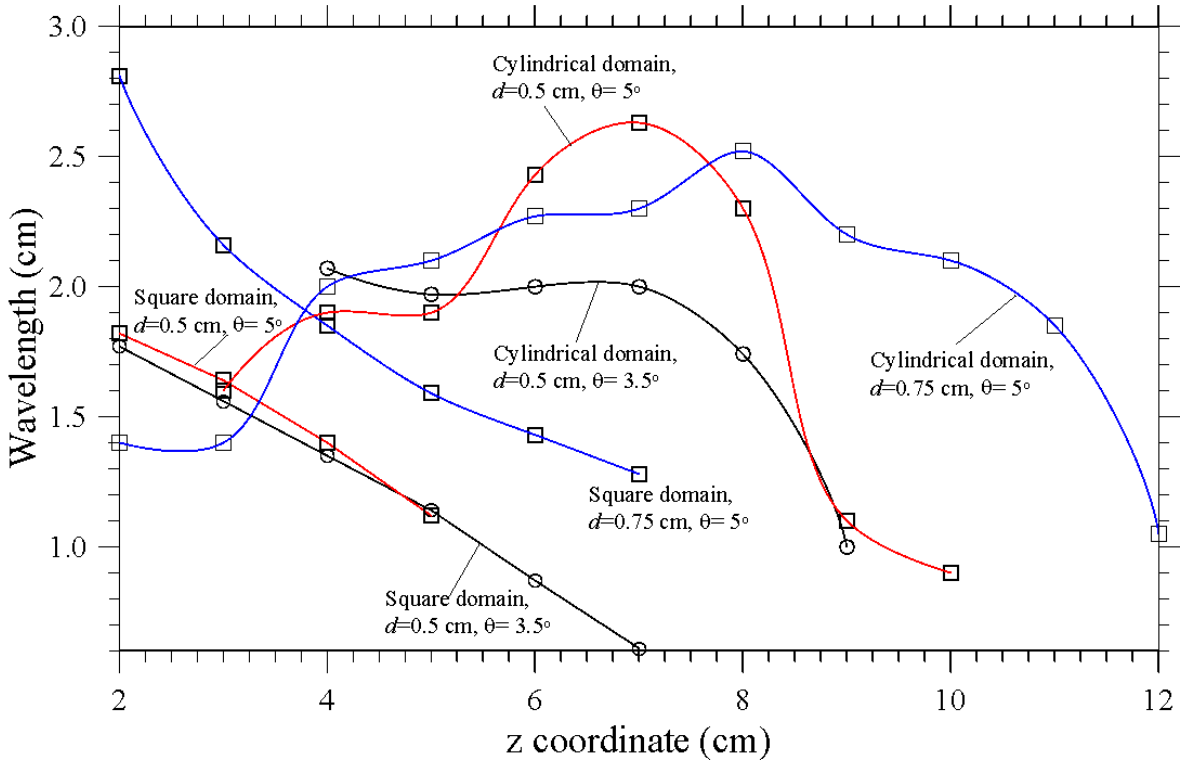

Figure 116: Transverse roll extension as a function of the longitudinal direction z for all the cases considered in the present work (ΔT = 27°C).

Figure 116 finally provides an ensemble perspective on the system response for all the cases considered in Sects. 9.2 and 9.3. A number of interesting functional dependences can be discerned accordingly. Besides the aforementioned tendency of the transverse wavelength to attain larger values as the inclination and/or the liquid average depth (volume) are increased (with the values for the cylindrical domain being generally located above the corresponding ones for the square container with smaller aspect ratio), some interesting non-monotonic behaviors can be spotted there.

In the cylindrical case, for d=0.5 cm ($Bo_{dyn}\cong$0.86) and $\vartheta \cong 5°$ the wavelength curve is entirely located above the corresponding one for the square domain (refer to the red branches in Fig. 116). The cylindrical case, however, displays a maximum for z = 7 cm, followed by a branch of decreasing behavior. Notably, an interval of the z coordinate can be identified accordingly where the wavelength for $\vartheta \cong 5°$ is smaller than that attained for the same average liquid depth (d=0.5 cm) and $\vartheta \cong 3.5°$ (z< 5.2 cm). The same concept applies to the curve for d=0.75 cm ($Bo_{dyn}\cong$1.94) and $\vartheta \cong 5°$. Although, the wavelength is larger than the corresponding one for d=0.5 cm over almost the entire longitudinal extension of the fluid domain, this relationship is inverted in the range 5.7<z<7.7 cm. This curve even intersects the corresponding one for the square container for z ≅3.8 cm (refer to the blue branches in Fig. 116), which indicates that

circumstances exists where the wavelength in the cylindrical case can become smaller than the equivalent square-domain value ($Bo_{dyn}\cong 1.94$, $\vartheta \cong 5°$ and z<3.8 cm).

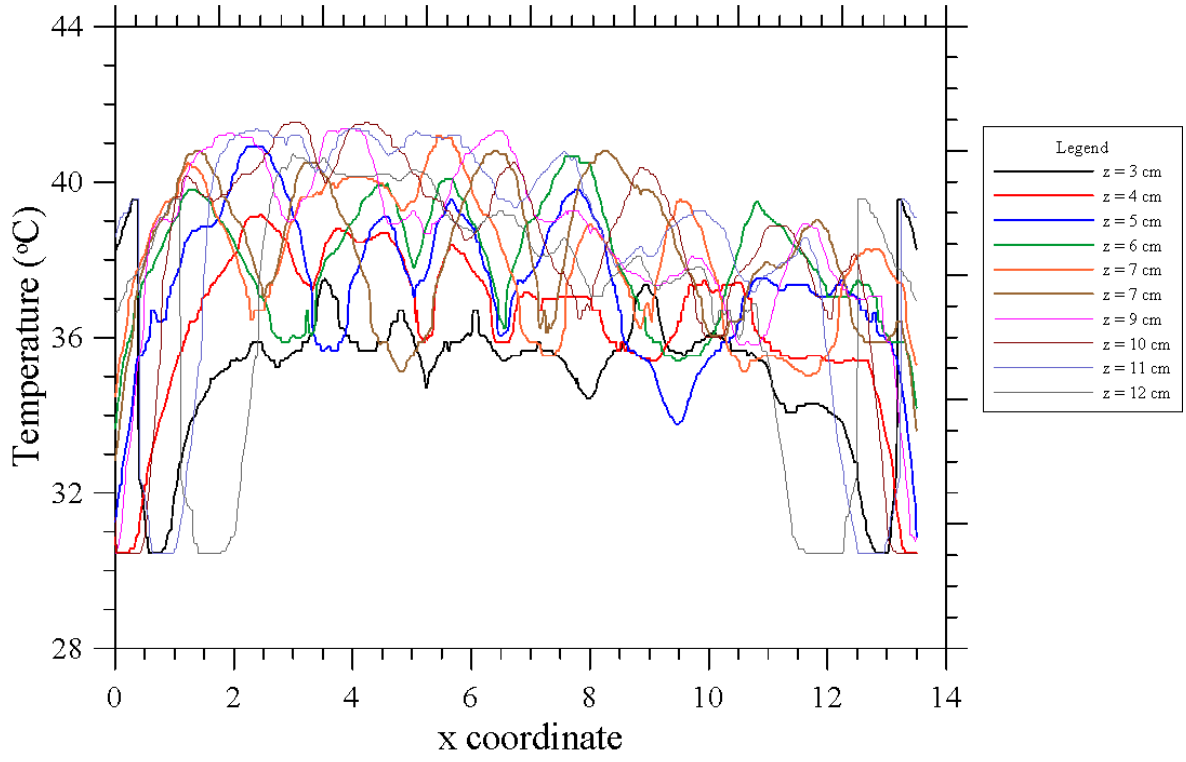

Figure 117: Profiles of temperature at different stations along the longitudinal direction z (cylindrical container, A=17.7, d = 0.75 cm, $Bo_{dyn}\cong 1.94$, ΔT = 27°C, $\vartheta \cong 5°$).

For the sake of completeness, Fig. 17 finally shows the distribution of temperature profiles in the cylindrical case for d = 0.75 cm and $\vartheta \cong 5°$.

9.4 Discussion:

It is a well-known concept that, regardless of whether the underpinning processes are different or not, systems that are driven out of equilibrium often display similar behaviors or patterns (Lappa, 2009). Therefore, in this section some effort is provided to emphasize on some prior research displaying some potential links with the results described in this chapter. In particular, the discussion is articulated along two different threads. Namely, first, the existing literature on surface-tension driven convection in horizontal layers with inclined temperature gradient is reviewed and then the existing studies on pure gravitational convection in inclined shallow enclosures with constant depth (geometries with a rectangular transverse section) is examined.

In the former case, some resemblances can be seen about the existence of a symmetry breaking shear flow, which can deeply influence the effective patterning behavior. In 2001, Nepomnyashchy performed a linear stability analysis, in which they provided a detailed

classification of the fundamental modes of surface-tension-driven convection in horizontal layers with an inclined temperature gradient (Nepomnyashchy, 2001). These were categorized as stationary longitudinal rolls, essentially driven by the same thermal effects that can produce classical MB convection, and transverse rolls for which shear plays a much more important role (Nepomnyashchy et al.2001). On the other hand, Hydrothermal waves were also identified in the case for which the horizontal component of the temperature gradient becomes so strong that it can obstruct the concurrent mechanisms driven by the vertical component. Due to lack of HTWs in the present experiments even for those cases where depth of the fluid layer is minimal, it can be concluded that present conditions are far from those for which these specific modes of convection can be excited. Another possible explanation could be rooted in another class of studies dealing with hybrid Marangoni-buoyancy convection in differentially heated liquid layers where the gradient of temperature is applied parallel to the free interface. In the literature, there is evidence that if buoyancy is sufficiently strong in comparison to surface-tension driven effects then HTW is taken over by longitudinal rolls with axes parallel to the (horizontal) temperature gradient.

In 2004, Nepomnyashchy and Shklyaev investigated thermocapillary flows under an inclined temperature gradient and provided useful information about the effective morphology of the emerging convection structures through non-linear numerical simulations (Shklyaev and Nepomnyashchy, 2004). For a sample liquid with Pr=7, they examined the morphological changes undergone by the compact cells typical of MB convection under the effect of a superimposed shear flow and showed that between the areas of the existence of the hexagonal patterns and the longitudinal rolls, there is a stability domain of “oblique rolls” , i.e. rolls inclined with respect to the direction of the horizontal temperature gradient. They also found states with half of the convective pattern consisting of oblique rolls with positive inclination angle and the other half displaying rolls with a negative inclination angle of the same modulus.

In 2002, Ueno et al. performed an experimental investigation on thermocapillary convection in thin liquid layer with temperature gradient inclined to free surface. They used silicon oil of 2, 5, 10 and 20 cSt as the test fluid. In this study, the temperature gradient was applied to the fluid layer with an inclination to the free surface. They found stationary longitudinal rolls and drifting cells in the convective pattern (Ueno et al. 2002). Later, Mizev and Schwabe conducted an experimental campaign to assess the role played in such dynamics by the depth of the layer (10 cSt silicone oil with a thickness d varying from 1.0 to 6.0 mm, Mizev and Schwabe, 2009). All these authors found that as the layer thickness increases the Bénard–Marangoni cells elongate along the direction of thermocapillary motion. When the longitudinal size of the cells reaches the horizontal size of the layer, a new flow structure appears in the form of LRs. More precisely, they also observed that for any depth of the layer in the considered range, while an increase in the horizontal component of the temperature gradient for a fixed vertical

contribution can cause a transition from drifting cells to LRs, vice versa, an increase in the vertical component of the temperature gradient for a fixed horizontal contribution leads to the opposite transition.

Several similarities could be identified between these behaviors and the present results. However, it must mention that in present case in addition to the inclination of the temperature gradient with respect to the free interface, the depth of the liquid layer is not constant. The related discussion could be started from a simple remark that for inclined systems subjected to buoyancy only and relatively small angles of inclination such as those considered in the present work, these systems tend to develop stationary longitudinal rolls, i.e. rolls of essentially buoyant nature that aligns with the direction of the shear flow are the typical outcome of the primary instability of these systems. Only for the case where inclination is relatively large then the ground is left to transverse rolls where rolls exist with axes perpendicular to the shear flow essentially driven by shear (Chen and Pearlstein, 1989). In 1993 Fujimura and Kelly clarified that the transition angle essentially depends on the Prandtl number of the considered fluid, and it is less than 90° only if the Prandtl number is smaller than 12.47 (Fujimura and Kelly, 1993) which further indicates that longitudinal rolls should be regarded as the primary pattern forming process in oils and other fluids with relatively large values of the Prandtl number.

The present findings, Fig 108 where buoyancy is dominant shows that such a trend (i.e. the tendency to favor LRs for small tilt angles) still holds although situations with non-constant depth of the layer have been considered. On the other hand, Figs 115 and 116 also provide a hint for another interesting connection with the dynamics described in the studies by (Shadid and Goldstein, 1990) and (Busse and Clever, 1992). Former authors performed experimental analysis on a fluid with Pr=90 and concluded that for low to moderate angles of inclination and a sufficiently high value of the Rayleigh number, the longitudinal rolls can become unstable against a three-dimensional “wavy” instability. By means of numerical simulations, Busse and Clever could confirm that a three-dimensional “wavy” instability is the main mechanisms responsible for the emergence of the so-called undulations patterns (Busse and Clever, 1992). Convective patterns observed in Figs 108 and 115 clearly reveal that the tendency of the present system to develop oblique rolls characterized by sinusoidal spatial distortions as the aspect ratio is increased from 10.6 to 17.7 and the straight (parallel) sidewalls are replaced by a curved boundary.

In Fig 103, it can be seen that the free surface of the inclined fluid layer leads to two remarkable effects where the surface temperature exhibits in that case an almost feature-free region localized in the part of the physical domain where the depth of the fluid layer is smaller. Moreover, the random distribution of rolls seen in the constant-depth case is taken over by a much more ordered arrangement where the convective features display a tendency to align with the z axis (the vertical direction in the figures, see, e.g., Fig. 103c). Then in next case, it was

also observed that an increase in ϑ (Fig. 106) can produce a mitigation of the aforementioned roll pinching mechanism (by which a single longitudinal roll can be split into two neighboring rolls with smaller wavelength). In addition, it causes a small (non-negligible) growth of the transverse extension of the rolls (this effect will be clarified later in this chapter).

9.4.1 Heat Sources Placed on Bottom Surface of Inclined Square Layer:

Fig 118 is showing the first glimpse of the convective patterns over free surface of the inclined fluid layer when one block is mounted on its bottom. Also in this case, it can be clearly seen that fluid layer is characterized by a feature-free region where its depth is smaller. On the opposite side, the convective pattern consists of longitudinal rolls along with one full spot created just over the block located in the middle of the domain. An increase in the temperature difference causes a small growth in the transverse extension of the rolls which then proceed towards feature-free region. In other words, due to the increase of the temperature difference, these rolls start to align with z axis and extend towards the other side where depth of fluid layer is relatively small.

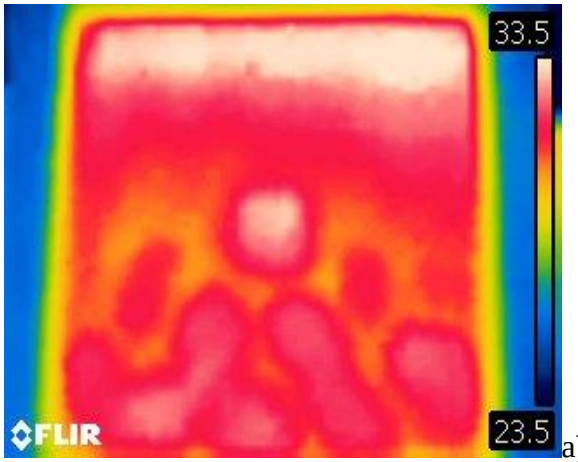

a)
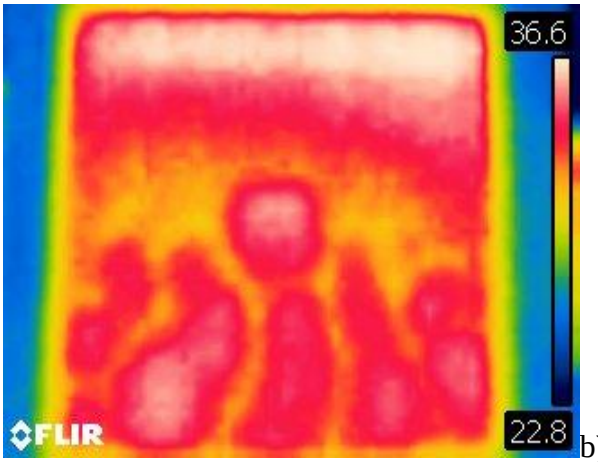

b)
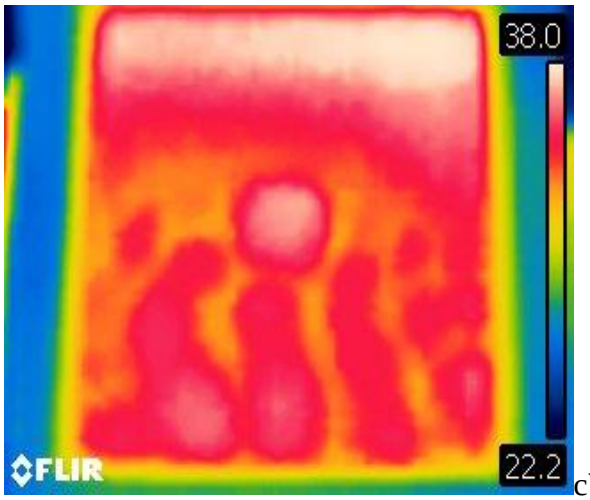

c)
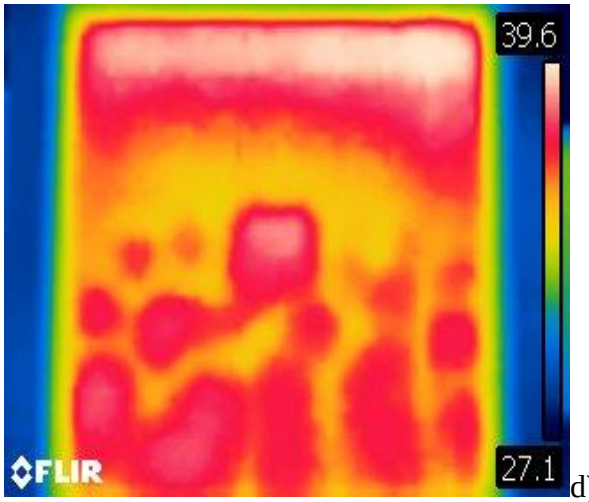

d)
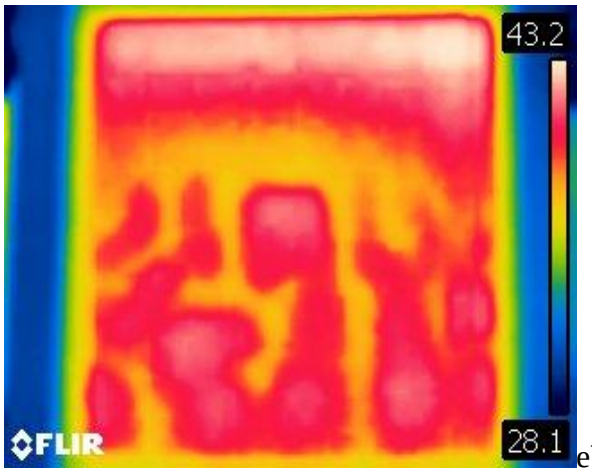

e)
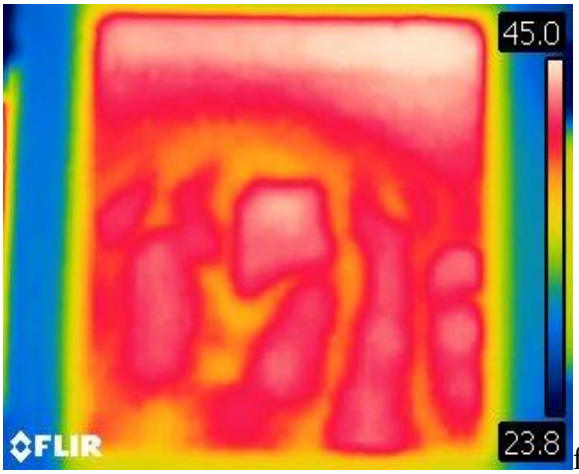

f)

Figure 118. Surface temperature distribution for d=0.50 cm (Ω = 32 ml), N=1 and $\vartheta \cong 5°$ (A=16, Bo_{dyn}≅0.86, Ra≅2.5x10^{2}xΔT, Ma≅2.94x10^{2}xΔT): a) ΔT=15°C, b) ΔT=18°C, c) ΔT=21°C, d) ΔT=24°C, e) ΔT=27°C, f) ΔT=30°C.

On increasing N to 2, the fluid layer still produces feature-free regions where its depth is smaller; blocks located in this region appear as hot objects which are in direct contact with the external gaseous environment. Notably, they do not produce any convective features (see fig 119). By contrast, on the other side, the blocks (where fluid depth is relatively large) produce donut-shape spots and the surface also features some other hot spots along the sidewalls and in between the blocks. When the temperature difference is increased then hot spots specially between the blocks convert into rolls and tend to extend progressively towards the feature-free region and align themselves w.r.t z-axis. On increasing N to 3, an almost saturated state is obtained where only the blocks placed in proximity to the sidewall where the fluid depth is larger, produce donut shape features. The main reason for these different behaviors is the distance between the block's top surface and free surface of the fluid layer which varies along z-axis due to inclination of the fluid layer (Fig 120).

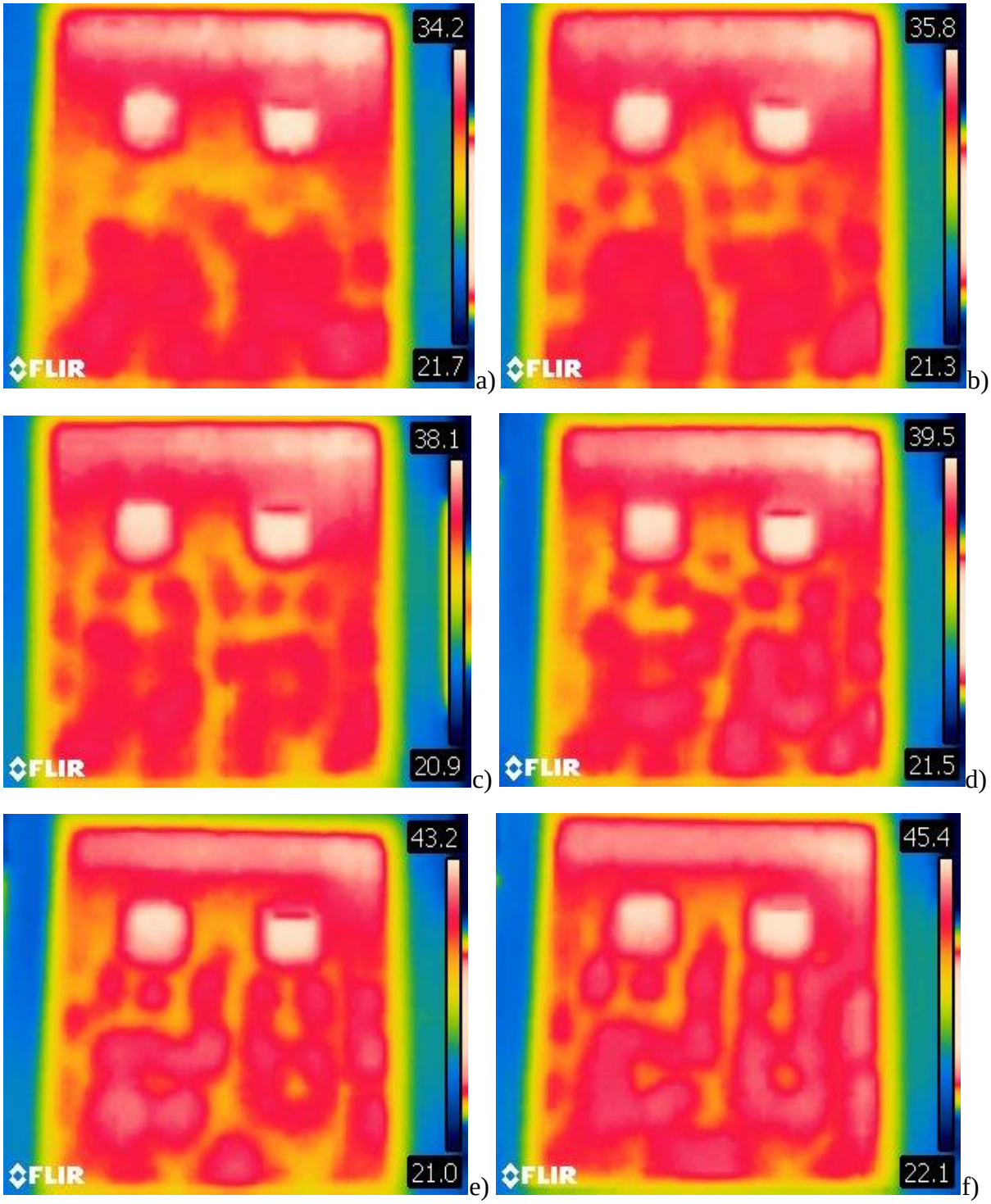

Figure 119. Surface temperature distribution for d=0.50 cm (Ω = 32 ml), N=2 and $\vartheta \cong 5°$ (A=16, Bo_{dyn}≅0.86, Ra≅2.5x10^{2}xΔT, Ma≅2.94x10^{2}xΔT): a) ΔT=15°C, b) ΔT=18°C, c) ΔT=21°C, d) ΔT=24°C, e) ΔT=27°C, f) ΔT=30°C.

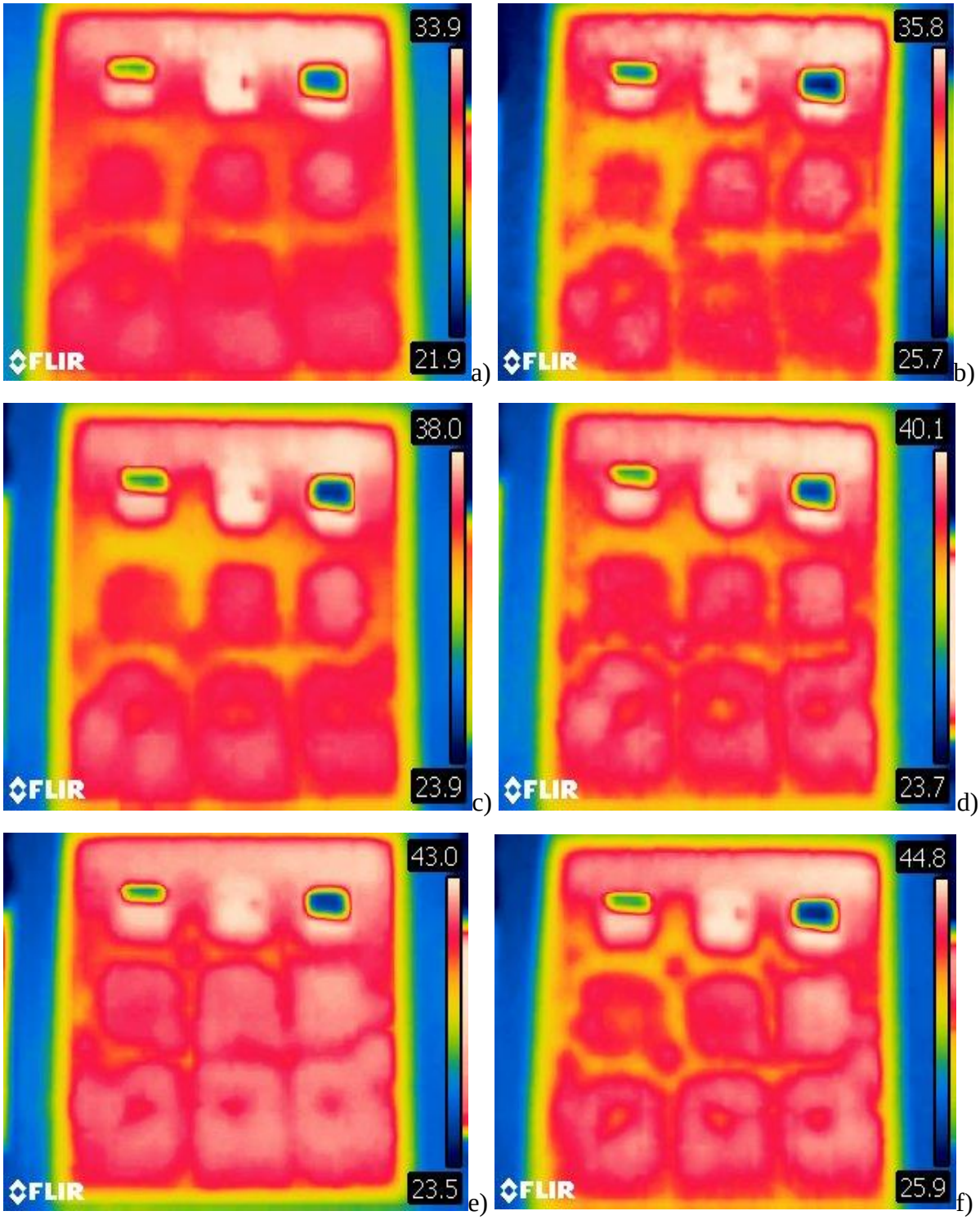

Figure 120. Surface temperature distribution for d=0.50 cm (Ω = 32 ml), N=3 and ϑ ≅ 5° (A=16, Bodyn≅0.86, Ra≅2.5x102xΔT, Ma≅2.94x102xΔT): a) ΔT=15°C, b) ΔT=18°C, c) ΔT=21°C, d) ΔT=24°C, e) ΔT=27°C, f) ΔT=30°C.

In the following the same angle of inclination is considered, but the depth of the fluid layer is increased from 0.5cm to 0.75cm in order to analyze the effects of a change in depth on the convective pattern. Along these lines, Fig 121 shows the convective pattern when just one block is placed in middle of the domain. Initially, for a relatively small temperature difference, there's feature-free region on the side where depth of the fluid layer is relatively small. In addition, a donut-shape hot spot is formed over the block. When the temperature difference is increased, however, the convective pattern shows that the feature-free region is taken over by full hot spots which exist along all side walls and around the block. At ΔT=21 and 24, an external observer would see that hot spots around the middle block have started to convert into rolls. Higher temperature differences cause growth in transverse extension of these rolls which then start to align themselves along z-axis and spread towards the opposite end.

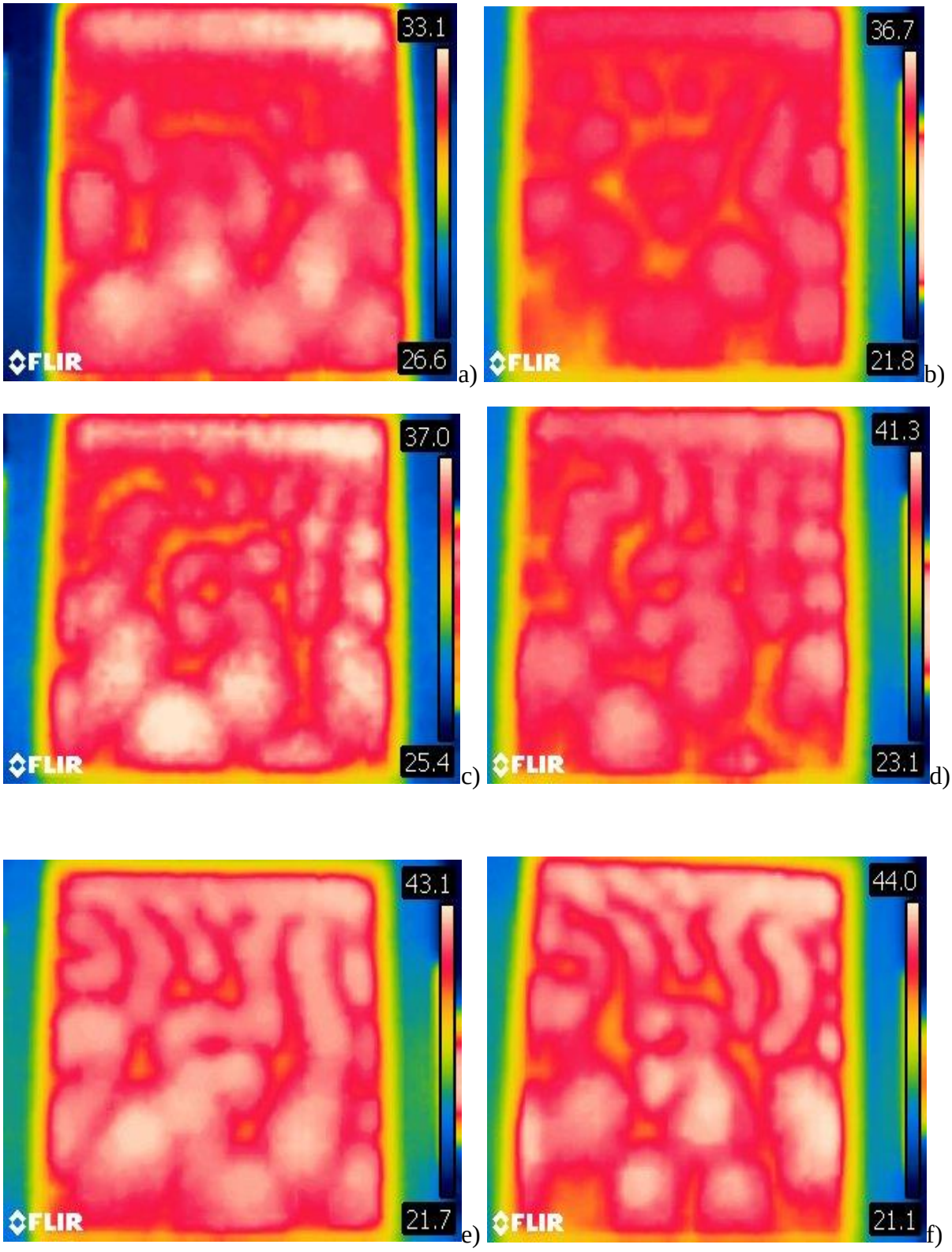

Figure 121. Surface temperature distribution for d=0.75 cm (Ω = 48 ml), N=1 and $\vartheta \cong 5°$ (A=16, Bo_{dyn}≅0.86, Ra≅2.5x10^{2}xΔT, Ma≅2.94x10^{2}xΔT): a) ΔT=15°C, b) ΔT=18°C, c) ΔT=21°C, d) ΔT=24°C, e) ΔT=27°C, f) ΔT=30°C.

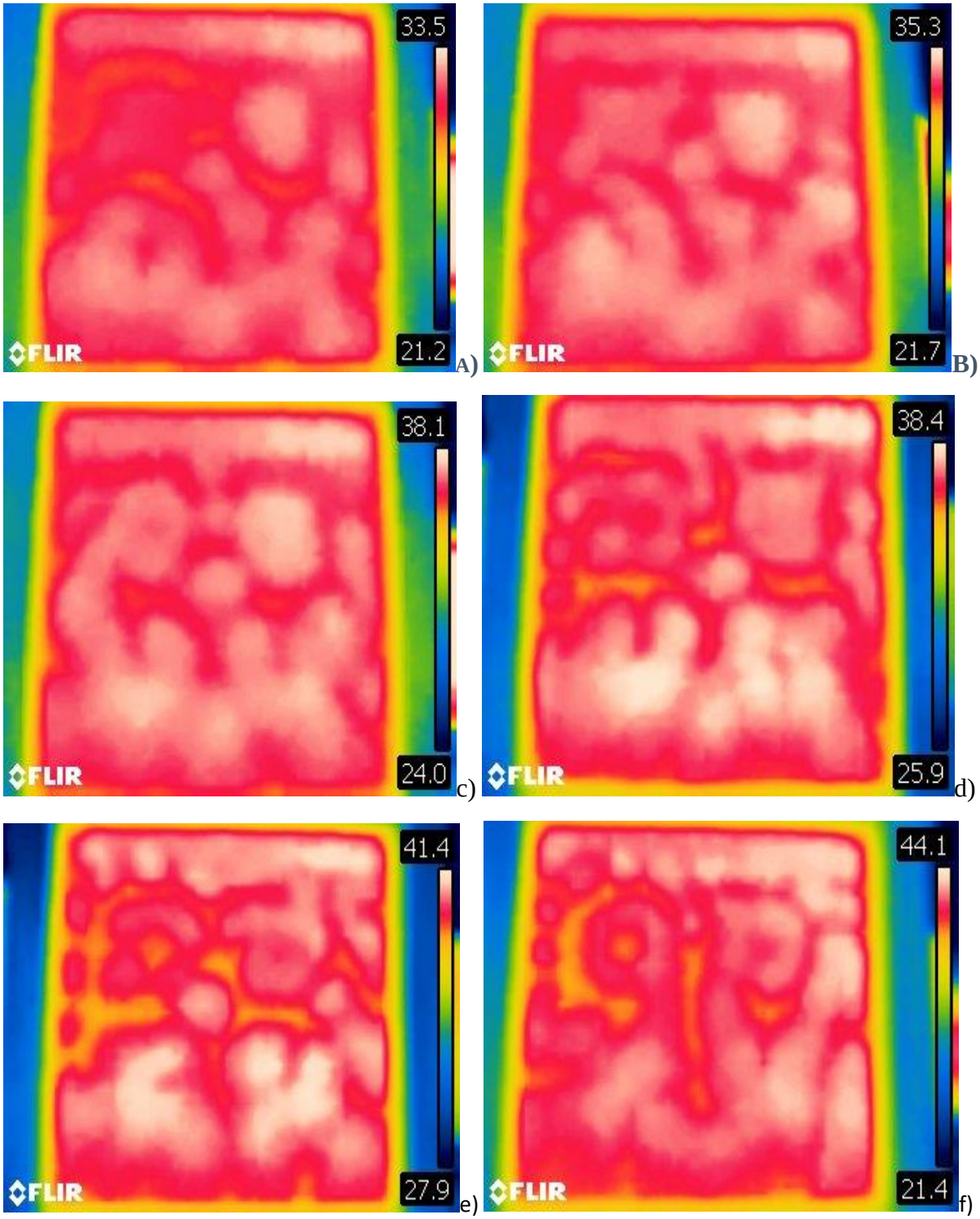

Figure 122. Surface temperature distribution for d=0.75 cm (Ω = 48 ml), N=2 and $\vartheta \cong 5°$ (A=16, Bo_{dyn}≅0.86, Ra≅2.5x10^{2}xΔT, Ma≅2.94x10^{2}xΔT): a) ΔT=15°C, b) ΔT=18°C, c) ΔT=21°C, d) ΔT=24°C, e) ΔT=27°C, f) ΔT=30°C.

On increasing N to 2 (Fig. 122), donut shape hot spots can be seen over each block, coexisting with other hot spots distributed along all side walls. One particular change w.r.t to previous case is the emergence of a full hot spot in the middle of domain. At higher temperature difference (ΔT=30), it can be seen that hot spots over entire free surface start to

interact with other spots, and then convert into rolls which further proceed towards the other side of the container. Finally, for the case with N=3, the following patterns confirm that the fluid layer is in a completely saturated state (Fig. 123).

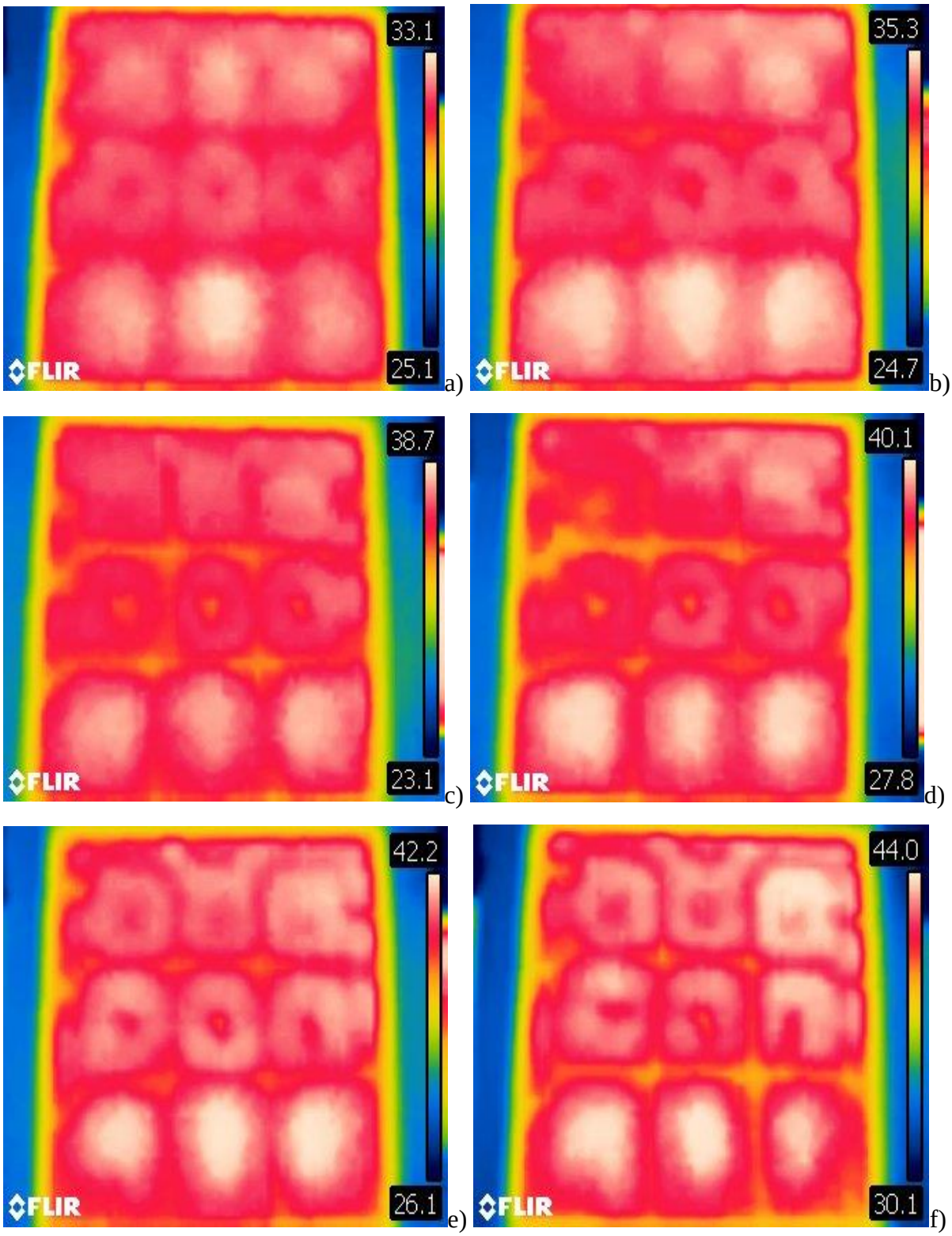

Figure 123. Surface temperature distribution for d=0.75 cm (Ω = 48 ml), N=3 and $\vartheta \cong 5°$ (A=16, Bo_{dyn}≅0.86, Ra≅2.5x10^{2}xΔT, Ma≅2.94x10^{2}xΔT): a) ΔT=15°C, b) ΔT=18°C, c) ΔT=21°C, d) ΔT=24°C, e) ΔT=27°C, f) ΔT=30°C.

9.5 Conclusion:

Hybrid Marangoni-buoyancy convection in a fluid domain with variable fluid depth and inclined temperature gradient with respect to the horizontal direction has been investigated in the attempt to enrich the current knowledge about the fluid-dynamic behavior of these systems. In particular, the unique examined configuration should be regarded as an intentional attempt to move beyond the models adopted so far by the community of theoretical physicists and engineers, which has essentially been based on the paradigm of a series of different idealized setups and has not yet branched out to heated systems with irregular transversal thickness.

It has been shown that, in analogy with the companion cases represented by Marangoni convection in horizontal layers with temperature gradient inclined to the free liquid-gas interface and buoyancy convection in constant-thickness tilted enclosures, the preferred (or dominant) mode of convection for relatively small tilt angles is represented by longitudinal rolls. These manifest with a wavelength that increases with the layer depth. A relaxation in the lateral confinement can also contribute to increase their transverse extension, which indirectly proves that the sidewalls play role in the wavenumber selection mechanism in the considered range of aspect ratios.

A coherent picture of the richness of possible scenarios in terms of roll transverse size, longitudinal extension, and orientation with respect to the tilt direction has been provided by varying parametrically the system influential factors, namely the temperature difference, liquid volume (average layer depth), inclination angle and the aspect ratio of the fluid container.

It has been shown that the hallmark of the considered dynamics is a modulation of the abovementioned transverse wavelength along the longitudinal direction, which should be regarded as an important distinguishing factor with respect to the “similar” behaviors displayed by these modes of convection in systems with a constant depth, regardless of whether the main driving force is represented by thermocapillary or buoyancy. An increase in the temperature difference generally causes an increase in the longitudinal extension of the rolls.

Future attempts shall be devoted to clarifying the nature of the interesting roll pinching mechanism (by which a single longitudinal roll can be split into two neighboring rolls with smaller wavelength), found in the case for which the lateral confinement is significant (small aspect ratio), and the layer depth is relatively small. Critical comparison with the existing literature has revealed that although most of existing results can be organized in well-studied universality classes, the interpretation of some experimental realizations is not always a relatively simple task. Factors contributing to the inherent complexity of this objective are the essentially counter-intuitive non-linear behavior displayed by these systems and the blending of convective modes (normally operating separately) due to nature of the specific problem considered here. Another open question relates to the influence of container shape. Although it has been proven here that the patterning behavior does not depend significantly on it

(longitudinal rolls being selected over the entire space of parameters) and that the main impact of a variation in the aspect ratio is limited to a modification of the transverse roll extension, additional care shall be put to discern separately the role played by the container aspect ratio and its shape. The latter might indeed be the root cause of the differences observed in terms of monotonic or non-monotonic nature of the curves providing the relationship between the roll wavelength and the longitudinal coordinate.

Conclusion:

In this dissertation, the dynamics of gravitational and surface-tension driven flows were investigated in fluid systems with periodically distributed hot blocks mounted on the bottom wall. The main objective was to understand how ensemble properties arise from the interplay of localized effects, i.e., different sources of heat and/or the specific topography present at the bottom. This research problem was actually designed in order to represent a variety of technological applications (at different scales) where thermal inhomogeneities induce in the surrounding fluid patterns that are similar to or reminiscent of the classical modes of Rayleigh–Bénard (RB) or Marangoni–Bénard (MB) convection. This subject has been addressed from both numerical and experimental points of view.

From a numerical point of view, initially simulations were performed to analyse topographically controlled Marangoni-Rayleigh-Benard convection in liquid metals through solution of the governing equations for mass, momentum, and energy. According to the results described in chapter#6, a topography at the bottom of a layer of liquid metal coupled with a thermal inhomogeneity can deeply change the flow with respect to the patterns, which would be produced in the equivalent conditions without blocks. In particular, the presence of obstructions prevents the layer from forming the horizontally extended rolls or the hexagonal cells, which would be typical of RB and MB convection, respectively. It was also observed that the outcomes of an increase in the height of the blocks are generally limited to a rise in the temperature of the hot spots, which are produced by rising thermal currents that meet the free surface, but an increase in their number can make the average temperature of the entire fluid layer much higher.

After examining the case of liquid metals, the role played by heat source location and multiplicity in topographically controlled thermal convection has been investigated numerically for the case of oils with almost constant (i.e., temperature-independent) viscosity (silicone oil). Three distinct regimes have been identified, namely, trivial modes of convection where the surface pattern simply reflects the ordered distribution of the underlying hot elements, states that display a notable degree of analogy with the ‘parent’ convective (RB and MB) mechanisms and a third category of flows represented by a kaleidoscope of possible solutions driven by intrinsic self-organization abilities of the considered system. For pure buoyancy convection, thermal plume interaction mechanisms cause transition from trivial patterns to more complex ones, where however the number of spots undergoes a decrease with respect to the dimension of the underlying grid of hot elements. When surface-tension effects are added, buoyancy can still play a role. This has been revealed through direct comparison of microgravity and terrestrial conditions, leading to the realization that the hot blocks evenly

spaced along the bottom can contribute to the regularity of the flow spatial organization through the creation of thermal pillars at fixed positions (when gravity is present).

It has been shown that for pure Marangoni convection and solid lateral walls, unsteadiness essentially manifests itself in the form of high frequency oscillations physically corresponding to the existence of vibrating spokes in the pattern, which cause localized cell breaking or coalescence effects. If buoyancy is also present, these high-frequency modes are complemented by long-period disturbances corresponding to the slow propagation of defects through the pattern. For periodic boundary conditions, this slow process is taken over by a different phenomenon by which cells undergo a faster relocation in time, accompanied by significant changes in their size and shape.

After examining the problem from a numerical point of view (in order to gain initial knowledge about the behaviours of these systems, which were still almost completely unknown), a thermographic technique has been used to investigate thermal convection in a shallow layer of liquid with an array of metallic (aluminium) cubic elements evenly spaced along the bottom. In this case, in order, to explore further the dynamic response of these systems, a relatively viscous oil with temperature-dependent properties has been considered. By doing so, it has been shown that system's response to a change in the number of blocks N is mediated by a number of factors, including, the depth of the layer, the height of blocks, the temperature difference, and the layer aspect ratio. Wavelength analysis of the digitized thermal patterns has revealed that for N=1, features of the parent classical forms of convection can be clearly identified. For small and intermediate depths of the layer, the features inherited from the parent RMB convection correspond to the quantized branches visible in the lower part of the figures (maps) providing the distribution of wavelength as a function of the temperature difference. On increasing the layer depth, however, the pattern-forming mechanism is transferred back to the parent form of convection. On the other hand, an increase in N has the opposite effect, i.e., the system gradually evolves towards topography-dominated solutions, whereas the properties of the parent forms of convection tend to be suppressed in favour of more system specific ones. Finally, a trivial (saturated) condition is obtained for N=3.

Comparison of these findings with those presented in Chapter 7 has led to the conclusion that consideration of a fluid with variable (temperature-dependent) physical properties can promote the emergence of self-organized states for smaller values of the parameter N.

Still using the same fluid (an oil with temperature-dependent viscosity, additional experiments have been conducted considering hybrid Marangoni-buoyancy convection in a fluid domain inclined with respect to the horizontal direction. It has been shown that for relatively small tilt angles the dominant convection mode is represented by longitudinal rolls, which manifest with a wavelength that increases with the layer depth. In addition, a relaxation in the lateral

confinement can also contribute to increase their transverse ex- tension. Different types of scenarios in this type of convection mode actually depend on multiple factors including the temperature difference, liquid volume (average layer depth), inclination angle and the aspect ratio of the fluid container, regardless of whether the main driving force is represented by thermocapillary or buoyancy. An increase in the temperature difference generally causes an increase in the longitudinal extension of the rolls. The presence of block can break such longitudinal rolls and lead to interesting complex patterns.

All the results presented in this thesis are intended to support the understanding of systems with multiple sources of heat and guide the design of the related cooling systems.

Future work shall be devoted to considering other types of fluids (e.g., water that is typically used in nuclear reactors as cooling fluid) and, obviously, air (for which the dynamics are driven by buoyancy only). In terms of numerical studies, simulations can be performed by using different fluids and circular container (to provide variations in Pr number and aspect ratio) where boundary conditions similar to experimental work can be adopted. Another interesting factor could be the selection of two types of fluids in experimental studies which are immiscible. In that case, convection can be analysed over liquid-liquid interface instead of liquid-gas interface in the presence of hot blocks on the bottom surface.

References:

Bachran A., Reinshaus P. and Seifert W., “Influence of thermal processing parameters and material properties on velocity configurations in semiconductor melts during the vertical bridgman growth technique,” *Crystal Research and Technology*, vol. 33, no. 1, pp. 27–36, 1998, doi: 10.1002/(sici)1521-4079(1998)33:1<27:aid-crat27>3.0.co;2-o.

Basara B., (2015), Fluid flow and conjugate heat transfer in a matrix of surface–mounted cubes: A pans study, Int. J. Heat Fluid Flow, 51, 166–174.

Bazylak A., Djilali N. and Sinton D. (2006), Natural convection in an enclosure with distributed heat sources, Numerical Heat Transfer, Part A 49, 655–667.

Bénard H., (1900), Les tourbillons cellulaires dans une nappe liquide, Rev. Gèn. Sci. Pure Appl., 11:1261–1271, 1309–1328

Bestehorn M., (1996), "Square patterns in Bénard-Marangoni convection", Phys. Rev. Lett., 76:46–49

Bestehorn M., Perez-Gracia C. and Echebarria B. (1998), Thermal Properties in surface tension driven convection, Phys. Rev. E 57, 475, doi: https://doi.org/10.1103/PhysRevE.57.475

Biswas N., Mahapatra P.S., Manna N.K., and Roy P.C., (2016), Influence of Heater Aspect Ratio on Natural Convection in a Rectangular Enclosure, Heat Transfer Engineering, 37(2), 125– 139.

Blackman K. and Perret L., (2016), Non-linear interactions in a boundary layer developing over an array of cubes using stochastic estimation, Phys. Fluids 28 (9), 095108.

Boeck T and Thess A., (1999), ″Bénard–Marangoni convection at low Prandtl number″, J. Fluid Mech., 399: 251-275.

Bratukhin Yu. K., Makarov S.O., and Mizyov A.I., (2000), Oscillating Thermocapillary Convection Regimes Driven by A Point Heat Source, Fluid Dynamics, 35(2), 232-241. Translated from Izvestiya Rossiiskoi Akademii Nauk, Mekhanika Zhidkosti i Gaza, No. 2, pp. 92-1

Busse F.H., (1994), “Spoke Pattern Convection”, Acta Mechanica (Suppl.), 4: 11-17.

Busse, F. and Clever, R. (1979). Instabilities of convection rolls in a fluid of moderate Prandtl number. *Journal of Fluid Mechanics*, *91*(2), 319-335. Doi:10.1017/S002211207900015X

Busse, F. and Clever, R. (1987). Nonlinear Oscillatory Convection. *Journal of Fluid Mechanics*, *176*, 403-417.Doi:10.1017/S0022112087000739

Busse, F. H., & Whitehead, J. A. (1971). Instabilities of convection rolls in a high Prandtl number fluid. *Journal of Fluid Mechanics*, *47*(2), 305-320.

Busse, F. H., & Whitehead, J. A. (1974). Oscillatory and Collective Instabilities in large Prandtl number fluid. *Journal of Fluid Mechanics*, *66*(1), 67-79. Doi: 10.1017/S0022112074000061

Castaing B., Gunaratne G., Heslot F., Kadanoff L., Libchaber A., Thomae S., Wu X., Zaleski S., and Zanetti G., (1989), "Scaling of hard thermal turbulence in Rayleigh-Bénard convection", J. Fluid Mech., 204: 1-30.

Cengel Y.A., Turner R.H., Cimbala J.M., (2016), Fundamentals of Thermal-Fluid Sciences, McGraw Hill; 5th Edition, 2016.

Chen Y. and Pearlstein A.J., (1989), Stability of free-convection flows of variable-viscosity fluids in vertical and inclined slots, J. Fluid Mech., 198, 513-541

Choi S.K., Nam H.Y., Cho M. (1994a), Systematic comparison of finite-volume calculation methods with staggered and non-staggered grid arrangement, Numer Heat Transfer, Part B 25 (2): 205–221

Choi S.K., Nam H.Y., Cho M., (1994b), Use of staggered and non-staggered grid arrangements for incompressible flow calculations on nonorthogonal grids, Numer Heat Transfer, Part B 25(2): 193–204.

Chuang S. H., Chiang J. S., and Kuo Y. M., (2003), Numerical Simulation of Heat Transfer in a Three-Dimensional Enclosure with Three Chips in Various Position Arrangements, Heat Transfer Engineering, 24(2), 42–59.

Clever R.M. and Busse F.H., (1994), "Steady and oscillatory bimodal convection", J. Fluid Mech., 271: 103-118.

Clever, R. M., & Busse, F. H. (1974). Transition to time-dependent convection. *Journal of Fluid Mechanics*, *65*(4), 625-645.

Clever, R. M., & Busse, F. H. (1991). Instabilities of longitudinal rolls in the presence of Poiseuille flow. *Journal of Fluid Mechanics*, *229*, 517-529.

Cliffe K.A. and Winters K.H., (1984), "A numerical study of the cusp catastrophe for Bénard convection in tilted cavities", J. Comput. Phys., 54, 531-534

Cloot A. and Lebon G., (1984), A nonlinear stability analysis of the. Bénard–Marangoni problem, J. Fluid Mech., 145: 447-469.

Coceal O., Dobre A., Thomas T.G., and Belcher S.E., "Structure of turbulent flow over regular arrays of cubical roughness," *J Fluid Mech*, vol. 589, pp. 375–409, Oct. 2007, doi: 10.1017/S002211200700794X.

Colinet P., Legros J. C., and Velarde M. G., Nonlinear Dynamics of Surface-Tension-Driven Instabilities (John Wiley, 2001).

Coriell, S.R., McFadden, G.B., Boisvert, R.F. and Sekerka, R.F. (1984) Effect of a forced Couette flow on coupled convective and morphological instabilities during unidirectional solidification, J. Cryst. Growth, 69 (1), 15-22

Daniels K.E., Plapp B.B. and Bodenschatz E., (2000), "Pattern Formation in Inclined Layer Convection", Phys. Rev. Lett., 84, 5320- 5323.

Daniels P.G. and Wang P., (1994), "Numerical study of thermal convection in tall laterally heated cavities", Int. J. Heat Mass Transfer, 37(3): 375-386.

Dauby P. C. and Lebon G., (1996), Bénard-Marangoni instability in rigid rectangular containers. J. Fluid Mech., 329:25–64

Dauby P.C. and Lebon G., “Bénard-Marangoni instability in rigid rectangular containers,” *J Fluid Mech*, vol. 329, pp. 25–64, Dec. 1996, doi: 10.1017/S0022112096008816.

Davis S.H, (1969), “Buoyancy-surface tension instability by the method of energy”, J. Fluid Mech., 39: 347-359

Davis S.H., (1967), "Convection in a box: linear theory", J. Fluid Mech., 30: 465-478

De A. K., Eswaran V., and Mishra P. K., (2017), Scaling of heat transport and energy spectra of turbulent Rayleigh-Bénard convection in a large-aspect-ratio box, Int. J. Heat Fluid Flow 67, 111–124.

De Vahl Davis G., (1968) Laminar natural convection in an enclosed rectangular cavity, International Journal of Heat and Mass Transfer, Volume 11, Issue 11,Pages 1675-1693,ISSN 0017-9310,https://doi.org/10.1016/0017-9310(68)90047-1.

Demircan A. and Seehafer N., (2001), Nonlinear square patterns in Rayleigh-Benard convection, Europhysics letters, Volume 53, Number 2, doi: 10.1209/epl/i2001-00137-2

Dustin, (2016). HOW HOT DO NUCLEAR FUEL RODS GET? Available at: https://unfocused.me/2016/09/11/how-hot-do-nuclear-fuel-rods-get/. [Accessed 12 Aug. 2022]

Eckert K., Bestehorn M., Thess A., (1998), Square cells in surface-tension-driven Bénard convection: experiments and theory, J. Fluid Mech., 356: 155-197 03, March-April 2000.

Energy APR., (2018). What is a Genset & What it is used for? Available at: https://www.aprenergy.com/what-is-a-genset-used-for/ [Accessed: 01 Sep. 2022].

Farrow, D.E. and Patterson, J.C. (1993) On the stability of the near shore waters of a lake when subject to solar heating, Int. J. Heat Mass Transfer, 36 (1), 89-100

Fauve S., “Henri Bénard and pattern-forming instabilities,” *Comptes Rendus Physique*, vol. 18, no. 9–10. Elsevier Masson s.r.l., pp. 531–543, Nov. 01, 2017. doi: 10.1016/j.crhy.2017.11.002.

Forth, S.A. and Wheeler, A. A. (1992) Coupled convective and morphological instability in a simple model of the solidification of a binary alloy, including a shear flow, J. Fluid Mech., 236, 61-94.

Fujimura K. and Kelly R.E., (1993), Mixed mode convection in an inclined slot, J. Fluid Mech., 246, 545-568.

Gaponenko Y., Yasnou V., Mialdun A., Nepomnyashchy A., & Shevtsova V. (2021), Hydrothermal waves in a liquid bridge subjected to a gas stream along the interface, J. Fluid Mech., 908, A34. doi:10.1017/jfm.2020.901

Gelfgat A. Yu., (2020), “Instability of natural convection of air in a laterally heated cube with perfectly insulated horizontal boundaries and perfectly conducting spanwise boundaries”, Phys. Rev. Fluids 5, 093901.

Getling A. V., Bénard–Rayleigh Convection: Structures and Dynamics, World Scientific, 1998

Goldstein R.J., "Visualization of longitudinal convection roll instabilities in an inclined enclosure heated from below," *J Fluid Mech*, vol. 215, pp. 61–84, 1990, doi: 10.1017/S0022112090002555.

Golubitsky M., Swift J.W. and Knobloch E., (1984), "Symmetries and Pattern selection in Rayleigh-Benard convection", Physica D, 10:249-276.

Gresho P.M., ''Some current CFD issues relevant to the incompressible Navier-Stokes equations,'' Computer Methods in Applied Mechanics and Engineering, Volume 87, Issues 2–3,1991,Pages 201-252,ISSN 0045-7825, https://doi.org/10.1016/0045-7825(91)90006-R.

Guermond J.-L. and Quartapelle L., (1998), On stability and convergence of projection methods based on pressure Poisson equation, Int. J. Numer. Meth. Fluids, 26: 1039-1053

Guermond J.-L., (1996), Some practical implementations of projection methods for Navier – Stokes equations, Model. Math. Anal. Num., 30: 637–667.

Guermond J.-L., Minev P. and Shen J., (2006), An Overview of Projection Methods for Incompressible Flows. Comput. Methods, Comput. Methods Appl. Mech. Eng., 195: 6011-6045.

Heindel T.J., Ramadhyani S. and Incropera F.P., Conjugate natural convection from an array of discrete heat sources: part 1 — two- and three-dimensional model validation, International Journal of Heat and Fluid Flow, Volume 16, Issue 6,1995,Pages 501-510,ISSN 0142-727X,https://doi.org/10.1016/0142-727X(95)00058-X.

Heindel T.J., Ramadhyani S. and Incropera F.P., Conjugate natural convection from an array of discrete heat sources: part 2 — a numerical parametric study, International Journal of Heat and Fluid Flow, Volume 16, Issue 6,1995,Pages 511-518,ISSN 0142-727X,https://doi.org/10.1016/0142-727X(95)00057-W.

Ichimiya K. and Saiki H., (2005), Behaviour of thermal plumes from two heat sources in an enclosure, International Journal of Heat and Mass Transfer 48(16), 3461–3468.

Ismagilov R.F., Rosmarin D., Gracias D.H., Stroock A.D., and Whitesides G.M., (2001), Competition of intrinsic and topographically imposed patterns in Bénard–Marangoni convection, Applied Physics Letters, 79(3), 439-441.

Jeffreys H., " LXXVI. The stability of a layer of fluid heated below ," *The London, Edinburgh, and Dublin Philosophical Magazine and Journal of Science*, vol. 2, no. 10, pp. 833–844, Oct. 1926, doi: 10.1080/14786442608564114.

Jones, A.D.W. (1983b) Spoke patterns, J. Cryst. Growth, 63, 70-76

Kaddeche S., Henry D. and Ben Hadid H., (2003), Magnetic stabilization of the buoyant convection between infinite horizontal walls with a horizontal temperature gradient, J. Fluid Mech., 480: 185-216.

Kelly R.E., "Mixed mode convection in an inclined slot," *J Fluid Mech*, vol. 246, pp. 545–568, 1993, doi: 10.1017/S0022112093000266.

Khan, S., Wang, K., Yuan, G. ul Haq M., Wu Z., Usman M., Song C., Han G. and Liu Y., (2017), Marangoni effect induced macro porous surface films prepared through a facile sol-gel route, Sci Rep 7, 5292. https://doi.org/10.1038/s41598-017-05506-7

Koschmieder E. L., (1993), Bénard Cells and Taylor Vortices. Cambridge University Press, 1993.

Krishnamurti R., (1970a), "On the Transition to Turbulent Convection: Part 1, the transition from two- to three-dimensional flow", J. Fluid Mech., 42: 295-307.

Krishnamurti R., (1970b), "On the Transition to Turbulent Convection: Part 2, the transition to time-dependent flow", J. Fluid Mech., 42: 309-320.

Krishnamurti R., (1973), "Some further studies on the transition to turbulent convection", J. Fluid. Mech., 60: 285-303.

Krishnamurti R., “On the transition to turbulent convection. Part 2. The transition to time-dependent flow,” *J Fluid Mech*, vol. 42, no. 2, pp. 309–320, Jun. 1970, doi: 10.1017/S0022112070001283.

Krmpotic D., Mindlin G.B., Pérez-García C., (1996), “Bénard-Marangoni convection in square containers”, Phys. Rev. E., 54(4): 3609-3613.

Kvarving A. M., Bjøntegaard T. and Rønquist E. M., (2012), On Pattern Selection in Three-Dimensional Bénard-Marangoni Flows, Commun. Comput. Phys., 11(3), 893-924. doi: 10.4208/cicp.280610.060411a

Lappa M. (2018), On the Formation and Propagation of Hydrothermal waves in Solidifying Liquid Layers, Computers & Fluids, 172, 741-760

Lappa M. and Ferialdi H., (2017), On the Oscillatory Hydrodynamic Instability of Gravitational Thermal Flows of Liquid Metals in Variable Cross-section Containers, Phys. Fluids, 29(6), 064106 (19 pages).

Lappa M. and Ferialdi H., (2018), Multiple solutions, Oscillons and Strange Attractors in Thermoviscoelastic Marangoni Convection, Physics of Fluids, 30(10), 104104 (19 pages).

Lappa M., (1997), Strategies for parallelizing the three-dimensional Navier-Stokes equations on the Cray T3E, Science and Supercomputing at CINECA, 11: 326-340.

Lappa M., (2005a), “On the nature and structure of possible three-dimensional steady flows in closed and open Parallelepipedic and cubical containers under different heating conditions and driving forces”, Fluid Dynamics & Materials Processing, 1(1): 1-19. DOI: 10.3970/fdmp.2005.001.001

Lappa M., (2005b) “Thermal convection and related instabilities in models of crystal growth from the melt on earth and in microgravity: Past history and current status”, Cryst. Res. Technol., 40(6): 531-549. DOI 10.1002/crat.200410381

Lappa M., (2009), Thermal Convection: Patterns, Evolution and Stability, John Wiley & Sons, Ltd (2009, Chichester, England).

Lappa M., (2012), Rotating Thermal Flows in Natural and Industrial Processes, John Wiley & Sons, Ltd (2012, Chichester, England).

Lappa M., (2016), On the onset of multi-wave patterns in laterally heated floating zones for slightly supercritical conditions, Phys. Fluids, 28(12): 124105 (22 pages).

Lappa M., (2017), On the oscillatory hydrodynamic modes in liquid metal layers with an obstruction located on the bottom, Int. J. Thermal Science, 118: 303–319.

Lappa, M. 2019a, On the highly unsteady dynamics of multiple thermal buoyant jets in cross flows. Phys. Fluids 31, 115105.

Lappa, M. 2019*b* A mathematical and numerical framework for the simulation of oscillatory buoyancy and Marangoni convection in rectangular cavities with variable cross section, Chapter 12. In *Computational Modeling of Bifurcations and Instabilities in Fluid Mechanics* (ed. A. Gelfgat), Springer Mathematical Series, 2018, Part of the Computational Methods in Applied Sciences book Series - Computmethods, volume 50, pp. 419–458. ISBN 978-3-319-91493-0.

Lappa, M. 2019*c*, On the gravitational suppression of hydrothermal modes in liquid layers with a blockage on the bottom wall. *Intl J. Therm. Sci.* 145, 105987

Leonardi S. and Castro I.P., (2010), Channel flow over large cube roughness: a direct numerical simulation study, J. Fluid Mech., 651, 519–539.

Lipps, F.B., (1971) Two-dimensional numerical experiments in thermal convention with vertical shear, J. Atm. Sci, 28, 3-19.

Liu Y. and Phan-Thien N., (2000), An Optimum Spacing Problem for Three Chips Mounted on a Vertical Substrate in an Enclosure, Numer. Heat Transfer, Part A, 37(6), 613–630.

Malkus, W. V. R. and Veronis, G., “Finite amplitude cellular convection”, Journal of Fluid Mechanics, vol. 4, pp. 225–260, 1958. doi:10.1017/S0022112058000410.

McLaughlin J.B. and Orszag S.A., (1982), “Transition from periodic to chaotic thermal convection”, J. Fluid Mech., 122: 123-142.

Medale M. and Cerisier P. , (2002), Numerical simulation of Bénard-Marangoni convection in small aspect ratio containers. Numerical Heat Transfer, Part A, 42:55–72.

Meinders E. and Hanjalic K., (1999), Vortex structure and heat transfer in turbulent flow over a wall-mounted matrix of cubes, Int. J. Heat Fluid Flow, 20 (3), 255–267.

Meinders E.R., Van Der Meer T.H. and Hanjalic K., ‘’Local convective heat transfer from an array of wall-mounted cubes,’’ International Journal of Heat and Mass Transfer, Volume 41, Issue 2,1998,Pages 335-346,ISSN 0017-9310, https://doi.org/10.1016/S0017-9310(97)00148-8.

Melnikov D.E. and Shevtsova V.M., (2005), Liquid Particles Tracing in Three-dimensional Buoyancy-driven Flows, Fluid Dyn. Mater. Process., 1(2): 189-200.

Mizev A.I. and Schwabe D., “Convective instabilities in liquid layers with free upper surface under the action of an inclined temperature gradient,” *Physics of Fluids*, vol. 21, no. 11, pp. 1–12, 2009, doi: 10.1063/1.3251755.

Mukutmoni D. and Yang K. T., 1993a, “Rayleigh-Benard Convection in a Small Aspect Ratio Enclosure: Part I—Bifurcation to Oscillation Convection,” *ASME JOURNAL OF HEAT TRANSFER*, Vol. 115, pp. 360–366.

Mukutmoni D. and Yang K. T., 1993b, “Rayleigh-Benard Convection in a Small Aspect Ratio Enclosure: Part I—Bifurcation to Choas,” *ASME JOURNAL OF HEAT TRANSFER*, Vol. 115, pp. 367–376.

Nadjib H., Adel S., Djamel S. and Abderrahmane D., (2018), Numerical Investigation of Combined Surface Radiation and Free Convection in a Square Enclosure with an Inside Finned Heater, FDMP, 14(3) 155-175.

Nakayama H., Takemi T., and Nagai H., (2011), “LES analysis of the aerodynamic surface properties for turbulent flows over building arrays with various geometries”, J. Appl. Meteorol. Climatol. 50, 1692–1712.

Nepomnyashchy A., and Simanovskii I., (1995), Oscillatory convection instabilities in systems with an interface, International Journal of Multiphase Flow, 21, 129-139

Nepomnyashchy A.A., Simanovskii I. B. and Braverman L. M., (2001), "Stability of thermocapillary flows with inclined temperature gradient", J. Fluid Mech., 442: 141-155

Nield, D. (1964). Surface Tension and buoyancy effects in cellular convection. *Journal of fluid mechanics,* 19(3), 341-352. doi:10.1017/S0022112064000763

Nitschke K. and Thess A.(1995), Secondary instability in surface-tension-driven Bénard convection, Physical Review E, 52:5772–5775.

Ondarcuhu T., Mindlin G. B., Mancini H. L., and Pérez García C., (1993a), "Dynamical patterns in Bénard-Marangoni convection in a square container", Phys. Rev. Lett. 70: 3892–3895.

Palm E., (1960), “On the tendency towards hexagonal cells in steady convection”, J. Fluid Mech., 8: 183-192.

Parm Mann, (2018). ASUS Marine Cool motherboard struts its stuff. Available at: https://m.hexus.net/tech/news/mainboard/17429-asus-marine-cool-motherboard-struts-stuff/ [Accessed 10 Aug. 2022].

Parmentier P.M., Regnier V.C., and Lebon G., (1996), “Nonlinear analysis of coupled gravitational and capillary thermoconvention in thin fluid layers", Phys. Rev. E 54: 411–423.

Patne R., Agnon Y. and Oron A., (2021), Thermocapillary instabilities in a liquid layer subjected to an oblique temperature gradient, J. Fluid Mech., 906, A12.

Pearson, J.R.A., (1958), On convection cells induced by surface tension, J. Fluid Mech., 4: 489- 500, doi: 10.1017/S0022112058000616.

Pellew, A., & Southwell, R. V. (1940). On Maintained Convective Motion in a Fluid Heated from below. *Proceedings of the Royal Society of London. Series A, Mathematical and Physical Sciences, 176*(966), 312–343. http://www.jstor.org/stable/97537

Piccolo C., Lappa M., Tortora A. and Carotenuto L., (2002), “Non-linear behaviour of lysozyme crystallization”, Physica A: Statistical Mechanics and its Applications, 314(1-4): 636-645.

Plapp B.B., (1997), “Spiral Pattern Formation in Rayleigh-Bénard Convection”, Ph.D. Thesis, Cornell University, Ithaca, NY

Plapp B.B., Egolf D.A., Bodenschatz E. and Pesch W., Dynamics and selection of giant spirals in Rayleigh–Bénard convection, Phys. Rev. Lett. 81 (1998) 5334–5337

Polentini, M. S., Ramadhyani, S. and Incropera, F. P. 1993. Single-phase thermosyphon cooling of an array of discrete heat sources in a rectangular cavity. Int. J. Heat Mass Transfer, 36, 3983- 3996

Rahman M.M., Alim M. A., Saha S. and Chowdhury M. K., (2008), Numerical study of mixed convection in a square cavity with a heat conducting square cylinder at different locations, Journal of Mechanical Engineering, Vol. ME39, No. 2, December 2008

Richter, F.M., (1973) Convection and the large-scale circulation of the mantle, J. Geophys. Res., 78, 8735-8745.

Saeedi M. and Wang B.-C., (2015), Large-eddy simulation of turbulent flow and dispersion over a matrix of wall-mounted cubes, Phys. Fluids, 27 (11), 115104.

Sakhy R. E., Omari K. E., Guer Y. L. and Blancher S., (2014), "Rayleigh-Benard-Marangoni convection in an open cylindrical container heated by a non-uniform flux", *Int. J. Thermal Sci*., 86, 198.209.

Sezai A.A.M., (2000), Natural convection from a discrete heat source on the bottom of a horizontal enclosure, Int. J. Heat Mass Transfer 43 (2000) 2257–2266.

Shadid J.N. and Goldstein R.J., (1990), "Visualization of longitudinal convection roll instabilities in an inclined enclosure heated from below", J. Fluid Mech., 215, 61-84

Shevtsova V., Melnikov D.E., Nepomnyashchy A., (2009), New flow regimes generated by mode coupling in buoyant-thermocapillary convection, Phys. Rev. Lett, 102: 134503.

Shevtsova V.M., Nepomnyashchy A.A. and Legros J.C., (2003), "Thermocapillary-buoyancy convection in a shallow cavity heated from the side", Phys. Rev. E 67, 066308 (14 pages).

Shklyaev O.E. and Nepomnyashchy A.A., (2004),Thermocapillary flows under an inclined temperature gradientJ. Fluid Mech., 504, 99–132.

Strikwerda J.C., Lee Y.S. and Numer Anal S.J., "THE ACCURACY OF THE FRACTIONAL STEP METHOD," SIAM journal on numerical analysis, vol. 37, Iss.1 (1999), doi:10.1137/S0036142997326938

Subramanian P., Brausch O., Daniels K.E., Bodenschatz E., Schneider T.M. and Pesch W., (2016), Spatio-temporal patterns in inclined layer convection, J. Fluid Mech., 794, 719-745.

Thess A. and Bestehorn M., (1995), "Planform selection in Bénard-Marangoni convection: l hexagons versus g hexagons", Phys. Rev. E, 52: 6358-6367.

Thess A. and Orszag S.A., (1994), Temperature spectrum in surface tension driven Benard convection, Phys. Rev. Lett. 73, 541-544.

Thess A. and Orszag S.A., (1995), Surface-tension-driven Benard convection at infinite Prandtl number, J. Fluid Mech. 283, 201-230.

Thess A., Spirn D. and Jiittner B., (1995), Viscous flow at infinite Marangoni number, Phys. Rev. Lett. 75, 4614-4617.

Thess A., Spirn D. and Jiittner B., (1996), A two-dimensional model for slow convection at infinite Marangoni number, J. Fluid Mech. 331, 283-312.

Thorpe, S. A., (1987) Transitional phenomena and the development of turbulence in stratified fluids: A review, J. Geophys. Res. 92C, 5231-5248.

Thual O., (1992), "Zero-Prandtl-number convection", J. Fluid Mech., 240: 229-258.

Tso, C. P., Jin L. F., Tou S. K. W. and Zhang X. F., (2004), Flow pattern in natural convection cooling from an array of discrete heat sources in a rectangular cavity at various orientations, International Journal of Heat and Mass Transfer 47(19-20), 4061-4073.

Tyacke J. and Tucker P., "LES of heat transfer in electronics," *Appl Math Model*, vol. 36, no. 7, pp. 3112–3133, Jul. 2012, doi: 10.1016/j.apm.2011.09.072.

Ueno I., Kurosawa T. and Kawamura H., (2002), "Thermocapillary Convection in Thin Liquid Layer with Temperature Gradient Inclined to Free Surface", IHTC12, Grenoble, France 18-23 Aug, 2002

Wang Y., ZongkaiYu Z., Mei D., Xue D., (2017), Fabrication of Micro-wavy Patterned Surfaces for Enhanced Cell Culturing, Procedia CIRP, Volume 65, 2017, Pages 279-283

Weber J.E., "On the stability of thermally driven shear flow heated from below," *J Fluid Mech*, vol. 87, no. 1, pp. 65–84, 1978, doi: 10.1017/S0022112078002931.

Widawski G., Rawiso M. and François B., (1994), Self-organized honeycomb morphology of star-polymer polystyrene films, Nature 369, 387-389.

Yaghoubi M. and Velayati E., (2005), Undeveloped convective heat transfer from an array of cubes in cross-stream direction, Int. J. Thermal Sci., 44 (8), 756–765

Zhao B, Moore JS, Beebe DJ. Surface-directed liquid flow inside microchannels. Science. 2001 Feb 9;291(5506):1023-6. doi: 10.1126/science.291.5506.1023. PMID: 11161212.